2009

Chaotic scattering in an open vase-shaped cavity: Topological, numerical, and experimental results

Jaison Allen Novick
College of William & Mary - Arts & Sciences

Chaotic Scattering in an Open Vase-shaped Cavity: Topological, Numerical, and Experimental Results

Jaison Allen Novick

West Mifflin, Pennsylvania

Master of Science, The College of William and Mary, January 2004
Bachelor of Science, Saint Vincent College, May 2002

A Dissertation presented to the Graduate Faculty
of the College of William and Mary in Candidacy for the Degree of
Doctor of Philosophy

Department of Physics

The College of William and Mary
August 2009

APPROVAL PAGE

This Dissertation is submitted in partial fulfillment of
the requirements for the degree of

Doctor of Philosophy

Jaison Allen Novick

Approved by the Committee, May, 2009

Committee Chair
Professor John Delos, Physics
The College of William & Mary

Professor Carl Carlson, Physics
The College of William & Mary

Professor Henry Krakauer, Physics
The College of William & Mary

Professor Eugene Tracy, Physics
The College of William & Mary

Professor Stephen Knudson, Chemistry
The College of William & Mary

ABSTRACT PAGE

We present a study of trajectories in a two-dimensional, open, vase-shaped cavity in the absence of forces. The classical trajectories freely propagate between elastic collisions. Bound trajectories, regular scattering trajectories, and chaotic scattering trajectories are present in the vase. Most importantly, we find that classical trajectories passing through the vase's mouth escape without return. In our simulations, we propagate bursts of trajectories from point sources located along the vase walls. We record the time for escaping trajectories to pass through the vase's neck. Constructing a plot of escape time versus the initial launch angle for the chaotic trajectories reveals a vastly complicated recursive structure or a fractal. This fractal structure can be understood by a suitable coordinate transform. Reducing the dynamics to two dimensions reveals that the chaotic dynamics are organized by a homoclinic tangle, which is formed by the union of infinitely long, intersecting stable and unstable manifolds.

This study is broken down into three major components. We first present a topological theory that extracts the essential topological information from a finite subset of the tangle and encodes this information in a set of symbolic dynamical equations. These equations can be used to predict a topologically forced minimal subset of the recursive structure seen in numerically computed escape time plots. We present three applications of the theory and compare these predictions to our simulations. The second component is a presentation of an experiment in which the vase was constructed from Teflon walls using an ultrasound transducer as a point source. We compare the escaping signal to a classical simulation and find agreement between the two. Finally, we present an approximate solution to the time independent Schrödinger Equation for escaping waves. We choose a set of points at which to evaluate the wave function and interpolate trajectories connecting the source point to each "detector point". We then construct the wave function directly from these classical trajectories using the two-dimensional WKB approximation. The wave function is Fourier Transformed using a Fast Fourier Transform algorithm resulting in a spectrum in which each peak corresponds to an interpolated trajectory. Our predictions are based on an imagined experiment that uses microwave propagation within an electromagnetic waveguide. Such an experiment exploits the fact that under suitable conditions both Maxwell's Equations and the Schrodinger Equation can be reduced to the Helmholtz Equation. Therefore, our predictions, while compared to the electromagnetic experiment, contain information about the quantum system. Identifying peaks in the transmission spectrum with chaotic trajectories will allow for an additional experimental verification of the intermediate recursive structure. Finally, we summarize our results and discuss possible extensions of this project.

-Table of Contents-

This work is dedicated to my mother Karen Kochmar, my grandmother Joyce Kochmar, and in loving memory of my grandfather John G. Kochmar

Acknowledgements

First, I would like to thank Dr. John Delos, my research advisor, for his guidance over the past five years. I thank Dr. Mathew Len Keeler for finding this project interesting enough to take on the laborious task of constructing the vase. I thank Nathan Baillie for all the good times that have kept me sane throughout this "adventure". Finally, and most importantly, the greatest thanks are extended to the Kochmar family: Mom, grandma, Daryl, Johnny, Sally, Michael, Danny, Kathy, Ted, Ashleigh, Alyssa, and Jessica. I thank you for the love, support, and rear-end prodding. *You're the only family I've ever known and the only family I'll ever need.*

-Introduction-

We present a study of an open chaotic dynamical system. A chaotic dynamical system is one that exhibits sensitive dependence on the initial conditions. This means that two nearby trajectories will remain close for some finite amount of time, but eventually, the two trajectories will begin to diverge such that as time approaches infinity, the two trajectories will be far away from each other. We will examine the dynamics of a specularly reflecting, open vase-shaped cavity. Reflections off the boundary respect the law of reflection, and the lack of forces results in free-particle motion between successive reflections. The vase is a simple open system in which both ray chaos and wave chaos can be studied. Also, the behavior of rays in the vase is surprisingly similar to the behavior of classical trajectories of an election in a hydrogen atom in constant parallel electric and magnetic fields [1]. The vase is essentially a macroscopic analogue of the hydrogen system and therefore it functions as an experimental tool to study the interesting phenomenon predicted for the hydrogen system.

Let us consider the atomic system first. Mitchell et al. [1-4] studied the ionization of electron trajectories launched from the nucleus. They showed that under a suitable set of transformations, one can find an unstable periodic orbit (UPO) near a saddle point in the potential energy. Points intersecting the UPO escape without return. Furthermore, near the nucleus, the electric potential dominates, leading to a potential well that contains orbits that are bound forever. Other trajectories can circulate within

the well for any length of time before escaping. Let us now consider a few sample trajectories and their counterparts in the vase.

The left side of Figure 0.1 shows the potential contours and several ionizing trajectories launched from the proton, and the right side shows the analogous rays in the vase. On the left are the potential contours in cylindrical coordinates. The blue line is the unstable periodic orbit that divides the "bound" regions from the "free" regions of phase space. On the right, the unstable periodic orbit is the vertical ray connecting the two points in the vase's neck at which the tangent lines are horizontal. We see that the magenta trajectories escape directly. The red trajectories approach the UPO, but are turned back; then on a second approach to the UPO, they escape. The green trajectories are similar, but they have an additional up and down oscillation before being turned back.

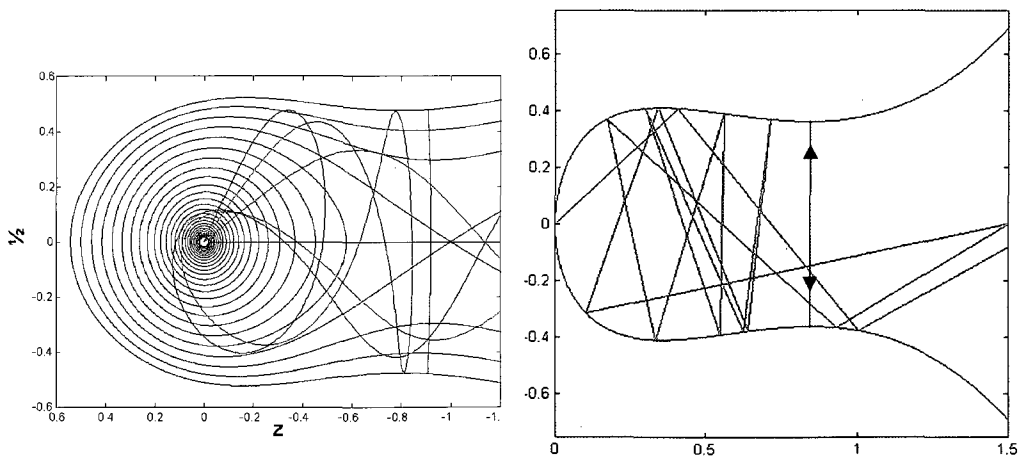

Figure 0.1: Trajectories in the H atom and the vase. The figure on the left can be found in [4,5].

Each of these systems possess regular and chaotic trajectories, the latter possessing a vastly complex structure. To reveal this structure, we consider an ensemble

of trajectories launched from a point, and examine the time for trajectories to intersect the UPO. For the atomic system, Mitchell et al. considered a burst of electronic trajectories launched from the vicinity of the nucleus. The initial conditions were parameterized by a launch angle. A detector array was imagined to lie past the UPO. They constructed a plot of the initial launch angle versus the arrival times for the escaping trajectories which is shown in Figure 0.2. In each figure, the horizontal axis is the initial launch angle θ. Figure 0.2a shows the continuous time for ionizing trajectories to reach the detector. The portion of the escape time shown is decomposed into a series of convex regions called *icicles*. Figure 0.2b shows a series of line segments in which each segment matches to an icicle. Each of these so-called *escape segments* counts the "number of iterates" to escape and represents a rectified icicle. (In Chapter 2, we will give a more rigorous definition of an escape segment.) Figure 0.2c is a magnification of the region $\theta \in [2.08, 2.24]$. It hints at the presence of a recursive structure lying within these escape time plots.

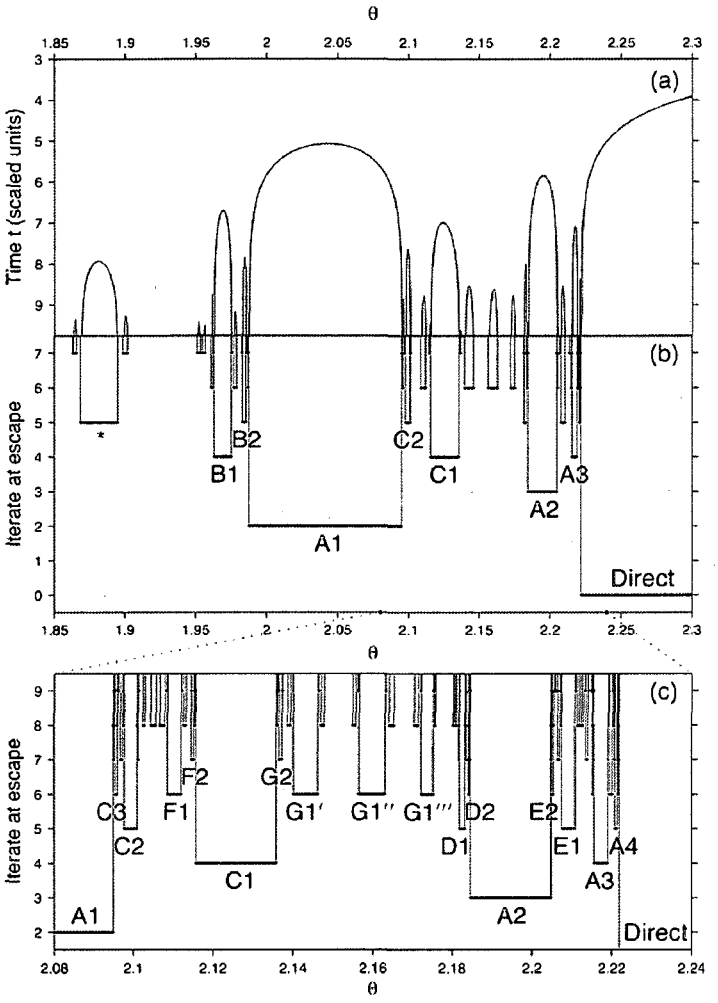

Figure 0.2: Figure 1 of [1]. In each figure, the horizontal axis is the angle at which an electron is launched from the nucleus. a.) Time to arrive at a detector. b.) corresponding iterates to escape. c.) Magnification of a region in b.

For the vase (as for the hydrogen system) we study the escape time. We launch a family of trajectories from a point on the upper wall. The initial launch angles form a half disk bounded by the tangent to the burst point. The initial velocities, set to unity, are uniformly parameterized by a polar angle. We choose a point x_D past the UPO and imagine a vertical line detector spanning the space between the walls at x_D. We record

the time to reach x_D, and plot this escape time versus the initial launch angle. Figure 0.3 shows the escape time for a burst of trajectories.

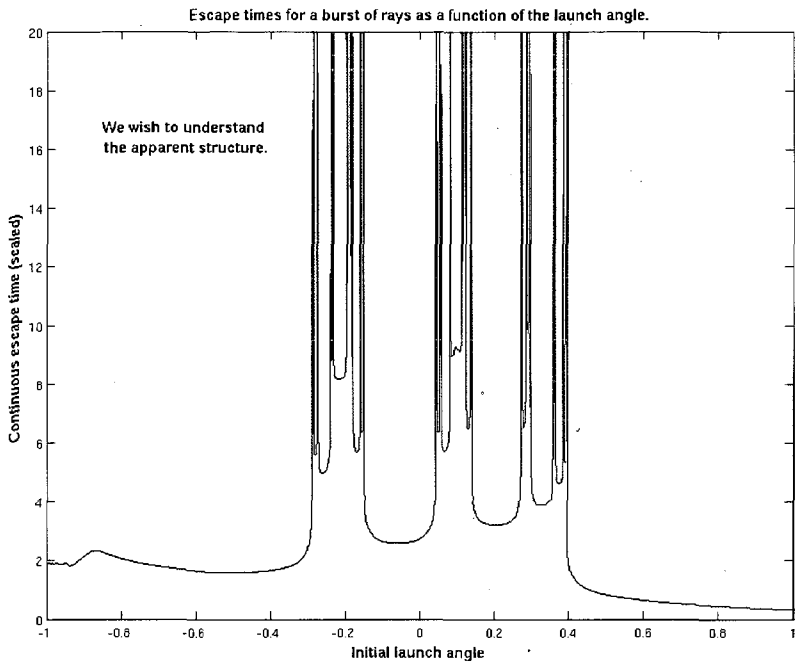

Figure 0.3: Escape time plot for a burst of trajectories.

A subset of the escape time plot for the vase is organized into collections of icicles. These regions hang down from infinity. Each icicle is in fact bounded by two trajectories that oscillate in the vase's neck forever, asymptotically converging to the UPO. Furthermore, the icicles are organized into infinitely long sequences where each sequence, called an *epistrophe*, converges to the endpoint of another icicle. We will now show that a complicated recursive structure lies in the escape time plot. Let us now magnify one region of Figure 0.3 and see the structure that appears.

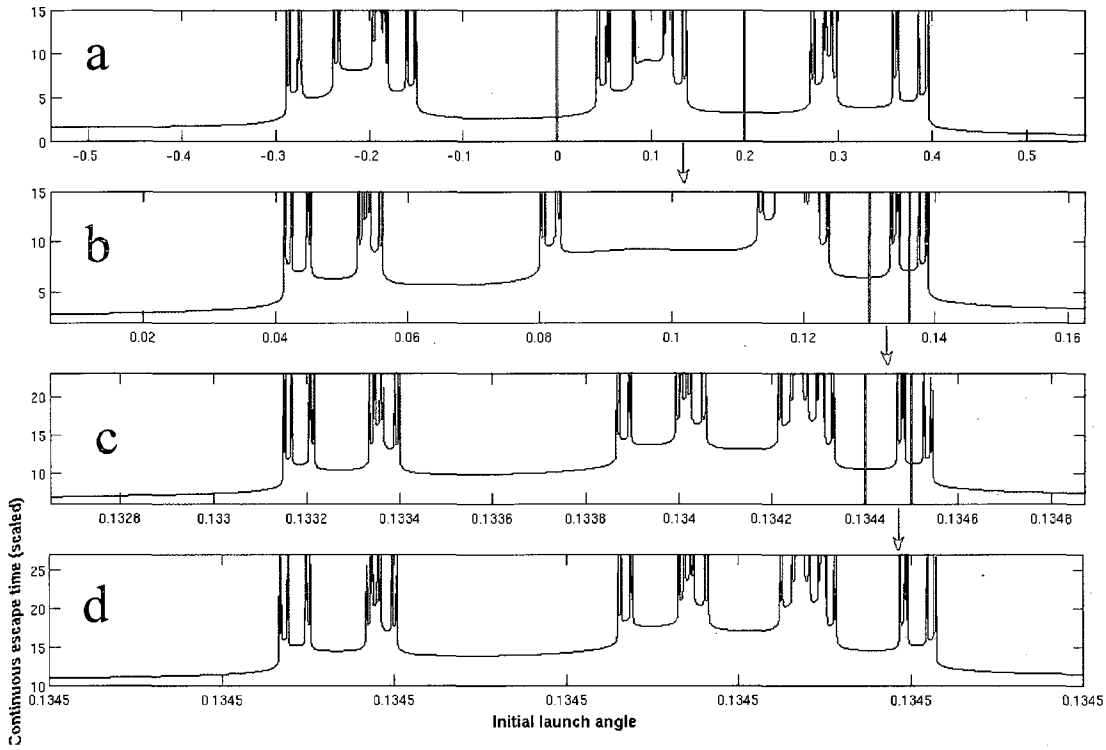

Figure 0.4: Magnifications of regions in Figure 0.3.

Figure 0.4a is a magnification of Figure 0.3. We magnify the region bounded by the red, vertical line segments and obtain Figure 0.4b. We see many more sequences of icicles. Furthermore, the two figures do *not* look as if they share a scaling factor. Again, we magnify the region bounded by the red, vertical line segments and shift our attention to Figure 0.4c. Again, we see the recursive appearance of additional sequences but the arrangements of the sequences are different compared to Figures 0.4a and 0.4b. Finally, we move to Figure 0.4d and we find something surprising. Again we see that there are more sequences present, yet we also see that the last two figures have almost identical arrangements. We conclude from Figure 0.4 that these escape time plots possess a vastly complicated recursive structure. We can now state one goal of this study: *Our*

goal is to compute a minimal subset of the recursive structure seen in numerically computed escape time plots.

This study is organized into five chapters as follows. In Chapter 1, we will discuss the fundamentals of the vase. Specifically, we will see how to numerically propagate trajectories and we will see a coordinate transformation that reveals the complicated structure underlying the vase. In Chapter 2, we will examine a topological theory that generates a set of symbolic dynamical equations describing the evolution of chaotic systems similar to the vase. In Chapter 3, these dynamical equations will be used to predict minimal subsets of numerically computed sets of escape segments. Chapter 4 is an analysis of the results from Chapter 3. Finally, in Chapter 5, we will examine experimental and numerical results of the vase.

-Introduction References-

[1] K. A. Mitchell and J. B. Delos, Physica D **229**, 9 (2007).

[2] K. A. Mitchell, J.P. Handley, B. Tighe, A. Flower, and J. B. Delos, Phys. Rev. A **70**, 043407 (2004).

[3] J. B. Delos, K. A. Mitchell, Few-Body Systems **0**, 1 (2005).

[4] K. A. Mitchell, J. P. Handley, B. Tighe, A. Flower, and J. B. Delos, Phys. Rev. Lett. **92**, 073001 (2004).

[5] P. Hansen, K. A. Mitchell, and J. B. Delos Phys. Rev. E **73**, 066226 (2006).

-Chapter 1-
The Vase: Part I

i.) Introduction

We begin our discussion of the vase. Here, we discuss how to numerically propagate large families of trajectories, and we give examples of the different kinds of trajectories present in the vase. Since this system is two-dimensional, the corresponding phase space for rectilinear motion is four-dimensional. We present a coordinate transformation that reduces the analysis to two dimensions. A brief introduction to how the chaotic trajectories are organized is given. It is meant as an introduction to the material in Chapter 2, which will give a more thorough explanation of the chaotic trajectories.

ii.) Fundamentals of the Vase

a.) Vase Boundary

The vase is shown in Figure 1.1 below. The vase walls are given by the function

$$y(x) = \pm\sqrt{x}\left(\frac{w}{2} + A(x-1)^2\right) = \pm f(x) \qquad (1.1)$$

The parameter w controls the neck's width and A controls how much the vase lips flare outward. In choosing the parameter values, we tried several set of values and looked for a pair that generated an early onset of chaos. We found that A, w = 0.75 were suitable, and from now on, A and w are fixed at these values. Figure 1 shows that within the vase's neck and bowl, there is a pair of points, both symmetric about the x-axis, for which $y'(x) = 0$. One can imagine a vertical ray connecting either pair of symmetric critical points. The ray lying within the vase's bowl is a stable periodic orbit (SPO),

while the one in the neck is an unstable periodic orbit (UPO). A bundle of rays emanating from the vase wall at the UPO will diverge due to intersections with the concave segments of the boundaries. This UPO is crucial to our analysis because *if a ray is launched from the interior of the vase and intersects the UPO, then the ray will escape without return.* We will see other orbits that bounce up and down in the vase's neck, approach the UPO, and then return into the vase's bowl. Hence the UPO can be called a repellor.

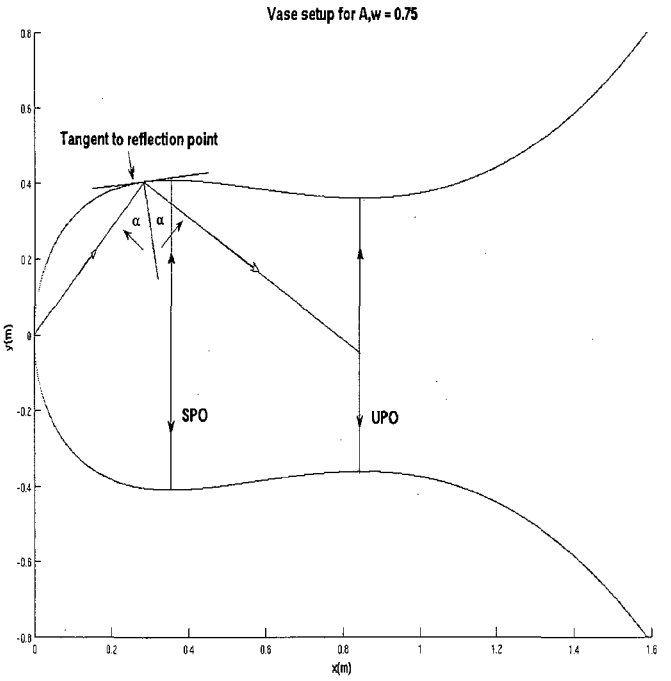

Figure 1.1: The vase for A, w = 075, a sample ray, the SPO, and the UPO

The physical laws governing ray propagation are simple. No forces are present so we have free particle propagation between reflections. When a ray hits the vase wall, the law of reflection determines the outgoing velocity. For an arbitrary smooth curved surface, the law of reflection is

$$\mathbf{v}_1 = 2\left\langle \mathbf{v}_0, \hat{\mathbf{T}} \right\rangle \hat{\mathbf{T}} - \mathbf{v}_0 \tag{1.2}$$

where $\mathbf{v}_0$ is the incoming velocity, $\mathbf{v}_1$ the outgoing velocity, and $\hat{\mathbf{T}}(x)$ is a unit vector tangent to the vase wall at the reflection point. $\hat{\mathbf{T}}(x)$ can be calculated from the derivative of the vase boundary. Examining eq. (1.1) shows that $y'(x)$ contains a factor of $1/\sqrt{x}$ resulting in $y'(x) \to \infty$ as $x \to 0$. Since we want $\hat{\mathbf{T}}(x)$ to be finite, we must carefully choose the representation of the boundary wall so that the derivative is finite, i.e. we use either $dy(x)/dx$ or $dx(y)/dy$. In his thesis, Hansen [2] examined the numerical errors in computing the derivatives using either x or y as the independent variable. He found that a useful cutoff is $\frac{x_{SPO}}{3} = x_{cutoff}$. That is to say, for $x \geq x_{cutoff}$, we use x as the independent variable and y as the independent variable otherwise. For our vase, this corresponds to a cutoff of about 0.12. Therefore, the tangent vector assumes one of the two following forms.

$$\hat{\mathbf{T}}(x) = \frac{1}{\sqrt{1+f'(x)^2}} \begin{pmatrix} 1 \\ \pm f'(x) \end{pmatrix} \text{ for } x \geq x_{cutoff}$$
$$\hat{\mathbf{T}}(x) = \frac{1}{\sqrt{1+\frac{1}{f'(x)^2}}} \begin{pmatrix} \pm\frac{1}{f'(x)} \\ 1 \end{pmatrix} \text{ for } x < x_{cutoff} \tag{1.3}$$

As we traverse the boundary wall from $y = -\infty$ to $y = \infty$, this definition of $\hat{\mathbf{T}}(x)$ possesses a clockwise orientation. Thus, for example, $\hat{\mathbf{T}}(0) = (0, 1)$, $\hat{\mathbf{T}}(x_{UPO}) = (0, \pm 1)$ where the plus and minus correspond to the upper and lower boundaries, respectively.

b.) Ray Propagation

Before we describe the different types of trajectories we find in the vase, we will explain how we propagate rays. Between reflections, rays propagate according to the kinematic equations.

$$\mathbf{r_f} = \mathbf{r_0} + \mathbf{v}t \tag{1.4}$$

In eq. (1.4), t is the propagation time, **v** is the constant velocity vector, and $\mathbf{r_0}$ and $\mathbf{r_f}$ are the initial and final position vectors, respectively. To compute the time between two reflections, we first insert eq. (1.4) into eq. (1.1).

$$y_0 + v_y t = \sqrt{x_0 + v_x t}\left(\frac{w}{2} + A(x_0 + v_x t - 1)^2\right) \tag{1.5}$$

We then square eq. (1.5) to obtain a 5^{th} order polynomial in the variable t. If we assume that the ray starts on the cavity wall, then $y_0 = f(x_0)$. One can verify that after squaring eq. (1.5), $f^2(x_0)$ appears on the right-hand side resulting in the constant term canceling. Thus, one of the solutions is t = 0 which corresponds to the ray remaining stationary. Dividing by t removes this solution, resulting in a 4^{th} order polynomial. We use Matlab's built-in routine roots to numerically compute the zeros to this "*intersection polynomial*", as it is a fast algorithm and allows us to propagate large ensembles of trajectories in a short time.

In general, the roots of the intersection polynomial can be complex, real negative, and real positive. Complex roots are ignored because they do not represent actual propagation times. Real negative roots are discarded as we are propagating rays forward in time. The real positive roots correspond to future intersections. However, some roots will correspond to a ray that passes out through the boundary and then back in through

the boundary. Therefore, we take the smallest positive real root as the time for the ray to arrive at the next reflection point, and we discard the remaining solutions. If no real positive root exists, then the ray escapes. If there is a reflection, then we compute the reflection point, reflect the incoming velocity vector using eq. (1.2) and eq. (1.3), and then continue the path to the next reflection.

For our simulations, we designate a point on the boundary as a source point. For rays propagating within the vase, the set of allowed velocity vectors spans a half-disk whose diameter is the line tangent to the vase at the source point. We choose a set of initial velocity vectors with unit length lying on this half-disk with uniformly-spaced initial polar launch angles. For each initial velocity, we propagate a ray from the source point for some specified number of reflections. At each reflection, we record its position and the outgoing velocity vector. Our primary interest is the set of rays that escape. Therefore, at some point past the UPO, we imagine a vertical line of detectors that span the space between the vase walls. At this detector line, we halt ray propagation and record the propagation time from the source to the detector. From now on, we fix the source at (0.3, 0.4067) and the detector line at $x = 1.5$.

After we have propagated a family of trajectories and saved those that escaped, we then construct an escape time plot. The escape time for a source at (0.3, 0.4067) is shown below in Figure 1.2. The horizontal axis is the initial velocity component parallel to the tangent line at the source point (called the initial condition in Figure 1.2). The vertical axis is the time required for a path to arrive at the detector line. Each of the well-shaped regions is called an *icicle* and each represents the escape times for a family

of chaotic trajectories. The discontinuities in slope are due to changes in the number of bounces to escape the vase. We will defer an explanation of these discontinuities to Chapter 5.

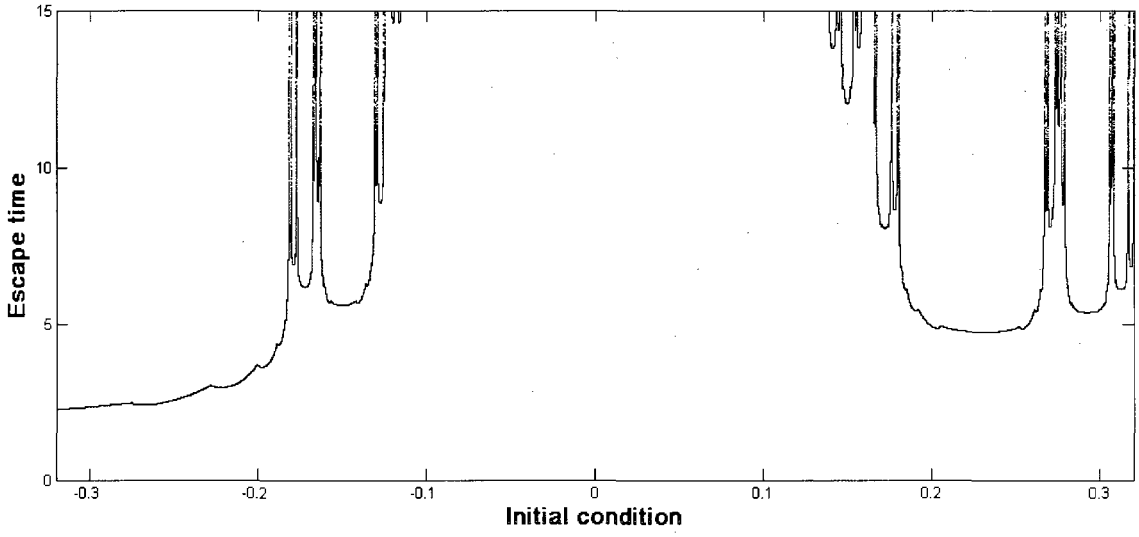

Figure 1.2: Escape time versus initial launch angle for burst launched from (0.3, 0.4067) at a vertical line detector placed at x = 1.5.

c.) Types of Trajectories

Let us now consider the kinds of trajectories that are present in the vase. The trajectories can be broadly categorized as either bound or scattering trajectories. Figure 1.1 shows that there is a stable orbit of period-2 in the vase's bowl. Near this periodic orbit is a collection of stable orbits that remain with the vase's bowl for all time. An example is shown in Figure 1.3a. Stable orbits of larger period also exist. The orbit shown in Figure 1.3b is a stable orbit that lingers near a periodic orbit of period-7.

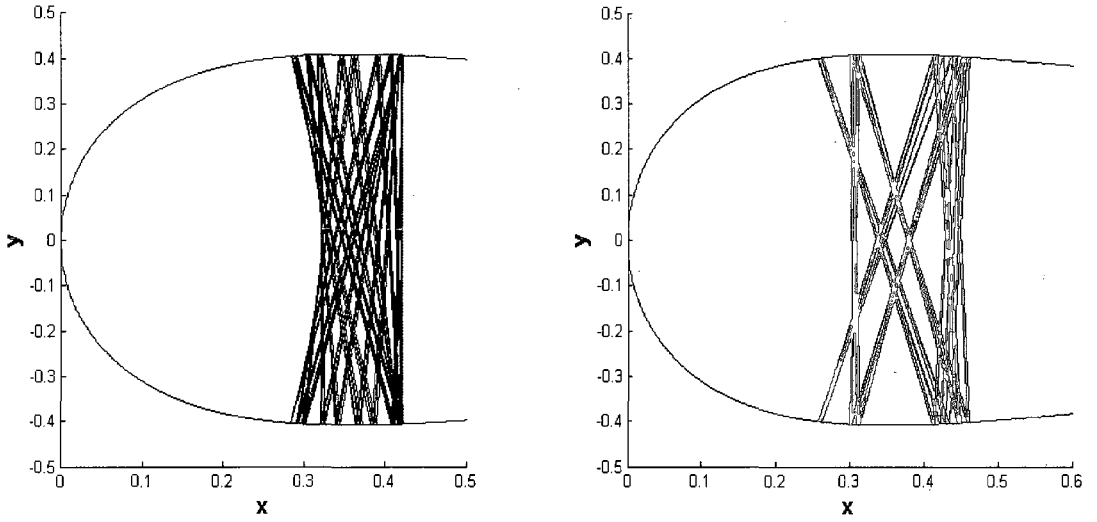

Figure 1.3: Two stable orbits in the convex region.

The other broad category is the set of scattering trajectories. These can be categorized as either regular or chaotic. Since our study focuses on ensembles launched from a point source, we will categorize the trajectories according to their future development. The simplest kinds of escaping trajectories launched from a point source are the direct trajectories. These rays escape the vase without reflecting off the cavity walls. Given a point source, the set of direct rays is a cone bounded by two grazing rays. The two grazing rays can be computed by solving the equation

$$\mathbf{T} \cdot \mathbf{v} = \pm 1 \tag{1.6}$$

This is a non-linear equation that must be solved numerically. A direct ray and two grazing rays are shown in Figure 1.4.

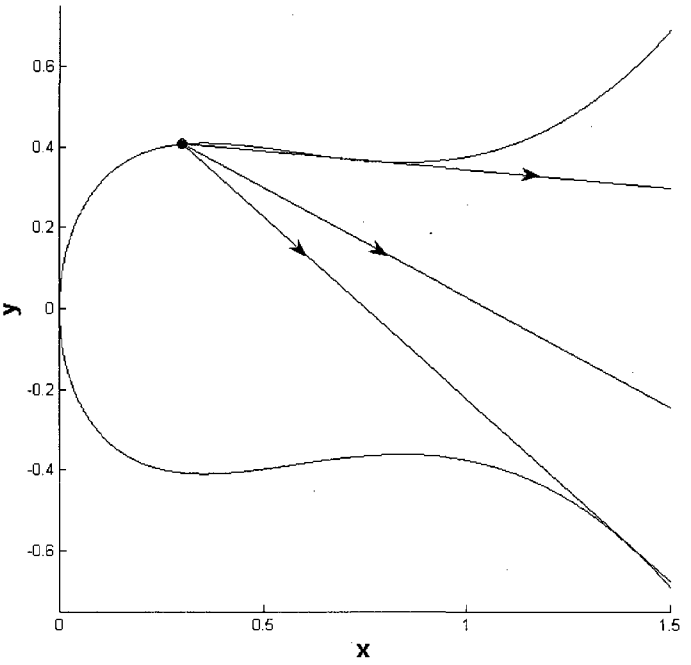

Figure 1.4: Direct ray and two grazing rays.

We also find trajectories that oscillate within the vase's neck any number of times (Figure 1.5). We note that they are similar to the rays that oscillate between two infinitely long, parallel mirrors. In this simple case, one would observe rays that form a sequence of isosceles triangles. For lack of a better term, we will call these parallel mirror rays.

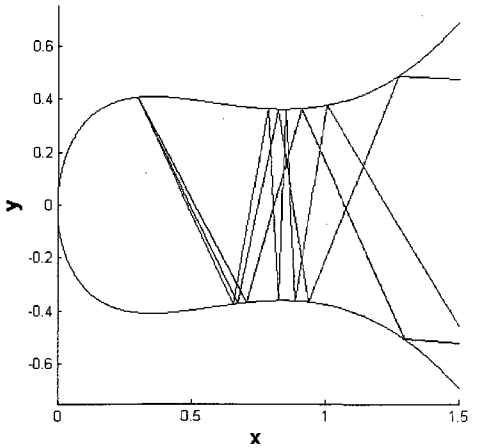

Figure 1.5: Rays oscillating through the vase's neck

Along the convex segments of the boundary walls we find whispering gallery trajectories. These trajectories hug the boundary walls and are essentially polygonal approximations to the convex segments. Given a source point in the convex region of the boundary, we can have whispering gallery trajectories that circulate either clockwise or counterclockwise. Two of these trajectories are shown in Figure 1.6 below.

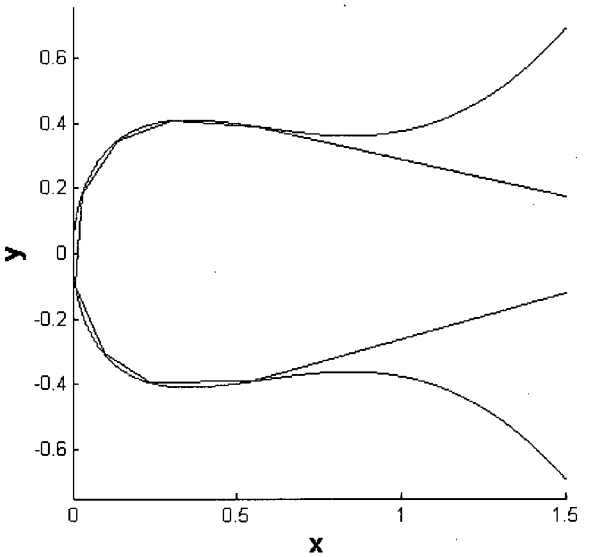

Figure 1.6: Clockwise (red) and counter-clockwise (blue) whispering gallery rays.

Finally, we have chaotic scattering trajectories. These trajectories form a vastly complicated set. A few sentences cannot adequately characterize the chaotic trajectories. We present a single sample trajectory in Figure 1.7 and defer discussing the chaotic trajectories to Chapter 5.

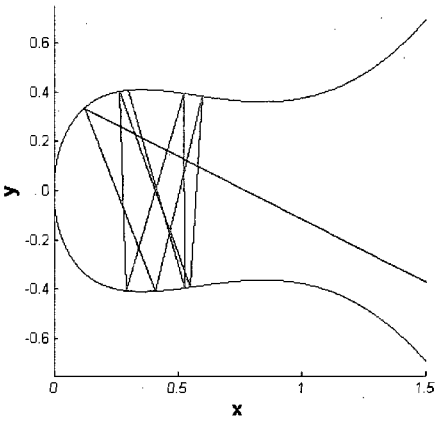

Figure 1.7: A sample of a chaotic trajectory.

iii.) Phase Space Transformation

a.) Coordinate Transformations

We have described how we propagate a ray and given a general classification of the rays found in the vase. Now we can examine the coordinate transformation that reveals the homoclinic tangle. Birckoff introduced the standard coordinates used to study ray propagation within a specularly reflecting cavity. To fully describe a trajectory within the vase, we use a collection of vectors each with four entries. Two of the entries give the position of the reflection and the remaining two give the outgoing velocity. Using this information and the kinematic equations contained in eq. (1.4), one can then construct the entire trajectory. Studying dynamics within a four-dimensional space is cumbersome and does not easily reveal the structure underlying the chaotic trajectories. So we define a pair of coordinates where each coordinate contains the essential information contained in the vectors **r** and **v**. The transformation ignores the free particle propagation and retains the location on the boundary wall and the outgoing

velocity. The position vector is replaced with the signed arclength measured along the vase boundary between the origin and the reflection point.

$$q(x) = \int_0^x dx \sqrt{1 + f'(x)^2} \tag{1.7}$$

The integrand is finite except at $x = 0$, where $f'(x)$ blows up. Therefore, we break up the integral into two pieces. The first piece is an integral evaluated near the origin and uses y as the independent variable. Far enough away from the origin, we can use x as the independent variable. Thus, we use the following sum to compute the arclength for $x > x_{cutoff}$.

$$q(x) = \int_0^{y(x_{cutoff})} dy \sqrt{1 + \left(\frac{dx}{dy}\right)^2} + \int_{x_{cutoff}}^{x} dx \sqrt{1 + \left(\frac{dy}{dx}\right)^2} \tag{1.8}$$

If $x < x_{cutoff}$, then we use the first term of the sum in eq. (1.8) to compute the arclength.

We replace the velocity vector with a number we call the momentum. At a reflection point, we can construct an orthonormal basis using the tangent vector $\hat{\mathbf{T}}(x)$ and the normal vector $\hat{\mathbf{N}}(x)$, an inward pointing unit vector orthogonal to $\hat{\mathbf{T}}(x)$. At the reflection point, we expand the velocity vector in the new basis.

$$\mathbf{v}(x) = v_x \hat{\mathbf{x}}(\hat{\mathbf{T}}(x), \hat{\mathbf{N}}(x)) + v_y \hat{\mathbf{y}}(\hat{\mathbf{T}}(x), \hat{\mathbf{N}}(x)) = v_T \hat{\mathbf{T}}(x) + v_N \hat{\mathbf{N}}(x) \tag{1.9}$$

The velocity component parallel to the tangent vector, v_T, is called the momentum. At each reflection, the momentum is computed by taking the dot product of the outgoing velocity vector and the tangent vector.

$$p = \mathbf{T} \cdot \mathbf{v}_{outgoing} \tag{1.10}$$

(The same momentum results if the outgoing velocity is replaced with the incoming velocity.) Then we use eq. (1.8) and eq. (1.10) to transform a trajectory with n + 1 position and velocity vectors into n+1 arclengths and momenta

$$\begin{pmatrix} \mathbf{r}_0 & \mathbf{v}_0 \\ \mathbf{r}_1 & \mathbf{v}_1 \\ \vdots & \vdots \\ \mathbf{r}_n & \mathbf{v}_n \end{pmatrix} \rightarrow \begin{pmatrix} q_0 & p_0 \\ q_1 & p_1 \\ \vdots & \vdots \\ q_n & p_n \end{pmatrix} \tag{1.11}$$

The transformation just described gives signed arclengths, $-\infty < q < \infty$. We can further simply the transformation by taking into account the mirror symmetry of the vase. If $q < 0$, we replace (q, p) with (-q, -p). This is equivalent to propagating the trajectory within a vase in which the lower boundary is replaced by an infinitely long horizontal mirror. The transformation is shown in Figure 1.9. This additional transformation changes both the SPO and UPO into stable and unstable fixed points. In summary, the dynamics in the vase induces a dynamical mapping on the coordinates (q, p) defined in eq. (1.8) and eq. (1.10). Now we can consider trajectories within this new representation.

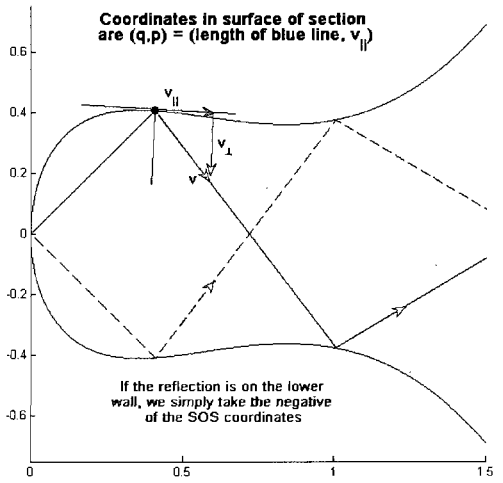

Figure 1.8: Transformation to phase space coordinates.

b.) Stable and Unstable Manifolds

To reveal the interesting structure underlying the vase within the new representation, we propagate points starting near the unstable fixed point. In the new representation, the unstable fixed point is given by the vector (1.1086, 0). We place a rectangle of initial points to the left of this vector. Points with negative momenta are propagated forward while those with positive momenta are propagated backwards. We first state a result: *iterates of the rectangle of initial points approach two one-dimensional curves that control the chaotic dynamics*. Let us consider this statement with the aid of Figure 1.9, where the horizontal axis is q (the arclength) and the vertical axis is p (the momentum). In Figure 1.9a, the two rectangles plotted in green and black comprise the initial conditions. The black points are propagated forwards while the green points are propagated backwards. In all six graphs in Figure 1.9, the blue points represent the first nine images of the black initial conditions while the red points represent the first nine pre-images of the green initial conditions. In Figure 1.9b, the

black points are the first image of the initial conditions with negative momenta while the green points are the first pre-image of the initial conditions with positive initial momenta. The points appear to have been stretched to flow along a diagonal line. Figure 1.9c shows the second iterates of the initial conditions. We see that the two sets are once again symmetrical about the q-axis. Furthermore, the two sets have been stretched by the mapping, are much thinner, and are becoming more curved. Figure 1.9d shows that on the next iterate, the curves have once again been stretched and contracted. Now they both jut out of the eyeball-shaped region bisected by the q-axis. Figure 1.9e shows that both sets have now exited, re-entered, and re-exited the eyeball shaped region. Finally, Figure 1.9f shows that the two sets have now exited the eyeball shaped region three times and re-entered the eyeball shaped region twice.

What general observations regarding the discrete flow phase points can we make? First, the two sets are not blobs of points rotating around the phase plane. Each set seems to have some points that remain near the unstable fixed point. Secondly, the mapping stretches and contracts the two sets in a complicated fashion. Third, it appears that the points are being guided along, or slowly approaching, smooth curves embedded in the phase plane. Finally, after some number of iterates, the points start a process of entering, exiting, and then re-entering the eyeball shaped region.

At this point, we can give a preliminary explanation of how points transport through the phase plane. Transport through the plane is controlled by two smooth curves called the *unstable and stable manifolds*. Each is an infinitely long curve attached to the unstable fixed point. The initial points with negative momenta are guided by the

unstable manifold. This curve repels points from the unstable fixed point. The blue and black points in Figure 1.9 are being guided along the unstable manifold forwards in time.

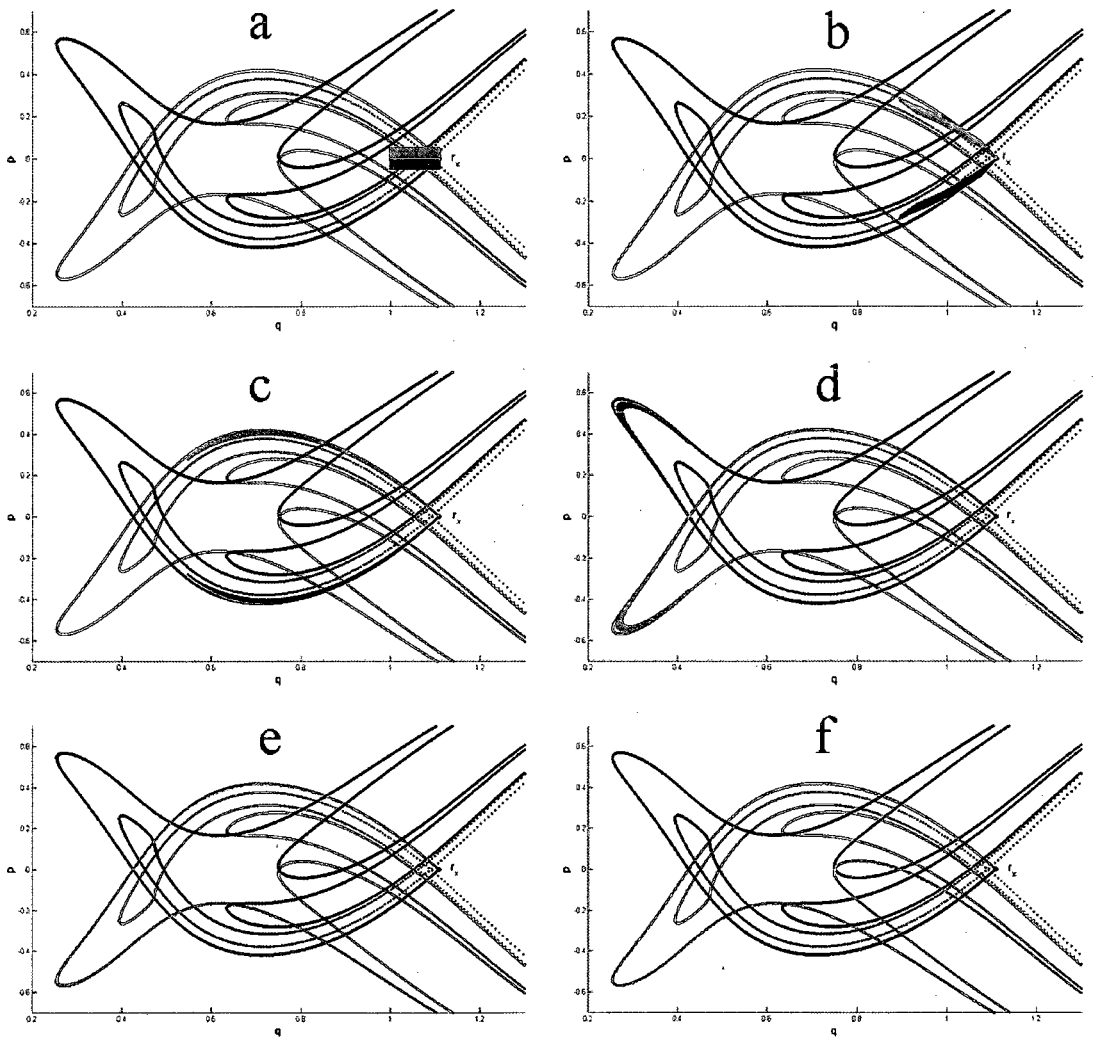

Figure 1.9: Traces of the stable and unstable manifolds. The red and green curves lie near the stable manifolds while the blue and black curves lie near the unstable manifolds. The two rectangles are the initial points. In each curve, the blue and green points represent iterates of the initial points: a.) zeroth iterate, b.) first iterate, c.) second iterate, d.) third iterate, e.) fourth iterate, f.) fifth iterate.

The initial points starting with positive momenta are being guided by the stable manifold. This is a smooth curve that attracts points to the unstable fixed point forwards

in time. The green and red points in Figure 1.9 are being guided by the stable manifold backwards in time.

Finally, we iterate points to the right of the unstable fixed point. Figure 1.10 shows several iterates of a rectangle of points. Again, red points are guided by the stable manifold and blue points are guided by the unstable manifold. We see that the points are being pushed along curves that are nearly straight lines. The segments of the manifolds to the right of the fixed point do not intersect. The stable manifold attracts points from infinity and the unstable manifold pushes points to infinity. Since these segments of the manifolds do not intersect, they are of no interest to us. Furthermore, in a small domain about the fixed point, the manifolds are approximately linear. The four segments roughly form the letter "x" and thus, the unstable fixed point is also known as an *x-point.*

In practice, we use the linearity of the manifolds near the x-point to find the exact manifolds. We first trace out the unstable manifold. We choose a test point near the x-point and propagate a set of initial conditions lying on the line segment connecting the test point and the x-point. We then check the points that are still near the x-point. If they are close to the line segment, then we use the slope and intercept of the line segment as the linear approximation of the unstable manifold. If the nearby points deviate from the line segment, then we repeat the procedure with a new test point. Due to the mirror symmetry, we only need to find an approximation to the unstable manifold.

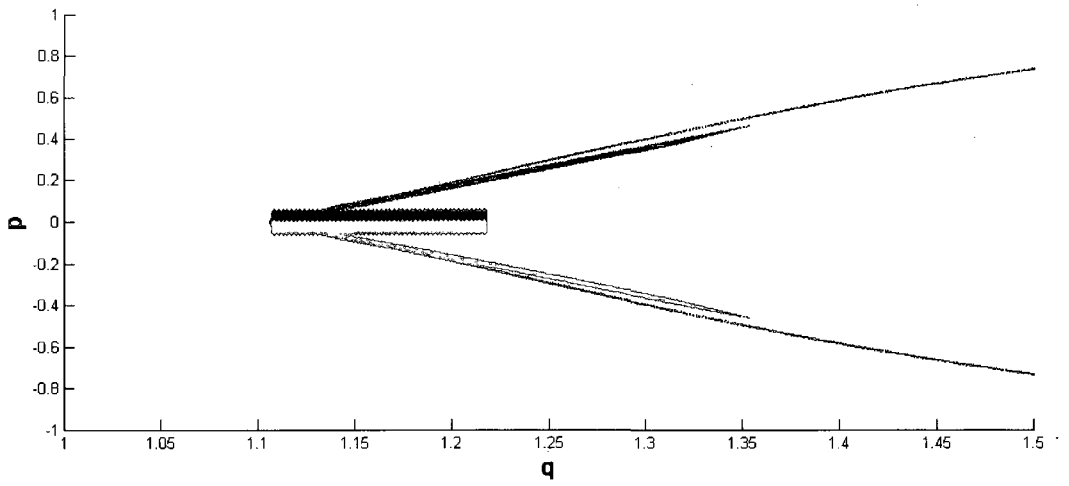

Figure 1.10: Traces of the stable and unstable segments lying to the right of the unstable fixed point. Blue points lie near the unstable manifold while red points lie near the stable manifold.

c.) Phase Space Representations of the Regular Trajectories.

Let us now consider the phase space representations of the stable orbits. The stable region is embedded within a chaotic region. Figure 1.11 shows multiple orbits in the stable region plotted along with segments of the actual stable and unstable manifolds. The black circles represent quasi-periodic orbits lying in the continent of stability. The ray in Figure 1.3a lies within this region. Surrounding the stable continent is an island of stability of period 7 plotted in green. Now refer back to Figure 1.3b, the stable orbit that wanders around 7 regions of the cavity walls. This orbit lies within the seven islands of stability surrounding the stable continent. The orbit picture in Figure 1.3b hops from one island to the other within the chain. Both stable regions are embedded in a sea of chaos. Some of these chaotic orbits are plotted in cyan. The boundary between the stable region and the chaotic sea is complicated but has no impact on our study. This topic is discussed in more detail in [4].

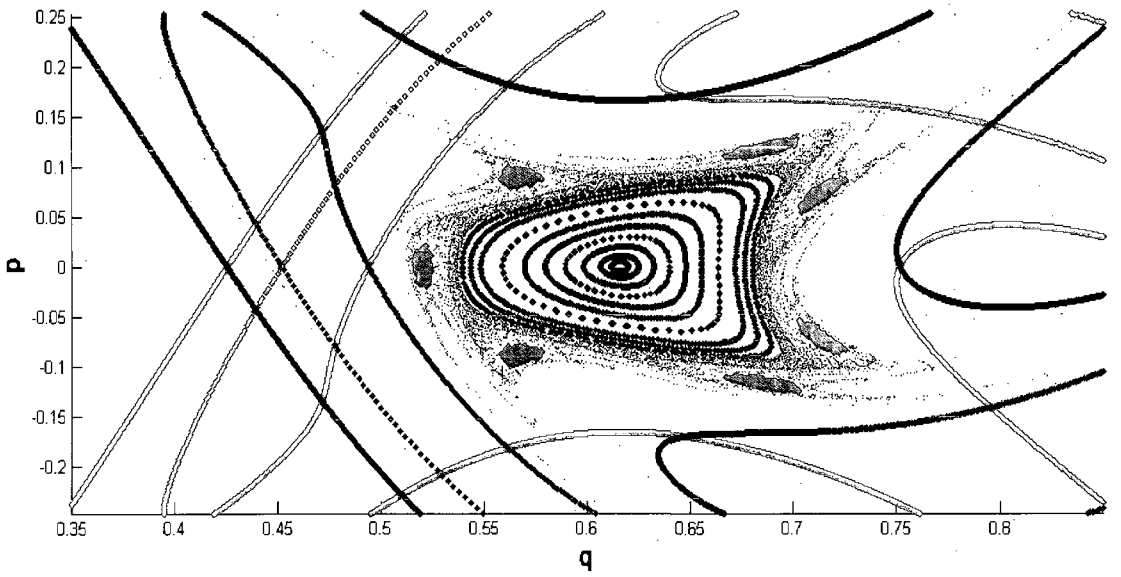

Figure 1.11: Stable regions near the stable periodic orbit and the homoclinic tangle.

We will not consider the direct trajectories, as they immediately escape and thus cannot be represented in phase space. Let us then consider the trajectories that oscillate within the vase's neck, or the so called parallel mirror trajectories. Figure 1.12 shows the first few images of a set of these trajectories plotted in black. The first few iterates are labeled with their iterate number. All of the trajectories are launched from the same point so the initial conditions are a vertical line segment, which is labeled as the zeroth iterate. The first, second, and third iterates march along near the stable manifold and approach the unstable fixed point. At this point, we can say that the stable manifold is guiding the trajectories. After each iterate, some of the trajectories escape the vase and thus map out of the phase plane.

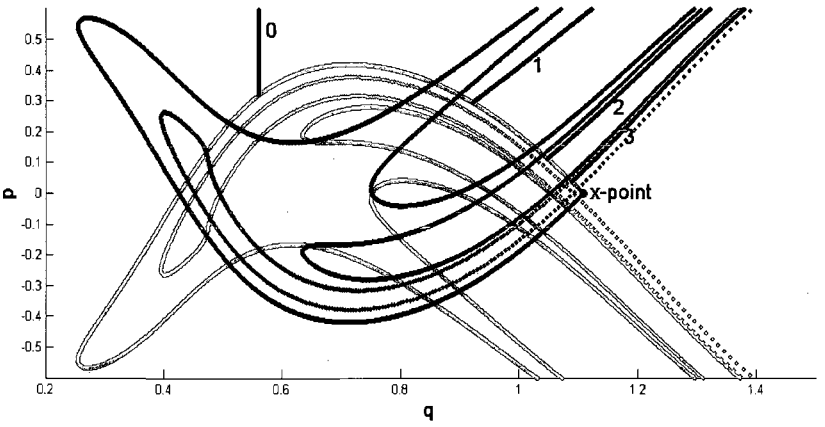

Figure 1.12: Phase space representations of the so-called parallel mirror trajectories.

Finally, we discuss the phase space representations of the whispering gallery trajectories. Whispering gallery trajectories are essentially polygonal approximations to convex segments of the vase's bowl. For a whispering gallery trajectory with a large number of reflections, the outgoing velocity vectors will be nearly parallel to the tangent vectors at the reflection points. Therefore, their corresponding momenta will be near ± 1. Since these trajectories are not in the chaotic set, we will ignore their phase space representations. However, the whispering gallery trajectories in the vase will become important to results discussed in Chapter 5.

iv.) Conclusions

In this chapter, we presented an introductory description of our system of interest. In section ii, we discussed how to propagate trajectories within the vase. The first step in integrating trajectories is numerically computing the roots to a polynomial which represents the intersections of a line with the vase boundaries. If the position and velocity allow for a reflection, then the propagation time to the next reflection is given

by the smallest real positive root. The Law of Reflection is used to reflect an incoming velocity vector at a point of reflection. We saw that there is a complex set of trajectories in the vase. There are stable orbits that endlessly wander around the vase's bowl. The scattering trajectories can be decomposed into regular and chaotic trajectories. The regular scattering trajectories include those that escape without reflection, trajectories that oscillate within the vase's neck any number of times, and whispering gallery trajectories. We also presented a sample chaotic trajectory and deferred discussing the set of chaotic trajectories to another chapter.

In section iii, we presented a coordinate transformation that hides the free particle propagation between successive reflections and transforms the reflection and velocity vectors into two coordinates that contain the same essential information. Using the transformation and the mirror symmetry of the vase, the unstable periodic orbit is transformed into an unstable fixed point. Propagating points near the fixed point allows us to trace out the stable and unstable manifolds that control the flow of points within the phase plane. Finally, we saw the phase plane representations of the stable and parallel mirror trajectories.

Our focus for the remainder of this study will primarily be studying families of chaotic trajectories. Understanding them requires an understanding of the stable and unstable manifolds. The next chapter provides a more detailed understanding of how the manifolds control phase space transport. Chapter 2 presents a theory that extracts the essential topological information of the manifolds and produces a set of symbolic equations that encode the dynamical evolution of the manifolds

-Chapter 1 References-

[1] Melissa Commisso, REU project report, College of William and Mary, 2003. (unpublished)

[2] P. Hansen, K. A. Mitchell, and J. B. Delos Phys. Rev. E **73**, 066226 (2006).

[3] P. Hansen *Chaotic Escape of Photons from a Fish-Shaped Reflecting Cavity*, thesis submitted for BS with honors in physics, College of William and Mary (May, 2004).

[4] K. A. Mitchell, J. P. Handley, B. Tighe, J. B. Delos, and S. K. Knudson, Chaos **13**, 880 (2003).

-CHAPTER 2-
The Topology of Homoclinic Tangles

i.) Introduction

Previously, we described the vase and the complicated set of dynamics. We stated that underlying the system is a homoclinic tangle, the intersection of infinitely long stable and unstable manifolds emanating from the unstable periodic orbit lying in the vase's neck. In this chapter, we will discuss the topology of stable and unstable manifolds, called Homotopic Lobe Dynamics (HLD). Specifically, we will show how a topological analysis will allow us to graphically extract a set of symbolic dynamical equations from a homoclinic tangle. These equations will allow us to predict a minimal subset of the icicle sequences seen in numerically computed escape time plots. This chapter is organized as follows. In section ii, we will discuss the mathematics we use, which is the concept of homotopy. In section iii, we will discuss how the homoclinic tangle is a mechanism for phase space transport. Section iv discusses the first incarnation of HLD to give the reader an intuitive understanding of the more general method laid out in section v.

ii.) Homotopy

Before we delve into the theory, we will discuss the underlying mathematics, which is the concept of homotopy. We are interested in curves in $\mathbb{R}^2$. If a curve can be continuously deformed into another curve, we say that the two curves are homotopic ([1]). A formal definition is unnecessary for the discussion but we present one for the sake of completeness.

Def: Let I = [0, 1] and $\alpha_1, \alpha_2 : I \to \mathbb{R}^2$ be continuous with $\alpha_1(0) = \alpha_2(0)$ and $\alpha_1(1) = \alpha_2(1)$ with the orientation starting at $\alpha_{1,2}(0)$ and ending at $\alpha_{1,2}(1)$. We denote the inverse curves as $\alpha_{1,2}^{-1}$ with the orientation starting at $\alpha_{1,2}(1)$ and ending at $\alpha_{1,2}(0)$. Then, two curves are said to be *homotopic* to one another if $\exists$ a continuous function $H(t,s): I \times I \to \mathbb{R}^2$ such that $H(t,0) = \alpha_1(t)$, $H(t,1) = \alpha_2(t)$, $H(0,s) = \alpha_1(0) = \alpha_2(0)$, and $H(1,s) = \alpha_1(1) = \alpha_2(1)$.

It is a simple exercise to verify that a homotopy relationship is an equivalence relationship. If two curves, α_1 and α_2, are homotopic, then we write $\alpha_1 \sim \alpha_2$ and denote the class as either $[\alpha_1]$ or $[\alpha_2]$. This definition may seem restrictive in that it assumes the endpoints remain fixed. However, we can alter the definition and allow for the homotopy mapping to move the endpoints as well. We will see in sections iv and v how this detail affects our discussion.

If we consider $\mathbb{R}^2$ endowed with the "usual topology", then for any point **x** all loops containing **x** homotope into **x** (i.e. any closed loop can be shrunk to a point), giving a single global homotopy class, which is defined to be the identity class. To obtain a nontrivial set of homotopy classes, we must alter the topology of $\mathbb{R}^2$. We can delete any number of open sets and alter what we mean by continuity in the plane. For example, by deleting a unit disk from $\mathbb{R}^2$, and thereby prohibiting any portion of a curve from entering that disc, a nontrivial homotopy class is then a class of curves that wind around the hole an integer

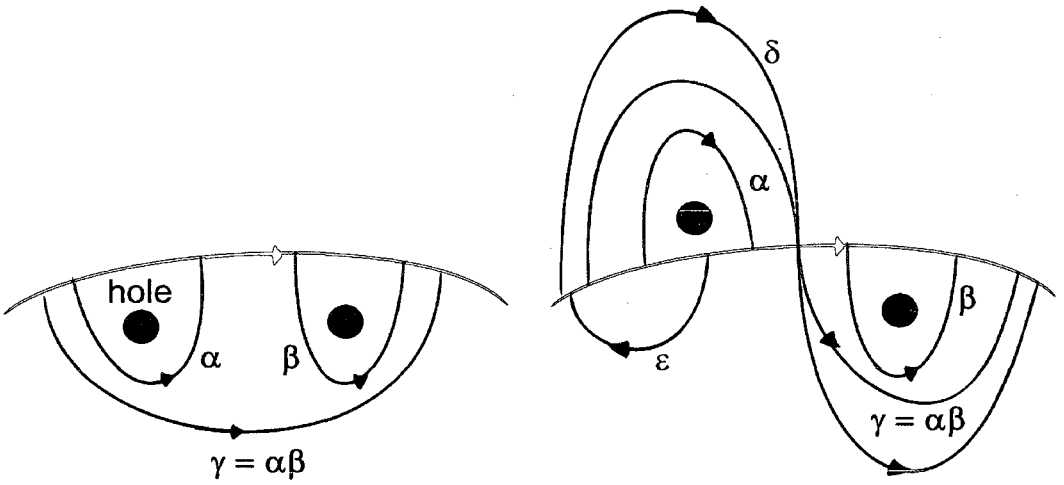

Figure 2.1: Two examples of curves winding around deleted regions which are represented by black disks.

number of times. The set of homotopy classes is isomorphic to $\mathbb{Z}$, with the sign of the integer indicating the orientation of the curves ([2]).

Figure 2.1 shows two examples of homotopy. In both cases, we have punched two holes from the plane, thereby creating a new topology. In discussing Figure 2.1, we allow the endpoints to slide along the red line. Consider the left figure in which two curves α and β are shown. Each encloses a disk of deleted points. Deforming either curve into the other would require the curve to pass through the deleted region, but this is not allowed.

Therefore, the curves α and β each represent unique homotopy classes, called $[\alpha]$ and $[\beta]$, respectively. On the right, we have a different situation in which the holes are punched on opposite sides of the red curve. Once again, α and β each enclose a hole

thus representing different homotopy classes. This figure also shows that α and ε represent different classes while γ and δ are equivalent.

Again, consider the curves α and β in either figure. If we slide together the endpoints of α and β nearest to each other and lift the newly formed intersection off the red curve, we obtain the path γ. Concatenation of the two classes $[\alpha]$ and $[\beta]$ results in a new class $[\gamma] = [\alpha][\beta]$. But curves that belong to the class $[\alpha][\beta]$ can be homotoped into the curve formed by concatenating α and β. This implies $[\alpha][\beta] = [\alpha\beta]$. This path construction suggest that a group structure underlies the set of homotopy classes for curves with endpoints lying on the red curve. This is indeed the case. Since α is oriented, α^{-1} exists and encloses the same hole as α. Reversing the orientation of curves equivalent to α gives curves equivalent to α^{-1} and thus $[\alpha^{-1}] = [\alpha]^{-1}$. The identity element (of which ε is a representative) is any curve that can be deformed to a point on the red curve. Taking the product of a curve and its inverse in either order gives a curve that can be contracted into a point.

iii.) Homoclinic Tangles

Now that we have explained the mathematics we will use, we will begin discussing homoclinic tangles. First, we will give definitions of the stable and unstable manifolds that make up a homoclinic tangle. Then we will discuss how the manifolds control the flow of points through phase space.

We consider diffeomorphisms $\mathcal{M}: \mathbb{R}^2 \to \mathbb{R}^2$ possessing a hyperbolic fixed point $\mathbf{q}_x$. We also assume that the mapping is *orientation preserving*, that is to say $\det(D\mathcal{M}(\mathbf{x})) > 0$, where $D\mathcal{M}$ is the Jacobian matrix of $\mathcal{M}(\mathbf{x})$. The global and local

stable/unstable manifold theorems [3] guarantee the existence of smooth, one dimensional curves emanating from $\mathbf{q}_x$ locally along the eigenvectors of $D\mathcal{M}$. Stable and unstable manifolds are curves defined by their asymptotic behavior:

Def: Let S and $\mathcal{U}$ represent the *stable and unstable manifolds*, respectively. The manifolds are invariant curves: $\mathcal{M}:S \to S$ and $\mathcal{M}:\mathcal{U} \to \mathcal{U}$ and $\forall\ \mathbf{x} \in S$ and $\forall\ \mathbf{y} \in \mathcal{U}$

$\lim_{n\to\infty} \mathcal{M}^n(\mathbf{x}) = \mathbf{q}_x$ and $\lim_{n\to\infty} \mathcal{M}^{-n}(\mathbf{y}) = \mathbf{q}_x$.

The first statement says that a point on either manifold does not map off the manifold. The second statement says that for sufficiently large n, a point on either manifold is close to $\mathbf{q}_x$, but is always a finite distance away measured along the manifold. Generally, a stable manifold attracts points toward $\mathbf{q}_x$ and an unstable manifold repels points away from $\mathbf{q}_x$. Neither manifold can self-intersect. This fact will have important consequences in our study of tangles. Finally, the manifolds are infinitely long. Sometimes, we may need to refer to a specific infinite segment of a manifold, called a branch.

Def: A *branch* of either S or $\mathcal{U}$ is the segment starting at $\mathbf{q}_x$ and running to infinity.

We are interested in studying how the manifolds control the flow of points through a bounded region. We will be discussing specific segments of the manifolds and thus need a suitable notation. A closed segment of either manifold with endpoints $\mathbf{q}_1$, $\mathbf{q}_2$ will be denoted by $S[\mathbf{q}_1,\mathbf{q}_2]$ and $\mathcal{U}[\mathbf{q}_1,\mathbf{q}_2]$. Half-open and open segments are denoted in the same way with the brackets replaced with parentheses. Since the manifolds are naturally oriented, we choose to reflect the orientation in the ordering of the points in the set notation. We write either $\mathcal{U}[\mathbf{x}_1, \mathbf{x}_2]$ or $S[\mathbf{x}_1, \mathbf{x}_2]$ if following the natural orientation of

the manifold we encounter $\mathbf{x}_1$ before encountering $\mathbf{x}_2$. Finally, if we are considering both the stable and unstable segments connecting $\mathbf{x}_1$ to $\mathbf{x}_2$, then we let $\mathcal{U}/S[\mathbf{x}_1, \mathbf{x}_2]$ denote the phrase "$\mathcal{U}[\mathbf{x}_1, \mathbf{x}_2]$ and $S[\mathbf{x}_1, \mathbf{x}_2]$".

Our analysis will concentrate on intersections between the stable and unstable manifolds.

Def: If $\mathbf{x} \in S \cap \mathcal{U}$, then $\mathbf{x}$ is called a *homoclinic intersection* or *homoclinic point.* We assume that all homoclinic points are *topologically transverse* [11].

Def: Two sub-manifolds X and Y embedded in an ambient manifold M are said to intersect *transversally* at $p \in X \cap Y$ if

$$T_pX \oplus T_pY = T_pM \text{ and } \dim(T_pX \cap T_pY) = \dim(T_pX) + \dim(T_pY) - \dim(M) \geq 0$$

This definition says that the tangent space of the ambient space at $\mathbf{p}$ is spanned by the vectors tangent to X and Y at $\mathbf{p}$. If a tangential intersection is present, then one can use a sufficiently small perturbation to remove the intersection.

For the remainder of this section, we will discuss the mechanism by which points enter and exit a bounded region (this material can be found in Wiggins [4]). To this end, we will consider in a special type of homoclinic point called a primary intersection point.

Def: a *primary intersection point (pip)* $\mathbf{p}$ is a homoclinic intersection such that $S(\mathbf{p}, \mathbf{q}_x) \cap \mathcal{U}(\mathbf{q}_x, \mathbf{p}) = \varnothing$.

Figure 2.2 shows two manifolds intersecting at a pip $\mathbf{p}$. We see that by starting at the hyperbolic point $\mathbf{q}_x$ and following each manifold only as far as the pip $\mathbf{p}$, the manifolds intersect only at the pip. We call the interior bounded by $\mathcal{U}/S[\mathbf{q}_x, \mathbf{p}]$ region I and its complement region II. We want to understand how points map between regions I and II.

First, consider $\mathcal{M}^{\pm 1}(\mathbf{p})$. Since $\mathbf{p} \in S$, mapping forward moves $\mathbf{p}$ along S towards $\mathbf{q}_x$. However, $\mathbf{p} \in \mathcal{U}$ as well, and the continuity of $\mathcal{U}$ requires that a segment of $\mathcal{U}$ passes through S at $\mathcal{M}(\mathbf{p})$. We ask ourselves in which direction does $\mathcal{U}$ cut across S. We attach two tangent vectors at $\mathbf{p}$ pointing in the same directions as the manifolds. The orientation of the parallelogram formed by these tangent vectors is preserved under the mapping. Therefore, the vectors tangent to $\mathcal{M}(\mathbf{p})$ will possess the same orientations as those tangent to $\mathbf{p}$. We see that for $\mathcal{U}$ to possess the same orientation and be continuous, it must run from region I to region II. For the segment $\mathcal{U}[\mathbf{p}, \mathcal{M}(\mathbf{p})]$ to be continuous, an additional homoclinic point in must lie in $\mathcal{U}[\mathbf{p}, \mathcal{M}(\mathbf{p})]$. We call this point $\mathcal{M}(\mathbf{q})$. Mapping $\mathbf{p}$ backwards and following the same argument gives the homoclinic point $\mathbf{q}$.

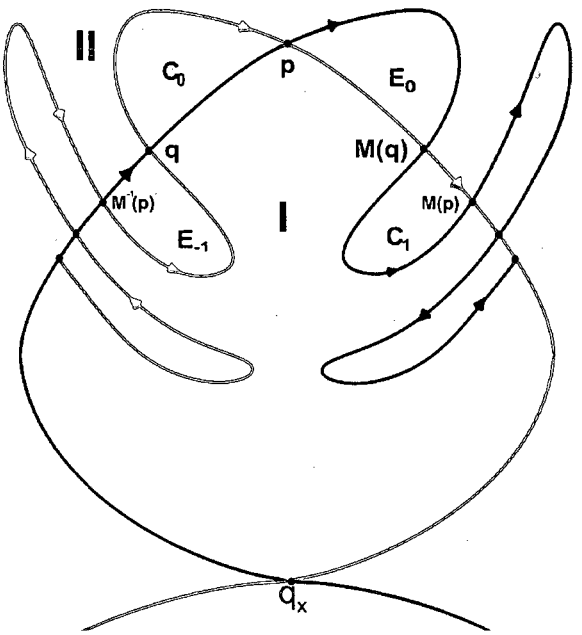

Figure 2.2: Stable (red) and unstable (blue) manifolds intersecting at a pip $\mathbf{p}$.

We can see from Figure 2.2 that $\mathcal{U}(\mathbf{q}_x, \mathbf{q}) \cap S(\mathbf{q}, \mathbf{q}_x)$ and $\mathcal{U}(\mathbf{q}_x, \mathcal{M}(\mathbf{q})) \cap S(\mathcal{M}(\mathbf{q}), \mathbf{q}_x)$ are both empty implying that $\mathbf{q}$ and $\mathcal{M}(\mathbf{q})$ are also pips. Furthermore, we see that the regions bounded by the segments $\mathcal{U}/S(\mathcal{M}^{-1}(\mathbf{p}), \mathbf{q})$, $\mathcal{U}/S(\mathbf{q}, \mathbf{p})$, $\mathcal{U}/S(\mathbf{p}, \mathcal{M}(\mathbf{q}))$, and $\mathcal{U}/S(\mathcal{M}(\mathbf{q}), \mathcal{M}(\mathbf{p}))$ possess a lobe-like structure motivating a definition.

Def: Let $\mathbf{q}_1$ and $\mathbf{q}_2$ be pips such that $S[\mathbf{q}_1, \mathbf{q}_2]$ and $\mathcal{U}[\mathbf{q}_1, \mathbf{q}_2]$ contain no other pips. Then, the interior region bounded by $S[\mathbf{q}_1, \mathbf{q}_2]$ and $\mathcal{U}[\mathbf{q}_1, \mathbf{q}_2]$ is called a *lobe.*

In Figure 2.2, eight lobes have been drawn. Let E_{-1} denote the lobe bounded by $\mathcal{U}/S[\mathcal{M}^{-1}(\mathbf{p}), \mathbf{q}]$. If we map E_{-1} forward, we have the region bounded by $\mathcal{U}/S[\mathbf{p}, \mathcal{M}(\mathbf{q})]$, or E_0. Immediately, we notice that by mapping from E_{-1} to E_0, points have moved from region I to region II. In other words, points have escaped region I. Therefore, we call E_{-1} and E_0 *escape lobes*. Similarly, the lobe bounded by $\mathcal{U}/S[\mathbf{q},\mathbf{p}]$ maps into the lobe bounded by $\mathcal{U}/S[\mathcal{M}(\mathbf{q}), \mathcal{M}(\mathbf{p})]$. Let the aforementioned lobes be called C_0 and C_1, respectively. We see from the figure that by mapping from C_0 to C_1, points have moved from region II to region I. If points map into region I, we can say that points have been captured by region I and call the lobes C_0 and C_1 *capture lobes*. The four lobes E_{-1}, E_0, C_0, and C_1 control how points enter and exit region I and are called the *turnstile*. From now on region I will be referred to as the *complex*. Objects lying inside the complex will be referred to as *internal* and those lying outside as *external.*

iv.) Homotopic Lobe Dynamics I

With the background material explained we can begin our discussion of Homotopic Lobe Dynamics (HLD). The central idea is to punch holes in regions in which the manifolds do not enter. The output of HLD is a set of dynamical equations

acting on the set of path classes in the new topology that encodes how the manifolds wind through the plane. This material can be found in [5].

In this section, we discuss the first version of HLD. Let us begin by examining the three different tangles shown in Figure 2.3. The complex is the region bounded by $\mathcal{U}/S[\mathbf{q_x},\mathbf{P_0}]$. In each tangle, the turnstile is composed of the four lobes labeled E_{-1}, E_0, C_0, C_1. We can iterate the escape and capture lobes forwards and backwards to generate a bi-infinite sequence of lobes. The boundaries of the n^{th} escape and capture lobes, E_n and C_n, are defined by the segments $\mathcal{U}/S[\mathbf{P_n}, \mathbf{Q_n}]$ and $\mathcal{U}/S[\mathbf{Q_{n-1}}, \mathbf{P_n}]$, respectively. Going from left to right, we see that in these different tangles C_2, C_3, and then C_4 respectively intersect E_0. Points enter the complex by iterating from C_0 to C_1. Each tangle possesses a capture lobe whose tip intersects E_0. This intersection represents a subset of C_1 that will land in E_0, hence escape the complex, after one iterate (2.3a), two iterates (2.3b), and three iterates (2.3c). In general, let D be an integer called the *minimum delay time.* After entering the complex, D represents the minimal number of mappings for a point to escape the complex. In Figures 2.3a, 2.3b, 2.3c, the minimum delay times are D = 1, 2, 3 respectively. In general, for a minimum escape time of D, C_{D+1} intersects E_0.

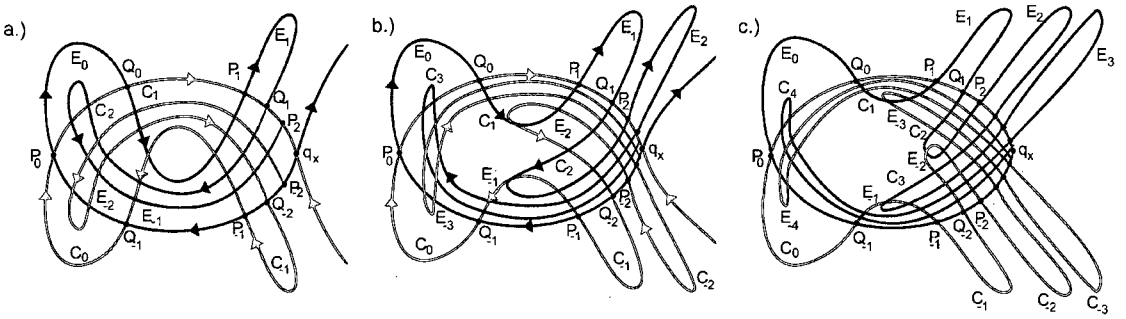

Figure 2.3: Three tangles with minimum delay times equal to a.) 1, b.) 2, and c.) 3.

We stated previously that the minimum delay time is the minimum number of iterates that a point remains within the complex after mapping into C_1, and that in general, the $D+1^{th}$ capture lobe intersects E_0. Let us consider the image of C_{D+1}. The image will produce the set $C_{D+2} \cap E_1$. The endpoints of C_{D+2} will remain on $S[\mathbf{P}_0, \mathbf{q}_x]$ mapping closer to $\mathbf{q}_x$. Since $\mathcal{U}$ cannot self-intersect, we conclude that C_{D+2} must first wind under C_{D+1}; then as it passes through E_0, it will wind over the tip of C_{D+1}; finally, C_{D+2} will wind under C_1 to intersect E_1. We can follow a similar argument to determine how C_{D+3} will wind through the phase plane in order to intersect E_2. However, the argument is a bit more complicated and needs to be explained in detail. We will now set $D = 1$ and explain how the mapping folds and stretches the images of C_1.

We consider the tangle shown in Figure 2.4 (this is a qualitative picture). What is important about this tangle is that there is a minimum delay time of 1 and that the unstable fixed point has attached to it two stable branches and two unstable branches. Two of the branches are not tangled and shoot out to infinity. The remaining two are tangled. Furthermore, *we assume that once points have exited the complex, they can never re-enter the complex.*

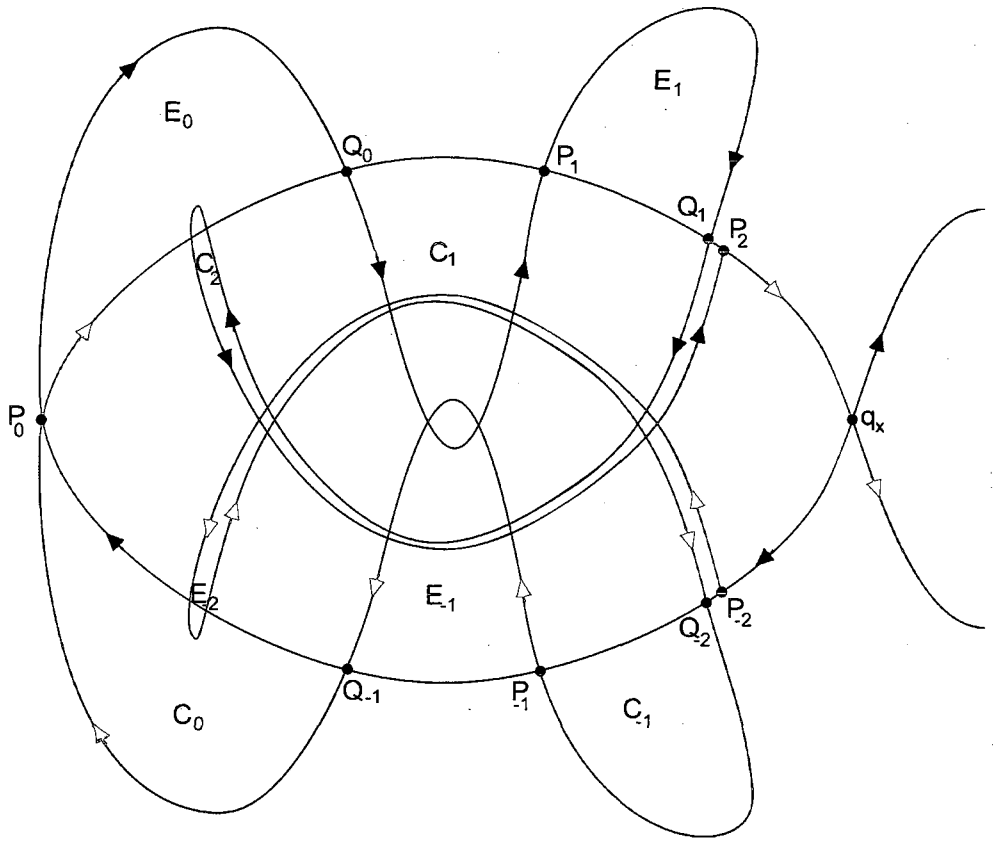

Figure 2.4: Qualitative sketch of D = 1 homoclinic tangle.

We assume a specific knowledge of the manifolds: namely we assume we have computed the segments $\mathcal{U}[\mathbf{q}_x, \mathbf{P}_2]$ and $S[\mathbf{P}_{-2}, \mathbf{q}_x]$. Based on this information, we ask: How do we qualitatively construct the third capture lobe? For simplicity, we will also assume that the tangle possesses mirror symmetry along the axis connecting $\mathbf{q}_x$ to $\mathbf{P}_0$. The mirror symmetric partner of the C_3 will be E_{-3}. We can construct C_3 by noting that its boundary curve, $\mathcal{C}_3$, must start at $\mathbf{Q}_2$ (which must lie between $\mathbf{P}_2$ and $\mathbf{q}_x$), it must pass through E_1, and it must end at $\mathbf{P}_3$ (which must lie between $\mathbf{Q}_2$ and $\mathbf{q}_x$), and it cannot intersect any other part of $\mathcal{U}$. That gives us the picture shown in Figure 2.7. Alternatively, we can construct it piece by piece using the following method.

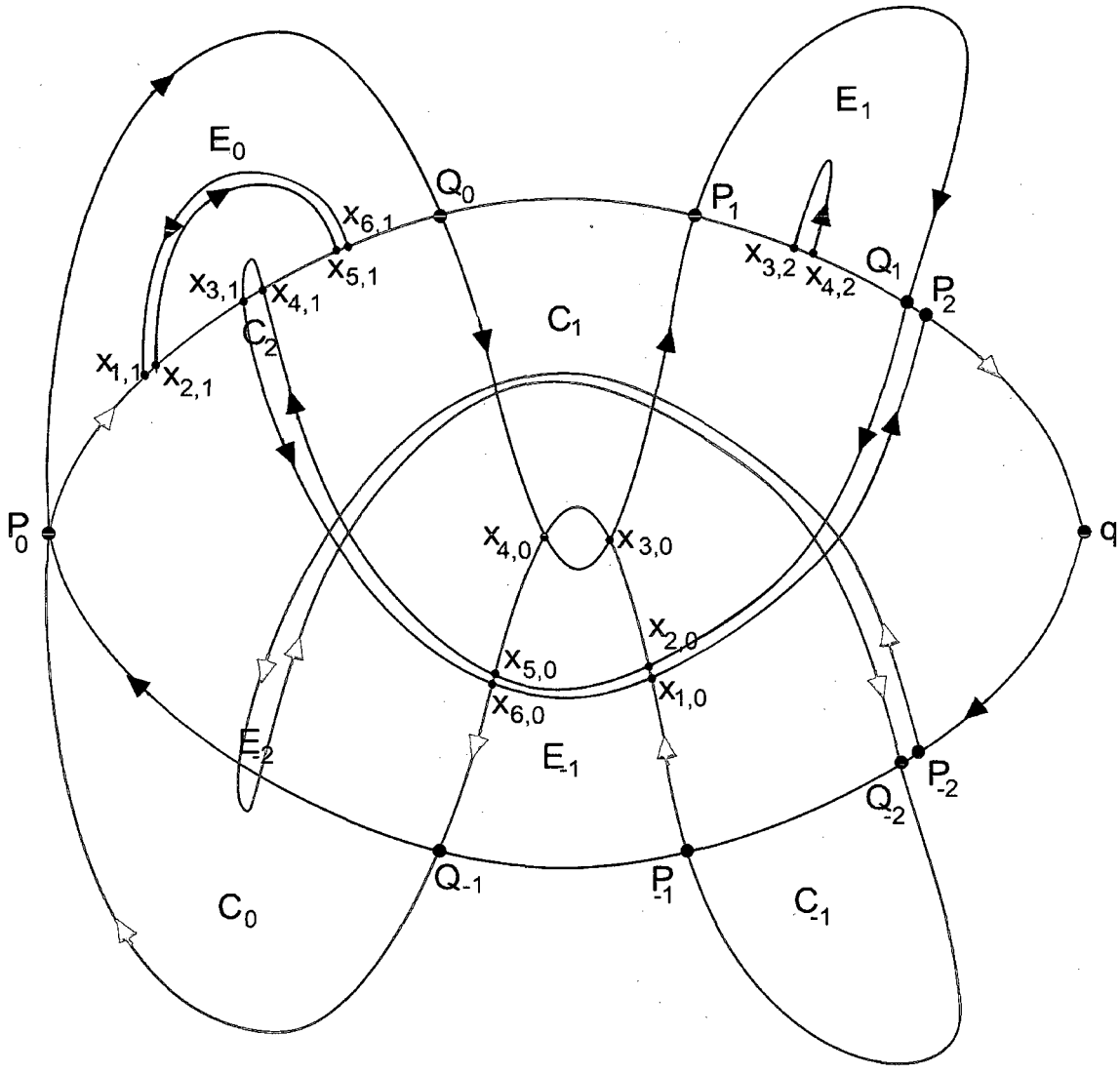

Figure 2.5: Three segments of $\mathcal{C}_3$.

a.) Construction of C_3

Let us consider Figure 2.5, which shows three segments of C_3 along with the known lobes. First, we state how we label homoclinic points. Each homoclinic point is assigned two integer subscripts separated by commas. The first subscript indicates the order of appearance in a sequence of points all labeled with the same letter. We choose to order the points as they are encountered traveling along the natural orientation of the

stable manifold. The first set of homoclinic points we consider are encountered along the segment $S[\mathbf{P}_{-1}, \mathbf{Q}_{-1}]$. We set the second subscript to be zero on each of these points. The second subscript will indicate the number of mappings applied to a point whose second subscript is set to zero.

We will construct C_3 by constructing pieces of its boundary and then connecting them. First, let us consider the segment of $\mathcal{C}_2$ lying in E_0, $\mathcal{U}[\mathbf{x}_{4,1}, \mathbf{x}_{3,1}]$. The image of this segment, $\mathcal{U}[\mathbf{x}_{4,2}, \mathbf{x}_{3,2}]$, must lie in E_1. Now, consider the intersection of C_2 and E_{-1}'s boundaries which contains the four homoclinic points, $\mathbf{x}_{1,0}$, $\mathbf{x}_{2,0}$, $\mathbf{x}_{5,0}$, and $\mathbf{x}_{6,0}$, connected in pairs by $\mathcal{U}[\mathbf{x}_{2,0}, \mathbf{x}_{5,0}]$ and $\mathcal{U}[\mathbf{x}_{6,0}, \mathbf{x}_{1,0}]$. The images of these segments are $\mathcal{U}[\mathbf{x}_{2,1}, \mathbf{x}_{5,1}]$ and $\mathcal{U}[\mathbf{x}_{6,1}, \mathbf{x}_{1,1}]$ and must lie in E_0, as indicated in Figure 2.5. Thus, we have found two segments that map out of the complex after one mapping. Since the mapping is orientation preserving, the ordering of the six homoclinic points is preserved along $S[\mathbf{P}_0, \mathbf{Q}_0]$ allowing us to sketch the two curves lying in E_0 shown in Figure 2.5.

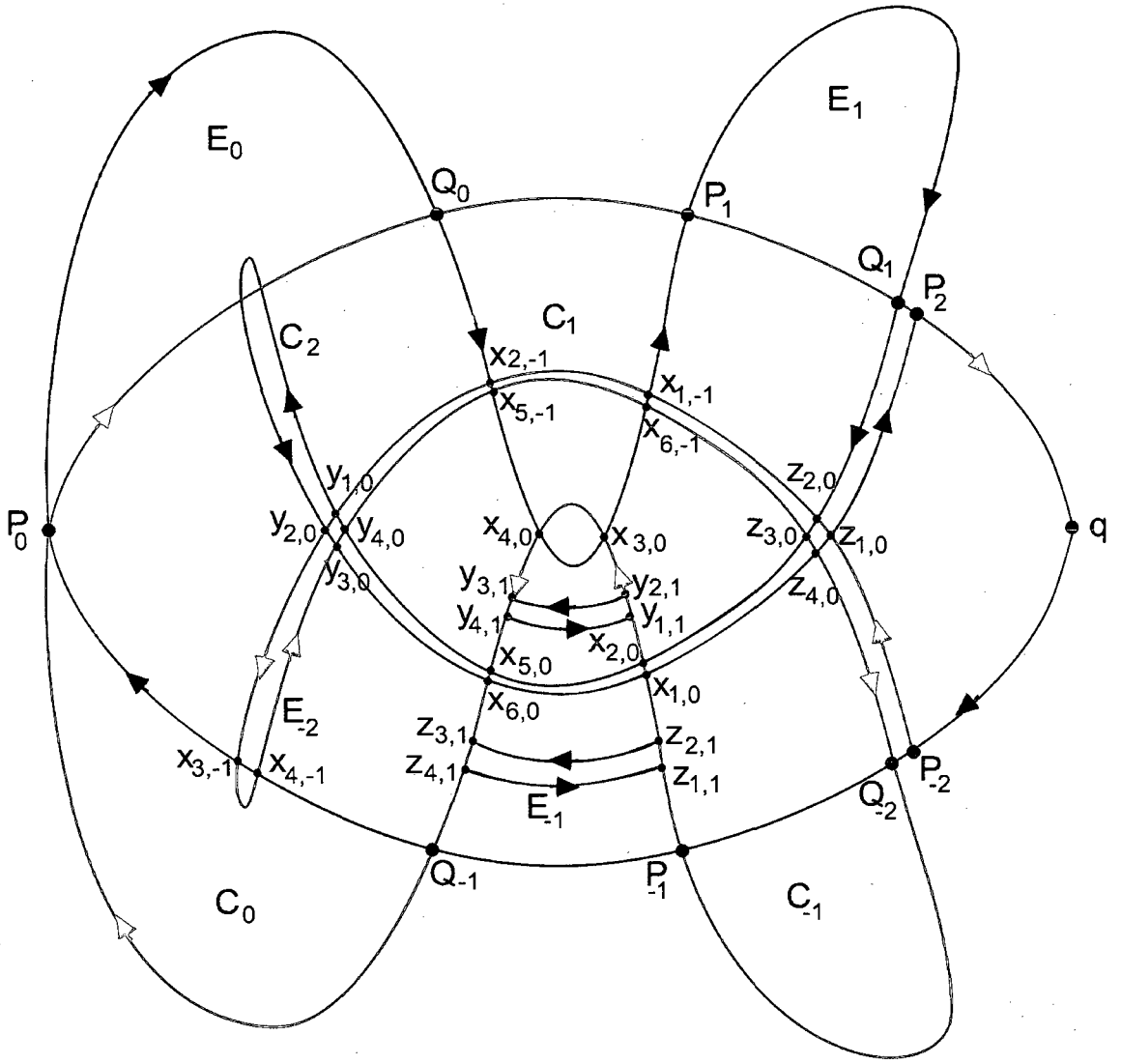

Figure 2.6: Intersection of C_3 and E_{-1}.

Four more segments of C_3's boundary can be constructed as follows. We consider the intersection of C_2 and E_{-2}, shown in Figure 2.6. This intersection produces eight homoclinic points, which we divide into two sets, the y-cluster on the left and the z-cluster on the right. These homoclinic points bound the segments $\mathcal{U}[\mathbf{y}_{4,0}, \mathbf{y}_{1,0}]$, $\mathcal{U}[\mathbf{y}_{2,0}, \mathbf{y}_{3,0}]$, $\mathcal{U}[\mathbf{z}_{2,0}, \mathbf{z}_{3,0}]$, and $\mathcal{U}[\mathbf{z}_{4,0}, \mathbf{z}_{1,0}]$. Mapping each of these four segments forward one

time gives four segments cutting across E_{-1}. If we follow $S[\mathbf{P}_{-2}, \mathbf{Q}_{-2}]$, we encounter the following points: $\mathbf{z}_{1,0}$, $\mathbf{z}_{2,0}$, $\mathbf{x}_{1,-1}$, $\mathbf{x}_{2,-1}$, $\mathbf{y}_{1,0}$, $\mathbf{y}_{2,0}$, $\mathbf{x}_{3,-1}$, $\mathbf{x}_{4,-1}$, $\mathbf{y}_{3,0}$, $\mathbf{y}_{4,0}$, $\mathbf{x}_{5,-1}$, $\mathbf{x}_{6,-1}$, $\mathbf{z}_{3,0}$, and $\mathbf{z}_{4,0}$. For each element in this sequence, we increment the second subscript by one and obtain the sequence of points encountered traversing $S[\mathbf{P}_{-1}, \mathbf{Q}_{-1}]$, $= \mathcal{M}(S[\mathbf{P}_{-2}, \mathbf{Q}_{-2}])$. Figure 2.6 shows the new sequence lying along the stable boundary of E_{-1}. To obtain the segments of $\mathcal{C}_3$ lying in E_{-1}, we connect the following points: $\mathbf{y}_{2,1}$ to $\mathbf{y}_{3,1}$, $\mathbf{y}_{4,1}$ to $\mathbf{y}_{1,1}$, $\mathbf{z}_{2,1}$ to $\mathbf{z}_{3,1}$, and $\mathbf{z}_{4,1}$ to $\mathbf{z}_{1,1}$. We finish constructing $\mathcal{C}_3$ by connecting the following pairs of homoclinic points: $\mathbf{Q}_2$ to $\mathbf{z}_{2,1}$, $\mathbf{z}_{3,1}$ to $\mathbf{x}_{2,1}$, $\mathbf{x}_{5,1}$ to $\mathbf{y}_{4,1}$, $\mathbf{y}_{1,1}$ to $\mathbf{x}_{4,2}$, $\mathbf{x}_{3,2}$ to $\mathbf{x}_{6,1}$, $\mathbf{x}_{1,1}$ to $\mathbf{z}_{4,1}$, and $\mathbf{z}_{1,1}$ to $\mathbf{P}_3$. Figure 2.7 shows the third capture lobe and its mirror symmetric partner E_{-1}.

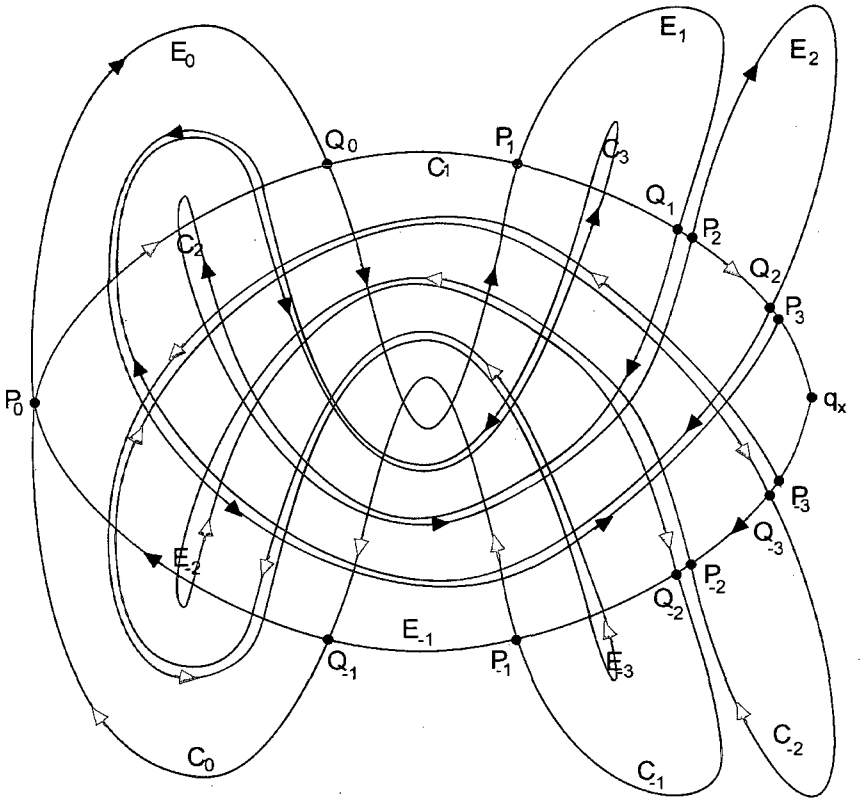

Figure 2.7: C_3 and E_{-3}.

b.) Digression: A First (Crude) Application of Homotopy Theory

Before going on to the construction of C_4, let us digress by discussing how we will apply homotopy theory. Based on the intersections of C_2 with E_0, E_{-1}, and E_{-2}, we were able to deduce how C_3 winds through the complex. We can make the interpretation that C_2 forces C_3 to wind through E_0 to intersect E_1 forcing the existence of two segments of C_3 that lie in E_0. Homotopy theory will allow us to quantify how the lobes wind through the plane. First, let us attach continuous lines to the ends of the two segments $\mathcal{U}[\mathbf{x}_{2,1}, \mathbf{x}_{5,1}]$ and $\mathcal{U}[\mathbf{x}_{6,1}, \mathbf{x}_{1,1}]$ (Figure 2.5) thereby connecting the unstable segments to the pips $\mathbf{P_0}$ and $\mathbf{Q_0}$. The new curves can be continuously deformed into the unstable boundary of E_0, a curve that connects the pips $\mathbf{P_0}$ and $\mathbf{Q_0}$. Furthermore, we can attach two continuous curves to the segment $\mathcal{U}[\mathbf{x}_{4,1}, \mathbf{x}_{3,1}]$ to connect it to the pips $\mathbf{P_0}$ and $\mathbf{Q_0}$. This new curve can also be continuously deformed into the unstable boundary of E_0. We then delete a set of points from the intersection of C_2 and E_0. This defines a new topology where curves cannot completely pass through the intersection of C_2 and E_0. We can define a unique homotopy class (and its inverse) that contains curves with endpoints $\mathbf{Q_0}$ and $\mathbf{P_0}$ that can be homotoped into the unstable boundary of E_0. After connecting the unstable segments $\mathcal{U}[\mathbf{x}_{2,1}, \mathbf{x}_{5,1}]$, $\mathcal{U}[\mathbf{x}_{6,1}, \mathbf{x}_{1,1}]$, and $\mathcal{U}[\mathbf{x}_{4,1}, \mathbf{x}_{3,1}]$ to $\mathbf{Q_0}$ and $\mathbf{P_0}$, all of these curves represent a single homotopy class induced by the new topology. This class and its inverse classes are important in that they are represented by curves that have just escaped the complex.

Let us now delete a set of points from $C_1 \cap E_{-1}$ inducing two unique homotopy classes (a class and its inverse) for curves that surround $C_1 \cap E_{-1}$ and starting and ending

on the points $\mathbf{Q}_0$ and $\mathbf{P}_1$. Now consider the two segments of $\mathcal{U}$ that wind around C_1 in Figure 2.5, $\mathcal{U}[\mathbf{x}_{5,1}, \mathbf{x}_{4,2}]$ and $\mathcal{U}[\mathbf{x}_{3,2}, \mathbf{x}_{6,1}]$. To each segment we attach continuous lines connecting the unstable segments to the pips $\mathbf{Q}_0$ and $\mathbf{P}_1$. With the endpoints fixed at the pips, these new lines can be homotoped into the homotopy class represented by the unstable boundary of C_1, $\mathcal{U}[\mathbf{Q}_0, \mathbf{P}_1]$ and its inverse.

c.) Construction of C_4

Let us return to the discussion and construct the fourth capture lobe. The result of our piece-by-piece construction is shown in Figure 2.9. Figure 2.8 shows C_1, C_2, C_3, and the images of C_3 that lie in E_0, E_1, and E_2. We know that the tip of C_4 will lie in E_2. C_3 was shown to possess two segments forced to wind through E_0 around the tip of C_2. The images of these two segments, $\mathcal{U}[\mathbf{x}_{2,2}, \mathbf{x}_{5,2}]$ and $\mathcal{U}[\mathbf{x}_{6,2}, \mathbf{x}_{1,2}]$ will wind around the tip of C_3. Finally, we see that four segments of C_3 pass through E_{-1} giving four segments of C_4 that will lie in E_0. C_3 was forced to wind above and below C_2. If we compare Figures 2.6 and 2.8, we can deduce that as C_4 winds through E_0, it will be forced to wind above and below C_3.

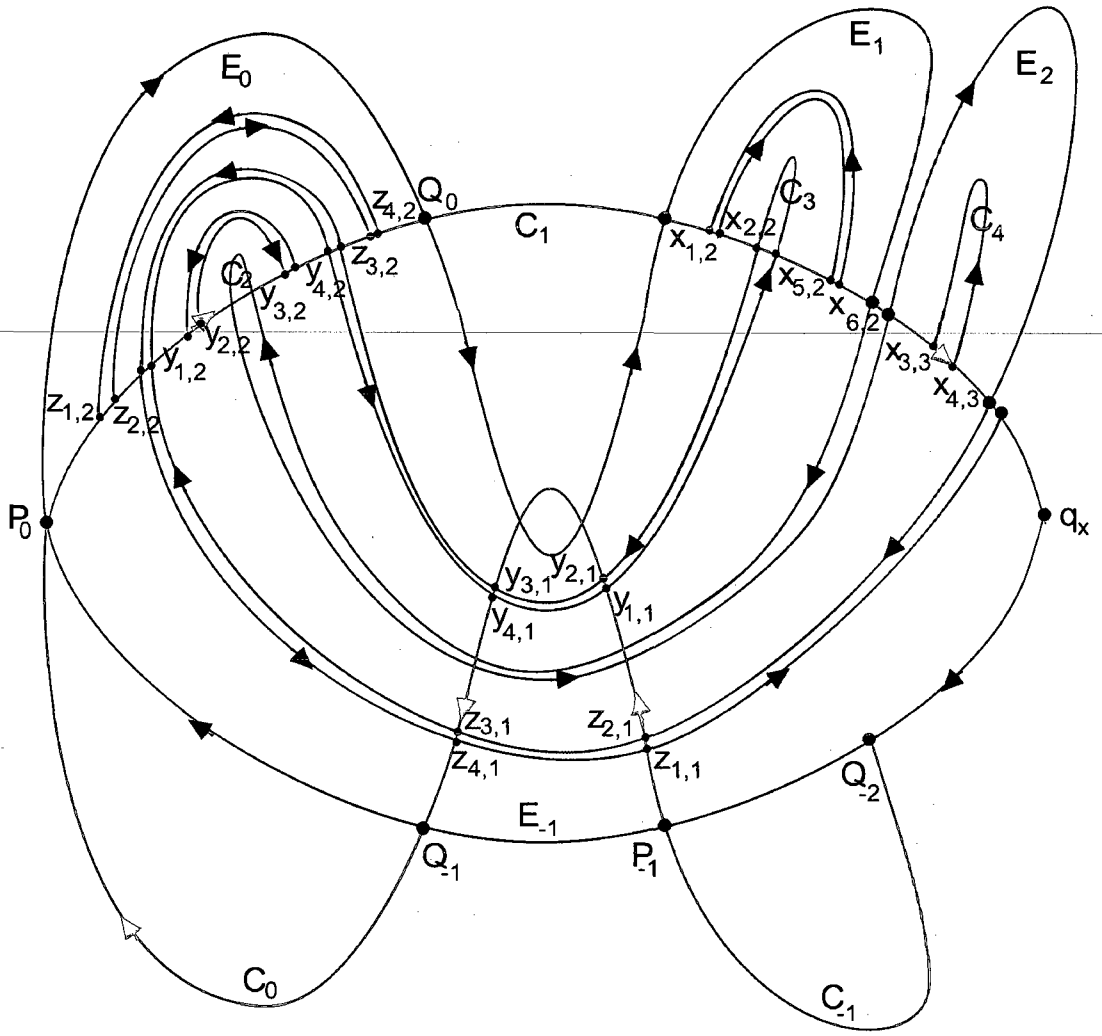

Figure 2.8: C_1, C_2, C_3, and C_4's intersections with E_0, E_1, and E_2.

We could continue the analysis by examining the intersections of C_3 with E_{-2} and E_{-3}. However, for the sake of brevity, we will take a short-cut. Let us now refer back to Figure 2.7. We see that $C_3 \cap E_{-2}$ contains eight segments of $\boldsymbol{u}$. We see from Figure 2.8 that we need another eight segments of $\boldsymbol{u}$ that pass through E_{-1} to fully connect the known segments of $\boldsymbol{c}_4$ (including the endpoints). The completed fourth capture lobe is shown along with its pre-images in Figure 2.9.

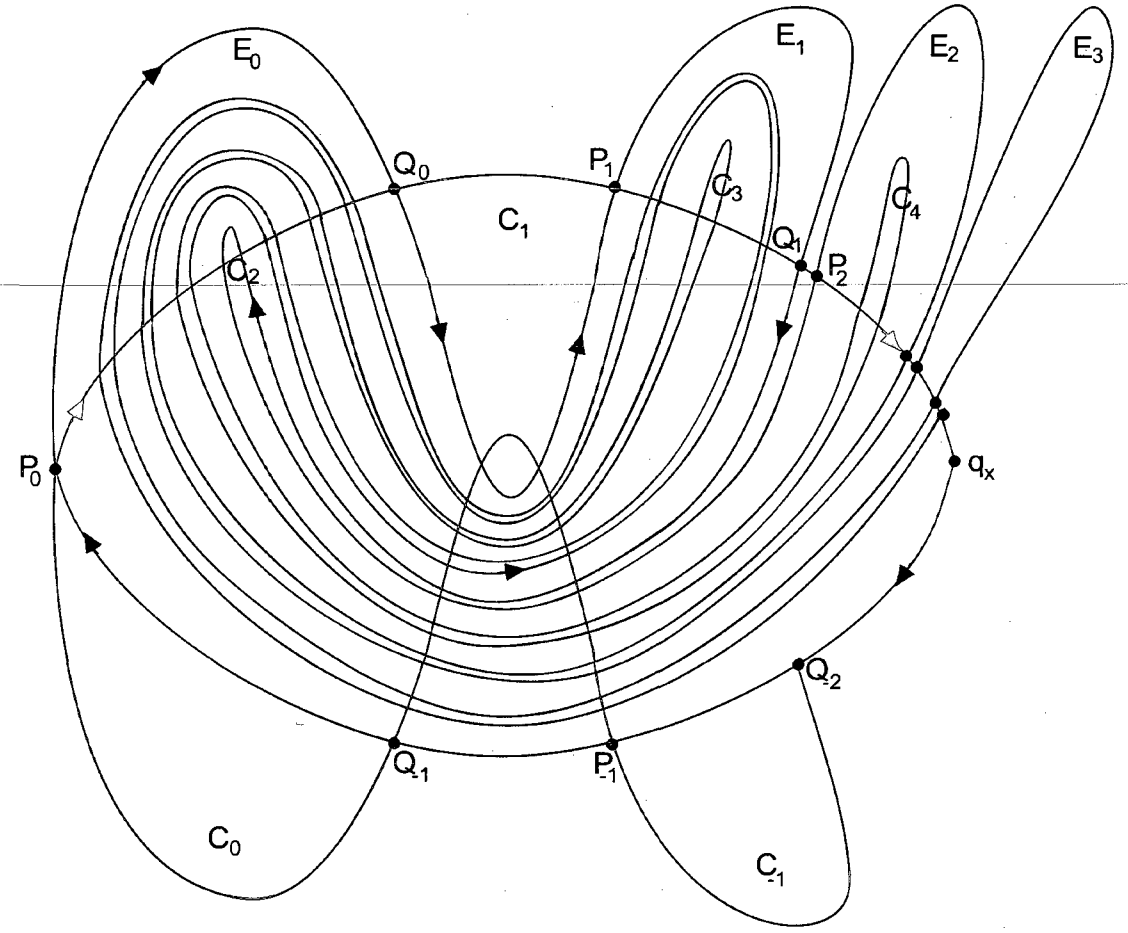

Figure 2.9: C_1, C_2, C_3, C_4, and E_{-1}.

We have discussed how to qualitatively compute the first few capture lobes based on a single piece of information: the minimum delay time. We have also discussed how segments of the unstable manifold can be assigned to unique homotopy classes once a new topology has been defined. We now discuss in detail how we alter the topology of the plane to induce a set of unique homotopy classes. We assume an arbitrary minimum delay time D. We begin the discussion by defining a hole.

d.) Defining Holes in the Plane

A *hole* is an open set of points that have been removed from $\mathbb{R}^2$. The first hole, H_0, is defined by the intersection $C_{D+1} \cap E_0$. Mapping this set forwards and backwards generates a bi-infinite sequence of open sets. Letting n be any integer, then the n^{th} hole is given by $H_n = C_{D+1+n} \cap E_n$. Setting n = -D-1 gives the hole formed from the set $C_0 \cap E_{-D-1}$. Since C_{D+1} is the first hole to intersect E_0, the first D capture lobes (mapping from C_0) all lie within the complex giving D holes within the complex. We collect the holes into the set $H = \bigcup_{n=-\infty}^{\infty} H_n$. Finally, we endow the usual topology to the set $\mathbb{R}^2 \backslash H$ and call this new set the punctured plane. We now consider the set of homotopy classes on the punctured plane which are naturally represented by the escape and capture lobe boundaries.

The boundary of each lobe is comprised of one stable segment and one unstable segment, each connecting a **P**-pip and a **Q**-pip. The n^{th} escape lobe and capture lobe are bounded by the segments $\mathcal{U}/\mathcal{S}[\mathbf{P}_n, \mathbf{Q}_n]$ and $\mathcal{U}/\mathcal{S}[\mathbf{Q}_{n-1}, \mathbf{P}_n]$, respectively. To each of these segments, we assign a unique symbol.

$$\begin{aligned} &\text{a.)}\partial E_n = \{\mathcal{U}_n \cup \mathcal{E}_n\},\ \mathcal{U}_n = \mathcal{U}[\mathbf{P}_n, \mathbf{Q}_n],\ \mathcal{E}_n = \mathcal{S}[\mathbf{P}_n, \mathbf{Q}_n] \\ &\text{b.)}\partial C_n = \{\mathcal{C}_n \cup \mathcal{S}_n\},\ \mathcal{C}_n = \mathcal{U}[\mathbf{Q}_{n-1}, \mathbf{P}_n],\ \mathcal{S}_n = \mathcal{S}[\mathbf{Q}_{n-1}, \mathbf{P}_n] \end{aligned} \tag{2.1}$$

Each of the symbols defined in eq. (2.1) represent curves with endpoints in the orbits generated by iterating the pips $\mathbf{P_0}$ and $\mathbf{Q_0}$ forwards and backwards an infinite number of times. We collect these two "pip orbits" into a set we call α as we will refer to this set often. Now, let us consider Figure 2.10 below, which is a qualitative picture of a tangle

with minimum delay time D. For the sake of clarity, we have omitted the escape lobes internal to the complex. Each capture lobe is forced to intersect a particular escape lobe based on the minimum time delay. The hole prevents the stable boundary from being deformed into the unstable boundary. Thus, each boundary is assigned to a unique homotopy class.

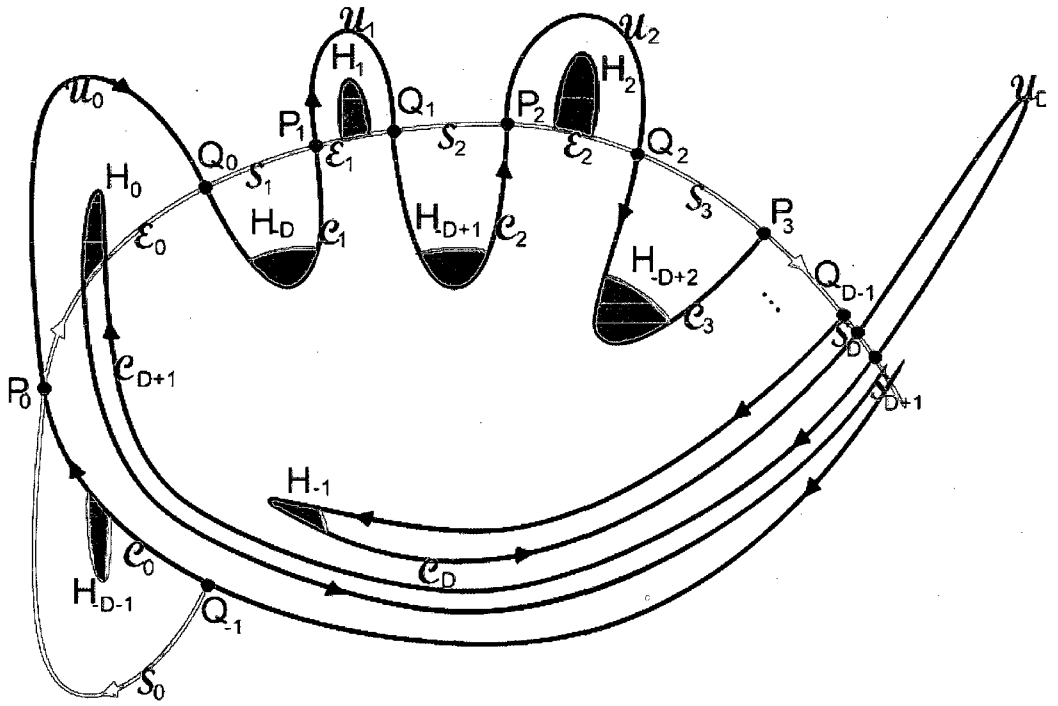

Figure 2.10: Qualitative tangle with minimum delay time D.

For example, consider the lobe C_0. The hole H_0 prevents $\mathcal{U}_0$ from being deformed into $\mathcal{E}_0$. Thus the four curves $\mathcal{U}_0$, $\mathcal{E}_0$, $\mathcal{U}_0^{-1}$, and $\mathcal{E}_0^{-1}$ each represent a unique homotopy class. Thus, a single hole formed from two intersecting lobes induces four homotopy classes represented by the stable and unstable segments bounding those lobes.

e.) Mapping Path-classes Forwards and Backward

We have seen that puncturing the plane induces a set of homotopy classes naturally arising from the intersection of C_{D+1} and E_0. Since the homotopy classes are represented by segments of the stable and unstable manifolds, the mapping on the punctured plane induces a new mapping (which we also call $\mathcal{M}$) on the set of homotopy classes. Letting lowercase letters denote homotopy classes, we can write out four dynamical equations, one for each of the curves in eq. (2.1).

$$\begin{array}{l} \forall n \in \mathbb{Z} \\ \text{a.)} \mathcal{M}^n(s_0^{\pm 1}) = s_n^{\pm 1} \text{ where } [\mathcal{S}_n] = s_n \\ \text{b.)} \mathcal{M}^n(u_0^{\pm}) = u_n^{\pm 1} \text{ where } [\mathcal{U}_n] = u_n \\ \text{c.)} \mathcal{M}^n(e_0^{\pm 1}) = e_n^{\pm 1} \text{ where } [\mathcal{E}_n] = e_n \\ \text{d.)} \mathcal{M}^n(c_0^{\pm 1}) = c_n^{\pm 1} \text{ where } [\mathcal{C}_n] = c_n \end{array} \tag{2.2}$$

Given the four symbols subscripted by 0 and all of their forwards and backwards iterates, no segment of the manifold is excluded. We note that the classes inherit the orientation of their representatives.

By definition, equivalency classes do not possess a preferred representative. This implies that a general curve can be assigned to a homotopy class. If this general curve represents a set of initial conditions for some dynamical system, then we can use eq. (2.2) to predict the dynamical development of those initial conditions. Therefore, we must establish a set of rules for assigning a general curve of initial conditions, which we will call $\mathcal{L}_0$, to a homotopy class. First and foremost, $\mathcal{L}_0$ cannot pass through a hole. If this is the case, then we allow for a small perturbation of $\mathcal{L}_0$ such that the intersection with the hole is removed. Secondly, $\mathcal{L}_0$ must have its endpoints in the set α. If this is

not the case then we add continuous curves to $\mathcal{L}_0$ linking it to points in α. All self-intersections in $\mathcal{L}_0$ are removed. Finally, we desire $[\mathcal{L}_0]$ to be unique and well-defined.

f.) A Basis of Path Classes

In order to assign general curves to unique homotopy classes, we must select a set of classes whose representatives do not intersect. Let us consider a tangle with minimum delay time = 1. Figure 2.11a shows such a tangle along with the relevant holes and a green curve homotopic to $\mathcal{C}_1$. Now consider the green curve in Figure 2.11b. This line represents the class $e_0^{-1}c_0^{-1}u_{-1}^{-1}e_{-1}c_0e_0s_1$. However, if we detach the curve from the points $\mathbf{Q_0}$ (the counter-clockwise curve connecting $\mathbf{P_0}$ to $\mathbf{Q_0}$), $\mathbf{P_0}$, $\mathbf{Q_{-1}}$, and $\mathbf{P_{-1}}$, we have the curve in Figure 2.11c. The curve in Figure 2.11c encircles H_{-1} in a counterclockwise sense just as the curve in Figure 2.11a. One can imagine distorting the curve in Figure 2.11c into the curve shown in Figure 2.11a.

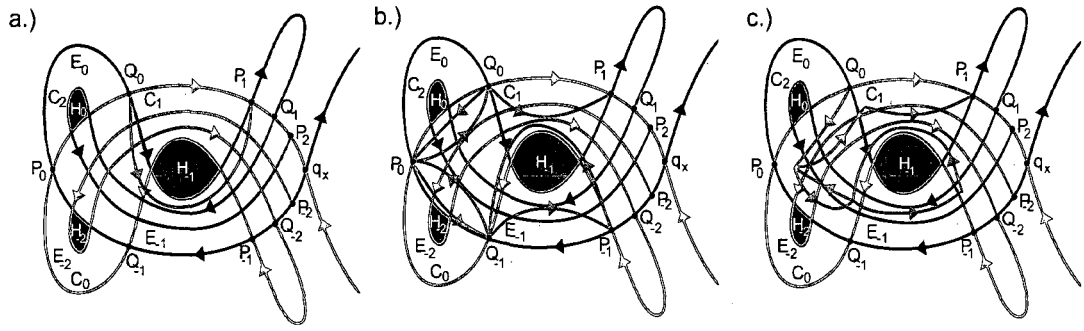

Figure 2.11: Homotopic curves assigned to different path classes.

The situation discussed in the previous paragraph illustrated the crucial fact behind choosing a suitable basis: each hole must be encircled by two path classes that do not intersect. The boundary of each hole is comprised of two segments, one from each

of the two lobes enclosing the hole. One segment is chosen so that the hole is uniquely enclosed by one class. For the internal holes, the simplest choices are either the unstable boundaries of the capture lobes or stable boundaries of the escape lobes. Since we are studying the evolution of some dynamical system forwards in time, we choose to let the classes represented by the unstable boundaries of the internal capture lobes, $\{c_n^{\pm 1}\}_{n=1}^{D}$, enclose the holes. The classes represented by the stable boundaries of the escape lobes are then ignored.

Now consider the sequence of holes lying within the external escape lobes. We choose to encircle them with the sequences $\{u_n^{\pm 1}\}_{n=0}^{\infty}$ and $\{e_n^{\pm 1}\}_{n=0}^{\infty}$. For the sequence of holes within the external capture lobes, we use the sequences $\{c_n^{\pm 1}\}_{n=-\infty}^{0}$ and $\{s_n^{\pm 1}\}_{n=-\infty}^{0}$. Finally, we desire to connect any pair of pips by a finite number of symbols and thus include the sequences $\{s_n^{\pm 1}\}_{n=0}^{\infty}$ and $\{u_n^{\pm 1}\}_{n=-\infty}^{0}$. The basis is then

$$B=\{...,c_{-1}^{\pm 1},c_0^{\pm 1}; c_1^{\pm 1},c_2^{\pm 1},...,c_D^{\pm 1}; e_0^{\pm 1},e_1^{\pm 1},e_2^{\pm 1},...; ...,s_{-1}^{\pm 1},s_0^{\pm 1},s_1^{\pm 1},...; ...,u_{-1}^{\pm 1},u_0^{\pm 1},u_1^{\pm 1},...\} \qquad (2.3)$$

We call this set the *untangled basis*. We see that the sequence $\{c_n^{\pm 1}\}_{n=D+1}^{\infty}$ has been excluded from B for reasons described above but each of these c_n's (in fact every class omitted from B) possesses a unique expansion within the untangled basis.

g.) Mapping a Line of Initial Conditions

So far, we have discussed the set of homotopy classes without mentioning how it relates to the escape time plot. For a dynamical system controlled by a homoclinic tangle, we choose a set of initial conditions represented by a continuous curve in the plane. We parameterize the initial conditions as the arclength measured along the curve

from some reference point. For all points on that line that start within or enter the complex, we count the number of iterates for those points to map out of the complex. We have stated that points that exit the complex must arrive in E_0. If points arrive in E_0 at the n^{th} iterate, then these points lie in the intersection of E_0 and $\mathcal{M}^n(\mathcal{L}_0)$. Iterating backwards n times reveals that a point escaping at n iterates lies in the intersection of $\mathcal{L}_0$ and E_{-n}. This fact motivates an important definition.

Def: We call a connected set of points in $\mathcal{L}_0 \cap E_{-n}$ an *escape segment.* Henceforth, we refer to a plot of the iterates to escape the complex versus the parameterized initial conditions as the *discrete escape time.*

When we compare the continuous and discrete escape times for some $\mathcal{L}_0$, the structure underlying the former becomes clear. Each icicle corresponds to a single escape segment. Sequences of icicles are rectified into sequences of escape segments. We call a sequence of escape segments an *epistrophe.* The relationship between the two escape time plots is shown below in Figure 2.12.

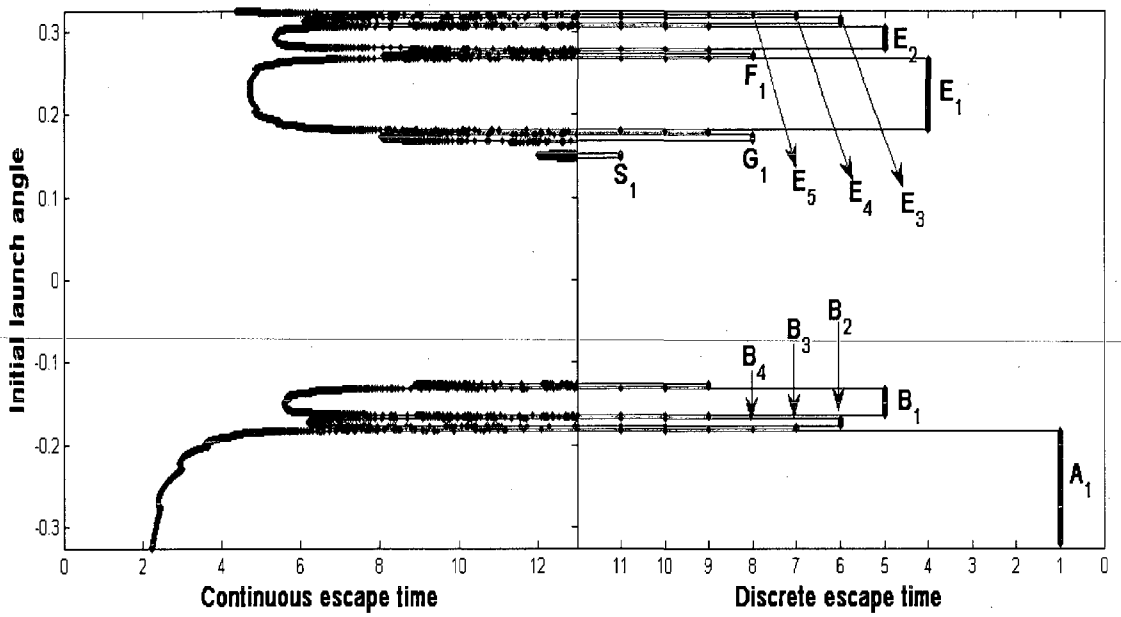

Figure 2.12: Continuous and discrete time plots on the left and right respectively.

Let us now state a few facts concerning epistrophes [6]. If the first segment appears at the n^{th} iterate, then segments appear at $n + m$ iterates for all $m > 1$. Asymptotically, the lengths and distances between adjacent segments in a single sequence go to zero geometrically at a rate given by the Lyapunov factor of the unstable fixed point. Finally, we assign an orientation to escape segments. We see from Figure 2.12 that the two sequences E_n and B_n starting at four and five iterates point in opposite directions. We want to define an orientation for the escape segments so that they point in the same direction as that of the corresponding sequence in the escape time plot. Figure 2.13 shows our convention. Running along the stable segment E_{-n}, we encounter the endpoints of the escape segment. The first point encountered is defined as the head and the second is defined as the tail.

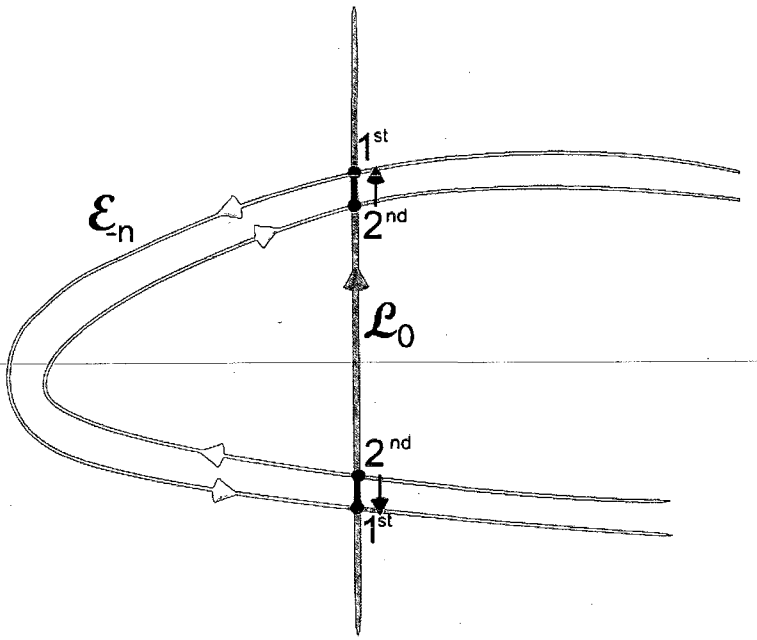

Figure 2.13: Convention for orientation of an escape segment.

h.) Minimal Sets

Before moving on to deriving the symbolic dynamical equations, we must discuss the concept of a minimal set. Let us consider Figure 2.14 below, which shows a D = 1 tangle and two curves. We immediately see that the brown curve is homotopic to the green curve. However, we see that the green curve will produce a single escape segment at the first iterate whereas the brown curve will produce five. As a result, the escape time plots will be drastically different. To go beyond the minimal set, i.e. for the symbolic dynamics to predict the additional structure due to the oscillations in the brown curve, additional sequences of holes would have to be removed. These holes would be have to be placed such that the brown curve does not represent the same path class as the green curve and none of the oscillations can be homotoped out.

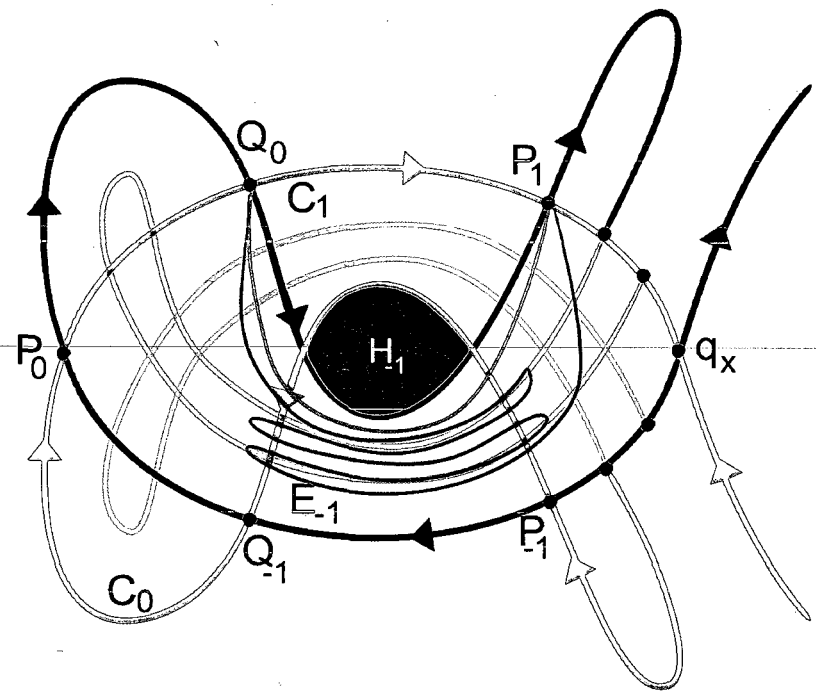

Figure 2.14: The green and brown curves are homotopic. Therefore, the minimal set for the brown curve contains a single escape segment just as the green curve.

To seek the minimal set means that we must seek the simplest possible development of the tangle. Figure 2.15 shows an alternative geometry for a tangle [7] (we will encounter this figure again in the following section and Chapter 4). In this case, C_2 intersects E_0 but overshoots E_0 to intersect E_{-1}. C_3 is topologically forced to wind over C_2 as it passes through E_0. However, C_3 contains a tendril that intersects E_0 just under the "finger" in C_2. This tendril will have a profound impact on the topologically forced development of the unstable manifold. However, for the dynamical equations we are about to examine, intersections like the one we just described are not considered. Another perspective is that we are considering the minimal sets of a class of tangles in which the intersection of the curve $\boldsymbol{c}_{D+1}$ and E_0 is a simply connected set.

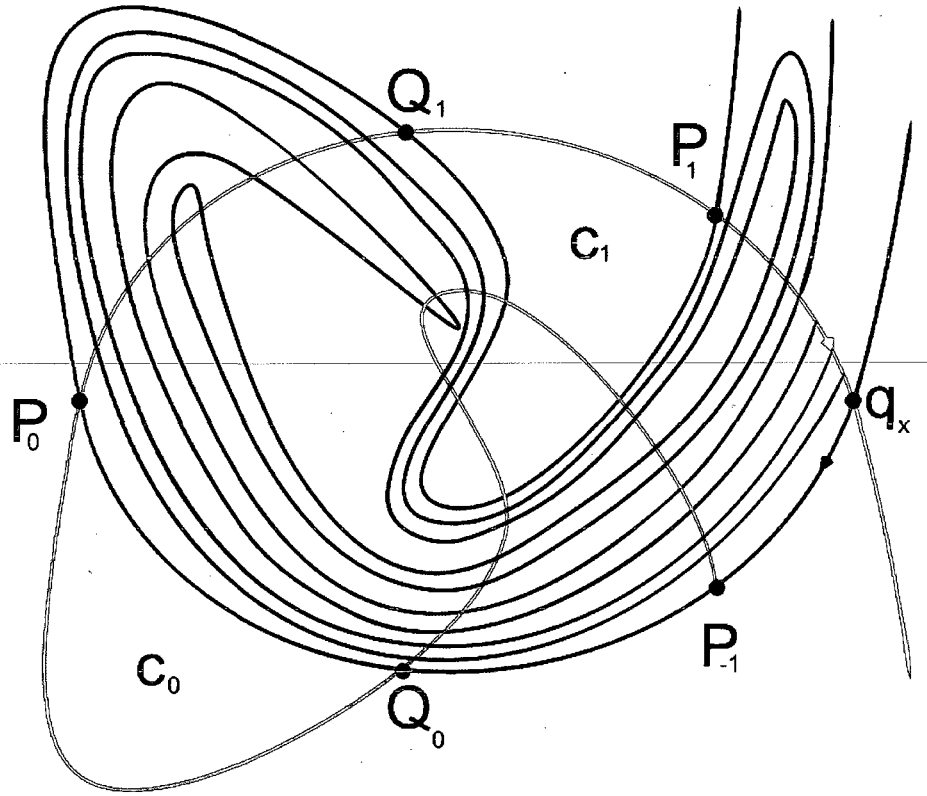

Figure 2.15: A D = 1 tangle in which C_2 intersects E_{-1} contains additional intersections that lead to a more complicated minimal set.

i.) Dynamics of Path Classes

We are now ready to derive the dynamical equations acting on the untangled basis for an arbitrary minimum delay time. We start by defining a path class that will simplify our calculations.

$$F = c_1 e_1 c_2 e_2 \cdots c_D e_D \tag{2.4}$$

One can see from Figure 2.10 that this class encloses all of the internal holes. From the same figure, one can then obtain the expansion of c_{D+1} which is the forward mapping of c_D.

$$\mathcal{M}(c_D) = F^{-1} u_0^{-1} e_0 F s_{D+1} \tag{2.5}$$

We first note that c_{D+1} is expressed entirely within the untangled basis. Secondly, $\mathcal{M}(c_D)$ contains the symbol u_0^{-1}. Following $\mathcal{C}_{D+1}$ along the direction of $\mathcal{U}$ indicates that this symbol is represented by the tip of $\mathcal{C}_{D+1}$. But this curve is an example of an escape segment. Therefore, the symbols u_0 and u_0^{-1} represent escape segments. Finally, to obtain eq. (2.5), one needs to verify the following somewhat unruly equation.

$$e_{-1} = u_{-1}(c_0 e_0 F e_D^{-1}) s_D^{-1} c_D (e_D F^{-1} e_0^{-1} c_0^{-1}) \tag{2.6}$$

This equation can be derived from a figure. The image of F follows directly from iterating eq. (2.5).

$$\mathcal{M}(F)=e_1^{-1}c_1^{-1}u_0^{-1}e_0 F s_{D+1} e_{D+1} \tag{2.7}$$

Given any curve assigned to a homotopy class, we can use eq. (2.2), eq. (2.5), and eq. (2.7) to compute the topologically forced, minimal set of escape segments. We will use the dynamical equations to compute a minimal set for D = 3 in section ii of the following chapter. The purpose of this section is to build an understanding for section v, which will explain a more general framework for extracting symbolic dynamics from homoclinic tangles. Finally, we state two important facts that can be derived from the dynamical equations. These are stated as the *Epistrophe Start and Continuation rules*. The theorem and its proof can be found in ([5]).

Theorem: Let $\mathcal{M}$ be a diffeomorphism possessing a hyperbolic fixed point with minimum delay time $D \geq 1$ and $\mathcal{L}_0$ a line of initial conditions assigned to a homotopy class. There exists an integer $N_0 > 0$ such that the minimal set of escape segments at iterates larger than N_0 can be computed using the following rules.

Epistrophe Continuation Rule: Every escape segment at n-1 iterates has on the side of its arrowhead an escape segment at n iterates pointing in the same direction.

Epistrophe Start Rule: Every escape segment at n iterates spawns immediately on both sides two escape segments at n+D+1 iterates pointing towards the segment at n iterates.

We will not directly apply these rules. We use them as a benchmark when applying the more general method.

v.) Homotopic Lobe Dynamics II

Now that we have discussed the original theory, we can move on to the more refined bridges approach. The approach presented in sec iv assumed the simplest development of the manifolds. We were able to derive a set of dynamical equations based on removing a single sequence of holes from the plane. The dynamical equations implied a minimal set of escape segments. However, one can examine an escape time plot, compare the actual set of escape segments to the predicted set, and find unpredicted segments. We want a method that will both reproduce and refine the minimal sets predicted by the Epistrophe Start and Continuation Rules. The key to refining the minimal set is to allow a more flexible way in which we alter the topology. In this section we will describe a method that allows us to construct symbolic dynamics on different topologies [7, 12]. As we encounter each concept within this method, we will apply it to the tangle in Figure 2.15 for a single topology (see [12] for the derivations). We will then apply the method to the same tangle but for a different topology. We will see how different topologies result in different sets of dynamical equations.

a.) Preliminaries

First, we must define the complex. We choose a pip $\mathbf{P_0}$ and let the complex Γ be the closed region bounded by the segments $\Gamma_{\mathcal{U}} = \mathcal{U}[\mathbf{q_x}, \mathbf{P_0}]$ and $\Gamma_S = S[\mathbf{q_x}, \mathbf{P_0}]$. The segment Γ_S is the sole segment of S that we will use to obtain the dynamical equations. The dynamical equations will encode the evolution of the unstable manifold. With $\mathbf{P_0}$ chosen, we define the fundamental $\mathcal{U}$ and S-segments.

Def: Let $S_0^F = S[\mathbf{P}_0, \mathbf{P}_1)$ and $\mathcal{U}_0^F = \mathcal{U}[\mathbf{P}_{-1}, \mathbf{P}_0)$ be the *fundamental S and $\mathcal{U}$-segments*.

The fundamental S-segment is a connected component of the stable boundary of the complex. Furthermore, the stable boundary of E_0 is contained within S_0^F. This segment is special in that we are interested in examining how the images of $\mathcal{U}_0^F$ intersect S_0^F. This motivates us to define the transition number.

Def: For any homoclinic point $\mathbf{x}$, let $m \in \mathbb{Z}$ such that $\mathcal{M}^m(x) \in \mathcal{U}_0^F$. The *transition number* n is an integer such that $\mathcal{M}^{m+n}(x) \in S_0^F$.

For points in $\mathcal{U}_0^F$, the transition number is the number of iterates for a homoclinic point to land in S_0^F. If we let $n > 0$, then for points in $S_0^F \cap \mathcal{U}_n^F$ the transition number is n.

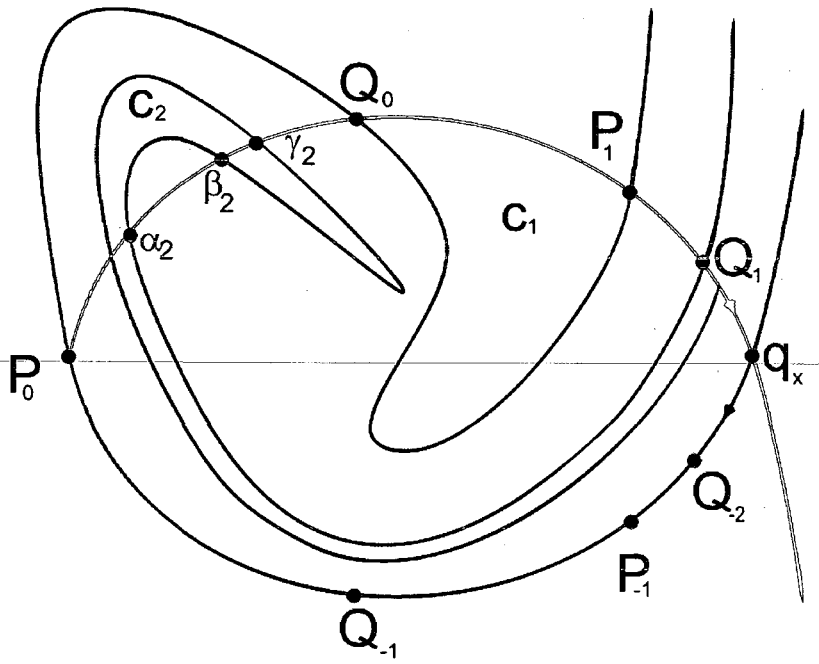

Figure 2.16: The first two capture lobes and corresponding 2-neighbors.

b.) Defining Holes in the Plane

We will use the notion of transition number to construct a new definition of a hole. We desire to remove more than one sequence of holes in order to predict more complex structure of a tangle. We begin the discussion by considering regions in which the manifolds do not enter.

Def: Let **x** and **x′** be homoclinic points. If $S(\mathbf{x}, \mathbf{x}')$ and $\mathcal{U}(\mathbf{x}, \mathbf{x}')$ contain no additional homoclinic points, then **x** and **x′** are said to be *neighbors*.

If we have a region bounded by manifolds connecting a pair of neighbors, then by definition, the manifolds do not enter this region. If either manifold entered such a region, then the manifold would have to intersect the region's boundary, thus resulting in a homoclinic point.

In order to prove that a pair of homoclinic points are neighbors, we need to know the behavior of S and $\mathcal{U}$ for arbitrary iterates of the map. We want a theory for which we input information from a finite number of iterates, and then predict future iterates. Therefore we present the following weaker definition.

Def: Let **x** and **x′** be homoclinic points. If **x** and **x′** have transition number less than or equal to j and both $S(\mathbf{x}, \mathbf{x}')$ and $\mathcal{U}(\mathbf{x}, \mathbf{x}')$ contain no homoclinic points of transition number less than or equal to j, then **x** and **x′** are said to be *pseudoneighbors of index j or j-neighbors.*

Let us consider the concept of pseudoneighbors with regards to Figure 2.16. It shows the first two capture lobes of the tangle shown in Figure 2.15. We have two pairs of homoclinic points we must consider: (α_2, β_2) and (β_2, γ_2). We immediately see that the segments $S(\alpha_2, \beta_2)$ and $S(\beta_2, \gamma_2)$ contain no homoclinic points of transition number ≤ 2. $\mathcal{U}(\alpha_2, \beta_2)$ and $\mathcal{U}(\beta_2, \gamma_2)$ also possess no homoclinic points with transition number ≤ 2. Therefore, by definition, the points α_2, β_2, and γ_2 are each pseudoneighbors of index = 2.

In other words, computing the first two capture lobes reveals two pairs of homoclinic points, (α_2, β_2) and (β_2, γ_2), that *appear* to be neighbors up to the 2nd iterate. In general, we compute J iterates of $\mathcal{U}_0^F$ and graphically obtain all pseudoneighbors of index J. For the tangles we are considering, the J-neighbors are found from the intersection of E_0 and $\bigcup_{i=0}^{J} \mathcal{U}_1^F$. We note that there are instances in which the manifolds tangentially

intersect. If we find tangential intersections in $S_0^F \cap \bigcup_{i=0}^{J} \mathcal{U}_i^F$, we remove them with a small perturbation.

Once we have identified the J-neighbors, we are ready to alter the topology. Let us now examine the new definition of a hole. The exact details of constructing a sequence of holes can be found in Ref. [7]. For simplicity, we will sketch the construction process. A *hole* is essentially a small, open set with a teardrop-shaped boundary. Each pair of J-neighbors is assigned a hole. Let **x** and **x'** be such a pair. We arbitrarily choose one point and anchor the hole to that point so that the hole lies in the region bounded by the two segments $S(\mathbf{x},\mathbf{x}')$ and $\mathcal{U}(\mathbf{x},\mathbf{x}')$ and is infinitesimally close to the anchor. Mapping a hole forwards generates an infinite sequence of holes that lie infinitesimally close to the stable segment Γ_S that may or may not lie inside Γ. Mapping each hole backwards results in a finite number of holes within the complex and a finite distance away from the complex's boundary. At some point a pre-image's anchor lands in $\mathcal{U}_0^F$ and thus lies an infinitesimal distance from $\Gamma_{\mathcal{U}}$. The remaining pre-images lie within an infinite sequence that asymptotically approach $\mathbf{q}_\mathbf{x}$ (but all lie an infinitesimal distance from $\Gamma_{\mathcal{U}}$ that again, may or may not lie inside Γ).

c.) Holes: Example

For the tangle in Figure 2.15, we have already identified the 2-neighbors. Our next step is to identify the holes and alter the topology. We first construct the holes for the pseudoneighbors shown in Figure 2.16. Then, we generate the bi-infinite orbit of each pseudoneighbor and thus the holes. Figure 2.17 shows the holes. For the sake of

clarity, we have displaced each of them a small distance away from their anchor points. Before we discuss these holes, we state a convention. When we plot holes using figures such as a square or a disk, we will refer to the hole by its name followed by an integer. For example, the disk-shaped hole in Figure 2.17 with a "2" adjacent to it will be called disk-2. The "2" follows from the fact that the hole is associated with the second iterate of a homoclinic point lying in $\mathcal{U}_0^F$.

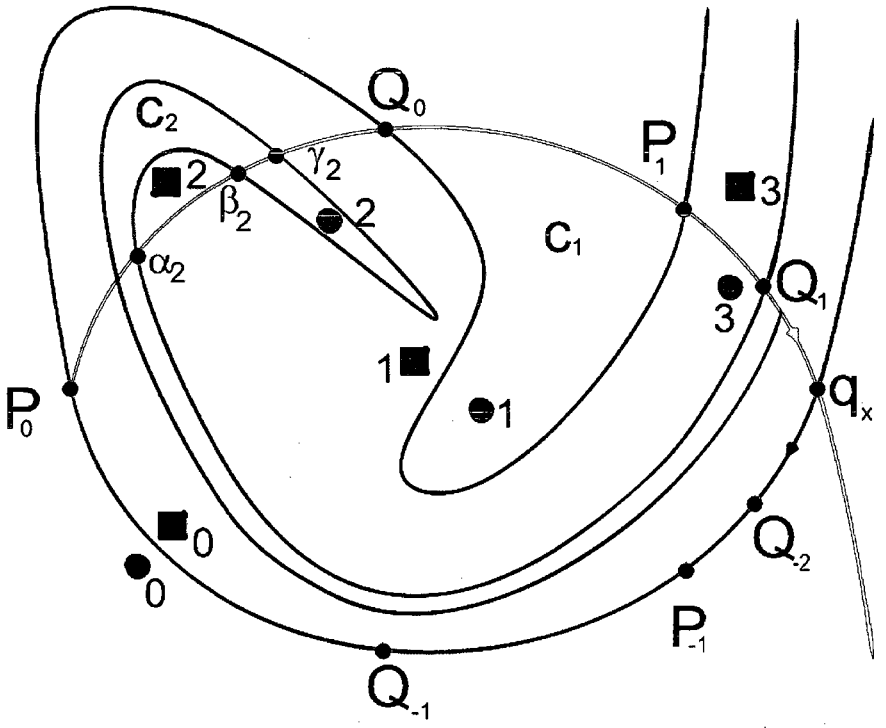

Figure 2.17: The sequences of holes constructed from the 2-neighbors.

Figure 2.18 shows that we have two sequences of holes, the square and disk sequences, for the case J = 2 because we found two pairs of 2-neighbors. Now, we must identify the holes lying within the complex. We need to compute the first and second pre-images of the two holes square-2 and disk-2. Taking the first pre-images result in square-1 and disk-1. We see that square-2 does not lie within C_2 thus indicating that all

of its images and pre-images will lie outside the corresponding capture lobes. We find that the second pre-image of disk-2 (disk-0) has mapped out of the complex whereas the second pre-image of square-2 remains inside the complex. All of the pre-images of disk-0 will remain outside the complex. As we shall see, we can ignore these pre-images as they will not be used in constructing the set of homotopy classes. The pre-images of square-0 will also play no role in constructing the set of homotopy classes. The future images of square-2 will remain outside the complex. Square-2 is the beginning of an infinite sequence of holes that are anchored to the stable boundary of the complex. The no recapture assumption prevents these holes from re-entering the complex. The future images of disk-2, however, lie inside the complex.

d.) Bridges and Bridge Classes

Now that the topology of the plane has been modified, we can identify the homotopy classes. We want to construct the set of homotopy classes in a way that is naturally accommodating to the intricate manner in which $\mathcal{U}$ intersects the stable boundary of the complex (see Figure 2.15). Therefore, we make the following definition.

Def: A closed segment of $\mathcal{U}$ that intersects Γ_S only at its endpoints is called a *bridge*. Two bridges can intersect only at their endpoints as $\mathcal{U}$ cannot self-intersect. This definition also includes the *unknown* segments of $\mathcal{U}$. This motivates us to define a *homotopy class* as a set of equivalent curves with endpoints lying in Γ_S. We allow for the endpoints to move but they cannot be lifted off the stable boundary of the complex. The new definition of a homotopy class implies that the identity class is the class of

curves that can be contracted into a point in Γ_S. Given this definition, we can define a class of bridges.

Def: A homotopy class represented by a bridge is called a *bridge class*. The orientation of a bridge class is defined such that measured along S, the final point of the curve is closer to $\mathbf{q}_x$ than the initial point. A bridge (and a bridge class) lying in Γ (the complex) is said to be *internal* and outside Γ *external*. Given that $\mathcal{U}$ can be decomposed into known and unknown segments, we can have several types of bridge classes. If a path class is represented by a known segment of $\mathcal{U}$, then we call the class a bridge class. However, there will be instances in which we will need to define a bridge class that is not represented by a known segment of $\mathcal{U}$ (i.e. a segment in $\{\mathcal{U}_1^F\}_{i=1}^J$). We call these *phantom bridge classes*. The word phantom means "merely apparent, illusory" [10]. We choose this modifier because certain bridge classes will appear that seem essential to the analysis but will not appear when a longer segment of $\mathcal{U}$ is used.

e.) Bridges and Bridge Classes: Example

Figure 2.18 shows the bridge classes enclosing the holes shown in Figure 2.17. The unstable boundary of E_0 is a bridge surrounding square-2. This bridge defines the bridge class u_0. At this point, we can introduce a new notation. We let the symbol"$\triangleleft$"denote the verb "encloses". So, $u_0 \triangleleft$ square-2 means that curves in the class u_0 (together with a portion of the stable manifold) enclose the hole labeled square-2. A bridge in $\mathcal{C}_2$ encloses disk-2. This bridge represents the class v_0. We see that the boundary of the first capture lobe is a bridge enclosing disk-1. We denote the corresponding bridge class by c_1. We also have square-1 lying just outside the bridge

representing c_1. The manifold does not naturally possess a bridge enclosing square-1 as it does disk-1. But Figure 2.15 shows that C_2 must wind under C_1 so C_2 must possess bridges that enclose square-1 (as well as disk-2 and disk-3). Therefore, we conclude that the bridge class a_1 must exist despite the fact that it is not represented by a known bridge, and that $a_1 \lhd$ square-1. This class is a phantom bridge class because our intuition tells us that the unstable manifold will wind under C_1 and thus will contain a segment that encloses square-1.

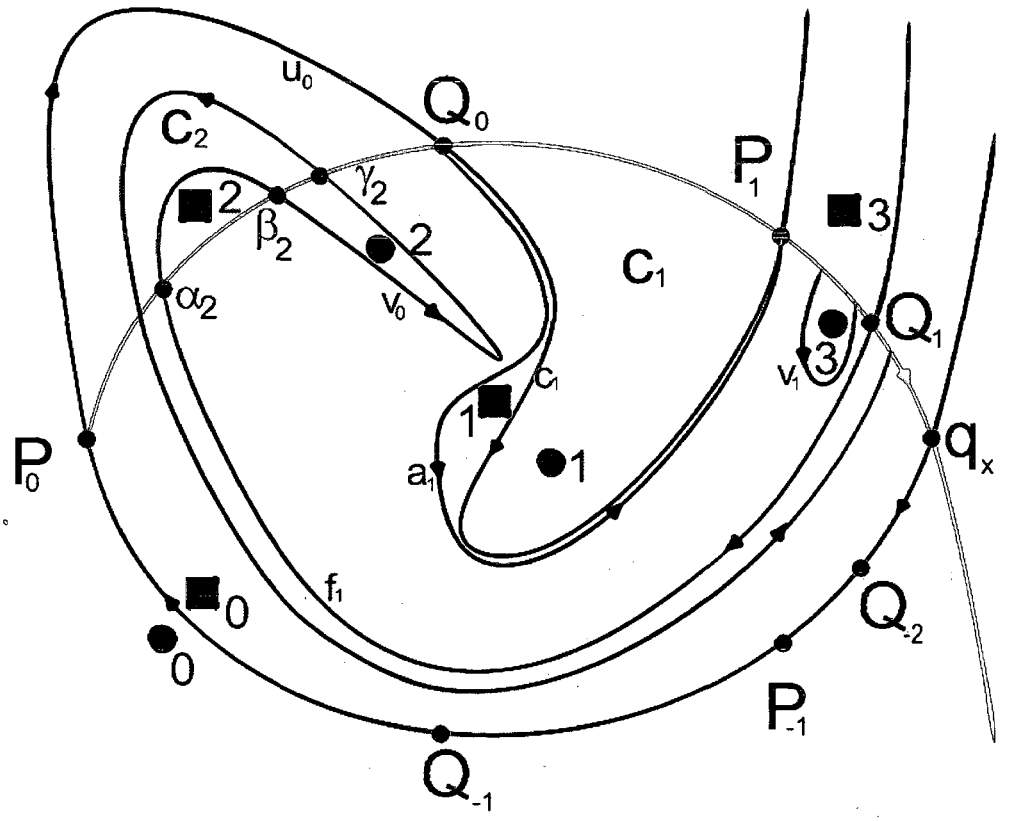

Figure 2.18: Bridge classes for J = 2.

f.) Dynamical Equations and the Bridge Basis

Now that we have identified the bridge classes, we can graphically derive a set of dynamical equations acting on the homotopy classes. As in the last section, the

dynamical mapping $\mathcal{M}$ induces a mapping on the set of homotopy classes which is also called $\mathcal{M}$. First, we consider the inert classes. A class is *inert* if mapping the class forward any number of times never produces an intersection with E_0. For our example, we have found two inert classes: u_0 and v_0. Square-2 is enclosed by the two classes $u_0^{\pm 1}$. Therefore, the images of square-2 are enclosed by the images of $u_0^{\pm 1}$. We can write down the following dynamical equation:

$$\mathcal{M}^n(u_0^{\pm 1}) = u_n^{\pm 1} \text{ where } u_n \lhd \text{square-}(n+2)\ \forall n \geq 0 \tag{2.8}$$

The second sequence of inert classes starts at $v_0^{\pm 1}$, which encloses disk-2. The same argument applied to $v_0^{\pm 1}$ leads to the following dynamical equation:

$$\mathcal{M}^n(v_0) = v_n \forall n \geq 0 \tag{2.9}$$

The images of v_0 are phantom bridge classes. Given our assumptions, we designate the bridges that enclose the images of disk-2 inert. However, our intuition tells us that since v_0 lies in the complex, the mapping will stretch and fold images of v_0 and eventually, force an intersection with E_0. Examining Figure 2.15 shows that the image of v_0 intersects E_0. But this results from setting J = 3.

The dynamical equation $\mathcal{M}(\mathcal{C}_i) = \mathcal{C}_{i+1}$ implies that $\mathcal{M}([\mathcal{C}_i]) = [\mathcal{C}_{i+1}]$. We use this fact to obtain the dynamical equations for the non-inert symbols. Let us assign the capture lobe boundaries to their respective homotopy classes.

$$\begin{aligned} &\text{a.)}[\mathcal{C}_1] = c_1 \\ &\text{b.)}[\mathcal{C}_2] = f_1^{-1} u_0 v_0 u_0^{-1} f_1 \end{aligned} \tag{2.10}$$

Since $\mathcal{M}([\mathcal{C}_1]) = [\mathcal{C}_2]$, we conclude that eq. (2.10b) is the dynamical equation for the path class c_1. The equation for a_1 can be found from Figure 2.18. We see that a_1 is represented by curves that enclose disk-1 and square-1. The image of a_1 is represented by curves that must enclose disk-2 and square-2. Considering this and the fact that a_1 looks a great deal like c_1, we have

$$\mathcal{M}(a_1) = f_1^{-1} v_0 u_0^{-1} f_1 \tag{2.11}$$

Using eq. (2.11) and the fact $f_1 = v_0 a_1 v_1$, we can obtain the equation for f_1.

$$\mathcal{M}(f_1) = a_1^{-1} u_0^{-1} f_1 v_2 \tag{2.12}$$

Now that we have obtained the dynamical equations, we must identify those symbols that can be used to uniquely express general curves of initial conditions. We must choose a set of symbols that allows us to uniquely expand general curves in the set of homotopy classes. In other words, we desire an untangled basis similar to the basis discussed in the last section. We call this set the *bridge basis*.

Def: An element in the *bridge basis* must directly enclose a finite number of holes with no other element directly enclosing those holes. In other words, if a is a bridge class and encloses hole H, then there is not a bridge class that satisfies the ordering $a \lhd b \lhd H$.

It follows from the definition that elements in the bridge basis are irreducible, i.e. they cannot be expressed as a product of other elements of the bridge basis. Let us now identify the bridge basis for Figure 2.18. Each of the inert classes encloses a single hole so each is an element of the bridge basis. The figure shows us that $c_1 \lhd$ disk-1 and $a_1 \lhd$ square-1 and that no other bridges enclose disk-1 or square-1. Therefore, the basis is the set

$$\{u_0^{\pm 1}, u_1^{\pm 1}, \ldots; v_0^{\pm 1}, v_1^{\pm 1}, \ldots; c_1^{\pm 1}, a_1^{\pm 1}\} \tag{2.13}$$

We have not included the class f_1 in the basis as it can be expressed as the sequence $v_0 a_1 v_1$, each of which is a member of the bridge basis. Therefore, the topological analysis is complete.

vi.) A Second Application of the New Method

Let us go over the method again by constructing a set of dynamical equations from 3-neighbors. In this case, we will compute a set of dynamical equations based on the development of the 3rd iterate of $\mathcal{U}_0^F$ (see [7] and [12]). We do this because of phenomena that will appear in calculations that we will examine in the next chapter.

a.) Identifying the Pseudoneighbors and Attaching the Holes

The first step is to graphically find the 3-neighbors and attach the holes. Figure 2.19 shows the tangle with the 2-neighbors and 3-neighbors plotted. We find one pair of 3-neighbors: the pair (δ_3, ε_3). The figure shows us that $S(\alpha_2, \beta_2)$ contains δ_3 and ε_3 thus indicating that α_2 and β_2 are not 3-neighbors. If we consider the segment $\mathcal{U}(\beta_2, \gamma_2)$, we find that the pre-images of δ_3 and ε_3 , δ_2 and ε_2, lie within this segment. By definition of J-neighbors, we conclude that β_2 and γ_2 are not 3-neighbors. Since we have a single pair of 3-neighbors, we have a single sequence of holes. We will attach a hole, called disk-3, to δ_3.

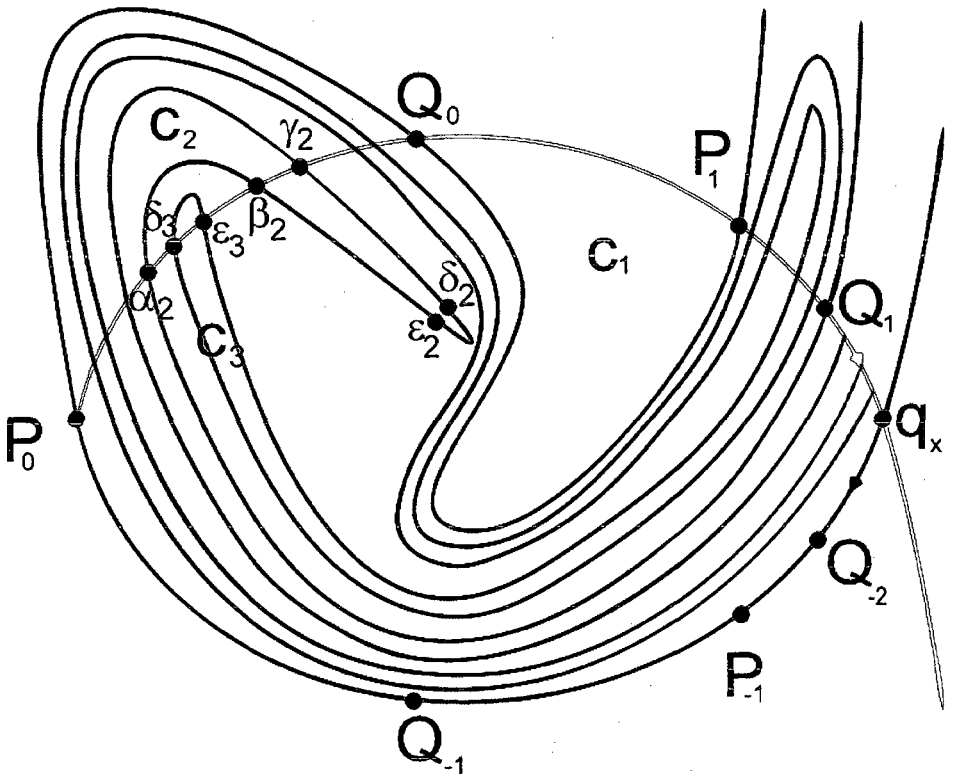

Figure 2.19: 2-neighbors and 3-neighbors for tangle the in Figure 15.

b.) Identifying the Bridge Classes and Their Dynamical Equations.

The next step is to map disk-3 forwards and backwards and identify the bridge classes. Figure 2.20 shows several of the holes in this sequence and the labels for the bridge classes. Mapping disk-3 forward generates an infinite sequence of holes lying outside the complex. The unstable boundary of E_0 encloses disk-3 and therefore the unstable boundary of each external escape lobe encloses an image of disk-3. We call the class enclosing disk-3 $u_0^{\pm 1}$. Its dynamical equation is

$$u_n^{\pm 1} = \mathcal{M}^n(u_0^{\pm 1}) \qquad (2.14)$$

Disk-0 and all of its pre-images lie outside the complex and thus can be ignored. The two pre-images of disk-3 (disk-2 and disk-1) lie within the complex. Disk-2 is

enclosed by a segment of the unstable boundary of C_2. Disk-1 is surrounded by a bridge from the unstable boundary of C_1. Since each of these two holes is surrounded by a bridge, we have two bridge classes.

$$a_1^{\pm 1} \lhd \text{disk-1}, a_2^{\pm 1} \lhd \text{disk-2} \tag{2.15}$$

Figure 2.20 also shows that the known segment of $\mathcal{U}$ possesses multiple bridges that enclose both disk-1 and disk-2. These bridges represent the classes $f^{\pm 1}$. Finally, we can compute the dynamical equations and identify the bridge basis.

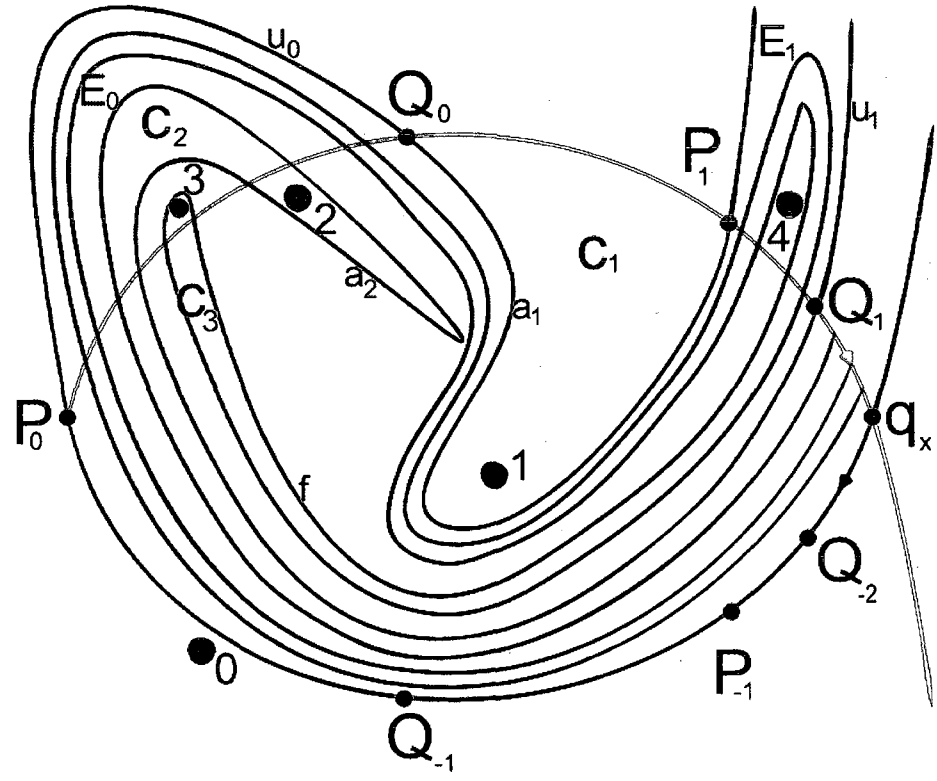

Figure 2.20: Holes constructed from the 3-neighbors.

We've already identified the dynamical equation for $u_0^{\pm 1}$. The dynamical equations for a_1, a_2, and f remain to be determined. Figure 2.20 immediately tells us that

$$[\mathcal{C}_1] = a_1 \Rightarrow \mathcal{M}(a_1) = \mathcal{M}([\mathcal{C}_1]) = [\mathcal{C}_2] \tag{2.16}$$

$[\mathcal{C}_2]$ can be found directly from Figure 2.20. Starting at $\mathbf{Q}_1$ we follow the natural orientation of $\mathcal{C}_2$. We see that the first and last bridges are f^{-1} and f, respectively. Two bridges wind through E_0 giving two escape classes with opposing orientations. Finally, the finger represents the class a_2. The dynamical equation for a_1 is then

$$\mathcal{M}(a_1) = f^{-1}u_0a_2u_0^{-1}f \tag{2.17}$$

We need to find the dynamical equation for f and a_2. First, we'll apply the map to eq. (2.17).

$$\mathcal{M}^2(a_1) = \mathcal{M}(f^{-1}u_0a_2u_0^{-1}f) = \mathcal{M}(f)^{-1}u_1\mathcal{M}(a_2)u_1^{-1}\mathcal{M}(f) \tag{2.18}$$

Expanding $[\mathcal{C}_3]$ in the basis and equating it to the right hand side of eq. (2.18) will determine the unknowns. Assigning $\mathcal{C}_3$ to its proper homotopy class is done by examining Figure 2.20.

$$\begin{aligned} [\mathcal{C}_3] &= (f^{-1}u_0a_1)u_1(f^{-1}u_0^{-1}f)u_1^{-1}(a_1^{-1}u_0^{-1}f) \\ \mathcal{M}(f) &= a_1^{-1}u_0^{-1}f \qquad \mathcal{M}(a_2) = f^{-1}u_0^{-1}f \end{aligned} \tag{2.19}$$

Before we identify the bridge basis, let us consider the analyses for J = 2 and 3. In the first example, the analysis resulted in defining the phantom bridge classes $\{v_n\}_{n=1}^{\infty}$ and a_1. Our assumptions led to v_0's role as the first element of an infinite sequence of inert classes despite v_0 lying in the complex. And the class a_1 resulted from a judicious guess that the images of $[\mathcal{C}_2]$ must wind under $\mathcal{C}_1$ and enclose square-1. Again, we must state that the *known segment of* $\mathcal{U}$ *did not contain a bridge that represented* a_1. We then redid the calculation by including an additional capture lobe. We found a single pair of 3-neighbors and that each bridge class was represented by a

bridge lying in the *known* segment of $\mathcal{U}$. Furthermore, the class v_0 (or a_2 in the J = 3 analysis) did not map into an inert class but stretched across the complex to intersect E_0. In summary, these two calculations demonstrate that phantom bridge classes can disappear upon increasing J.

c.) Identifying the Bridge Basis.

Figure 2.20 shows that $f = a_2 a_1$. Thus, all of the bridge classes discussed so far excluding $f^{\pm 1}$ are in the bridge basis.

$$\{u_0^{\pm 1}, u_1^{\pm 1}, \ldots; a_1^{\pm 1}, a_2^{\pm 1}\} \tag{2.20}$$

The topological analysis is complete. In Chapter 4, the dynamical equations derived within this section will be used to compute the topologically forced sets of escape segments (or equivalently homoclinic intersections) for $\mathcal{U}_0^F$.

vii.) Topological Entropy

We will now discuss the complexity encoded in a set of dynamical equations. If we are given a continuous function acting on a compact space, then the topological entropy measures to what extent the mapping "mixes" regions of its domain [8]. It can also be viewed as a measure of the dynamical system's complexity. In our case, we want a simple measure of the growth rate in the number of symbols as the mapping is applied to an initial homotopy class. Thus, an increase in the topological entropy should correspond to higher complexity of the iterates of the initial homotopy class. Mitchell [7] proposed a new definition of topological entropy that is suitable for our purposes. However, it requires use of a particular representation of the symbolic dynamics, called the concise representation. To compute the topological entropy for a set of dynamical

equations we will construct a matrix representation of the symbolic equations in the concise representation. The entropy results from taking the natural logarithm of the largest positive eigenvalue of this matrix.

The purpose of the concise representation is to ensure that when the map is applied to a symbol sequence, it will give a new sequence in which there are no cancellations of symbols. Then the growth rate of the number of symbols will not be overestimated. We define a concise representation such that each iterate of $\mathcal{U}_0^F$ is comprised of a sequence of alternating internal and external symbols. For example, in the case where $f = c_1c_2c_3$, the right-hand side consists of three adjacent internal symbols. A concise representation is one in which all sequences of the form $(c_1c_2c_3)^{\pm 1}$ are replaced by $f^{\pm 1}$ and $f^{\pm 1}$ must be directly surrounded by external symbols. A concise representation produces a minimal set of intersections with the stable manifold. The topological entropy measuring the growth rate of the symbol strings also measures the growth rate of the number of homoclinic intersections. Consideration of the definition of a concise representation and the fact that internal symbols map to sequences that begin and end with internal symbols leads to the conclusion that the cancellation of symbols is impossible. To compute the topological entropy, we must construct a matrix representation of the concise symbolic dynamics.

First, consider an arbitrary symbolic sequence in a concise representation. We count the number of times a symbol and its inverse appear in the sequence. This collection of integers is organized into a column vector where each element of the vector is uniquely assigned to one of the symbols. If a symbol does not appear in the symbolic

expression, the corresponding element in the vector is assigned a 0. Let us consider an example using eq. (2.10b), which is the expansion of $\mathcal{C}_3$ in the basis constructed from the 2-neighbors.

$$\begin{array}{c} [\mathcal{C}_2] = f_1^{-1}u_0v_0u_0^{-1}f_1 \\ \Updownarrow \\ \begin{array}{cccccccccc} c_1^{\pm1} & a_1^{\pm1} & f_1^{\pm1} & u_0^{\pm1} & u_1^{\pm1} & \cdots & v_0^{\pm1} & v_1^{\pm1} & \cdots \\ (0 & 0 & 2 & 2 & 0 & \cdots & 1 & 0 & \cdots)^T \end{array} \end{array} \tag{2.21}$$

The string contains three distinct symbols (for this calculation, u_0 and u_0^{-1} are identified) so only three elements of the vector are non-zero. The vector is infinitely long, with zeros assigned to the vector elements corresponding to all u_n and v_n for $n > 1$. We also note that with the exception of f_1, all of the slots in the vector correspond to members of the bridge basis. We will explain the reasoning behind this shortly.

Each of the dynamical equations represents a relationship between a symbol and a string of symbols. Therefore, the dynamical equation for an arbitrary symbol s_i is a relationship between two vectors. These two vectors are related by a matrix containing the dynamics; i.e. dynamics on the symbols induces dynamics on the vectors

$$\mathcal{M}(s_i) = t_1t_2\cdots t_{n_i} \quad \Rightarrow \quad \underset{\sim}{T}\mathbf{v}_{s_i} = \mathbf{v}_{\mathcal{M}(s_i)} \tag{2.22}$$

The vector representing s_i is a basis vector in that it contains one non-zero element. Therefore, the matrix equation in eq. (2.22) tells us that the i^{th} column of $\underset{\sim}{T}$ is the vector representing the string $\mathcal{M}(s_i)$. The matrix $\underset{\sim}{T}$ is defined to have elements

$$T_{g_2,g_1} = \begin{cases} j & \text{if } \mathcal{M}(g_1^{\pm1}) \text{ contains } j \text{ factors of } g_2^{\pm1} \\ 0 & \text{otherwise} \end{cases} \tag{2.23}$$

Eq. (2.23) has the same form as that of a transition matrix for a topological Markov chain [9]. The difference is that for a transition matrix representing a Markov chain, each matrix element is either 0 or 1, representing whether or not the dynamics connects two states. Ref. [8] provides an example of a dynamical system (Arnold's Cat Map) in which the topological entropy defined therein is shown to be directly related to the largest eigenvalue of the mapping.

Let us consider the infinite sequences of inert classes whose existence forces the matrix to have an infinite size. For our purposes, the matrix must have a finite size. We can circumnavigate this problem by identifying all of the inert classes as a single symbol, $u^* = \{u_n^{\pm 1}\}_{n=0}^{\infty}$, $\mathcal{M}u^* \rightarrow u^*$ since $\mathcal{M}(u_0^{\pm 1}) = u_n^{\pm 1}$. By replacing the rows and columns associated with the u_n's and v_n's by u^* and v^*, the matrix is transformed into a finite dimensional matrix. Once we have a finite-dimensional matrix, we can compute its eigenvalues. We define the natural logarithm of the modulus of the largest eigenvalue to be the topological entropy.

Let us now obtain the matrix representations and topological entropies for the two examples we have considered in the last section. First, we must obtain concise representations. To compute the eigenvalues of the matrix representation, we use Matlab's built-in function eig. The two sets of dynamical equations are

$J = 2$	$J = 3$
a.) $\mathcal{M}(c_1) = f_1^{-1}u_0v_0u_0^{-1}f_1$	f.) $\mathcal{M}(a_1) = f^{-1}u_0a_2u_0^{-1}f$
b.) $\mathcal{M}(a_1) = f_1^{-1}v_0u_0^{-1}f_1$	g.) $\mathcal{M}(f) = a_1^{-1}u_0^{-1}f$
c.) $\mathcal{M}(f_1) = a_1^{-1}u_0^{-1}f_1v_2$	h.) $\mathcal{M}(a_2) = f^{-1}u_0^{-1}f$
d.) $\mathcal{M}^n(u_0) = u_n$	i.) $\mathcal{M}^n(u_0) = u_n$
e.) $\mathcal{M}^n(v_0) = v_n$	

(2.24)

Consider the dynamical equations for J = 3. Each equation is a sequence of symbols that alternate between internal and external symbols. These equations are already in concise form. However, if we examine the equations for J = 2, we see that in eq. (2.24b), the sequence $f_1^{-1}v_0$ is a sequence of two internal classes. The same applies to the sequence f_1v_2 in eq. (2.24c). Therefore, we must construct a concise set of dynamical equations. First, let us define a new bridge class $a_2 = a_1v_1$. Since $f_1 = v_0a_1v_1$, we have $f_1 = v_0a_2$ and

$$f_1^{-1}v_0 = v_1^{-1}a_1^{-1}v_0^{-1}v_0 = a_2^{-1} \tag{2.25}$$

Defining the bridge class a_2 puts eq. (2.24b) in concise form. $\mathcal{M}(a_2)$ comes directly from eq. (2.24b) and eq. (2.24e).

$$\mathcal{M}(a_2) = \mathcal{M}(a_1)\mathcal{M}(v_1) = a_2^{-1}u_0^{-1}f_1v_2 = a_2^{-1}u_0^{-1}f_2 \tag{2.26}$$

Now, let us define the sequence of classes $f_k = f_1v_2v_3...v_k$. Using eq. (2.24), the dynamical equation for f_k is

$$\mathcal{M}(f_k) = a_1^{-1}u_0^{-1}f_1v_2v_3v_4\cdots v_kv_{k+1} = a_1^{-1}u_0^{-1}f_{k+1} \tag{2.27}$$

Eq. (2.24c) is replaced by eq. (2.27). The concise dynamical equations are

$$\begin{aligned}
&\text{a.)}\mathcal{M}(c_1) = f_1^{-1}u_0v_0u_0^{-1}f_1\\
&\text{b.)}\mathcal{M}(a_1) = a_2^{-1}u_0^{-1}f_1\\
&\text{c.)}\mathcal{M}(a_2) = a_2^{-1}u_0^{-1}f_2\\
&\text{d.)}\mathcal{M}(f_k) = a_1^{-1}u_0^{-1}f_k\\
&\text{e.)}\mathcal{M}^n(u_0) = u_n\\
&\text{f.)}\mathcal{M}^n(v_0) = v_n
\end{aligned} \tag{2.28}$$

Inspection shows that each equation is a sequence of symbols alternating between internal and external symbols. To construct a finite matrix representation, we will consider $\{f_i\}_{i=1}^{\infty} = f^*$as a single set so that $\mathcal{M}f^* \rightarrow f^*$. The matrix representation of eq. (2.28) is

$$\begin{array}{c} \\ c_1 \\ a_1 \\ a_2 \\ f^* \\ u^* \\ v^* \end{array} \begin{array}{c} \begin{array}{cccccc} c_1 & a_1 & a_2 & f^* & u^* & v^* \end{array} \\ \begin{pmatrix} 0 & 0 & 0 & 0 & 0 & 0 \\ 0 & 0 & 0 & 1 & 0 & 0 \\ 0 & 1 & 1 & 0 & 0 & 0 \\ 2 & 1 & 1 & 1 & 0 & 0 \\ 2 & 1 & 1 & 1 & 1 & 0 \\ 1 & 0 & 0 & 0 & 0 & 1 \end{pmatrix} \end{array} \tag{2.29}$$

The topological entropy of this matrix is ln(2). The matrix representation for J = 3 is

$$\begin{array}{c} \\ a_1 \\ a_2 \\ f \\ u^* \end{array} \begin{array}{c} \begin{array}{cccc} a_1 & a_2 & f & u^* \end{array} \\ \begin{pmatrix} 0 & 0 & 1 & 0 \\ 1 & 0 & 0 & 0 \\ 2 & 2 & 1 & 0 \\ 2 & 1 & 1 & 1 \end{pmatrix} \end{array} \tag{2.30}$$

Its topological entropy is ln2.2695. These calculations tell us that the dynamical equations constructed from the 3-neighbors are more complex than those constructed from the 2-neighbors. Alternatively we can say that we have acquired more information about the tangle by using the 3-neighbors. In fact, the topological entropy for a D = 1 tangle with no overshoot is ln2. The dynamical equations constructed from the 2-neighbors essentially the same information as a D = 1 tangle. The number of homoclinic points grows at the same rate for both of these tangles.

viii.) Conclusions

In this chapter, we have explained how the homoclinic tangle arises from the intersection of stable and unstable manifolds emanating from an unstable fixed point. The tangle's function is to stretch and fold sets within the plane. In sec. iv, we showed the most basic approach towards characterizing the stretching and folding. By judiciously removing a set of holes from the plane, we were able to obtain a set of

nontrivial homotopy classes represented by segments of the manifolds. The dynamical mapping acting on these homotopy classes induced a set of dynamical equations on the set of homotopy classes. These dynamical equations imply the existence of a topologically forced minimal set of escape segments resulting from the dynamical equations.

The method laid out in sec iv was a first step towards a more general characterization of homoclinic tangles. In reality, tangles possess a great deal more structure that cannot be characterized by the first method. We altered the definition of homotopy class to allow for the endpoints of curves to move. We then created a different but more general definition of a hole that allowed for using multiple sequences of holes based on a finite development of the unstable manifold. We saw that these modifications also led to a set of dynamical equations that encoded the evolution of the unstable manifold.

We presented two applications of the theory to a tangle with minimum delay time of 1 but with a capture lobe that overshot E_0. The first application was based on 2-neighbors. We calculated a set of dynamical equations that included so-called phantom bridge classes. The first phantom class, a_1, seemed to exist due to the hole (square-1) outside the first capture lobe. This hole was not directly enclosed by a known bridge. Furthermore, we found a sequence of inert classes internal to the complex. Since points are stretched and folded in the complex, we believed that these bridge classes should not exist. Our intuition was confirmed upon calculating dynamical equations based on 3-neighbors. We found that no hole lay outside C_1 and thus were not forced to postulate

that an additional bridge class was present. We also found that instead of mapping to an inert class, the class represented by the overshoot was mapped to a lobe that stretched through the complex to intersect E_0 at the 3-neighbors.

Finally, we discussed topological entropy as a means of calculating the asymptotic growth rates of symbolic expressions for a given set of dynamical equations. The dynamical equations were first converted into a representation known as a concise representation. Images of $[\mathcal{U}_0^F]$ were represented by symbolic sequences that alternate between internal and external symbols. In this representation, the dynamical equations were then organized into a kind of transition matrix whose largest eigenvalue was the topological entropy. We showed that for the case of the 2-neighbors, the topological entropy was the same as if there were no overshoot present. This result implied that the information contained within both sets of dynamical equations is the same. However, the topological entropy for the 3-neighbors was larger indicating that the symbolic sequences would grow at a faster rate.

While we have said that these methods allow us to compute minimal sets of escape segments, we have not shown these segments in an escape-time plot. The following chapter will be concerned with comparing minimal sets to numerically computed sets of epistrophes. In Chapter 3, we will compute minimal sets using both methods for comparison to numerically computed sets of escape segments. We will also compare the theoretical predictions to the actual results for a point burst of rays.

-Chapter 2 References-

[1] W. S. Massey, *Algebraic Topology: An Introduction* (Harcourt, Brace & World, Inc., 1967), Ch 2, M. Nakahara, *Geometry, Topology, and Physics* (IOP, Bristol, 1990), A. T. Fomenko, D. B. Fuchs, and V. L. Gutenmacher, *Homotopic Topology* (Akadémiai Kiadó, Budapest, 1986).

[2] W. Fulton, *Algebraic Topology* (Springer, New York, 1995), p. 39.

[3] K. R. Meyer and G. R. Hall, *Introduction to Hamiltonian Dynamical Systems and the N-Body Problem* (Springer, New York, 1992), pp. 224–225.

[4] S. Wiggins, *Chaotic Transport in Dynamical Systems* (Springer-Verlag, New York, 1992), Ch. 2.

[5] K. A. Mitchell, J. P. Handley, J. B. Delos, and S. K. Knudson, Chaos **13**, 892 (2003).

[6] K. A. Mitchell, J. P. Handley, B. Tighe, J. B. Delos, and S. K. Knudson, Chaos **13**, 880 (2003).

[7] K. A. Mitchell and J. B. Delos, Physica D **221**, 170 (2006).

[8] E. A. Jackson, *Perspectives of Nonlinear Dynamics* (Cambridge University Press, Cambridge 1990), Vol. 2, p. 101.

[9] R. Gilmore and M Lefranc, *The Topology of Chaos* (Wiley, New York, 2002), p. 59.

[10] *The Oxford Encyclopedic English Dictionary*, edited by J. Pearsall and B. Trumble (Oxford University Press, New York, 1996).

[11] T. Poston and I. Stewart, *Catastrophe Theory and its Applications* (Pitman, London, 1978), p. 67.

[12] K. A. Mitchell, Physica D **238**, 737 (2009).

-Chapter 3-
Topological Analysis of a Homoclinc Tangle Underlying an Open, Specularly-reflecting Vase-Shaped Cavity

i.) Introduction

In the last chapter, we discussed the development of Homotopic Lobe Dynamics applied to homoclinic tangles. We compute finite segments of the stable and unstable manifolds and punch holes in regions in which the manifolds are assumed to never enter. We then graphically obtain a set of symbolic dynamical equations that encode how the known segment of the unstable manifold stretches and folds through phase space. We now apply the theory to the homoclinic tangle shown in Figure 3.1.

We present three calculations showing how increasing J in $\mathcal{U}_J^F$ allows one to compute a new bridge basis that enlarges the topologically forced, minimal set of homoclinic points (or escape segments). For each basis, we derive a set of dynamical equations acting on the basis encoding how $\{\mathcal{U}_i^F\}_{i=1}^J$ stretches and folds through phase space. Each basis allows one to expand the sequence of capture lobes $\{\mathcal{C}_i\}_{i=1}^{20}$. From these sequences we can obtain the minimal set of homoclinic points appearing at each iterate. We compare these minimal sets to the actual set of homoclinic points up to iterate 20 for the tangle shown in Figure 3.1. We then apply the theory to a point burst in the vase represented as the vertical line in Figure 3.1. We show the minimal set of escape segments predicted by two of these bases and compare them to the numerically computed set of escape segments.

The input to the theory is $\mathcal{M}^J(\mathcal{U}_0^F)$ for J = 4, 12, and 16 and $\mathcal{U}_0^F = \mathcal{U}(\mathbf{P_{-1}}, \mathbf{P_0})$. An examination of the tangle would show that there is no new information appearing at intermediate values of J. We begin by stating our conventions. Unless indicated otherwise, red and blue curves denote the stable and unstable manifolds respectively. The region bounded by $S/\mathcal{U}[\mathbf{q_x}, \mathbf{P_0}]$ is called the complex and denoted by Γ. We call the region bounded by $S/\mathcal{U}[\mathbf{P_0}, \mathbf{Q_0}]$ escape zone 0 or E_0. Points escaping Γ must arrive in E_0. Let $\mathcal{C}_0 = \mathcal{U}(\mathbf{Q_{-1}}, \mathbf{P_0})$ denote the unstable boundary of capture lobe 0 and C_0 the lobe itself. Then, the unstable boundary of the i^{th} capture lobe is $\mathcal{C}_i = \mathcal{M}^i(\mathcal{C}_0)$ and lobes themselves are $C_i = \mathcal{M}^i(C_0)$. Finally, to differentiate the path classes within different bases, we choose the following notational convention. Let $[\mathcal{B}]_J$ denote the homotopy class of curve $\mathcal{B}$ in basis J where J indicates the number of times $\mathcal{U}_0^F$ has been iterated. Finally, the axes in our figures are labeled as either "q" or "p".

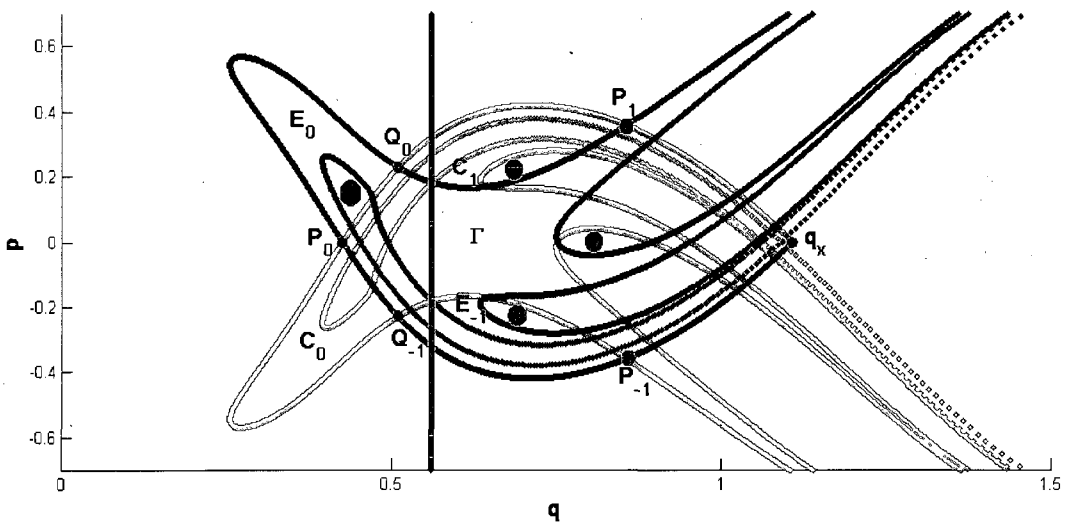

Figure 3.1: Vase's homoclinic tangle for A,w = 0.75 with vertical line representing a point burst.

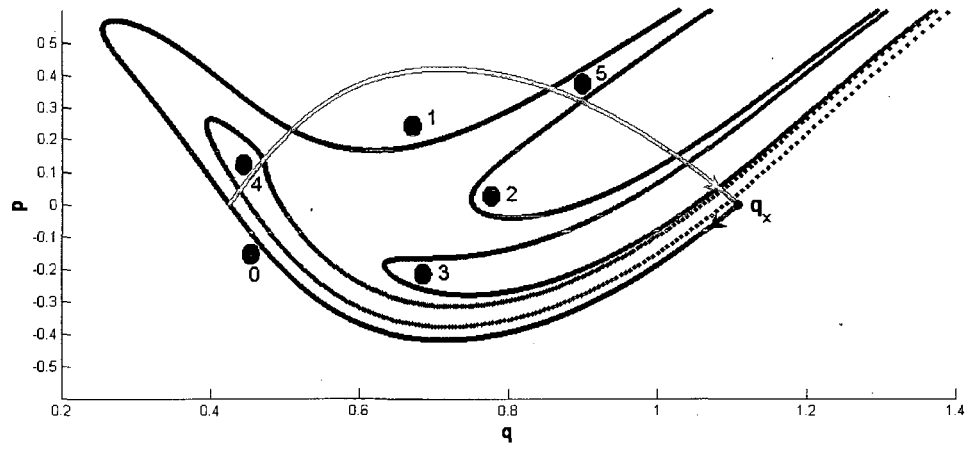

Figure 3.2: Punctured plane used to derive eq. (3.1).

ii.) The 4-basis.

a.) Derivation of the 4-basis

We begin our discussion with the 4-basis. We compute $\{\mathcal{U}_i^F\}_{i=1}^4$, or the first three internal capture lobes and the first lobe to intersect E_0. $C_4 \cap E_0$ gives a pair of 4-neighbors, α_4 and β_4 in Figure 3.2, giving the minimal amount of topological information necessary to obtain nontrivial dynamics. To obtain the sequence of holes, we arbitrarily choose one homoclinic point from the pair (α_4, β_4) and punch a hole as described in Chapter 2. We call that hole H_4, and represent it by the black disk labeled 4 in Figure 3.2. We then iterate that hole forwards and backwards an infinite number of times. Figure 3.2 shows a subset of the hole sequence as disks with integer labels. Iterating H_4 (or hole 4) forwards gives a sequence of inert bridge classes representing the unstable boundaries of the external escape lobes. We call the bridge class surrounding H_4 u_0 and its n^{th} image $u_n = \mathcal{M}^n(u_0)$. Iterating H_4 backwards 3 times gives the internal

holes labeled 3, 2, and 1. Around each of these holes is a bridge from an internal capture lobe defining the bridge classes $[\mathcal{C}_i]_4 = c_i \lhd H_i$ for i=1,2,3.

The dynamical equations acting on the bridge basis are

$$\begin{aligned} &\text{a.) } \mathcal{M}(c_1) = c_2 \\ &\text{b.) } \mathcal{M}(c_2) = c_3 \\ &\text{c.) } \mathcal{M}(c_3) = f^{-1}u_0^{-1}f \quad \text{where } f = c_1c_2c_3 \\ &\text{d.) } \mathcal{M}(f) = c_1^{-1}u_0^{-1}f \\ &\text{e.) } \mathcal{M}^n(u_0) = u_n \end{aligned} \tag{3.1}$$

Let us first discuss eq. (3.1). The minimum delay time for the tangle under consideration is three. This means that a point maps into the complex and must iterate at least three times to escape. The first two equations say curves in c_1 will map into the class represented by $\mathcal{C}_3$ after two iterates. An additional iteration will force a segment of any one of those curves to wind through E_0 producing an escape segment represented by the symbol u_0^{-1}. The symbol f is represented by curves that traverse the breadth of Γ enclosing the internal holes.

b.) Predictions of the 4-basis

Using these dynamical equations, we can iterate $[\mathcal{C}_4]$ past the 4th iterate to compute the topologically forced development of the tangle. This calculation also produces the minimal forced set of homoclinic intersections. We show the first 8 iterates of $\mathcal{U}_0^F$ in eq. (3.2). At each iterate, the newborn escape segments are in boldface.

$$
\begin{aligned}
&\text{a.)}\ [\mathcal{U}_1^F]_4 = u_0 c_1 \\
&\text{b.)}\ [\mathcal{U}_2^F]_4 = u_1 c_2 \\
&\text{c.)}\ [\mathcal{U}_3^F]_4 = u_2 c_3 \\
&\text{d.)}\ [\mathcal{U}_4^F]_4 = u_3 f^{-1} \mathbb{u}_0^{-1} f \\
&\text{e.)}\ [\mathcal{U}_5^F]_4 = u_4 f^{-1} \mathbb{u}_0 c_1 u_1^{-1} c_1^{-1} \mathbb{u}_0^{-1} f \\
&\text{f.)}\ [\mathcal{U}_6^F]_4 = u_5 f^{-1} \mathbb{u}_0 c_1 u_1 c_2 u_2^{-1} c_2^{-1} u_1^{-1} c_1^{-1} \mathbb{u}_0^{-1} f \\
&\text{g.)}\ [\mathcal{U}_7^F]_4 = u_6 f^{-1} \mathbb{u}_0 c_1 u_1 c_2 u_2 c_3 u_3^{-1} c_3^{-1} u_2^{-1} c_2^{-1} u_1^{-1} c_1^{-1} \mathbb{u}_0^{-1} f \\
&\text{h.)}\ [\mathcal{U}_8^F]_4 = u_7 f^{-1} \mathbb{u}_0 c_1 u_1 c_2 u_2 c_3 u_3 f^{-1} \mathbb{u}_0^{-1} f u_4^{-1} f^{-1} \mathbb{u}_0 f u_3^{-1} \\
&\qquad\qquad c_3^{-1} u_2^{-1} c_2^{-1} u_1^{-1} c_1^{-1} \mathbb{u}_0^{-1} f
\end{aligned}
\tag{3.2}
$$

Each symbolic expression starts with an inert class because $\mathcal{U}[\mathbf{P}_{-1}, \mathbf{Q}_{-1}]$ maps into the unstable boundary of E_0 which is represented by u_0. Therefore, $[\mathcal{U}_i^F]_4 = u_{i-1}[\mathcal{C}_i]_4$ for $i>0$. Eq. (3.2d) shows that an epistrophe starts at the 4th iterate pointing to the right. Eq. (3.2e) contains a factor of u_0^{-1} to the right of u_1^{-1} representing the continuation of the epistrophe started in eq. (3.2d). The factor u_0 represents the birth of a new epistrophe with left-pointing orientation. The escape segments in eqs. (3.2f) and (3.2g) merely propagate the two known sequences. Finally, eq. (3.2h) shows the birth of two new epistrophes. The symbol u_4^{-1} in $[\mathcal{C}_8]_4$ is flanked by its children, u_0 and u_0^{-1}. Note that the orientations indicate that the segments point toward u_4^{-1}. The second and next to last symbols represent the continuation of the first two epistrophes. All subsequent escape segments will result from the continuation of the existing epistrophes and the spawning of new epistrophes from the segments in eq. (3.2).

c.) Predictions of the First Theory

We can compare these results to those of the first incarnation of the theory. Using the dynamical equations in eqs. (2.2), (2.4), (2.5), and (2.7) with D = 3 we find

$$
\begin{aligned}
&\text{a.)}\ [\mathcal{C}_1] = c_1 \\
&\text{b.)}\ [\mathcal{C}_2] = c_2 \\
&\text{c.)}\ [\mathcal{C}_3] = c_3 \\
&\text{d.)}\ [\mathcal{C}_4] = F^{-1}\mathbb{U}_0^{-1}F \\
&\text{e.)}\ [\mathcal{C}_5] = F^{-1}\mathbb{U}_0 c_1 u_1^{-1} c_1^{-1}\mathbb{U}_0^{-1}F \\
&\text{f.)}\ [\mathcal{C}_6] = F^{-1}\mathbb{U}_0 c_1 u_1 c_2 u_2^{-1} c_2^{-1} u_1^{-1} c_1^{-1}\mathbb{U}_0^{-1}F \\
&\text{g.)}\ [\mathcal{C}_7] = F^{-1}\mathbb{U}_0 c_1 u_1 c_2 u_2 c_3 u_3^{-1} c_3^{-1} u_2^{-1} c_2^{-1} \\
&\qquad\qquad u_1^{-1} c_1^{-1}\mathbb{U}_0^{-1}F \\
&\text{h.)}\ [\mathcal{C}_8] = F^{-1}\mathbb{U}_0 c_1 u_1 c_2 u_2 c_3 u_3 F^{-1}\mathbb{U}_0^{-1} F u_4^{-1} \\
&\qquad\qquad F^{-1}\mathbb{U}_0 F u_3^{-1} c_3^{-1} u_2^{-1} c_2^{-1} u_1^{-1} c_1^{-1}\mathbb{U}_0^{-1}F
\end{aligned}
\tag{3.3}
$$

Comparing the minimal set predicted by eq. (3.3) and eq. (3.2), we see they match in number and orientations at each iterate. We can apply the Epistrophe Start and Continuation rules to eq. (3.3h) to predict the minimal set to any arbitrary iterate. However, within the more general bridges framework, we cannot use those rules for dynamical equations constructed from pseudo-neighbors as they have not been proven within the bridges framework.

iii) The 12-basis

a.) Derivation of the 12-basis

The homoclinic points (α_4, β_4) are true neighbors thus giving a region to which both manifolds are denied entry. This tells us that they must appear for any value of J. But for a new value of J, the pair (α_4, β_4) will be called J-neighbors. For convenience,

we will leave their subscripts unchanged. Going past the 4th iterate of $\mathcal{U}_F^0$, we find the two new pairs of pseudoneighbors (γ_{12}, δ_{12}) and (δ_{12}, ε_{12}) in $\mathcal{U}_F^{12}$ shown in Figure 3.3. We choose δ_{12} as the anchor for the holes and (γ_{12}, δ_{12}) and (δ_{12}, ε_{12}) are associated with the "square" and "plus" holes respectively. Again we attach the "circle" hole to β_4.

Mapping the circle hole forwards and backwards generates the same holes shown in Figure 3.2. Again, we let the inert sequence generated by mapping the hole forward $u_n = \mathcal{M}^n(u_0)$. Mapping the square and plus holes forward generates an infinite sequence of inert classes that asymptotically converge to $\mathbf{q}_x$. We call $v_n = \mathcal{M}^n(v_0)$ and $x_n = \mathcal{M}^n(x_0)$ respectively. The forward iterates of the square lie outside the complex while those of the plus lie inside. Mapping the square and plus sequences backwards produces additional holes in the complex. Since the known segment of $\mathcal{U}$ is long, we present a schematic representation of the holes and bridge classes in Figure 3.4.

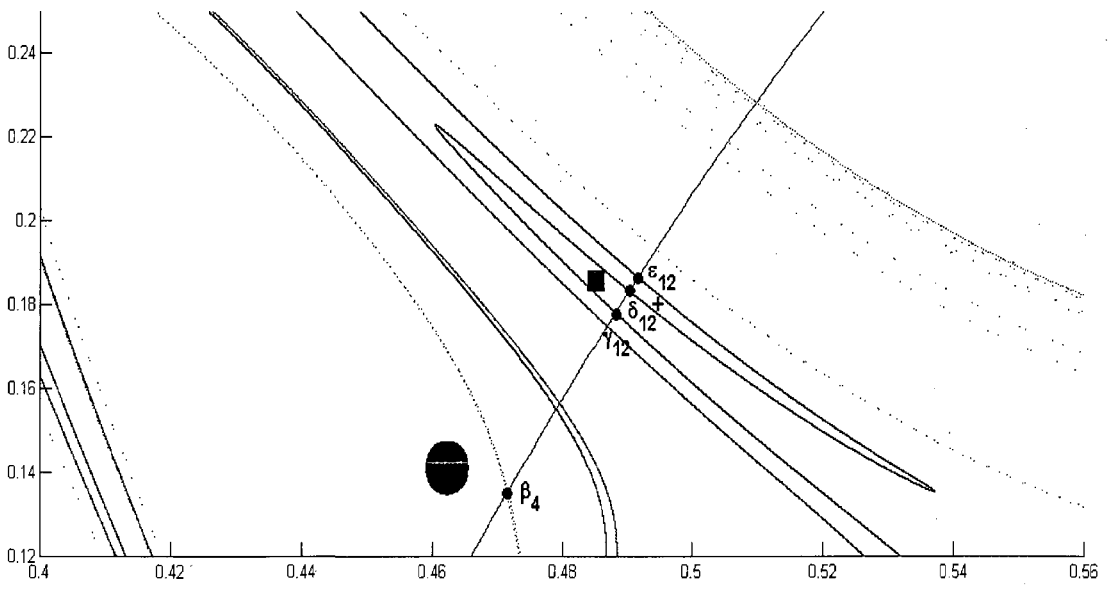

Figure 3.3: Holes attached12-neighbors found from computing $\{\mathcal{U}_i^F\}_{i=1}^{12}$.

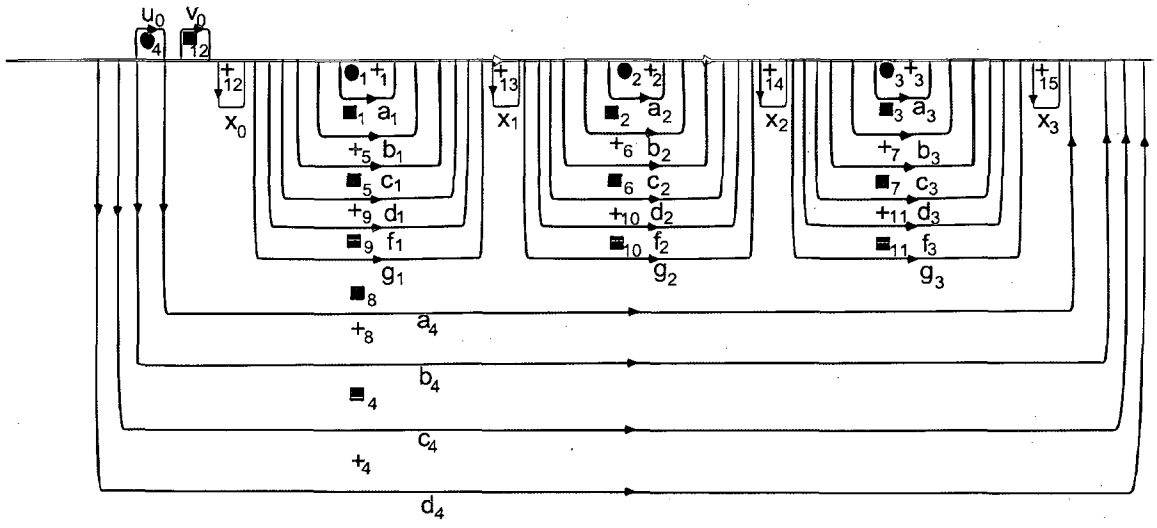

Figure 3.4: Schematic representation of the 12-basis.

The schematic in Figure 3.4 shows the orientations and the nesting of the bridge classes. Each bridge's label lies below the bridge itself. For instance, a_1 encloses the holes plus-1 and disk-1 and b_1 encloses square-1. We define a convention for labeling the bridge classes that naturally follows the nesting of the bridge classes. Since there are three internal capture lobes, bridge classes represented by bridges that wind around the internal lobes will be given the same subscript. Moving outward away from the internal lobe, we follow the standard ordering of the alphabet in labeling in assigning a label to a bridge. The topological analysis gives eq. (3.4), the dynamical equations that act on the bridge basis shown in Figure 3.4.

$$
\begin{aligned}
&a.)\mathcal{M}(a_1) = a_2 \\
&b.)\mathcal{M}(a_2) = a_3 \\
&c.)\mathcal{M}(a_3) = c_4^{-1}u_0^{-1}d_4 \\
&d.)\mathcal{M}(a_4) = f_1^{-1}w_0^{-1}d_4x_4 \\
&e.)\mathcal{M}(b_1) = b_2 \\
&f.)\mathcal{M}(b_2) = b_3 \\
&g.)\mathcal{M}(b_3) = b_4^{-1}u_0^{-1}d_4 \\
&h.)\mathcal{M}(b_4) = d_1^{-1}w_0^{-1}d_4x_4 \\
&i.)\mathcal{M}(c_1) = c_2 \\
&j.)\mathcal{M}(c_2) = c_3 \\
&k.)\mathcal{M}(c_3) = a_4^{-1}u_0^{-1}d_4 \\
&l.)\mathcal{M}(c_4) = c_1^{-1}w_0^{-1}d_4x_4 \\
&m.)\mathcal{M}(d_1) = d_2 \\
&n.)\mathcal{M}(d_2) = d_3 \\
&o.)\mathcal{M}(d_3) = g^{-1}u_0^{-1}d_4 \\
&p.)\mathcal{M}(d_4) = b_1^{-1}w_0^{-1}d_4x_4 \\
&q.)\mathcal{M}(f_1) = f_2 \\
&r.)\mathcal{M}(f_2) = f_3 \\
&s.)\mathcal{M}(f_3) = g^{-1}v_0x_0w_0^{-1}d_4 \\
&t.)\mathcal{M}(g_1) = g_2 \\
&u.)\mathcal{M}(g_2) = g_3 \\
&v.)\mathcal{M}(g_3) = g^{-1}x_0w_0^{-1}d_4 \\
&w.)\mathcal{M}(g) = g_1^{-1}w_0^{-1}d_4x_4 \quad \text{with } g = x_0g_1x_1g_2x_2g_3x_3 \\
&x.)\mathcal{M}^n(v_0) = v_n \\
&y.)\mathcal{M}^n(u_0) = u_n \\
&\text{let } w_0 = v_0u_0 \\
&z.)\mathcal{M}^n(w_0) = w_n \quad \text{with } w_0 = v_0u_0 \\
&aa.)\mathcal{M}^n(x_0) = x_n
\end{aligned}
\tag{3.4}
$$

Before deriving eq. (3.4), we must comment on the inert sequence $\{x_i\}_{i=0}^{\infty}$. Figure 3.3 shows that x_0 is indeed a bridge class as it encloses plus-12 and is represented by a known segment of the unstable manifold. Given the known segment of $\mathcal{U}$, we predict that the i^{th} image of $\mathcal{C}_{12}$ will contain a small "bump" representing the class x_i. In actuality, only the first three images of x_0's representative bridge remain within the complex (we will see this in the J = 16 calculation). However, even without this knowledge, we can make the claim that $\{x_i\}_{i=1}^{\infty}$ is not really a sequence of inert classes

because they lie in the complex, and eventually must map out of the complex. Therefore, the sequence $\{x_i\}_{i=1}^{\infty}$ is a sequence of phantom bridge classes.

In the remainder of this section, we show why Eqs. (3.4) are true. After punching the holes in the complex, we expand a capture lobe and its image in the basis by plotting the lobes along with the holes. Equating the two bridge classes gives an algebraic relationship containing at least one dynamical equation. We start by examining the first four capture lobes in Figure 3.5. We note that in practice, the holes are placed a distance of about 10^{-6} away from the homoclinic point. The sizes and locations of the holes in our figures are altered to make the figures clear.

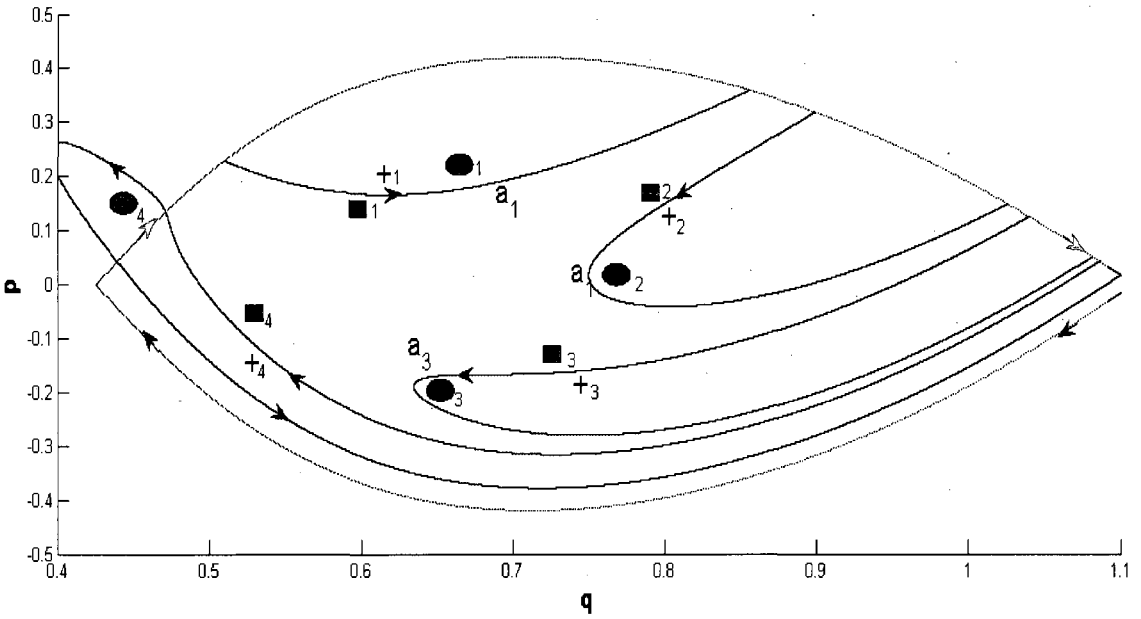

Figure 3.5: First four capture lobes and the 12-basis holes.

The unstable boundaries of capture lobes one, two, and three each define a bridge enclosing plus and disk holes. The mapping acting on the lobes induces two dynamical equations eq. (3.4a) and eq. (3.4b)

$$\begin{aligned} \mathcal{M}([\mathcal{C}_1]_{12}) = [\mathcal{C}_2]_{12} \quad &\Leftrightarrow \quad \mathcal{M}(a_1) = a_2 \\ \mathcal{M}([\mathcal{C}_2]_{12}) = [\mathcal{C}_3]_{12} \quad &\Leftrightarrow \quad \mathcal{M}(a_2) = a_3 \end{aligned} \tag{3.5}$$

Iterating the 3rd lobe gives C_4, the first lobe to intersect E_0. Following the natural orientation, one bridge encloses the hole square-4, giving a factor of c_4^{-1}. The bridge lying in E_0 encloses disk-4 giving a factor of u_0^{-1}. Finally, the last bridge encloses plus-4. Expanding the 4th capture lobe in the basis results in eq. (3.5c).

$$\mathcal{M}([\mathcal{C}_3]_{12}) = [\mathcal{C}_4]_{12} = \mathcal{M}(a_3) = c_4^{-1}u_0^{-1}d_4 \tag{3.6}$$

Figure 3.6 shows C_5 and its associated holes. Since C_4 intersects E_0, applying the map once implies that C_5 intersects E_1. Furthermore, C_4's endpoints must approach $\mathbf{q_x}$ under the mapping. Since the unstable manifold cannot self-intersect, C_5 must wind under and over C_4 to intersect E_1. This means that $[\mathcal{C}_5]_{12}$ must start with d_4^{-1} and end with d_4. Furthermore, two bridges are forced to wind through E_0 to connect to E_1. In this case, the two bridges enclose disk-4 and square-16. Finally, the two remaining bridges winding around C_1 represent two new classes. We let b_1 denote the class enclosing square-1 and c_1 denote the class enclosing plus-5. Computing $\mathcal{M}([\mathcal{C}_4]_{12})$ and equating it with $[\mathcal{C}_5]_{12}$ gives eq. (3.4l) and eq. (3.4p).

$$\mathcal{M}([\mathcal{C}_4]_{12}) = \mathcal{M}(c_4^{-1})u_1^{-1}\mathcal{M}(d_4) = [\mathcal{C}_5]_{12} = x_4^{-1}d_4^{-1}w_0c_1u_1^{-1}b_1^{-1}w_0^{-1}d_4x_4 \tag{3.7}$$

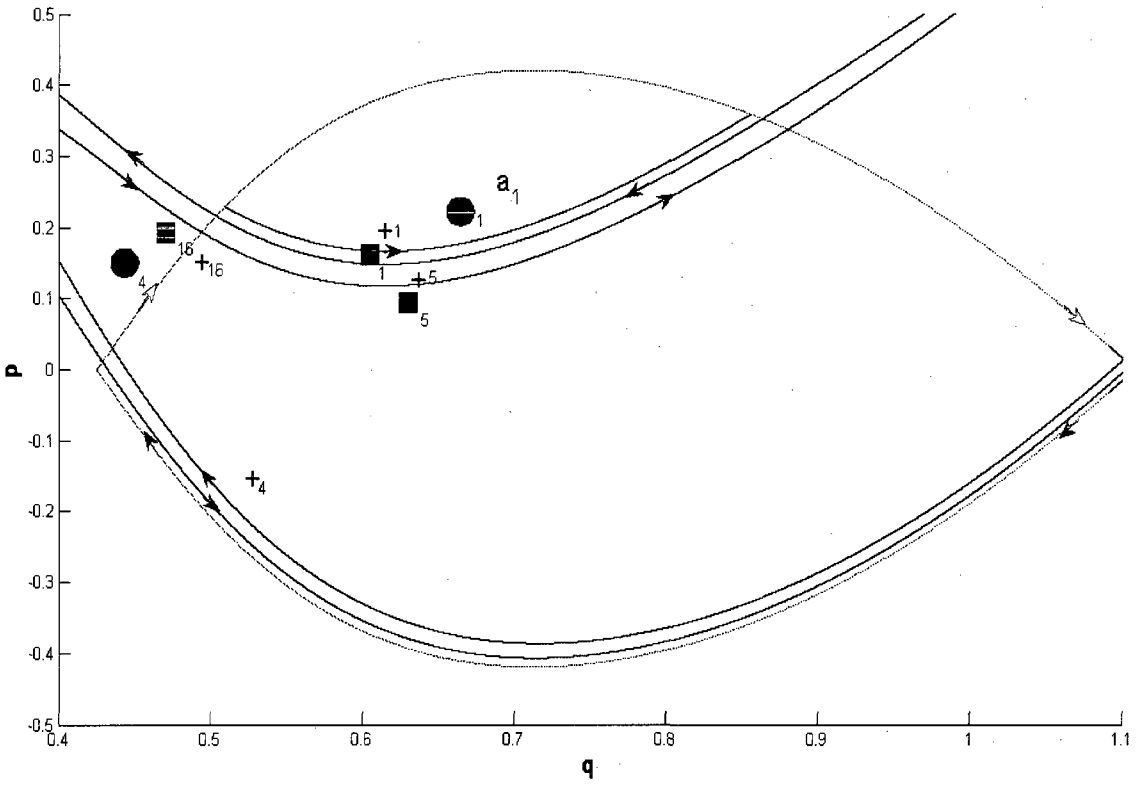

Figure 3.6: C_5 and the 12-basis holes around which the lobe winds.

We will now determine the action of the map on c_1 and b_1 using Figure 3.7. Applying the map to the representatives of c_1 and b_1 we find two bridges enclosing the holes plus-6 and square-2, respectively. These new bridges represent two new classes c_2 and b_2. Applying the map to the representatives of c_2 and b_2 we find two bridges enclosing the holes plus-7 and square-3 representing the classes c_3 and b_3. These simple results reflect the existence of the minimum delay time. If a curve nests around C_1 (with endpoints on Γ_S), then that curve is forced to intersect E_{-3} due to E_{-3}'s intersection with C_1 (see Figure 3.1).

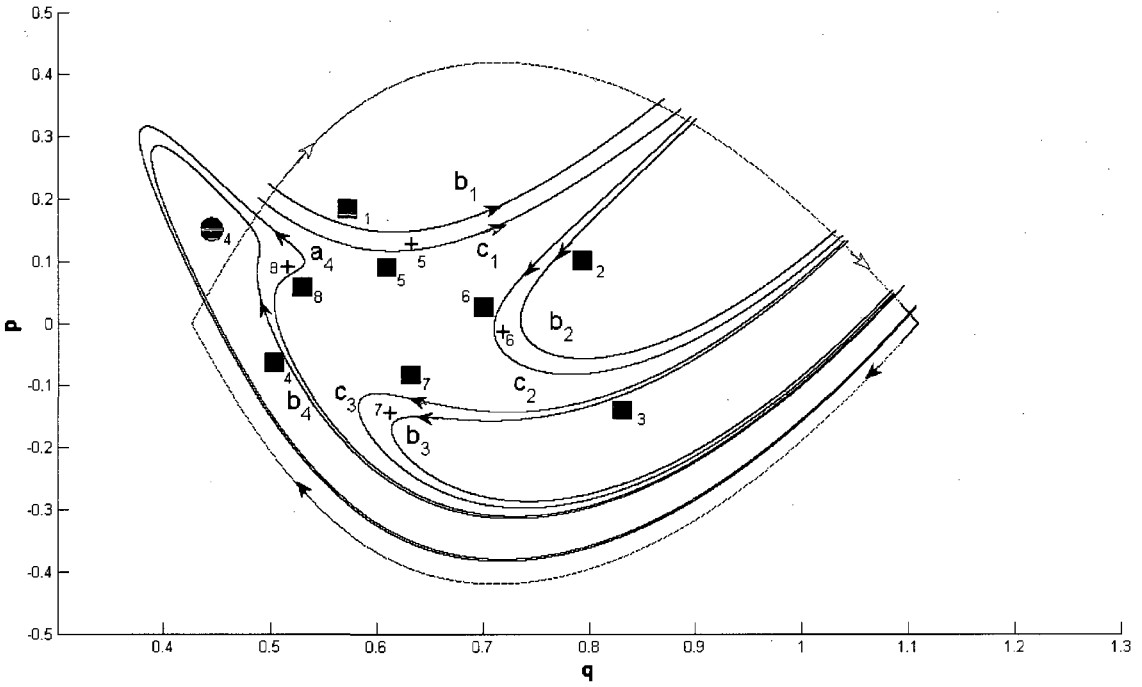

Figure 3.7: Representatives of the "b" and "c" classes.

Nontrivial dynamical equations result when we iterate the representatives of c_3 and b_3. Both representatives can be thought of as lobes that enclose the holes square-3 and disk-3 (not shown). Therefore, their images must enclose the holes square-4 and disk-4. We consider the blue curve in Figure 3.7 first, which is the image of b_3's representative. Following the natural orientation of the curve, we see that the first bridge encloses plus-8, representing the bridge class b_4^{-1}. Since b_3's representative directly encloses disk-3, its mapping produces an escape segment representing u_0^{-1}. Finally, we find the last bridge represents d_4 thus completing the dynamical equation for b_3 (eq. (3.4g)).

$$\mathcal{M}(b_3) = b_4^{-1} u_0^{-1} d_4 \tag{3.8}$$

Now consider the black curve representing c_3, which surrounds b_3's representative. Thus, this curve encloses the same holes as b_3 in addition to plus-7. Mapping the representative forward gives a lobe enclosing plus-8 in addition to disk-4 and square-4. Enclosing plus-8 forces the nose in Figure 3.7. Again, we follow the natural orientation of the black curve to determine the bridge classes. The first bridge, the bridge containing the nose, encloses square-8 and therefore represents the class a_4^{-1}. Again, the lobe intersects the escape zone giving an escape segment u_0^{-1}. The third and final bridge directly encloses square-4 and is thus assigned to the class d_4 completing the dynamical equation for c_3 (eq. (3.4k)).

$$\mathcal{M}(c_3) = a_4^{-1}u_0^{-1}d_4 \tag{3.9}$$

The dynamical equations obtained thus far were found from expanding the first eight capture lobes in the 12-basis. To obtain the remaining dynamical equations, we can decompose $\mathcal{C}_9$, $\mathcal{C}_{10}$, $\mathcal{C}_{11}$, and $\mathcal{C}_{12}$ into bridges and assign each to a well-defined bridge class. Arriving at this goal is hastened by making an observation. $\mathcal{C}_9$, $\mathcal{C}_{10}$, and $\mathcal{C}_{11}$ each possess two bridges that are forced to wind around the lobes C_1, C_2, and C_3 respectively. Furthermore, each of the lobes C_9, C_{10}, and C_{11} will contain a "plus" hole and wind under a "square" hole. These observations indicate that the three aforementioned capture lobes each contain within their boundaries two segments representing new distinct basis elements. We denote these basis elements by d_i and f_i for i = 1, 2, and 3.

Figure 3.8 shows the d series of basis elements. The classes d_1, d_2, and d_3 each are represented by a bridge contained in $\mathcal{C}_9$, $\mathcal{C}_{10}$, and $\mathcal{C}_{11}$, respectively. We can immediately derive two dynamical equations.

$$\text{a.)}\mathcal{M}(d_1) = d_2$$
$$\text{b.)}\mathcal{M}(d_2) = d_3 \tag{3.10}$$

Mapping the representative of d_3 produces a curve that is decomposed into three bridges. Again, we follow the natural orientation of the curve to determine its expansion in the bridge basis. The first bridge does not represent an element in the bridge basis. However, if we define $g = x_0 g_1 x_1 g_2 x_2 g_3 x_3$ and compare the figure to the schematic in Figure 3.4, we can see that the first bridge indeed represents g^{-1}. The second bridge encloses disk-4 giving a factor of u_0^{-1}. Finally, the last bridge is simply d_4 giving the dynamical equation

$$\mathcal{M}(d_3) = g^{-1}u_0^{-1}d_4 \tag{3.11}$$

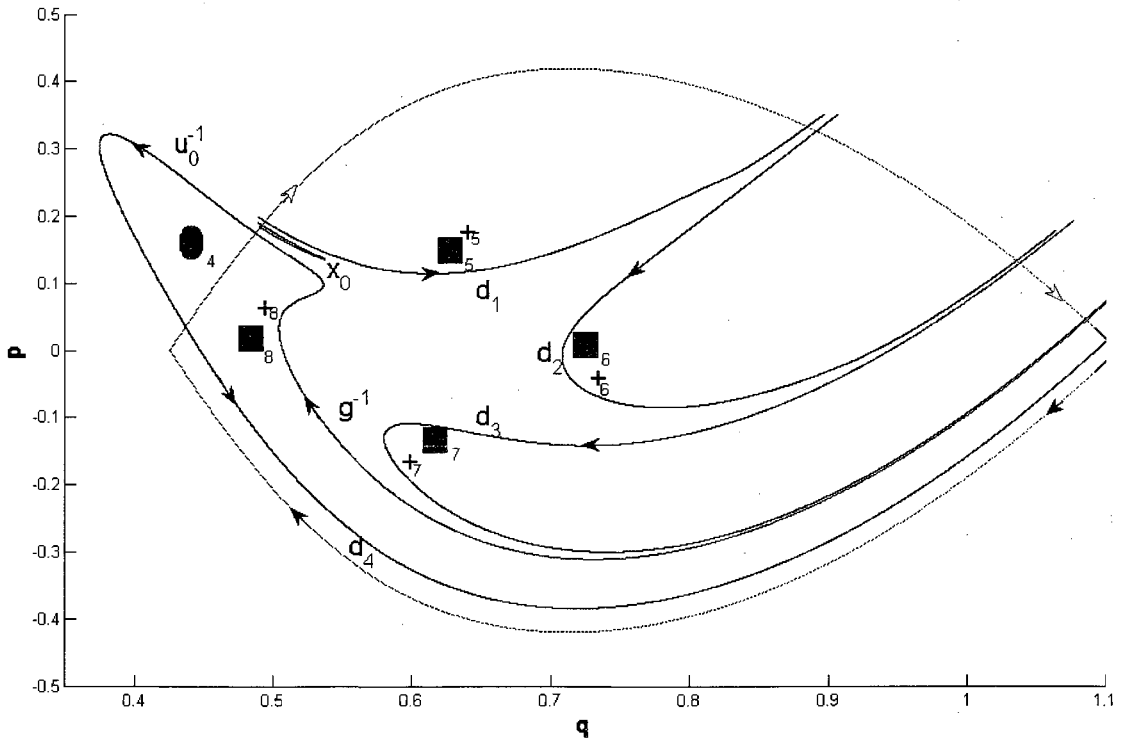

Figure 3.8: The "d" basis elements.

The same argument is applied to the "f" basis elements shown in Figure 3.9. Since a representative of f_1 bounds C_9, the lobe encloses plus-9. Applying the mapping once and then twice to the representative of f_1 produces two dynamical equations.

$$\begin{aligned} &\text{a.)}\mathcal{M}([\mathcal{C}_9]_{12}) = [\mathcal{C}_{10}]_{12} \Leftrightarrow \mathcal{M}(f_1) = f_2 \\ &\text{b.)}\mathcal{M}([\mathcal{C}_{10}]_{12}) = [\mathcal{C}_{11}]_{12} \Leftrightarrow \mathcal{M}(f_2) = f_3 \end{aligned} \tag{3.12}$$

Mapping a representative of f_3 forward produces an intersection with E_0. Figure 3.9 shows that the representative's image contains an additional finger. The first bridge does not directly enclose any holes meaning it does not represent an element in the bridge basis. However, if we deform the bridge into the nearest bridge basis elements, we can assign the bridge to the bridge class g^{-1}. The last bridge is again d_4. To determine the remaining classes, we use Figure 3.10 which shows a close-up of the escape zone E_0. We see that mapping f_3 forward produces two escape classes, v_0 and w_0^{-1}. Using the two figures we can obtain the dynamical equation of f_3.

$$\mathcal{M}(f_3) = g^{-1}v_0x_0w_0^{-1}d_4 \tag{3.13}$$

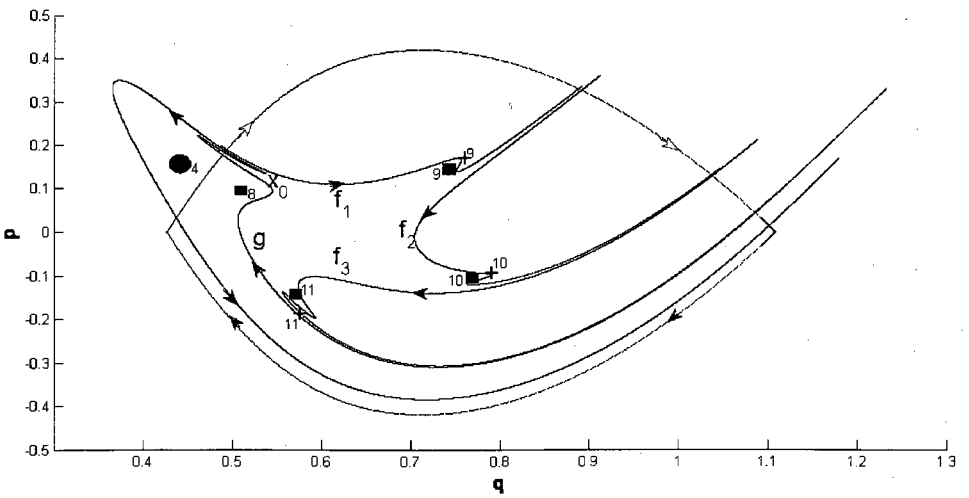

Figure 3.9: Unstable representatives of the "f" elements.

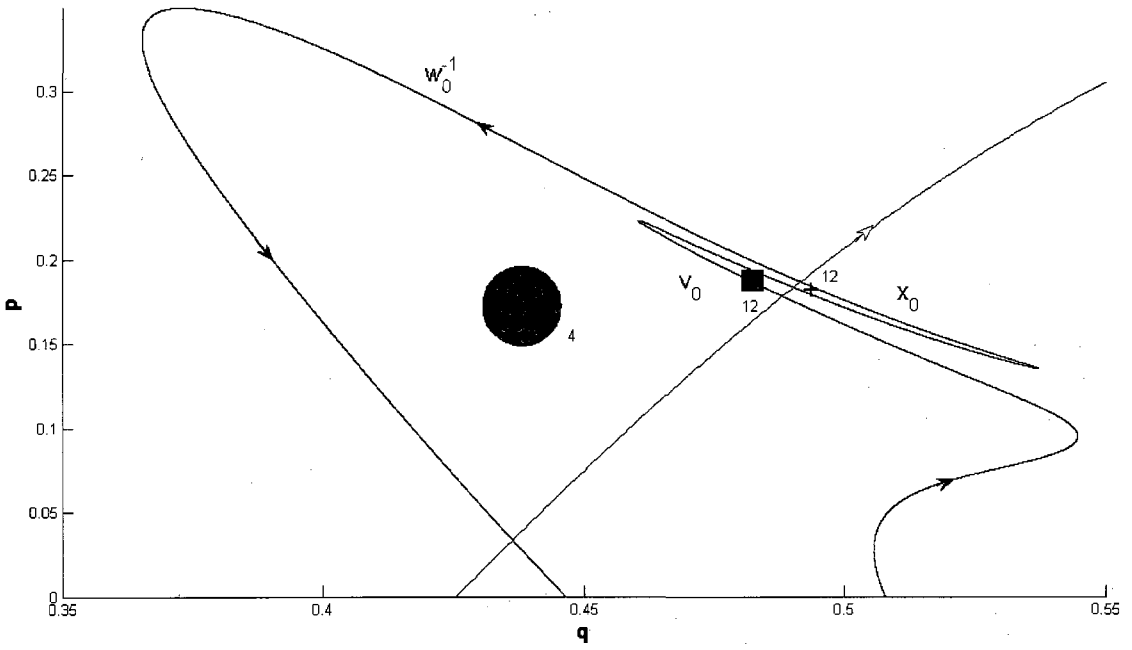

Figure 3.10: Close up of escape zone in Figure 3.9.

Now we consider the dynamical map acting on the basis elements g_1, g_2, and g_3 which enclose squares-9, 10, and 11, respectively. Figure 3.9 shows that segments of $\mathcal{C}_9$, $\mathcal{C}_{10}$, and $\mathcal{C}_{11}$ enclose pluses-9, 10, and 11. The *known* segment of $\mathcal{U}$ does not possess any bridges that naturally enclose squares-9, 10, and 11. However, we found a bridge, representing the class g^{-1}, that can be homotoped into a curve directly enclosing squares-9, 10, and 11 simultaneously. Furthermore, we expect the unknown segment of $\mathcal{U}$ to directly enclose one of these holes. Therefore, g_1, g_2, and g_3 are phantom bridge classes. Given that $\mathcal{M}$(square-9) = square-10 and $\mathcal{M}$(square-10) = square-11, we can derive two dynamical equations.

$$\begin{aligned} &\text{a.)}\mathcal{M}(g_1) = g_2 \\ &\text{b.)}\mathcal{M}(g_2) = g_3 \end{aligned} \tag{3.14}$$

To obtain the action of the map on g_3, we use one fact: all bridge classes, and hence the corresponding holes, with the subscript "3" are nested within g_3. The image of g_3 must enclose the images of the holes enclosed by g_3. Furthermore, g_3 looks comparable to f_3 so $\mathcal{M}(g_3)$ should be comparable to $\mathcal{M}(f_3)$. Therefore, $\mathcal{M}(g_3)$ should begin with g^{-1} and end with d_4. If we consider $\mathcal{M}(g_3)$ as a lobe, the lobe must contain disk-4, square-12, and plus-12. The lobe $\mathcal{M}(f_3)$ only contained disk-4 and plus-12 implying that $\mathcal{M}(g_3)$ does *not* contain a factor of v_0. Finally, the tip of $\mathcal{M}(g_3)$ must wind around square-12 and disk-4 implying that $\mathcal{M}(g_3)$ contains a factor of w_0^{-1}.

$$\mathcal{M}(g_3) = g^{-1}x_0w_0^{-1}d_4 \tag{3.15}$$

We complete the derivation by computing the dynamical equation for a_4. Figure 3.11 shows a_4 and its image. Following the orientation of $\mathcal{M}(a_4)$, we see the first class is simply f_1^{-1}. The second bridge winds around disk-4 and square-16. Finally, the last bridge is simply d_4. The dynamical equation for a_4 is

$$\mathcal{M}(a_4) = f_1^{-1}w_0^{-1}d_4 \tag{3.16}$$

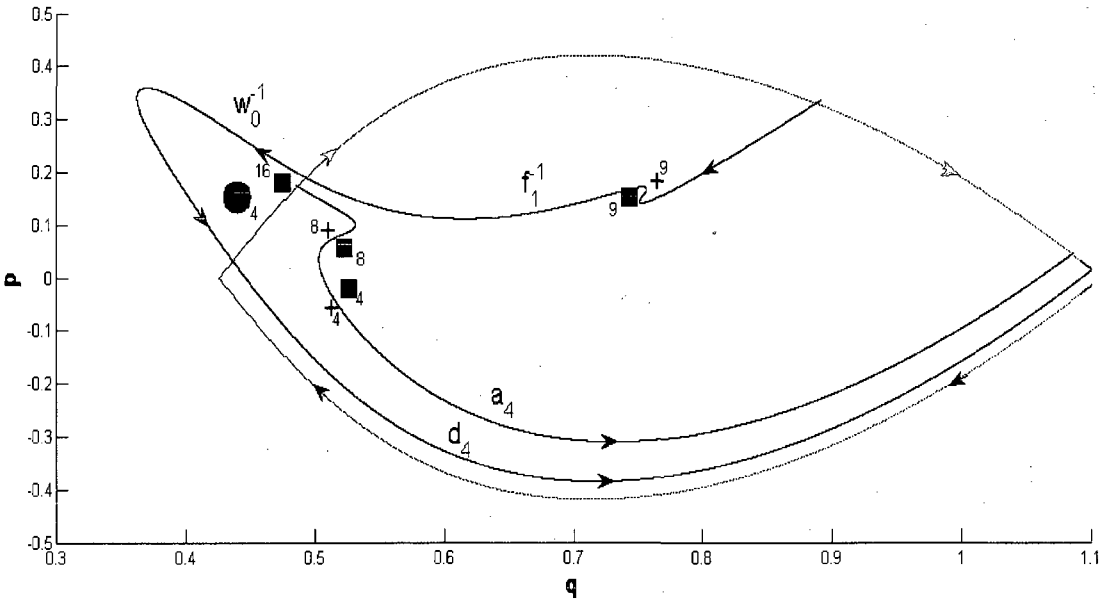

Figure 3.11: The basis class a_4 and the bridge class $\mathcal{M}(a_4)$.

b.) Predictions of the 12-basis.

We can use the dynamical equations to compute the 1st eight iterates of $[\mathcal{U}_0^F]_{12}$ for comparison to the 4-basis. Again, we remind the reader that $[\mathcal{U}_1^F]_{12} = u_{i-1}[\mathcal{C}_1]_{12}$.

$$
\begin{aligned}
&\text{a.)}[\mathcal{U}_1^F]_{12} = \mathbb{w}_0 a_1 \\
&\text{b.)}[\mathcal{U}_2^F]_{12} = u_1 a_2 \\
&\text{c.)}[\mathcal{U}_3^F]_{12} = u_2 a_3 \\
&\text{d.)}[\mathcal{U}_4^F]_{12} = u_3 c_4^{-1} \mathbb{w}_0^{-1} d_4 \\
&\text{e.)}[\mathcal{U}_5^F]_{12} = u_4 x_4^{-1} d_4^{-1} \mathbb{w}_0 c_1 u_1^{-1} b_1^{-1} \mathbb{w}_0^{-1} d_4 x_4 \\
&\text{f.)}[\mathcal{U}_6^F]_{12} = u_5 x_5^{-1} x_4^{-1} d_4^{-1} \mathbb{w}_0 b_1 w_1 c_2 u_2^{-1} b_2^{-1} w_1^{-1} b_1^{-1} \mathbb{w}_0^{-1} d_4 x_4 x_5 \\
&\text{g.)}[\mathcal{U}_7^F]_{12} = u_6 x_6^{-1} x_5^{-1} x_4^{-1} d_4^{-1} \mathbb{w}_0 b_1 w_1 b_2 w_2 c_3 u_3^{-1} b_3^{-1} w_2^{-1} b_2^{-1} w_1^{-1} \\
&\qquad\qquad b_1^{-1} \mathbb{w}_0^{-1} d_4 x_4 x_5 x_6 \\
&\text{h.)}[\mathcal{U}_8^F]_{12} = u_7 x_7^{-1} x_6^{-1} x_5^{-1} x_4^{-1} d_4^{-1} \mathbb{w}_0 b_1 w_1 b_2 w_2 b_3 w_3 a_4^{-1} \mathbb{w}_0^{-1} d_4 u_4^{-1} \\
&\qquad\qquad d_4^{-1} \mathbb{w}_0 b_4 w_3^{-1} b_3^{-1} w_2^{-1} b_2^{-1} w_1^{-1} b_1^{-1} \mathbb{w}_0^{-1} d_4 x_4 x_5 x_6 x_7
\end{aligned}
\tag{3.17}
$$

The new escape segments appearing at each iterate of $\{[\mathcal{U}_1^F]_{12}\}_{i=1}^{12}$ are in boldface. Eq. (3.17) the new basis predicts epistrophes starting at the 4th and 5th iterates with opposing orientation. However, we see there are two different classes representing escape segments. The segment at four iterates is given by u_0^{-1} which winds around only disk-4 while the segment at five iterates is given by w_0 and winds around both disk-4 and square-4. Furthermore, $[\mathcal{U}_5^F]_{12}$, $[\mathcal{U}_6^F]_{12}$, and $[\mathcal{U}_7^F]_{12}$ also possess segments that wind around both of these holes. In $[\mathcal{U}_8^F]_{12}$, the 2nd and next to last escape segments represent such curves but the inner symbols are u_0, indicating that the segments wind only around disk-4. The appearance of different escape segment classes indicates a more complex behavior in how images of $\mathcal{U}_F^0$ wind through Γ.

Computing $[\mathcal{U}_9^F]_{12}$, $[\mathcal{U}_{10}^F]_{12}$, and $[\mathcal{U}_{11}^F]_{12}$ one finds the same number of escape segments as in $[\mathcal{U}_9^F]_4$, $[\mathcal{U}_{10}^F]_4$, and $[\mathcal{U}_{11}^F]_4$. However, there is a difference between the aforementioned classes. $[\mathcal{U}_9^F]_4$, $[\mathcal{U}_{10}^F]_4$, and $[\mathcal{U}_{11}^F]_4$ are considered output of the theory while $[\mathcal{U}_9^F]_{12}$, $[\mathcal{U}_{10}^F]_{12}$, and $[\mathcal{U}_{11}^F]_{12}$ are input. Comparing $[\mathcal{U}_{12}^F]_4$ to $[\mathcal{U}_{12}^F]_{12}$ we find that the class represented by the finger, v_0, appears for the first time in $[\mathcal{U}_{12}^F]_{12}$.

$$\left[\mathcal{U}_{12}^F\right]_{12} = u_{11}x_{11}^{-1}\ldots g^{-1}\mathbb{v}_0 x_0 \mathbb{w}_0^{-1} d_4 \ldots x_{11} \tag{3.18}$$

The Epistrophe Start Rule tells us that the symbol v_4 in $[\mathcal{C}_{16}]_{12}$ might contain epistrophes on either side of v_4 pointing towards v_4. However, when we examine $[\mathcal{C}_{16}]_{12}$, we find that this is not the case. The symbols immediately surrounding w_4 are

$$\left[\mathcal{U}_{16}^F\right]_{12} = u_{15}x_{15}^{-1}\ldots g^{-1}x_0 w_0^{-1} d_4 v_4 x_4 w_4^{-1} d_4^{-1} u_0 \ldots x_{15} \tag{3.19}$$

Figure 3.12 below schematically represents the escape segments in the subsequence shown in eq. (3.19). Contrary to our expectations, no escape segments are predicted to lie between v_4 and w_4^{-1}. This lack of epistrophe birthing is not confined to the finger. The number of escape segments appearing in $[\mathcal{U}_1^F]_{12}$ for i =13, 14, ..., 20 matches the numbers predicted by the 4-basis. The escape segment counts for all 3 bases up to iterate 20 are shown in Table 3.1 at the end of section vii.

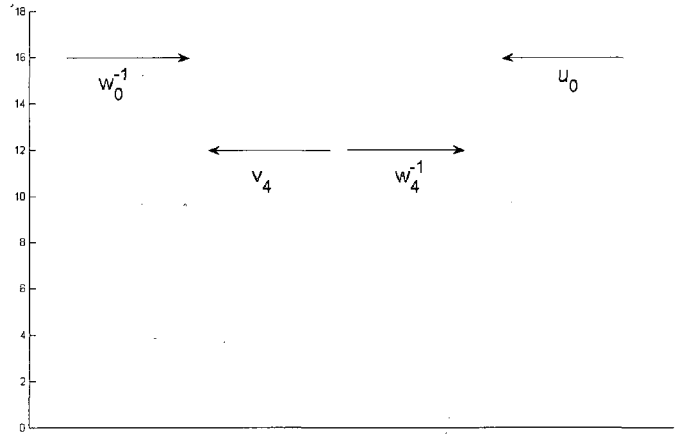

Figure 3.12: Minimal set generated by subsequence in eq. (3.19).

iv.) The 16-basis

a.) Derivation of the 16-basis

Finally, we examine the 16-basis which is generated by the 16-neighbors (α_4, β_4), (θ_{16}, ι_{16}), (ξ_{16}, η_{16}) shown in Figure 3.13. The left side of Figure 3.13 shows C_{16} winding through E_0. Since the curves are pushed closely together, we present a schematic of C_{16} with the holes and 16-neighbors labeled. Again, (α_4, β_4) are present with a "disk" hole attached to β_4. In addition, two new 16-neighbor pairs have been found: (θ_{16}, ι_{16}) producing a long narrow tendril and (ξ_{16}, η_{16}) producing a finger to the

right of the circle hole. We let $t_0 \triangleleft$ "plus" hole, $u_0 \triangleleft$ "circle" hole, $v_0 \triangleleft$ "square" hole. Mapping the holes forwards generates three sequences of inert classes representing escape segments: $t_n = \mathcal{M}^n(t_0)$, $u_n = \mathcal{M}^n(u_0)$, and $v_n = \mathcal{M}^n(v_0)$. Mapping the 16-neighbors backwards generates the holes internal to the complex. Computing the first three pre-images of β_4 will give three internal holes. All other pre-images will lie outside the complex and are ignored. Computing the first 15 pre-images of ξ_{16} and ι_{16} generate 30 internal holes. All other pre-images lie outside the complex and are also ignored.

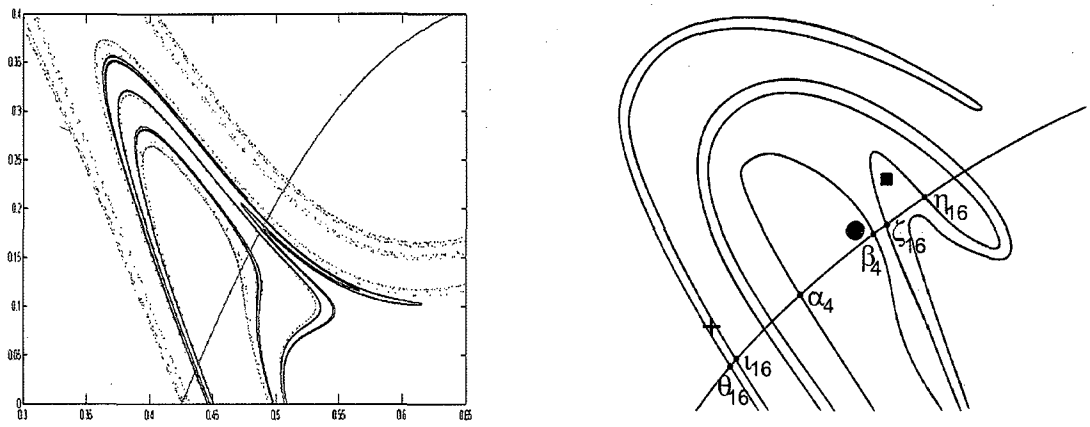

Figure 3.13: 16-neighbors found from computing $\{\mathcal{U}_\Gamma^i\}_{i=1}^{16}$.

To discuss the 16-basis, first we present a schematic of the basis in Figure 3.14. In Figure 3.14, the thick red line represents Γ_S. To denote a hole, we will again use a noun describing the hole's shape followed by a hyphen and an integer giving its place in the sequence generated by the 16-neighbors. An example is given in eq. (3.20). Each bridge's symbol is given under the representative curves. Now we explain how to construct the dynamical equations that act on the basis.

$d_1 \triangleleft$ square-12
$c_1 \triangleleft$ square-9, plus-9
$b_1 \triangleleft$ square-5, plus-5
$a_1 \triangleleft$ disk-1, square-1, plus-1 (3.20)

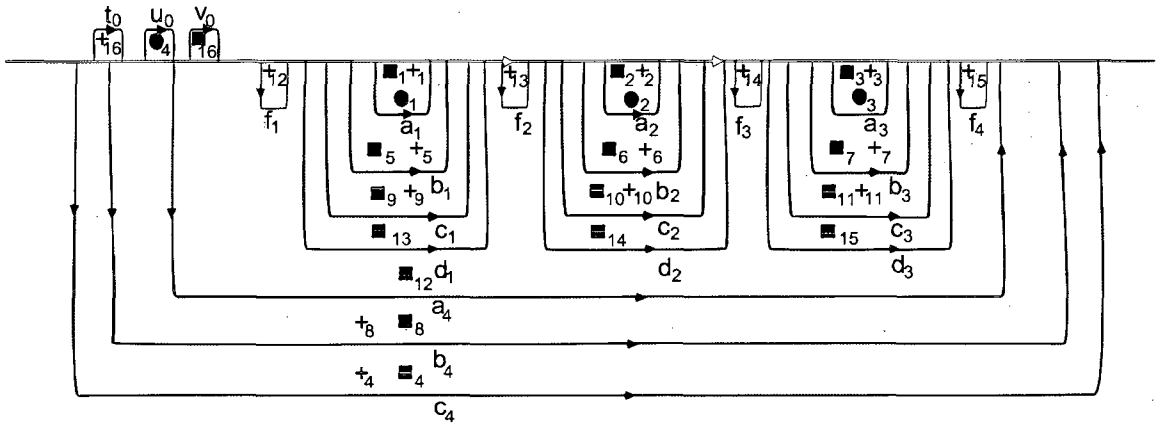

Figure 3.14: Schematic of 16-basis.

The dynamical equations acting on the 16-basis are given below.

a.) $\mathcal{M}(a_1) = a_2$ f.) $\mathcal{M}(a_2) = a_3$ k.) $\mathcal{M}(a_3) = b_4^{-1}u_0^{-1}c_4$
b.) $\mathcal{M}(b_1) = b_2$ g.) $\mathcal{M}(b_2) = b_3$ l.) $\mathcal{M}(b_3) = a_4^{-1}u_0^{-1}c_4$
c.) $\mathcal{M}(c_1) = c_2$ h.) $\mathcal{M}(c_2) = c_3$ m.) $\mathcal{M}(c_3) = f_4^{-1}d_3^{-1}f_3^{-1}d_2^{-1}f_2^{-1}d_1^{-1}f_1^{-1}v_0f_1x_0^{-1}c_4$
d.) $\mathcal{M}(d_1) = d_2$ i.) $\mathcal{M}(d_2) = d_3$ n.) $\mathcal{M}(d_3) = f_4^{-1}d_3^{-1}f_3^{-1}d_2^{-1}f_2^{-1}d_1^{-1}x_0^{-1}c_4$
e.) $\mathcal{M}(f_1) = f_2$ j.) $\mathcal{M}(f_2) = f_3$ o.) $\mathcal{M}(f_3) = f_4$

p.) $\mathcal{M}(a_4) = c_1^{-1}w_0^{-1}c_4$
q.) $\mathcal{M}(b_4) = b_1^{-1}w_0^{-1}c_4$ (3.21)
r.) $\mathcal{M}(c_4) = a_1^{-1}w_0^{-1}c_4$
s.) $\mathcal{M}(f_4) = c_4^{-1}t_0^{-1}c_4$

$\mathcal{M}^n(t_0) = t^n$ let $x_0 = u_0v_0$ $\mathcal{M}^n(x_0) = x^n$
$\mathcal{M}^n(u_0) = u^n$ $y_0 = t_0u_0$ $\mathcal{M}^n(y_0) = y^n$
$\mathcal{M}^n(v_0) = v^n$ $w_0 = t_0u_0v_0$ $\mathcal{M}^n(w_0) = w^n$

We begin the discussion with the 1st three internal capture lobes.

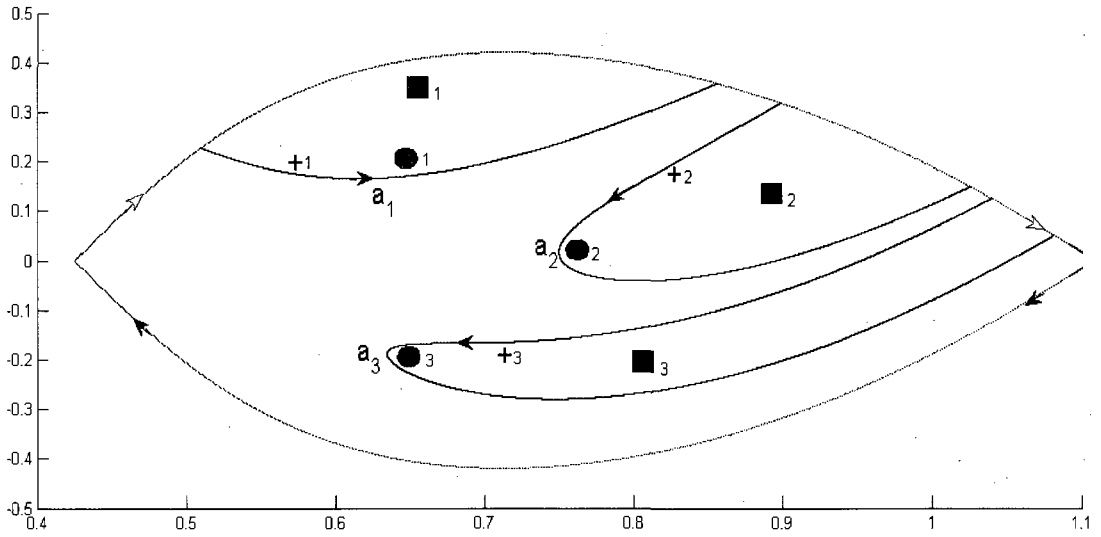

Figure 3.15: $\mathcal{C}_1$, $\mathcal{C}_2$, and $\mathcal{C}_3$ and the holes each encloses.

The lobes' unstable boundaries each enclose three holes. Therefore, each boundary represents a unique bridge class in the 16-basis. Each class is denoted by "a" and subscripted with an integer indicating the lobe.

$$\begin{aligned} &\text{a.)}\ [\mathcal{C}_1]_{16} = a_1 \\ &\text{b.)}\ [\mathcal{C}_2]_{16} = a_2 \\ &\text{c.)}\ [\mathcal{C}_3]_{16} = a_3 \end{aligned} \tag{3.22}$$

Using the facts $\mathcal{M}(C_1) = C_2$ and $\mathcal{M}(C_2) = C_3$ result in eq. (3.21a) and eq. (3.21f).

The next capture lobe, C_4, will be a sequence of three bridges as it intersects Γ_S four times. Mapping C_3 to C_4 induces a mapping on the basis.

$$\mathcal{M}(C_3) = C_4 \Rightarrow \mathcal{M}([\mathcal{C}_3]_{16}) = [\mathcal{C}_4]_{16} \tag{3.23}$$

Figure 3.16 shows C_4 in blue, the holes lying in C_4, and square-8 and plus-8. Following the natural orientation, the 1st bridge encloses square-8 and plus-8 and represents the bridge b_4^{-1}. This bridge class will in fact be represented by a bridge contained in $\mathcal{C}_8$. The second bridge winds through E_0 around disk-4 representing the escape segment

class u_0^{-1}. Finally, the last bridge encloses square-4 and plus-4 as well as b_4. We call the class represented by this bridge c_4. Using eq. (3.23), we can compute the dynamical eq. (3.21f).

$$[\mathcal{C}_4]_{16} = b_4^{-1}u_0^{-1}c_4 = \mathcal{M}(a_3) \tag{3.24}$$

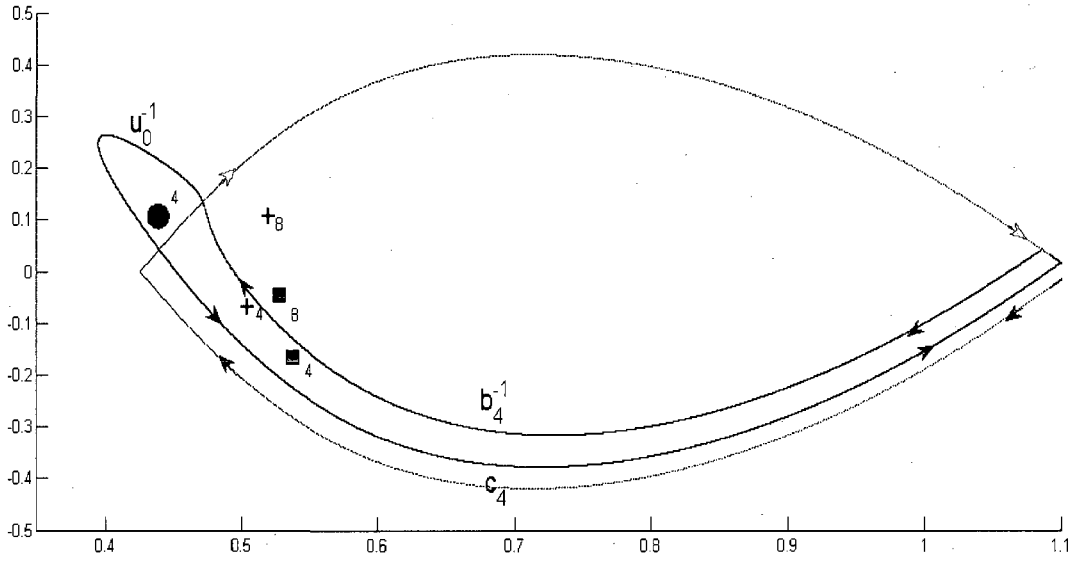

Figure 3.16: $\mathcal{C}_4$'s expansion in the 16-basis.

To find the dynamical equations for b_4 and c_4, we must expand $\mathcal{C}_5$ in the 16-basis. Mapping the previous equation forward gives a factor of u_1^{-1} Figure 3.17 shows $\mathcal{C}_5$ in blue and $\mathcal{C}_1$ in green. Since the tip of C_4 intersects E_0, the tip of C_5 must intersect E_1. And since the manifold cannot self-intersect, C_5 will wind under C_4, indicating that $\mathcal{C}_5$ (in fact, all images of C_4) starts with c_4^{-1} and ends with c_4. The second and next-to-last bridges wind around the three holes lying in E_0 thus giving factors of w_0 and w_0^{-1}. Finally, we see two bridges winding around C_1. We see one bridge homotopes into the class a_1^{-1}. The other bridge surrounding C_1 encloses square-5 and plus-5 and represents

the class b_1. We can now write out $[\mathcal{C}_5]_{16}$ and equate it with $\mathcal{M}([\mathcal{C}_4]_{16})$ to obtain eq. (3.21q) and eq. (3.21r).

$$\mathcal{M}([\mathcal{C}_4]_{16}) = \mathcal{M}(b_4^{-1})u_1^{-1}\mathcal{M}(c_4) = [\mathcal{C}_5]_{16} = c_4^{-1}w_0b_1u_1^{-1}a_1^{-1}w_0^{-1}c_4 \tag{3.25}$$

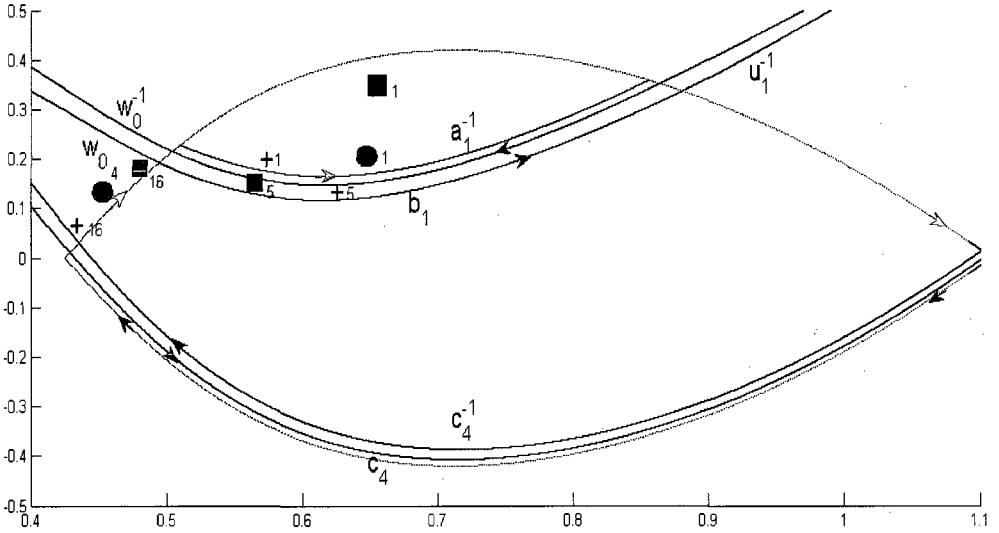

Figure 3.17: $\mathcal{C}_5$ expanded in the 16-basis.

Let us compute the image of the previous equation.

$$\mathcal{M}([\mathcal{C}_5]_{16}) = c_4^{-1}w_0a_1w_1\mathcal{M}(b_1)u_2^{-1}a_2^{-1}w_1^{-1}a_1^{-1}w_0^{-1}c_4 \tag{3.26}$$

We need only compute the image of the class b_1. Figure 3.18 shows C_6 and the holes contained therein along with C_1, C_2, and C_3 and their respective holes. The class b_1 is represented by curves that enclose square-5 and plus-5. We see that $\mathcal{C}_6$ possesses a bridge that encloses the images of square-5 and plus-5 indicating that b_1's image is simply b_2.

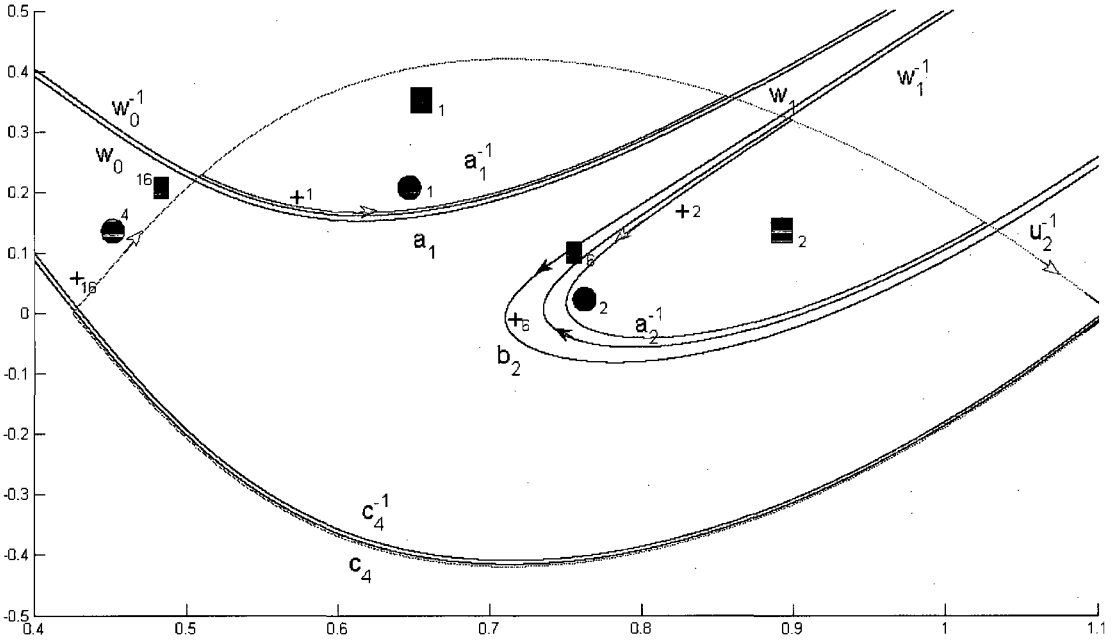

Figure 3.18: $\mathcal{C}_6$ expanded in the 16-basis.

Substituting b_2 for b_1 in eq. (3.26), we see that all the images of the symbols present are known except for that of b_2. To compute b_2's image, we examine a figure of C_7. Figure 3.19 shows that $\mathcal{C}_7$ possesses a bridge that encloses the holes square-7 and plus-7 representing a class designated as b_3. Since the holes square-7 and plus-7 are the images of square-6 and plus-6, b_3 is the image of b_2. We can now expand the unstable boundary of C_7 in the 16-basis.

$$[\mathcal{C}_7]_{16} = c_4^{-1}w_0a_1w_1a_2w_2b_3u_3^{-1}a_3^{-1}w_2^{-1}a_2^{-1}w_1^{-1}a_1^{-1}w_0^{-1}c_4 \tag{3.27}$$

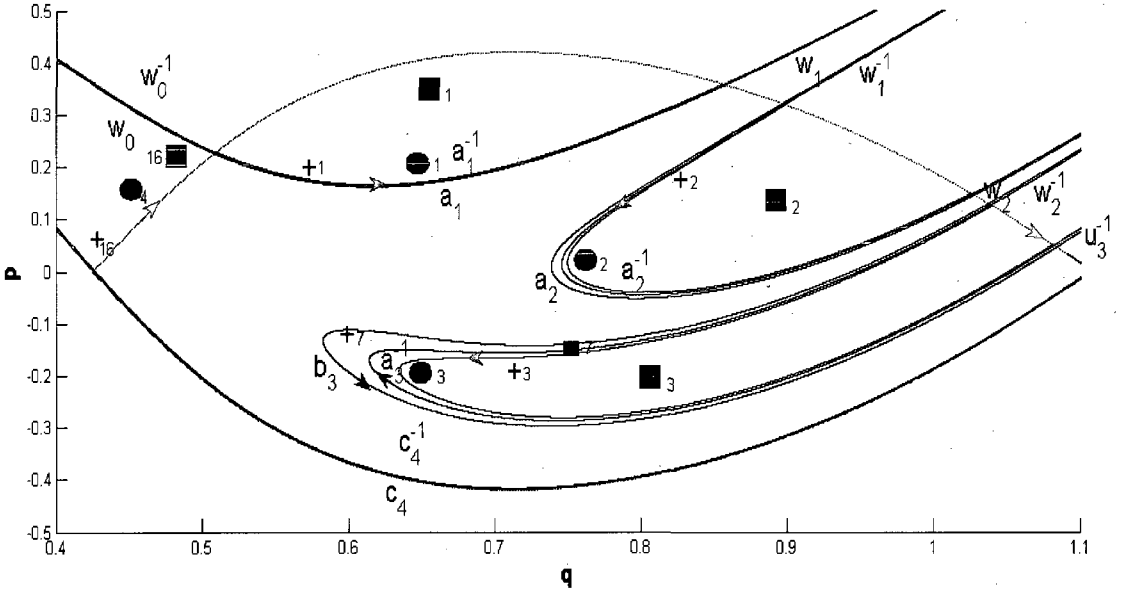

Figure 3.19: $\mathcal{C}_7$ expanded in the 16-basis.

We compute the image of the last equation and find that we must obtain the dynamical equation for b_3.

$$\mathcal{M}([\mathcal{C}_7]_{16}) = c_4^{-1}w_0a_1w_1a_2w_2a_3w_3\mathcal{M}(b_3)u_4^{-1}c_4^{-1}u_0b_4w_3^{-1}a_3^{-1}w_2^{-1}a_2^{-1}w_1^{-1}a_1^{-1}w_0^{-1}c_4 \quad (3.28)$$

From the previous figures, it is obvious the unstable boundaries of the capture lobes are becoming long and squeezed tightly together. Instead of plotting the entire boundary and graphically obtaining the bridge class it represents, we choose to examine individual bridges. We will consider a bridge representing a class whose dynamical equation has not been discussed. We then graph the bridge's image to graphically obtain the corresponding bridge class and desired dynamical equation.

We use Figure 3.20 to determine the desired bridge class. The black curve is a bridge contained in $\mathcal{C}_7$ representing the class b_3 and the blue curve is its image. The

figure shows that the blue curve is decomposed into three bridges (in parenthesis below) thus giving the dynamical equation for b_3.

$$[\mathcal{C}_8]_{16} = \mathcal{M}([\mathcal{C}_7]_{16}) = c_4^{-1}w_0a_1w_1a_2w_2a_3w_3(a_4^{-1}u_0^{-1}c_4)u_4^{-1}c_4^{-1}u_0b_4w_3^{-1}a_3^{-1}w_2^{-1}a_2^{-1}w_1^{-1}a_1^{-1}w_0^{-1}c_4$$
$$\mathcal{M}(b_3) = a_4^{-1}u_0^{-1}c_4 \tag{3.29}$$

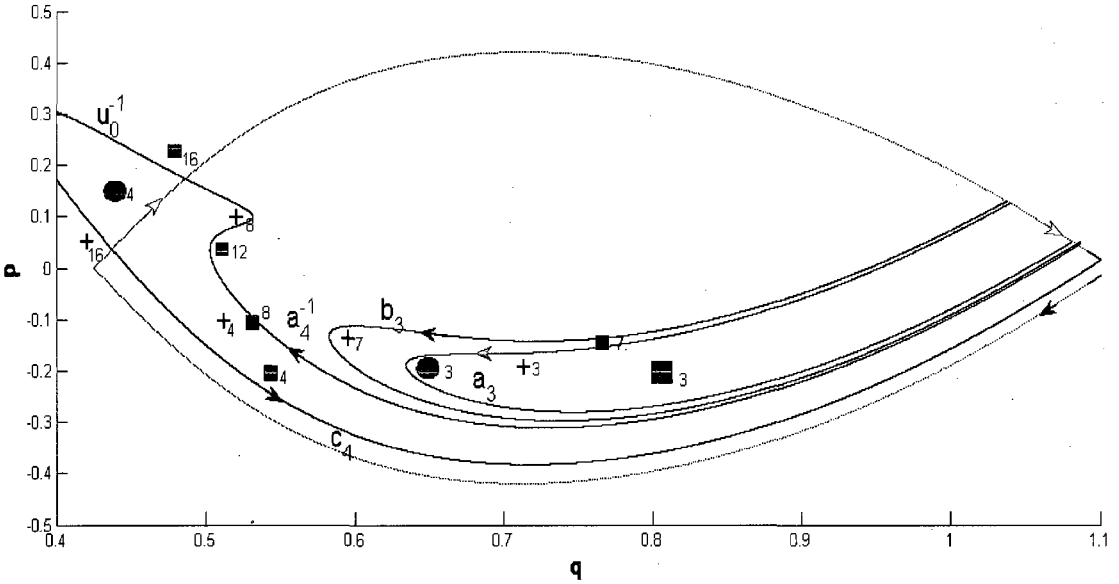

Figure 3.20: Image of the class b_3.

We make an observation to expedite the explanation of the dynamical equations. The bridge-classes a_1 and b_1 map to a_2 and b_2, which in turn map to a_3 and b_3. Furthermore, each of the aforementioned classes is represented by curves that wind around an internal capture lobe with the same subscript. Therefore, the same will apply to the bridge-classes c_1, c_2, c_3, d_1, d_2, d_3, f_1, f_2, and f_3. Figure 3.21a shows the bridges representing the classes c_1, c_2, and c_3. For comparison to Figure 3.14, we have included the bridges representing a_1, a_2, and a_3 nested within the corresponding "c" classes. Since c_1 encloses square-9 and plus-9, we call the classes enclosing square-10 and plus-10 $c_2 = \mathcal{M}(c_1)$ and square-11 and plus-11 $c_3 = \mathcal{M}(c_2)$.

Now consider the "d" and "f" classes. Figure (3.21b) shows d_1, d_2, and d_3. The same argument applied to the "c" classes in the previous paragraph gives $d_2 = \mathcal{M}(d_1)$ and $d_3 = \mathcal{M}(d_2)$. However, Figure 3.21b shows a difference: Each of the "d" classes encircles only square holes. The plus holes, plus-12, 13, 14, and 15 are now enclosed by the "f" classes shown in Figure 3.21c. While these bridges appear to be single curves they are in fact tightly folded bridges. We have surrounded f_1 by a rectangle and provided a close-up of the bridge to the right to verify its nature as a bridge. The remaining three bridges are iterates of the bridge representing f_1. The mapping acting on the groupoid then induces the three dynamical equations $f_2 = \mathcal{M}(f_1)$, $f_3 = \mathcal{M}(f_2)$, $f_4 = \mathcal{M}(f_3)$, or eq. (3.21e), eq. (3.21j), and eq. (3.21o).

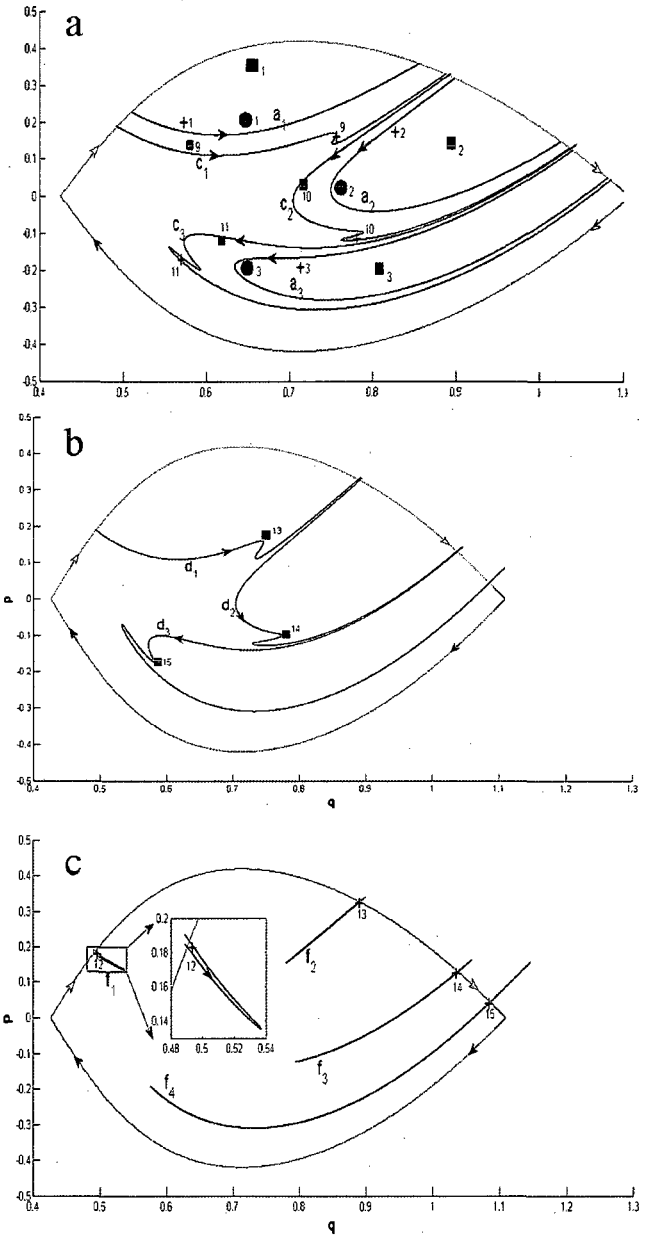

Figure 3.21: The "c", "d", and "f" sequence of bridge basis elements.

Now, we consider the dynamical equation of c_3. Figure 3.22 shows the image of the bridge representing c_3 shown in Figure 3.21a in green. The curve possesses a counterclockwise orientation. The blue curves are the "d" classes and the black curves are the "f" classes. Following the natural orientation, the 1st bridge stretches across the

breadth of the complex. There are no holes between the bridge of interest and the bridges it encloses. Therefore can be written as a product of the bridges it encloses. Inspection of Figure 3.22 reveals this product to be $f_4^{-1}d_3^{-1}f_3^{-1}d_2^{-1}f_2^{-1}d_1^{-1}f_1^{-1}$. The last bridge winds under C_4 giving a factor of c_4.

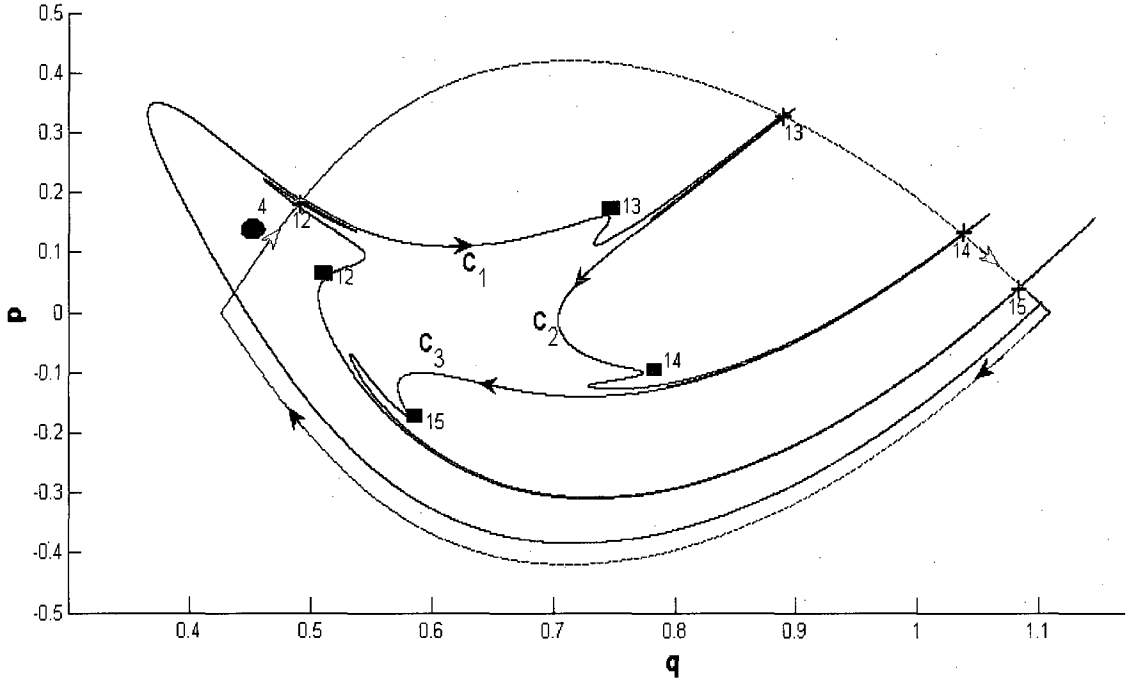

Figure 3.22: Image of c_3.

To determine the bridge classes near the escape zone, we will examine a close-up of the escape zone presented in Figure 3.23. The figure shows an escape class containing disk-4 and square-16, denoted by x_0^{-1}. Furthermore, we see an additional bridge enclosing only square-12 and a bridge enclosing plus-12 yielding a factor of f_1. From these observations, we can write out the desired dynamical equation.

$$\mathcal{M}(c_3) = f_4^{-1}d_3^{-1}f_3^{-1}d_2^{-1}f_2^{-1}d_1^{-1}f_1^{-1}v_0f_1x_0^{-1}c_4 \qquad (3.30)$$

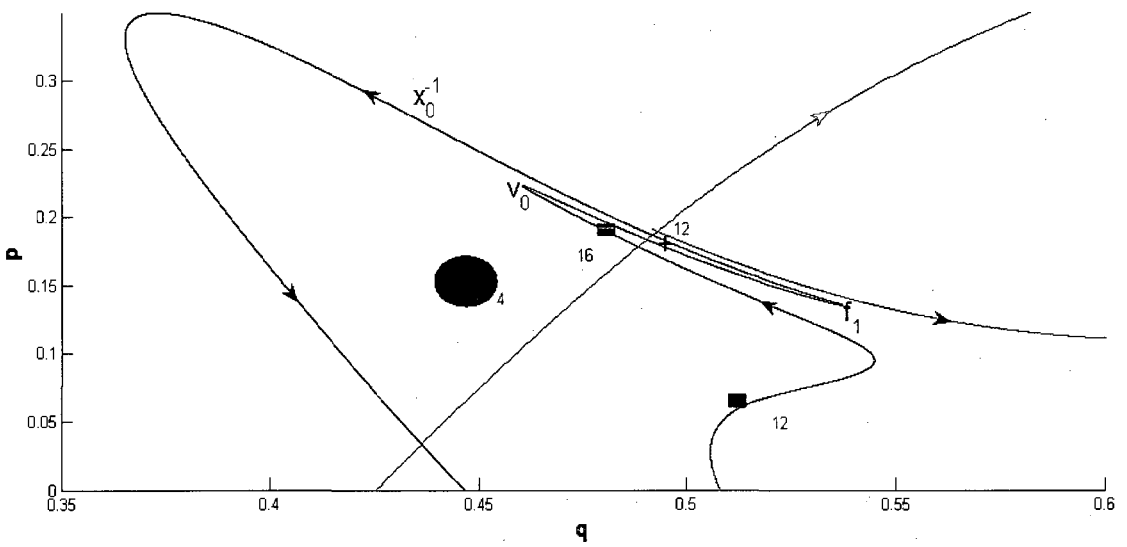

Figure 3.23: Close-up of escape zone along with a representative of $\mathcal{M}(c_3)$.

We move on to the dynamical equation of d_3 for which we use Figure 3.24 to determine eq. (3.21n). Figure 3.24a shows the representative segment in green, the "d" representative bridges in blue, and the "f" representative bridges in black squeezed between the "d" representatives. Following the natural orientation, we see that the first bridge spans the width of Γ and does not enclose square-12 but homotopes into the sequence $f_4^{-1}d_3^{-1}f_3^{-1}d_2^{-1}f_2^{-1}d_1^{-1}$. Let us consider Figure 3.24b, which is a close-up of the escape zone. One sees why the previously mentioned sequence does not end in f_1^{-1}. The fold in the bridge (just after the nose following the natural orientation) does not intersect Γ_S and can be distorted in such a way so as to not enclose plus-12. Continuing along the segment, we see a bridge enclosing disk-4 and square-16 giving a factor of x_0^{-1}. The final bridge is simply c_4 and completes the expansion in the bridge basis.

$$\mathcal{M}(d_3) = f_4^{-1}d_3^{-1}f_3^{-1}d_2^{-1}f_2^{-1}d_1^{-1}x_0^{-1}c_4 \tag{3.31}$$

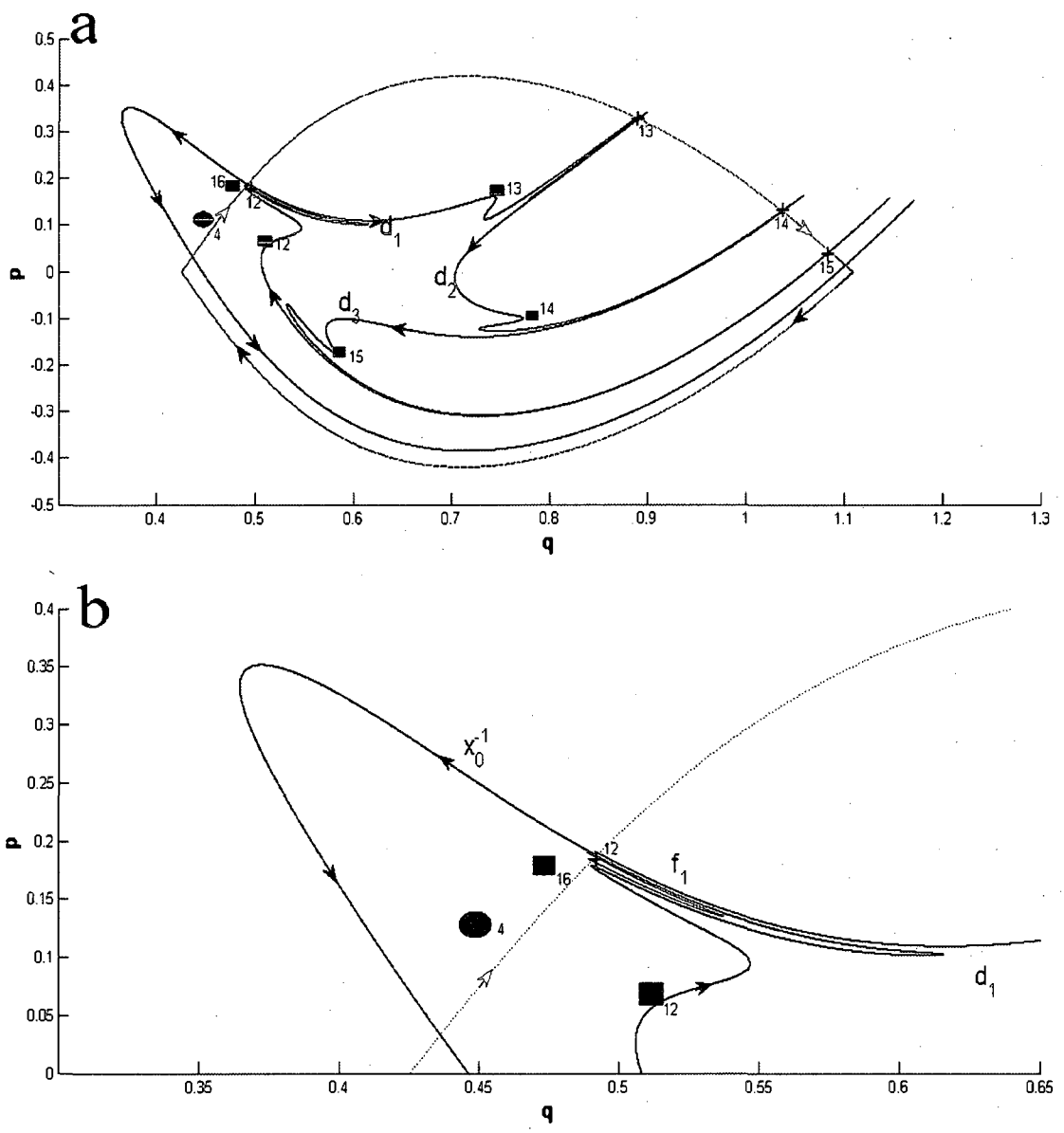

Figure 3.24: a.) $\mathcal{M}(d_3)$ expanded in the 16-basis. b.) Close-up of E_0.

Finally, we come to the dynamical equation for f_4. The bridge representing f_4 is shown in Figure 3.21c. The image of this bridge is shown in Figure 3.25. This curve is comprised of three bridges, two of which wind under C_4 as shown in Figure 3.25. The class f_4's representative curves possess a counter-clockwise orientation which is preserved under the mapping. For $\mathcal{M}(f_4)$ to possess this orientation, it must start with

c_4^{-1} and end with c_4. The middle bridge encloses plus-16, the long thin tendril winding through E_0. Considering the counter-clockwise orientation, we can write down the last dynamical equation.

$$\mathcal{M}(f_4) = c_4^{-1} t_0^{-1} c_4 \tag{3.32}$$

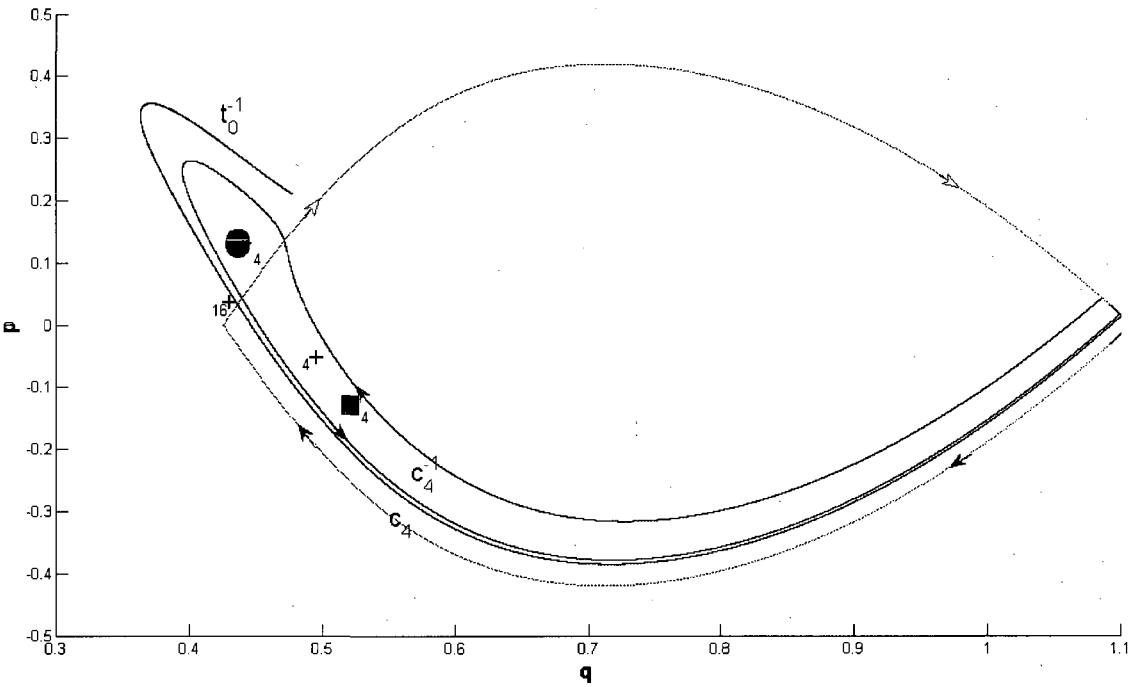

Figure 3.25: Bridge class of $\mathcal{M}(f_4)$.

We conclude our discussion by deriving the dynamical mapping acting on class a_4, or eq. (3.21p). Figure 3.26 shows the bridge, which is a segment of $\mathcal{C}_{12}$, representing a_4 in blue and its image in green. Following the orientation of the green curve we can pick off its bridge class to obtain the desired dynamical equation.

$$\mathcal{M}(a_4) = c_1^{-1} w_0^{-1} c_4 \tag{3.33}$$

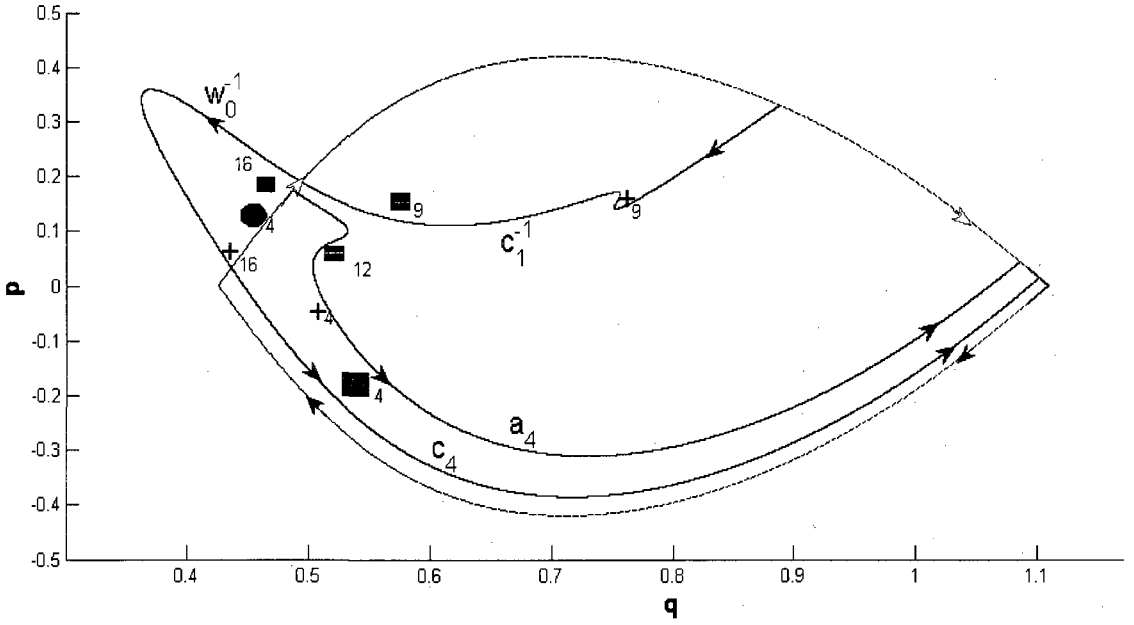

Figure 3.26: The bridge class a_4 and its image.

b.) Predictions of the 16-basis and a Comparison to the Previous Predictions

Now that we have explained the calculation of the dynamical equations, we can compare the predictions of the three bases. Within the context of the 16-basis, the bridge classes of the first 16 capture lobes are not predictions. However, we present $\{[\mathcal{U}_1^F]_{16}\}_{i=1}^8$ in eq. (3.34) for comparison to eq. (3.2) and eq. (3.17). At each iterate, the newborn escape segments are in boldface.

$$
\begin{aligned}
&\text{a.)}\ [\mathcal{U}_1^F]_{16} = \mathbb{u}_0 a_1 \\
&\text{b.)}\ [\mathcal{U}_2^F]_{16} = u_1 a_2 \\
&\text{c.)}\ [\mathcal{U}_3^F]_{16} = u_2 a_3 \\
&\text{d.)}\ [\mathcal{U}_4^F]_{16} = u_3 b_4^{-1} \mathbb{u}_0^{-1} c_4 \\
&\text{e.)}\ [\mathcal{U}_5^F]_{16} = u_4 c_4^{-1} \mathbb{w}_0 b_1 u_1^{-1} a_1^{-1} \mathbb{w}_0^{-1} c_4 \\
&\text{f.)}\ [\mathcal{U}_6^F]_{16} = u_5 c_4^{-1} \mathbb{w}_0 a_1 w_1 b_2 u_2^{-1} a_2^{-1} w_1^{-1} a_1^{-1} \mathbb{w}_0^{-1} c_4 \\
&\text{g.)}\ [\mathcal{U}_7^F]_{16} = u_6 c_4^{-1} \mathbb{w}_0 a_1 w_1 a_2 w_2 b_3 u_3^{-1} a_3^{-1} w_2^{-1} a_2^{-1} w_1^{-1} a_1^{-1} \mathbb{w}_0^{-1} c_4 \\
&\text{h.)}\ [\mathcal{U}_8^F]_{16} = u_7 c_4^{-1} \mathbb{w}_0 a_1 w_1 a_2 w_2 a_3 w_3 a_4^{-1} \mathbb{u}_0^{-1} c_4 u_4^{-1} c_4^{-1} \mathbb{u}_0 b_4 w_3^{-1} a_3^{-1} w_2^{-1} a_2^{-1} w_1^{-1} a_1^{-1} \mathbb{w}_0^{-1} c_4
\end{aligned}
\tag{3.34}
$$

We see that the number and relative orientations of the escape segments match those in eq. (3.2) and eq. (3.17). The class u_0 is represented by curves that wind around (α_4, β_4) in all three bases. In either the 12 or 16-bases, w_0 winds around all of the holes in E_0. Symbolically, the minimal sets produced by the 12 and 16-bases are identical up to eight iterates. In fact, one would find that the minimal sets are identical up to 11 iterates. At this level, however, the symbolic expressions are so long that their display would slow the discussion.

New structure appears in C_{12}. Therefore, we will jump ahead and examine the finger v_0 in $[\mathcal{U}_{12}^F]_{16}$. We choose not to show the entire bridge class as it contains far too many symbols and instead elect to show a subsequence containing the segment representing the finger.

$$
\left[\mathcal{U}_{12}^F\right]_{16} = u_{11} c_4^{-1} \ldots d_1^{-1} f_1^{-1} \mathbb{v}_0 f_1 \mathbb{x}_0^{-1} c_4 u_4^{-1} \ldots c_4 \tag{3.35}
$$

Again, v_0's appearance is forced by construction as it represents the finger in C_{12}. Counting the total number of escape segments, one finds 25 escape segments in $[\mathcal{U}_{12}^{F}]_{16}$, matching the number in $[\mathcal{U}_{12}^{F}]_{12}$. However, examining $[\mathcal{U}_{18}^{F}]_{16}$, we find

$$\left[\mathcal{U}_{18}^{F}\right]_{16} = c_4^{-1} \ldots x_2^{-1} a_2 w_1^{-1} a_1^{-1} w_0^{-1} c_4 v_6 c_4^{-1} w_0 a_1 w_1 a_2 \\ t_2^{-1} a_2^{-1} w_1^{-1} a_1^{-1} w_0^{-1} c_4 x_6^{-1} c_4^{-1} w_0 a_4 w_1 a_2 u_2 \ldots c_4 \tag{3.36}$$

We can graph the subset of the minimal set presented in eq. (3.36). Figure 3.27 shows that between the 4th iterate of the finger in $[\mathcal{U}_{12}^{F}]_{16}$ (v_6) and its nearest neighbor (x_6^{-1}) there exists five escape segments. Again, the Epistrophe Start Rule suggests (for the tangle in Figure 3.1) that an escape segment will spawn on both sides two new sequences after four iterates. Here, we see that v_4 spawns one sequence after four iterates and the second sequence after five iterates. This new spawning rule is not a consequence of the 12-basis.

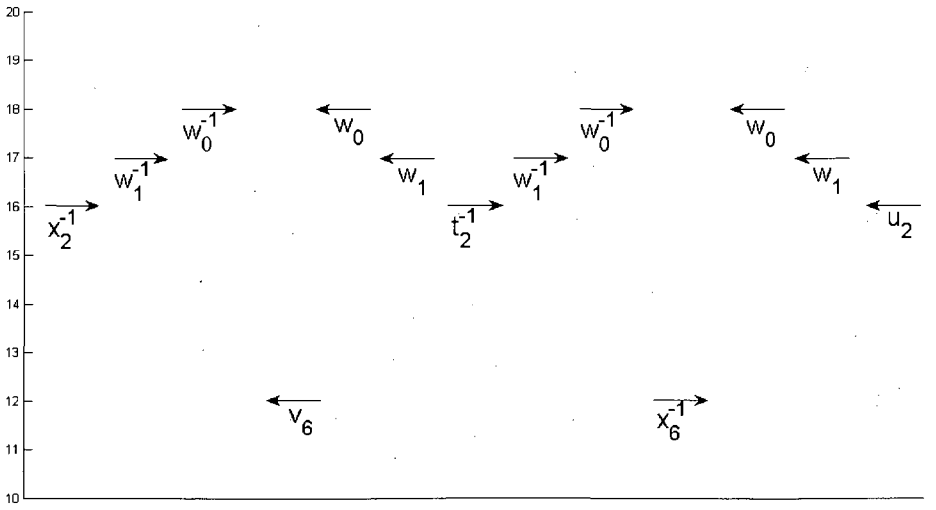

Figure 3.27: Schematic of escape time plot derived from eq.(3.36).

v.) Comparison of the Predicted Minimal Sets to the Simulation.

We compare the numerically computed escape time plot shown in Figure 3.28 to the predictions of the three different bases. We remind the reader that each escape segment in Figure 3.28 is bounded by two homoclinic points. The abscissa in Figure 3.28 is the initial condition, which we have chosen to be the arclength measured along $\mathcal{U}$ from the pip $\mathbf{Q}_0$, or Δq_0. The ordinate is the number of iterates to map into E_0. We see that the earliest epistrophes start at 4 and 5 iterates and possess opposing orientations. The earliest epistrophes and their progeny are produced by all three bases.

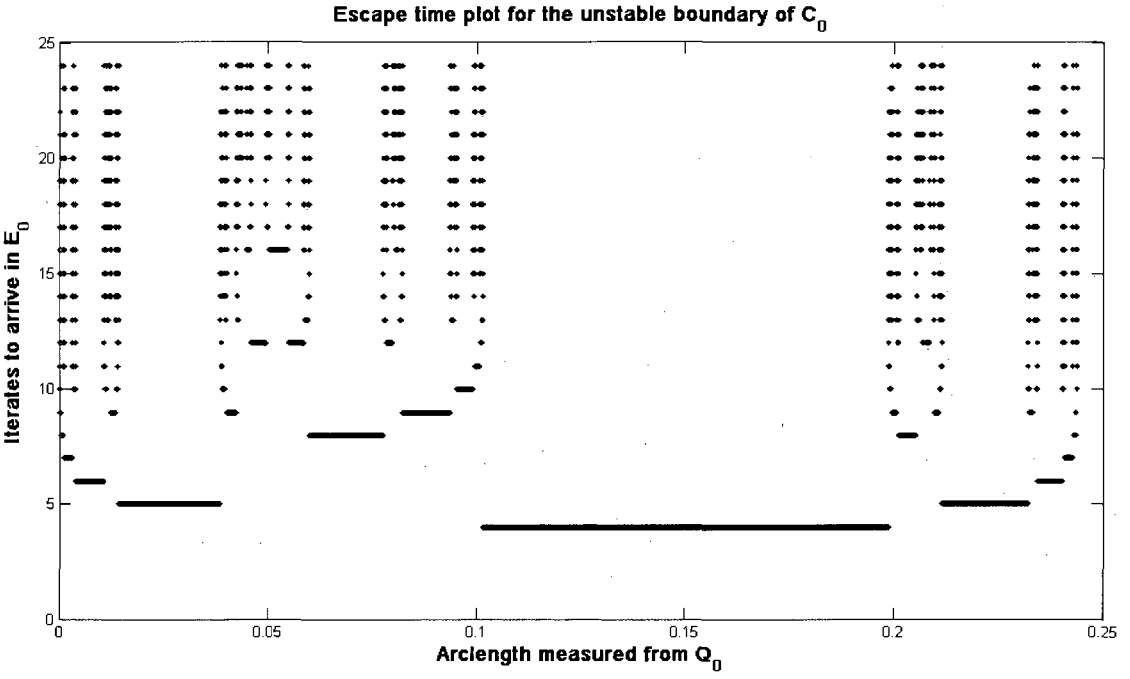

Figure 3.28: Numerically computed escape time plot for $\mathcal{U}_F^0$.

Looking closely at (0.05, 12) in Figure 3.28 reveals an isolated escape segment. A close-up is shown in Figure 3.29. This isolated escape segment is in fact the segment $\mathcal{U}[\gamma_{12}, \delta_{12}]$. Comparing Figures 3.12 and 3.29 shows that the 12-basis fails to predict the

structure seen in the numerical escape time plot. Comparing Figure 3.29 to Figure 3.27 shows that the actual structure is correctly accounted for by the 16-basis.

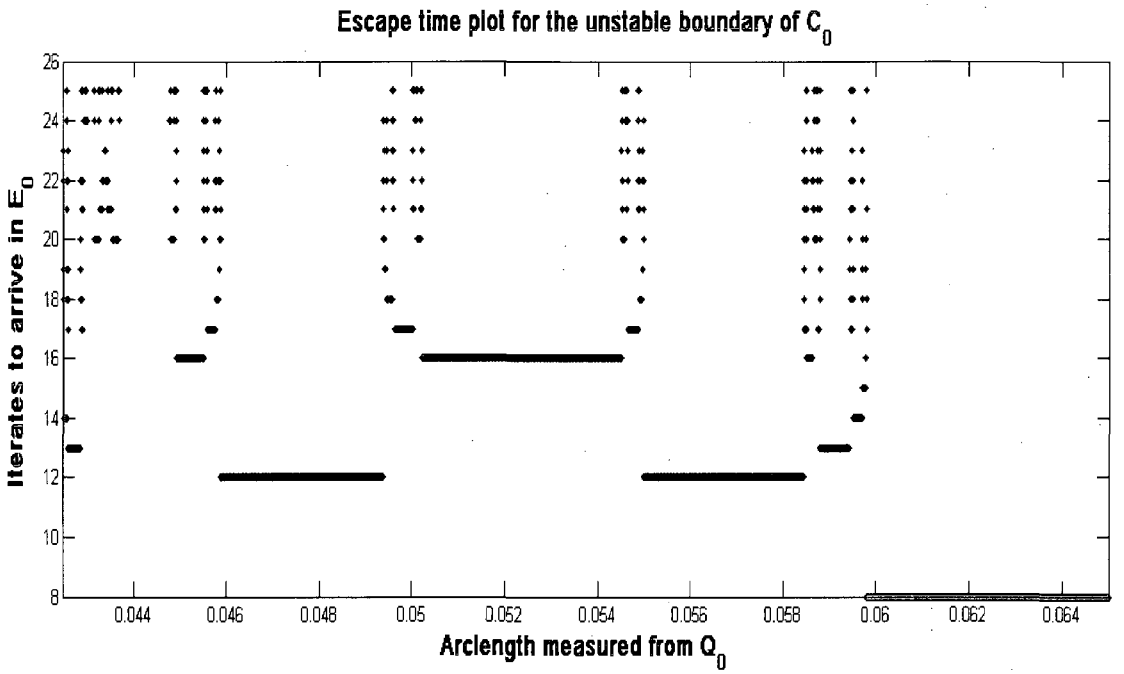

Figure 3.29: Close up of finger in $\mathcal{C}_{12}$.

In addition to the new structure shown in eq. (3.36), a factor of v_0^{-1} appears in $[\mathcal{U}_{16}^F]_{16}$. Eq. (3.37a) shows the additional factor in a subsequence lying to the right of v_4. This new factor is represented by the unstable segment $\mathcal{U}[\xi_{16}, \eta_{16}]$, which is bounded by two of the 16-neighbors. We compute $[\mathcal{U}_{21}^F]_{16}$ and examine the structure immediately surrounding the factor of v_5^{-1}. This is shown in eq. (3.37b) where the relevant symbols are shown in bold.

$$\begin{aligned} &a.)\left[\mathcal{U}_{16}^F\right]_{16} = u_{15}c_4^{-1}\ldots d_1^{-1}x_0^{-1}c_4v_4c_4^{-1}t_0^{-1}c_4x_4^{-1}c_4^{-1}u_0b_4\ldots x_0f_1^{-1}v_0^{-1}f_1d_1\ldots c_4 \\ &b.)[\mathcal{U}_{21}^F]_{16} = u_{20}c_4^{-1}\cdots u_1^{-1}a_1^{-1}w_0^{-1}c_4x_5c_4^{-1}w_0a_1t_1a_1^{-1}w_0^{-1}c_4v_5^{-1}c_4^{-1}w_0a_1x_1\cdots c_4 \end{aligned} \tag{3.37}$$

The subsequence shown predicts the same structure seen in Figure 3.27. More importantly, the factor of v_5^{-1} spawns its left sequence at five iterates and its right sequence at 4 iterates. We can compare this predicted structure to the actual escape segments near the isolated escape segment in Figure 3.29. Figure 3.30 shows the finger in the homoclinic tangle (in black) on the left and the escape segments near the isolated segment on the right. In actuality, this segment spawns both sequences at four iterates.

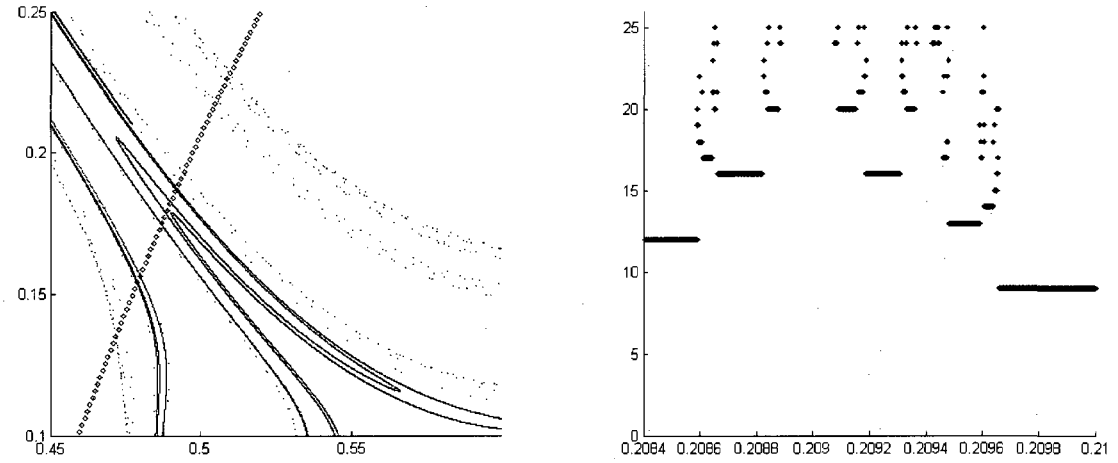

Figure 3.30: $\mathcal{U}[\xi_{16}, \eta_{16}]$ and its location in the escape time plot.

Examining $[\mathcal{U}_{17}^{F}]_{16}$ we find a factor of v_0 and a factor of v_0^{-1}. Examining the neighbors of v_4 and v_4^{-1} in $[\mathcal{U}_{21}^{F}]_{16}$, one finds that v_4 and v_4^{-1} each spawn one sequence after 4 iterates. When one examines the escape time plot, shown in Figure 3.31, one indeed finds two isolated escape segments at 17 iterates. However, upon examining the figure we find that each segment in fact spawns two sequences at 21 iterates.

$$[\mathcal{U}_{21}^{F}]_{16} = u_{20}c_4^{-1}\cdots w_1a_2w_2a_3w_3f_4^{-1}d_3^{-1}f_3^{-1}d_2^{-1}f_2^{-1}d_1^{-1}$$
$$x_0^{-1}c_4v_4c_4^{-1}t_0^{-1}c_4x_4^{-1}c_4^{-1}u_0b_4w_3^{-1}\cdots w_1a_2w_2a_3w_3 \qquad (3.38)$$
$$b_4^{-1}u_0^{-1}c_4x_4c_4^{-1}t_0c_4v_4^{-1}c_4^{-1}x_0d_1f_2d_2f_3d_3f_4w_3^{-1}\cdots c_4$$

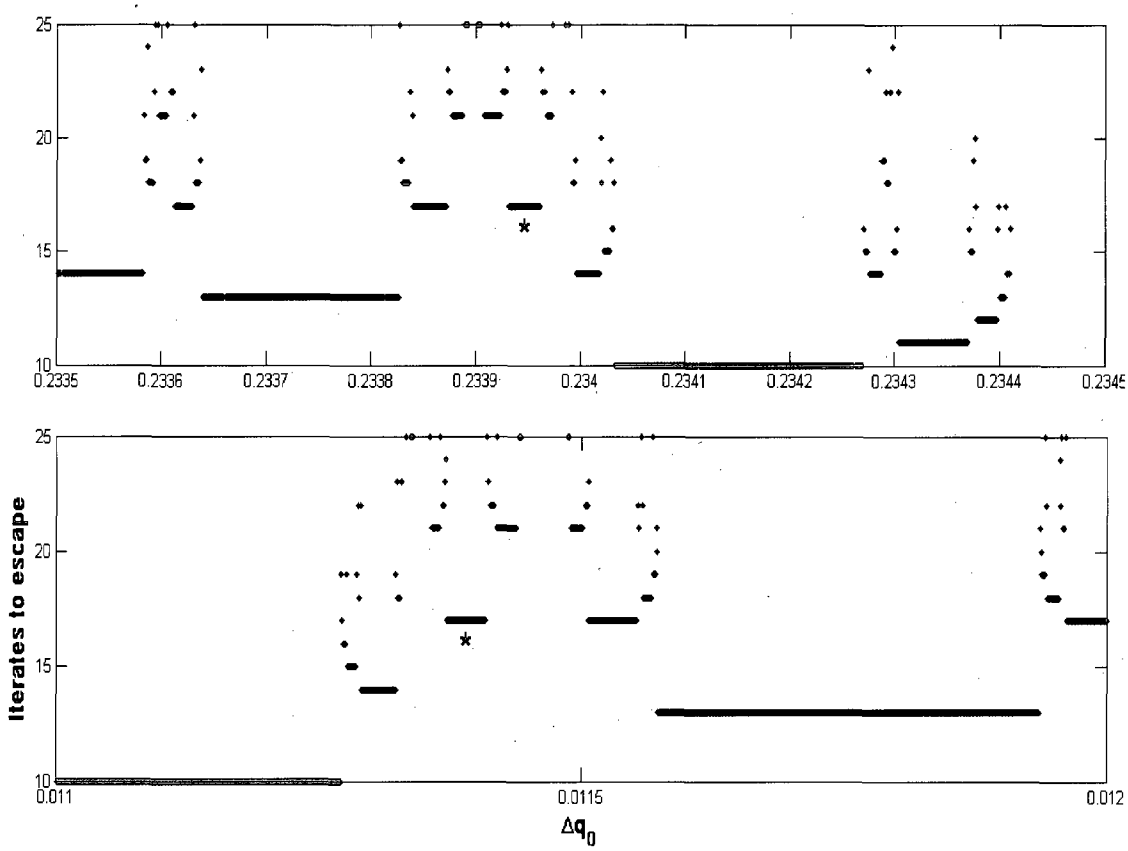

Figure 3.31: Isolated escape segments at 17 iterates; each is marked by an asterisk.

To conclude our discussion on the three bases, we present a gross summary of our results in the form of a table showing the number of escape segments appearing in $[\mathcal{U}_i^{F}]_J$ for i = 1, 2,..., 20 and J = 4, 12, and 16. We see that the first 11 classes expanded in all three bases contain the same number of escape segments. New pseudo-neighbors appear at the 12th iterate. At iterate 12, the $[\mathcal{U}_{12}^{F}]_4$ predicts 24 segments in the minimal

set while $[\mathcal{U}_{12}^F]_{12}$ and $[\mathcal{U}_{12}^F]_{16}$ both correctly account for 25 segments. However, we see that up to 20 iterates, the 4 and 12-bases predict the same number of segments. This says that the additional pseudo-neighbors used in constructing the 12-basis were not true topological information and that the only true topological information came from the 4-neighbors.

Iterate	J = 4	J = 12	J = 16	Iterate	J = 4	J = 12	J = 16
1	0	0	0	**11**	16	16	16
2	0	0	0	**12**	24	25	25
3	0	0	0	**13**	40	40	40
4	1	1	1	**14**	64	64	64
5	2	2	2	**15**	96	96	96
6	2	2	2	**16**	144	144	146
7	2	4	2	**17**	224	224	228
8	4	4	4	**18**	352	352	356
9	8	8	8	**19**	544	544	548
10	12	12	12	**20**	832	832	841

Table 3.1: Number of escape segments in $[\mathcal{U}_n^F]_J$, n = 1,..., 20 and J = 4, 12, and 16.

Since a new escape segment appeared at the 12th iterate, we expect the new segment to spawn two epistrophes at 16 iterates. It is not a surprise that no additional structure will appear in $[\mathcal{U}_{13}^F]_{16}$, $[\mathcal{U}_{14}^F]_{16}$, and $[\mathcal{U}_{15}^F]_{16}$. Furthermore, we know that at the 16th iterate, the 16-neighbors $(\theta_{16}, \iota_{16})$ and (ξ_{16}, η_{16}) appear accounting for the two additional escape segments seen in $[\mathcal{U}_{16}^F]_{16}$. $[\mathcal{U}_{17}^F]_{16}$, $[\mathcal{U}_{18}^F]_{16}$, and $[\mathcal{U}_{19}^F]_{16}$ each contain 4 more escape segments than their counterparts in the 4-basis and 12-basis. $[\mathcal{U}_{17}^F]_{16}$, $[\mathcal{U}_{18}^F]_{16}$, and $[\mathcal{U}_{19}^F]_{16}$ each will contain two children of the isolated escape segment v_0

appearing in $[\mathcal{U}_{12}^{F}]_{16}$. The remaining two segments predicted at each iterate are therefore additional isolated segments.

vi.) Expanding a General Line of Initial Conditions in Each Basis

Finally, we use the three bases to make our predictions for a point burst launched from within the vase. In the surface-of-section coordinates, a point burst with all allowed launch angles is rectified into a vertical line segment of length two. This line, plotted in Figure 3.1, represents the initial conditions for a particular family of trajectories to be examined in Chapter 5. The numerically computed set of epistrophes is given in Figure 3.32. Possibly the most obvious aspect of the escape time plot is the area devoid of escape segments. The line passes through a continent of stability surrounding the stable periodic orbit (p = 0). Thus it includes trajectories that never escape.

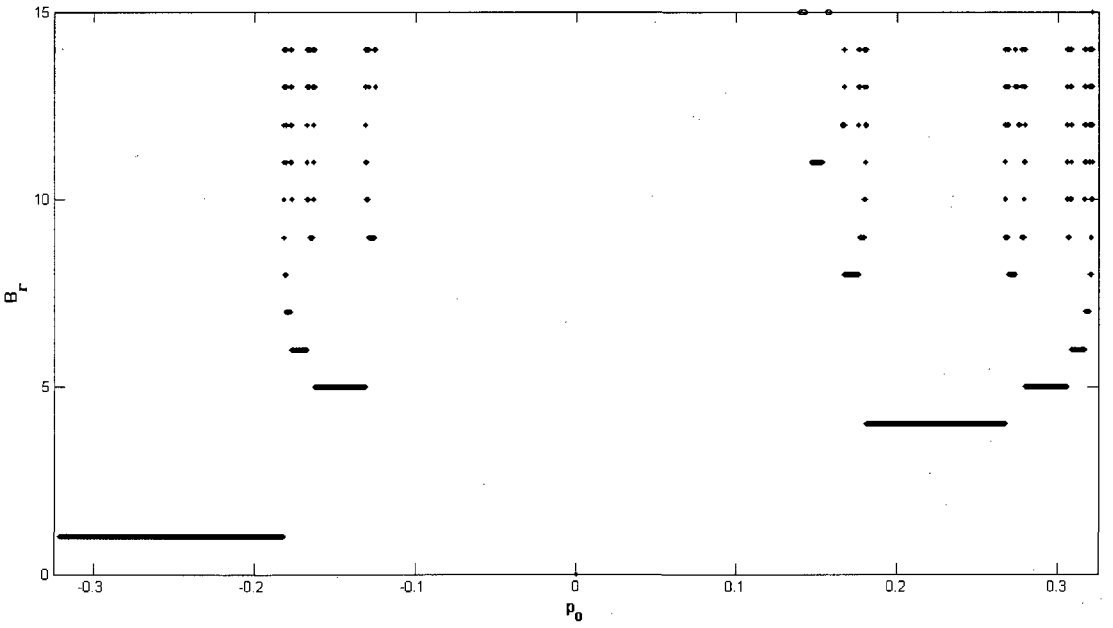

Figure 3.32: Epistrophes for ultrasound burst.

The line of initial conditions, $\mathcal{L}_0$, must be iterated once so that both endpoints intersect Γ_S for assignment to a well-defined path-class in the 4 and 16-bases. We will not discuss the expansion of $\mathcal{L}_0$ in the 12-basis as the minimal set is identical to that produced by the 4-basis. Figure 3.1 shows that $\mathcal{L}_0$ intersects E_{-1} producing an escape segment appearing at the first iterate. Therefore, $[\mathcal{L}_1]_4$ and $[\mathcal{L}_1]_{16}$ both start with an inert class representing this segment. We can ignore the first symbol since it will not produce any additional non-inert classes. To obtain $[\mathcal{L}_1]_4$, we plot $\mathcal{L}_1$ along with the known segment of $\mathcal{U}$ and the internal holes to find $[\mathcal{L}_1]_4 = c_1$. Since c_1 is the class represented by the unstable boundary of C_1, the minimal set generated by iterating $[\mathcal{L}_1]_4$ is already given by eq. (3.2). To compute $[\mathcal{L}_1]_{16}$, we present the schematic of the 16-basis given in Figure 3.33 with an additional curve topologically equivalent to $\mathcal{L}_1$. We immediately see from Figure 3.33 that $[\mathcal{L}_1]_{16} = d_1 f_2$.

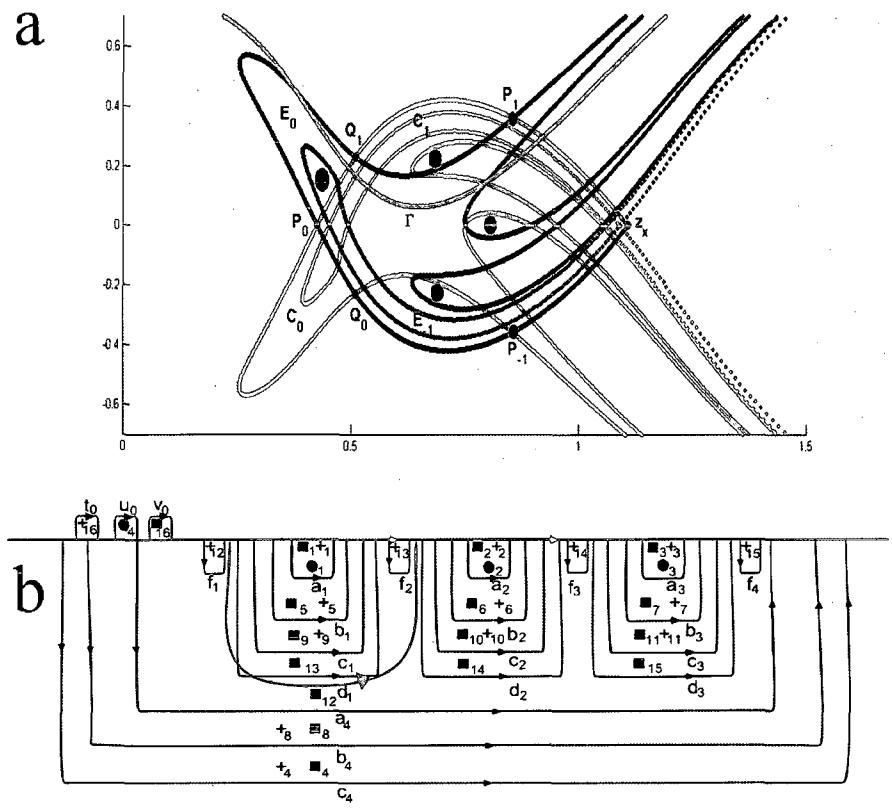

Figure 3.33: a.) Tangle with 4-basis holes and first iterate of burst b.) Schematic of 16-basis with curve topologically equivalent to first iterate of burst plotted in green

a.) Digression: Phase Space Representations of the Chaotic Trajectories and the Symbolic Dynamics

Before we iterate $[\mathcal{L}_0]_{16}$, we will digress to examine the images of $\mathcal{L}_0$ and their homotopy classes. To show the relationship between the curve and its homotopy class, we will examine the first eight iterates of $\mathcal{L}_0$ and their expansions in the 4-basis. These eight path classes are reproduced in eq. (3.39) below.

$$
\begin{aligned}
&\text{a.) } [\mathcal{L}_1]_4 = \mathbb{u}_0 c_1 \\
&\text{b.) } [\mathcal{L}_2]_4 = u_1 c_2 \\
&\text{c.) } [\mathcal{L}_3]_4 = u_2 c_3 \\
&\text{d.) } [\mathcal{L}_4]_4 = u_3 f^{-1} \mathbb{u}_0^{-1} f \\
&\text{e.) } [\mathcal{L}_5]_4 = u_4 f^{-1} \mathbb{u}_0 c_1 u_1^{-1} c_1^{-1} \mathbb{u}_0^{-1} f \\
&\text{f.) } [\mathcal{L}_6]_4 = u_5 f^{-1} \mathbb{u}_0 c_1 u_1 c_2 u_2^{-1} c_2^{-1} u_1^{-1} c_1^{-1} \mathbb{u}_0^{-1} f \\
&\text{g.) } [\mathcal{L}_7]_4 = u_6 f^{-1} \mathbb{u}_0 c_1 u_1 c_2 u_2 c_3 u_3^{-1} c_3^{-1} u_2^{-1} c_2^{-1} u_1^{-1} c_1^{-1} \mathbb{u}_0^{-1} f \\
&\text{h.) } [\mathcal{L}_8]_4 = u_7 f^{-1} \mathbb{u}_0 c_1 u_1 c_2 u_2 c_3 u_3 f^{-1} \mathbb{u}_0^{-1} f u_4^{-1} f^{-1} \mathbb{u}_0 f u_3^{-1} c_3^{-1} u_2^{-1} c_2^{-1} u_1^{-1} c_1^{-1} \mathbb{u}_0^{-1} f
\end{aligned}
\tag{3.39}
$$

First, recall that $f = c_1 c_2 c_3$. Let us consider the first three images of $\mathcal{L}_0$ in Figure 3.34 below and their path classes. The burst is plotted in black, the first image in green, the second in yellow, and the third in brown. The first three classes correspond to curves that homotope into the unstable boundaries of the first three capture lobes. We see that each image of $\mathcal{L}_0$ homotopes into a capture lobe.

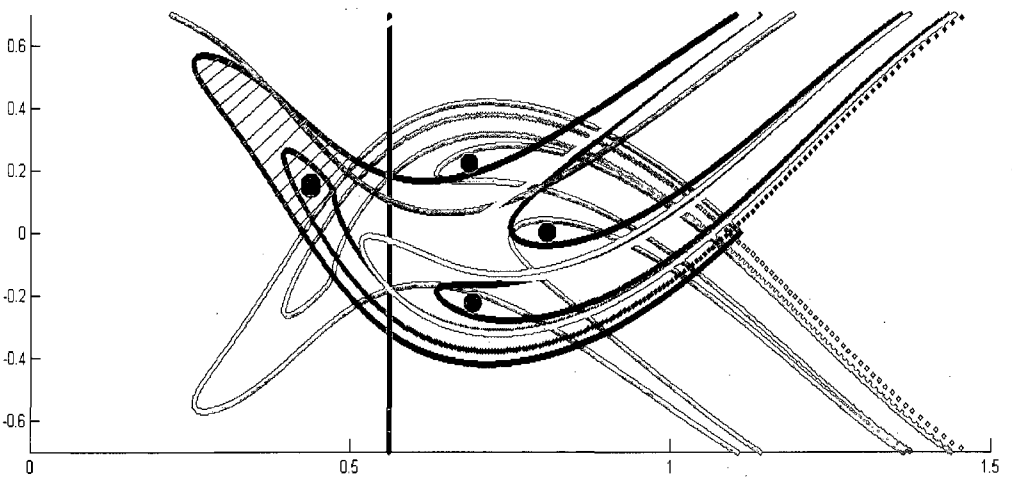

Figure 3.34: The point burst, and its first three images. The burst is plotted in black, the first iterate is plotted in green, the second iterate is plotted in yellow, and the third iterate is plotted in brown.

Eq. (3.39d) predicts that the 4^{th} image of $\mathcal{L}_0$ is predicted to look a lot like the fourth capture lobe. Figure 3.35a shows that this is indeed the case. Figure 3.35a also shows that $\mathcal{L}_4$ has developed a nose-like structure. This nose does not enclose any holes and therefore can be removed by distortion. This implies that the nose represents structure that cannot be predicted by the 4-basis. The symbolic dynamics predicts that the remaining path classes begin with a factor of f^{-1} and end with a factor of f. This class represents curves that enclose all three internal holes. Figures 3.35b, 3.35c, and 3.35d show the 5^{th}, 6^{th}, and 7^{th} iterates of $\mathcal{L}_0$. The initial and final curves of $\mathcal{L}_5$, $\mathcal{L}_6$, and $\mathcal{L}_7$ each enclose all three holes.

The 4^{th} and 6^{th} factors in $[\mathcal{L}_5]_4$ are c_1 and c_1^{-1}. To intersect E_1, $\mathcal{L}_5$ is forced to wind under C_1 and thus possess two segments that homotope into $\mathcal{C}_1$. The 4^{th} and 10^{th} factors in $[\mathcal{L}_6]_4$ correspond to two curves that homotope into $\mathcal{C}_1$. The 6^{th} and 8^{th} factors correspond to curves that homotope into $\mathcal{C}_2$. In other words, $\mathcal{L}_6$ is predicted to wind under both C_1 and C_2. Figure 3.35c shows that $\mathcal{L}_6$ possesses segments that homotope into C_1 and C_2. $[\mathcal{L}_7]_4$ is predicted to wind under C_1, C_2, ad C_3. Again, Figure 3.35d shows that $\mathcal{L}_7$ indeed possesses the predicted segments. Finally, Figure 3.36 shows $\mathcal{L}_8$. The nose has become fairly distorted at the eight iterate. Again, if we homotope the nose away, we can compare the bridges in $\mathcal{L}_8$ to $[\mathcal{L}_8]_4$ and verify that each bridge class in $[\mathcal{L}_8]_4$ is represented by a bridge in $\mathcal{L}_8$.

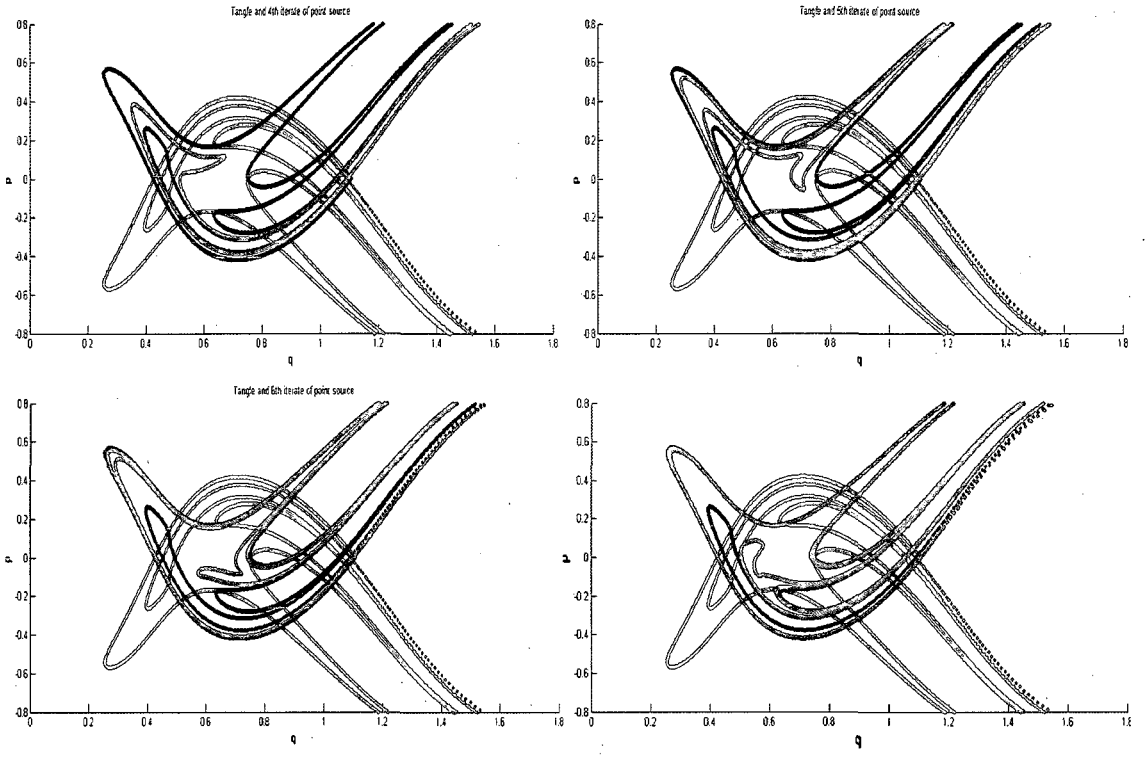

Figure 3.35: a.) 4th, b.) 5th, c.) 6th, and d.) 7th iterates of burst shown in Figure 3.34.

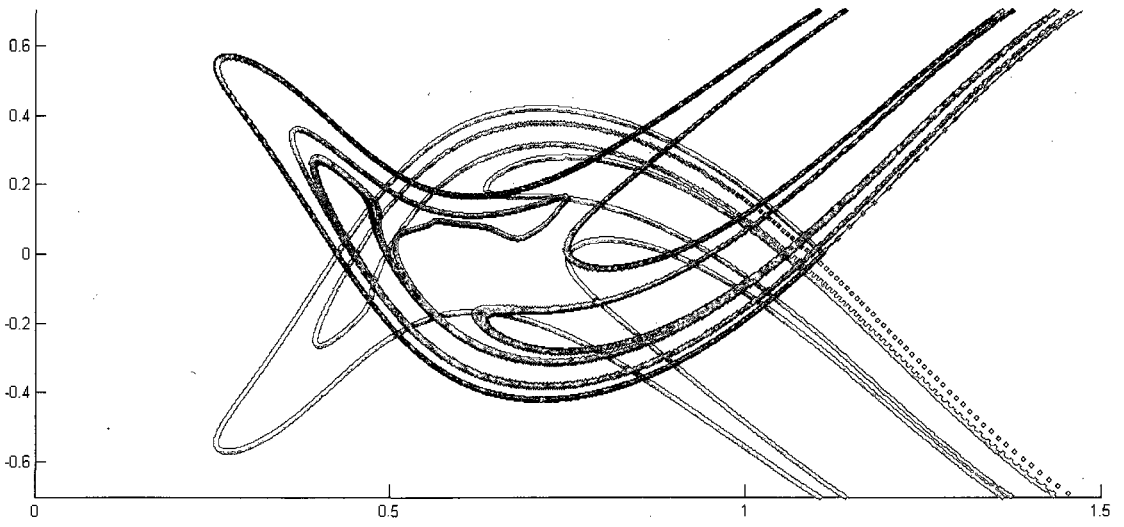

Figure 3.36: Eight iterate of $\mathcal{L}_0$.

b.) Predicted Minimal Set of $\mathcal{L}_0$ in the 16-basis.

We use eqs. (3.21) to iterate d_1f_2 seven times to obtain the minimal set to eight iterates.

$$
\begin{aligned}
&a.)[\mathcal{L}_1]_{16} = d_1f_2 \\
&b.)[\mathcal{L}_2]_{16} = d_2f_3 \\
&c.)[\mathcal{L}_3]_{16} = d_3f_4 \\
&d.)[\mathcal{L}_4]_{16} = f_4^{-1}d_3^{-1}f_3^{-1}d_2^{-1}f_2^{-1}d_1^{-1}w_0^{-1}c_4 \\
&e.)[\mathcal{L}_5]_{16} = c_4^{-1}w_0d_1f_2w_1^{-1}a_1^{-1}w_0^{-1}c_4 \\
&f.)[\mathcal{L}_6]_{16} = c_4^{-1}w_0a_1w_1d_2f_3w_2^{-1}a_2^{-1}w_1^{-1}a_1^{-1}w_0^{-1}c_4 \\
&g.)[\mathcal{L}_7]_{16} = c_4^{-1}w_0a_1w_1a_2w_2d_3f_4w_3^{-1}a_3^{-1}w_2^{-1}a_2^{-1}w_1^{-1}a_1^{-1}w_0^{-1}c_4 \\
&h.)[\mathcal{L}_8]_{16} = c_4^{-1}w_0a_1w_1a_2w_2a_3w_3f_4^{-1}d_3^{-1}f_3^{-1}d_2^{-1}f_2^{-1}d_1^{-1}w_0^{-1}c_4 \\
&\qquad\qquad w_4^{-1}c_4^{-1}u_0b_4w_3^{-1}a_3^{-1}w_2^{-1}a_2^{-1}w_1^{-1}a_1^{-1}w_0^{-1}c_4
\end{aligned}
\tag{3.40}
$$

Comparing eq. (3.40) to eq. (3.2) shows that the minimal sets are identical. However, the 16-basis allows for more variation in how the curve winds around the holes in E_0. Let us compare the minimal set to how $\mathcal{M}^n(\mathcal{L}_0)$ actually winds through E_0 for n = 4,5,…,8. Figure 3.37 shows iterates of $\mathcal{L}_0$ winding through E_0 plotted in black. The holes are placed near their actual anchors. $\mathcal{L}_4$, $\mathcal{L}_5$, $\mathcal{L}_6$, and $\mathcal{L}_7$ each contain segments that wind around all three holes. This is reflected in the symbolic sequences by the appearance of either w_0 or w_0^{-1}. Examining the 8th iterate, we see three segments winding around the three holes while one winds around disk-4, which again is produced by the intersection $C_4 \cap E_0$. This variation is reflected in eq. (3.40). The third segment predicted is u_0, which encloses only disk-4 and remaining three predicted escape segments enclosing all three holes.

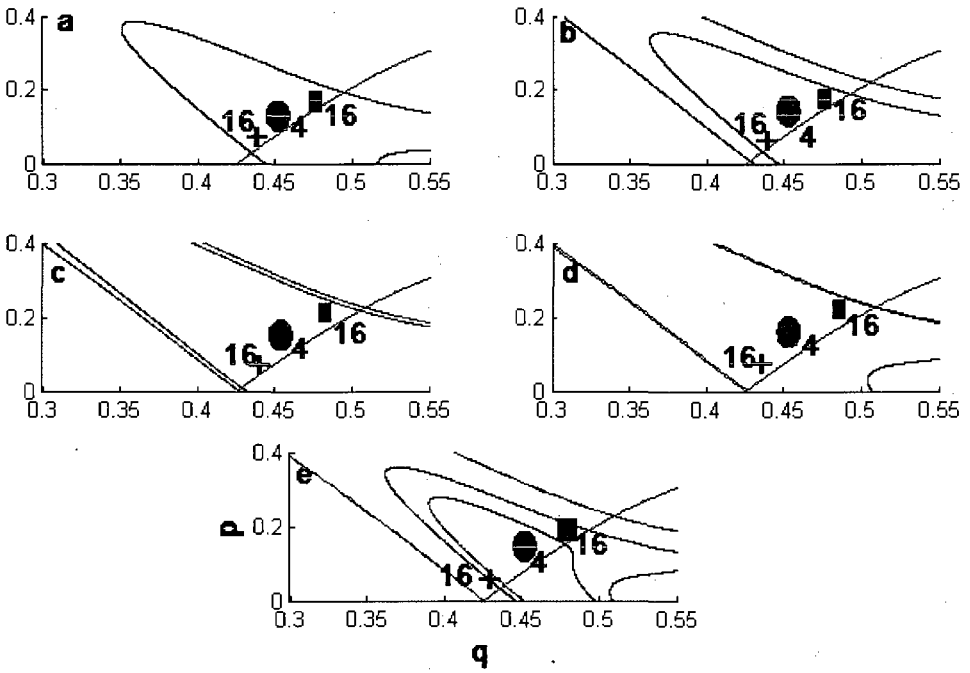

Figure 3.37: Escape segments of ultrasound burst for iterates: a.) 4, b.) 5, c.) 6, d.) 7, e.)8.

We have shown that by computing a longer segment of $\mathcal{U}$, we have been able to predict more complicated structure. However, the 16-basis does not predict all the escape segments. The first isolated escape segment appears at the 11^{th} iterate near $p_0 = 0.15$ in Figure 3.32 (a close-up is presented in Figure 3.39). This segment will spawn an unending lineage of epistrophes that will not appear in the symbolic expressions. The reason this segment goes unpredicted is simple. If we examine a figure of $\mathcal{L}_0 \cap E_{-11}$ (Figure 3.38), we see that the isolated segment is due to the intersection of $\mathcal{L}_0$ with a finger in E_{-11}. If we slightly perturb $\mathcal{L}_0$ to the left removing the intersection with the finger and iterate the new line one time, we can assign it to a homotopy class. The perturbed line in fact belongs to the same homotopy class as $\mathcal{L}_0$ and possesses the same

minimal set. There is topological information unaccounted for that would produce a hole in the finger and thus result in the perturbed line being assigned to a different class.

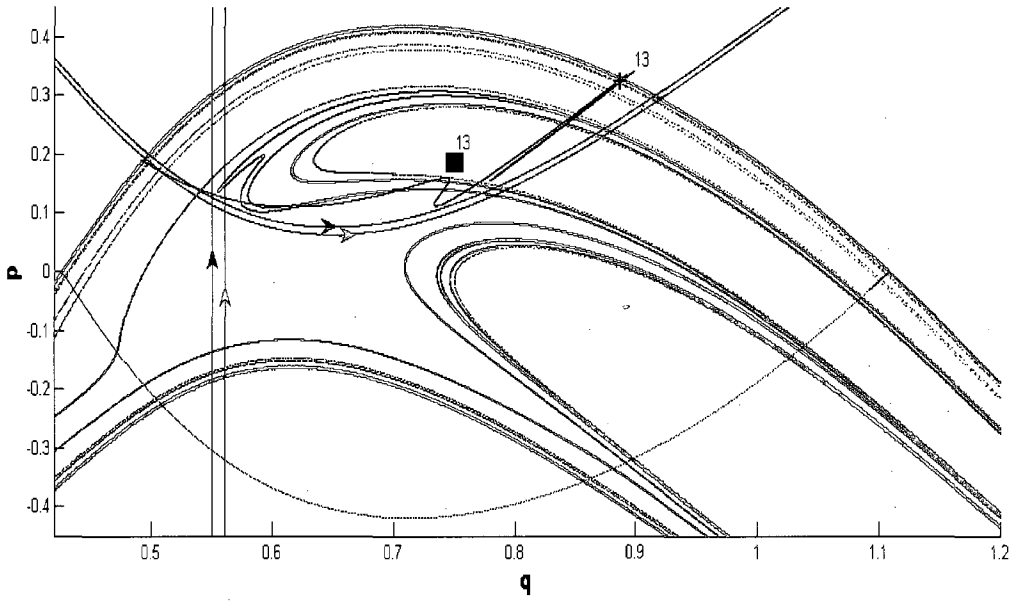

Figure 3.38: $\mathcal{L}_1$ and perturbed source expanded in 16-basis.

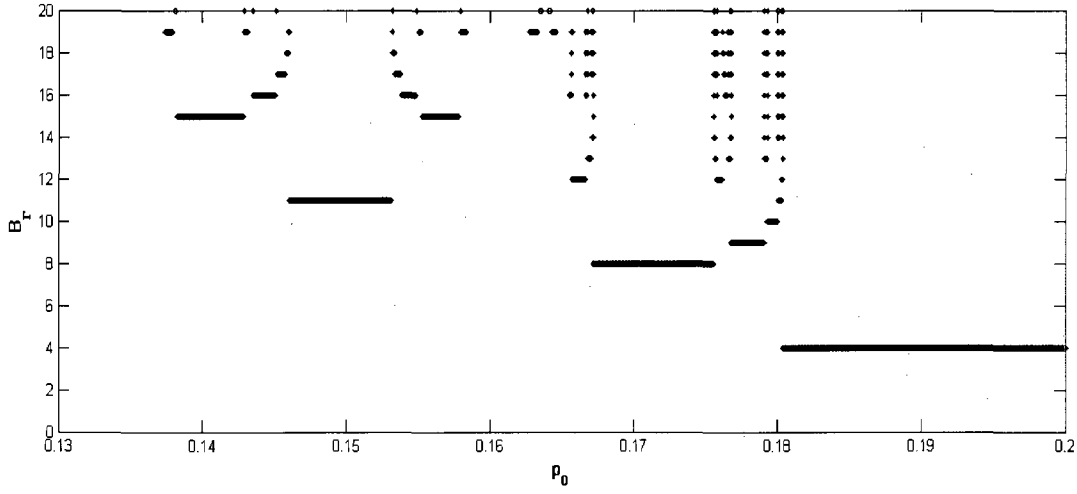

Figure 3.39: 1st unpredicted escape segment for the point burst.

Before continuing, we summarize our results in Table 3.2 below. The second and third columns give the number of escape segments predicted in $\{[\mathcal{L}_i]_J\}_{i=1}^{16}$ for J = 4

and 16, respectively. The fourth column shows the actual number of escape segments. Up to the 10^{th} iterate of the burst, both sets of dynamical equations correctly predict the number of escape segments. At the 11^{th} iterate, one escape segment is unpredicted as we previously stated. No new escape segments appear at iterates 12, 13, and 14. At the 15^{th} iterate, both bases predict that 96 segments appear compared to the actual 98. The isolated escape segment at 11 iterates spawns its first children at 15 iterates accounting for the two unpredicted segments.

Iterate	4-basis	16-basis	Actual	Iterate	4-basis	16-basis	Actual
1	0	0	0	**9**	8	8	8
2	0	0	0	**10**	12	12	12
3	0	0	0	**11**	16	16	17
4	1	1	1	**12**	24	24	24
5	2	2	2	**13**	40	40	40
6	2	2	2	**14**	64	64	64
7	2	2	2	**15**	96	96	98
8	4	4	4	**16**	144	145	149

Table 3.2: Predicted number of escape segments for $[\mathcal{L}_0]$

At the 16^{th} iterate, the minimum number of escape segments is predicted to be 144 segments by the 4-basis. In actuality, there are 149 segments, two of which are the children of the isolated segment at 11 iterates. The 16-basis predicts only one of the remaining three segments. In Figure 3.40, we present the five additional segments as they wind through E_0.

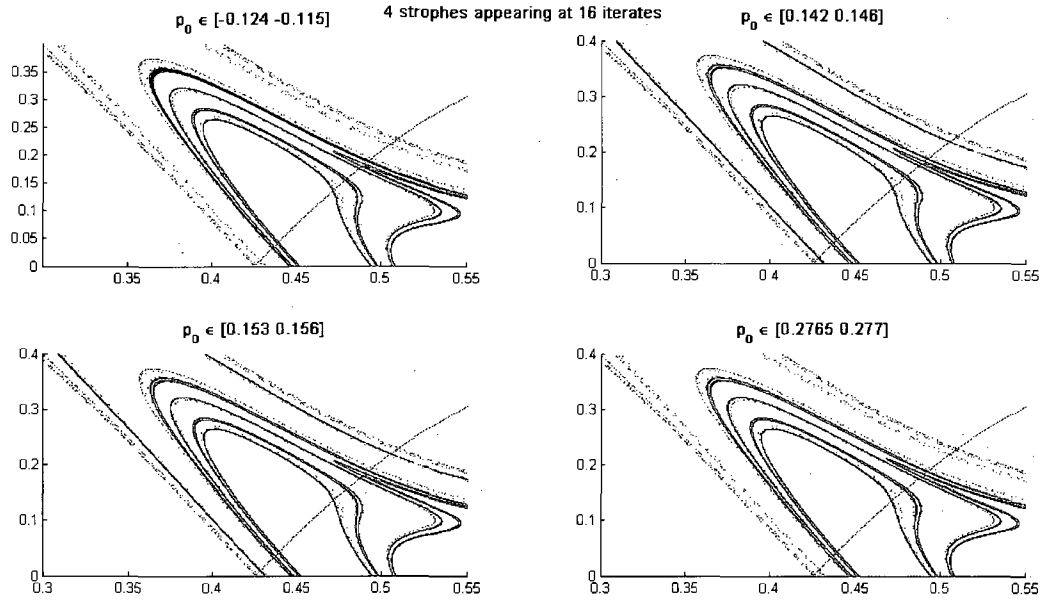

Figure 3.40: The phase space representations of the four isolated escape segments born at 16 iterates.

Let us focus on the lower right figure which shows the additional segment predicted by the 16-basis. This segment represents the class v_0. We iterate five more times and find a subsequence containing v_5^{-1}, which is shown in eq. (3.41).

$$[\mathcal{L}_{21}]_{16} = c_4^{-1}\cdots u_1^{-1}a_1^{-1}w_0^{-1}c_4x_5c_4^{-1}w_0a_1t_1a_1^{-1}w_0^{-1}c_4v_5^{-1}c_4^{-1}w_0a_1x_1\cdots c_4 \qquad (3.41)$$

Eq. (3.41) predicts one epistrophe starts four iterates later and the other starts after five iterates. However, when we examine the escape time plot about the isolated segment (Figure 3.41), we see that both epistrophes start after four iterates.

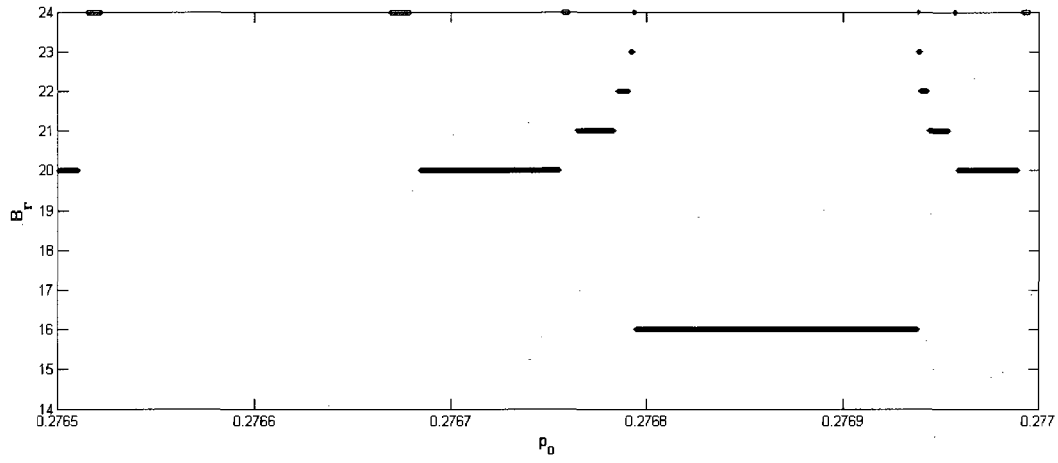

Figure 3.41: Predicted isolated escape segment at 16 iterates and its children.

Let us return to Figure 3.40. The upper right and lower left figures are children of the isolated escape segment at eleven iterates. It is interesting to note here that while these segments are not predicted, we see that each belongs to a well-defined bridge class (w_0). The upper left corner shows two unpredicted segments sandwiched together. We make two observations with regards to these two isolated segments. Figure 3.42a shows their location in the escape time plot, contained within the range $p_0 \in [-0.125\ -0.11]$, which is a bundle of rays spread over a ninth of a degree. Despite how small this bundle of rays this is, there is a vast amount of structure present. Our second observation concerns Figure 3.42b, which shows a close-up of the epistrophes lying between the isolated escape segments shown in Figure 3.42a. Since the isolated segments at 16 iterates in Figure 3.42a were not predicted, their descendants also remain unpredicted. In Figure 3.42b, we see that their second generation epistrophes share an escape segment yet they remain unpredicted.

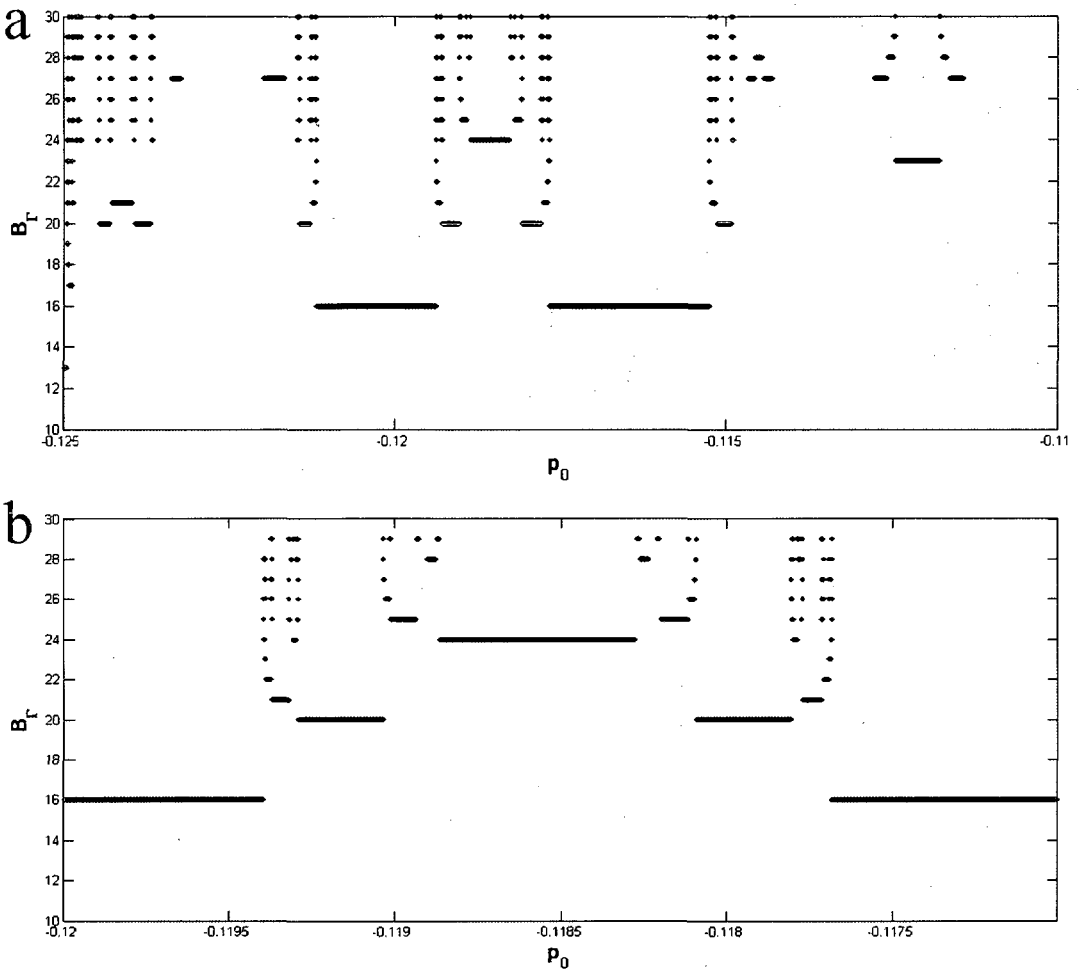

Figure 3.42: Subsets of the discrete escape time plot shown in Figure 3.32. a.) Two unpredicted isolated segments at sixteen iterates. b.) Unexpected spawning appearing between the strophes in a.

vii.) Conclusions

In this chapter, we have studied the homoclinic tangle underlying an open vase-shaped billiard using Homotopic Lobe Dynamics. For each set of dynamical equations, we obtained the minimal set of escape segments for $\mathcal{U}_0^F$ and a point burst of rays ($\mathcal{L}_0$). Each minimal set was compared to the numerically computed set of escape segments. The first calculation used the minimal amount of information: the 4-neighbors that

resulted from the intersection of C_4 and E_0. The minimal sets were contained within the numerically computed escape time plots. We also found that the minimal set predicted by the original theory was identical to that of the 4-neighbors.

As expected, additional structure was found in both numerical escape time plots. A finger in $\mathcal{C}_{12}$ resulted in an isolated escape segment. At the 11^{th} iterate, an isolated segment at the 11^{th} iterate appeared in the escape time plot for $\mathcal{L}_0$. We then set out to refine the 4-basis with the goal of predicting these isolated escape segments. We found that new pseudoneighbors appeared in $\mathcal{U}_{12}^{F}$. The number of dynamical equations became very large compared to the set acting on the 4-basis. We saw that the new equations predicted the additional segment but otherwise the same minimal set as the equations acting on the 4-basis. Furthermore, the minimal set predicted for $\mathcal{L}_0$ was identical to that predicted by the 4-basis.

Afterwards, we recalculated the basis using 16-neighbors. Again, we graphically derived a set of dynamical equations and computed the minimal sets for $\mathcal{U}_0^{F}$ and $\mathcal{L}_0$. For the minimal set of $\mathcal{U}_0^{F}$, we correctly predicted the isolated segment at twelve iterates. Furthermore, we found a surprise. Near the isolated segment at 12 iterates, the epistrophes spawn in an unexpected way. We expected each escape segment to spawn two epistrophes after four iterates. However, the isolated segment at twelve iterates spawned one at 16 iterates and the second at 17 iterates. This unexpected epistrophe spawning was predicted by the dynamical equations. In addition, two new isolated escape segments appeared at 17 iterates that were also correctly predicted by the dynamical equations. However, we predicted that each of these segments would

produce one epistrophe at 21 iterates and one epistrophe at 22 iterates where in fact both spawned two epistrophes at 21 iterates.

Finally, we computed the minimal sets within the three bases for a burst of rays launched from the upper vase boundary. The minimal sets generated by the 4 and 12-bases were identical. The minimal set generated by the 16-basis reproduced the results of the 4 and 12-bases and predicted one additional escape segment at the 16^{th} iterate. The isolated escape segment at 11 iterates was not predicted within any of the three bases. The escape time plot showed that this isolated segment spawns two children at 15 iterates which also could not be predicted. At 16 iterates, there were four isolated escape segments. Two of these are the children of the isolated segment at 11 iterates. One is an additional isolated segment that was also not predicted. The last isolated segment represented the finger class v_0, which was correctly predicted. The 16-basis predicted that this isolated segment would spawn an epistrophe after four iterates and an epistrophe after five iterates. The escape time plot showed however that both epistrophes were spawned after four iterates.

Now that we have completed our topological analysis of the vase's escape time plot, we will move on to examining the three bases. Specifically, we will address why the 12-basis reproduced the results of the 4-basis. We will compare our topological calculation of the vase with those of the overshoot example we used in Chapter 2. Specifically, we will examine the parallels between both sets of calculations. We will also take into consideration the topological entropies of the vase calculation

-Chapter 4-
Comparison of the Dynamical Equations Acting On the 4, 12, and 16-Bases

i.) Introduction

We have seen that the bridges theory allows us to obtain minimal sets of escape segments for comparison to the numerically computed escape time plots. Our three calculations show that one can compute more than one segment $\mathcal{U}$, obtain a set of dynamical equations for each segment, and find that the new calculation doesn't change the minimal set. We want to understand the difference in constructing symbolic dynamics from approximate neighbors and true neighbors. We approach this problem in two ways. First, we will compute the minimal sets of $\mathcal{U}_0^F$ generated by the dynamical equations derived in sec v of Chapter 2. We will see differences in the minimal sets similar to those between the minimal sets generated by the 12-neighbors and 16-neighbors in the last chapter. Secondly, we will construct flow charts that qualitatively represent the dynamical equations acting on the 4, 12, and 16-bases. We will use these flow charts to show why the 12-neighbors fail to enlarge the minimal set generated by the 4-basis. Finally, we will compare the topological entropies of the matrix representations of the three sets of dynamical equations derived from the vase's tangle. These calculations quantify our observations about the difference between approximate neighbors and true neighbors.

ii.) **Minimal Sets for the Finger Overshoot Tangle**

We consider the D = 1 tangle shown in Figure 4.1. This is the same tangle shown in Figure 2.15. The tangle shown in Figure 4.1 is a sketch of a tangle produced from the Hydrogen atom in parallel electric and magnetic fields [1]. From now on, we will refer to it as the hydrogen tangle. We derived two bases and two sets of dynamical equations for the hydrogen tangle in Chapter 2. We will now compute the minimal sets of $\mathcal{U}_0^F = \mathcal{U}[P_{-1}, P_0]$ up to the fifth iterate within the 2 and 3-bases. A comparison of these two minimal sets will help illuminate differences between minimal sets generated from the 4, 12, and 16-bases.

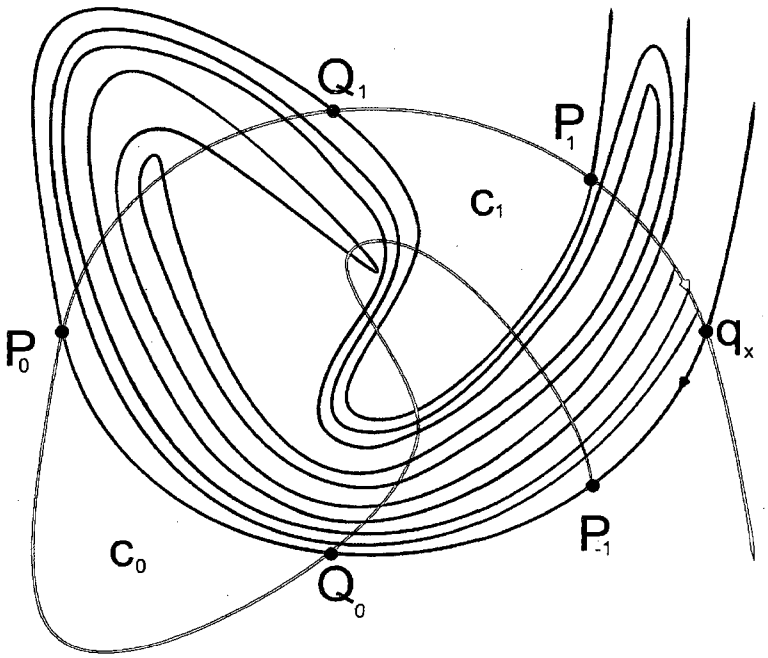

Figure 4.1: Tangle with finger in C_2 forced by C_3.

First, let us compute the minimal set in the absence of the overshoot. We can refer to Figure 2.14. In this case, there is one internal hole surrounded by the bridge class which we call c_1. The unstable boundary of E_0 represents the inert class u_0. This class is the first member of an infinite sequence of inert classes. We can immediately write down the two dynamical equations.

$$\begin{aligned} \mathcal{M}(c_1) &= c_1^{-1}u_0^{-1}c_1 \text{ where } c_1 = [\mathcal{C}_1] \\ \mathcal{M}^n(u_0^{\pm 1}) &= u_n^{\pm 1} \end{aligned} \tag{4.1}$$

We use these two equations to compute the first five iterates of $\mathcal{U}_0^F$ and construct the escape time plot up to the fifth iterate. Figure 4.2 graphically represents the escape time plot given by eq. (2).

$$\begin{aligned} &a.)[\mathcal{U}_1^F] = \mathbb{U}_0 f \\ &b.)[\mathcal{U}_2^F] = u_1 f^{-1}\mathbb{U}_0^{-1} f \\ &c.)[\mathcal{U}_3^F] = u_2 f^{-1}\mathbb{U}_0 f u_1^{-1} f^{-1}\mathbb{U}_0^{-1} f \\ &d.)[\mathcal{U}_4^F] = u_3 f^{-1}\mathbb{U}_0 f u_1 f^{-1}\mathbb{U}_0^{-1} f u_2^{-1} f^{-1}\mathbb{U}_0 f u_1^{-1} f^{-1}\mathbb{U}_0^{-1} f \\ &e.)[\mathcal{U}_5^F] = u_4 f^{-1}\mathbb{U}_0 f u_1 f^{-1}\mathbb{U}_0^{-1} f u_2 f^{-1}\mathbb{U}_0 f u_1^{-1} f^{-1}\mathbb{U}_0^{-1} f u_3^{-1} f^{-1}\mathbb{U}_0 f u_1 f^{-1}\mathbb{U}_0^{-1} f u_2^{-1} f^{-1}\mathbb{U}_0 f u_1^{-1} f^{-1}\mathbb{U}_0^{-1} f \end{aligned} \tag{4.2}$$

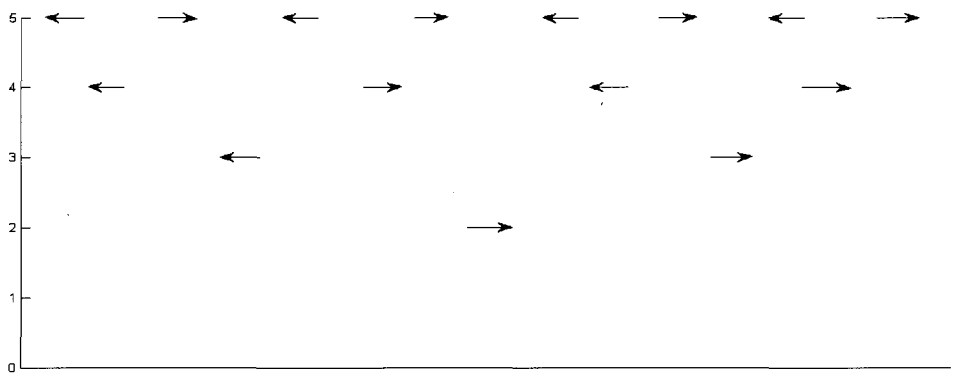

Figure 4.2: Escape time plot generated from eq. (4.2).

Since C_2 is the first capture lobe to intersect E_0, the first escape segment must appear at the second iterate. The sequence is continued by the right-pointing segments extending to the right edge of the figure. The second sequence starts at the third iterate and extends to the left edge of the figure.

We will compare this minimal set to one generated by the dynamical equations acting on the 2-basis for the hydrogen tangle. Recall that the 2-basis incorporates the overshoot. The following dynamical equations are taken from Chapter 2, section vi.

$$\begin{aligned}
&\text{a.)}\mathcal{M}(c_1) = f_1^{-1}u_0v_0u_0^{-1}f_1 \\
&\text{b.)}\mathcal{M}(a_1) = a_2^{-1}u_0^{-1}f_1 \\
&\text{c.)}\mathcal{M}(a_2) = a_2^{-1}u_0^{-1}f_2 \\
&\text{d.)}\mathcal{M}(f_k) = a_1^{-1}u_0^{-1}f_k \\
&\text{e.)}\mathcal{M}^n(u_0) = u_n \\
&\text{f.)}\mathcal{M}^n(v_0) = v_n
\end{aligned} \tag{4.3}$$

Iterating $[\mathcal{U}_1^F]_2$ we obtain the following symbolic expressions and compute the first five iterates of $\mathcal{U}_0^F$ in eq. (4.4). The minimal set is graphed in Figure 4.3 below.

$$\begin{aligned}
&\text{a.) } [\mathcal{U}_1^F]_2 = \mathbb{u}_0c_1 \\
&\text{b.) } [\mathcal{U}_2^F]_2 = u_1f_1^{-1}\mathbb{u}_0v_0\mathbb{u}_0^{-1}f_1^{-1} \\
&\text{c.) } [\mathcal{U}_3^F]_2 = u_2f_2^{-1}\mathbb{u}_0a_1u_1v_1u_1^{-1}a_1^{-1}\mathbb{u}_0^{-1}f_2 \\
&\text{d.) } [\mathcal{U}_4^F]_2 = u_3f_3^{-1}\mathbb{u}_0a_1u_1a_2^{-1}\mathbb{u}_0^{-1}f_1u_2v_2u_2^{-1}f_1^{-1}\mathbb{u}_0a_2u_1^{-1}a_1^{-1}\mathbb{u}_0^{-1}f_3 \\
&\text{e.) } [\mathcal{U}_5^F]_2 = u_4f_4^{-1}\mathbb{u}_0a_1u_1a_2^{-1}\mathbb{u}_0^{-1}f_1u_2f_2^{-1}\mathbb{u}_0a_2u_1^{-1}a_1^{-1}\mathbb{u}_0^{-1}f_2u_3v_3u_3^{-1} \\
&\qquad f_2^{-1}\mathbb{u}_0a_1u_1a_2^{-1}\mathbb{u}_0^{-1}f_2u_2^{-1}f_1^{-1}\mathbb{u}_0a_2u_1^{-1}a_1^{-1}\mathbb{u}_0^{-1}f_4
\end{aligned} \tag{4.4}$$

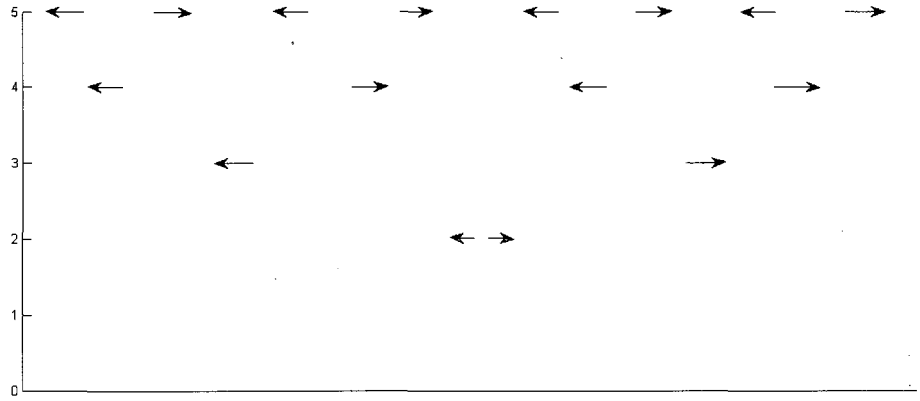

Figure 4.3: Escape time plot generated from eq. (4.4).

Comparing eq. (4.4) to eq. (4.2), we see that the minimal sets are almost identical. We see an additional segment in Figure 4.3 at the second iterate adjacent to the segment predicted by eq. (4.2). The most important aspect of Figure 4.3 is its relation to the minimal set of $\mathcal{U}_0^F$ generated by the 12-basis in the vase tangle. Once again, we see two adjacent escape segments with their tails facing each other and no escape segments predicted to lie between the tails. The Epistrophe Theorem tells us that each escape segment must spawn a sequence converging to its tail. The theorem does not tell us at what iterate this sequence begins. Here we see that the topological theory using the 2-basis (hydrogen) or the 12-basis (vase) also does not contain enough information to predict the beginnings of these sequences.

Finally, let us consider the dynamical equations acting on the 3-basis. Again, we reproduce results from Chapter 2, section v.

$$\begin{aligned} &\text{a.)}\ f = a_2 a_1 \\ &\text{b.)}\ \mathcal{M}(f) = a_1^{-1} u_0^{-1} f \\ &\text{c.)}\ \mathcal{M}(a_1) = f^{-1} u_0 a_2 u_0^{-1} f \\ &\text{d.)}\ \mathcal{M}(a_2) = f^{-1} u_0^{-1} f \end{aligned} \tag{4.5}$$

a.) $[\mathcal{U}_1^F]_3 = u_0 a_1$

b.) $[\mathcal{U}_2^F]_3 = u_1 f^{-1} \mathbb{U}_0 a_2 \mathbb{U}_0^{-1} f$

c) $[\mathcal{U}_3^F]_3 = u_2 f^{-1} \mathbb{U}_0 a_1 u_1 f^{-1} \mathbb{U}_0^{-1} f u_1^{-1} a_1^{-1} \mathbb{U}_0^{-1} f$

d.) $[\mathcal{U}_4^F]_4 = u_3 f^{-1} \mathbb{U}_0 a_1 u_1 f^{-1} \mathbb{U}_0 a_2 \mathbb{U}_0^{-1} f u_2 f^{-1} \mathbb{U}_0 a_1 u_1^{-1} a_1^{-1} \mathbb{U}_0^{-1} f u_2^{-1} f^{-1} \mathbb{U}_0 a_2^{-1} \mathbb{U}_0^{-1} f u_1^{-1} a_1^{-1} \mathbb{U}_0^{-1} f$ (4.6)

e.) $[\mathcal{U}_5^F]_5 = u_4 f^{-1} \mathbb{U}_0 a_1 u_1 f^{-1} \mathbb{U}_0 a_2 \mathbb{U}_0^{-1} f u_2 f^{-1} \mathbb{U}_0 a_1 u_1 f^{-1} \mathbb{U}_0^{-1} f u_1^{-1} a_1^{-1} \mathbb{U}_0^{-1} f u_3 f^{-1} \mathbb{U}_0 a_1 u_1 f^{-1} \mathbb{U}_0$

$a_2 \mathbb{U}_0^{-1} f u_2^{-1} f^{-1} \mathbb{U}_0 a_2^{-1} \mathbb{U}_0^{-1} f u_1^{-1} a_1^{-1} \mathbb{U}_0^{-1} f u_3^{-1} f^{-1} \mathbb{U}_0 a_1 u_1 f^{-1} \mathbb{U}_0 f u_1^{-1} a_1^{-1} \mathbb{U}_0^{-1} f u_2^{-1} f^{-1} \mathbb{U}_0$

$a_2^{-1} \mathbb{U}_0^{-1} f u_1^{-1} a_1^{-1} \mathbb{U}_0^{-1} f$

We see in $[\mathcal{U}_2^F]_3$ that two escape segments are predicted. However, upon examining their neighbors in $[\mathcal{U}_5^F]_3$ (the neighbors of the factors u_3 and u_3^{-1}), we see that each has spawned two epistrophes. Furthermore, if we count the total number of escape segments lying between u_3 and u_3^{-1}, we see that nine escape segments are predicted to appear by the fifth iterate.

Let us consider our results. We saw in Figure 4.3 that the 2-basis predicted the correct escape segments at the second iterate. The Epistrophe Theorem tells us that each of these escape segments must spawn two epistrophes. However, our calculations predicted that each segment spawns one epistrophe. Furthermore, the minimal set was almost identical to that produced by a tangle without the overshoot. We conclude that constructing a basis using the 2-neighbors is (almost) identical to removing the overshoot. However, we found that the 3-basis predicts that each of the earliest escape segments must spawn two epistrophes. This is due to the fact that the 2-neighbors are not true neighbors whereas the 3-neighbors are true neighbors (see Figure 2.19).

In Figure 4.1 we see that C_2 is forced to wind under C_1 and thus includes two bridges that span most of the width of the complex. Within the 2-basis, these two bridges represent the factors of $f_1^{\pm 1}$. If we examine Figure 2.17, which shows the holes resulting from the 2-basis, we see that square-1 prevents a representative of f_1 from homotoping into the unstable boundary of C_1. In fact, eq. (4.3) shows that none of the bridge classes produce a factor of c_1 under the action of the map. This observation tells us that unless c_1 appears in the initial string of symbols, then c_1 cannot appear in any symbolic expression. Furthermore, the class c_1 is the only symbol whose image produces two classes represented by escape segments. This observation suggests that if c_1 appears in the initial symbol string, then the minimal set will contain two escape segments whose tails face each other and that each spawn a single epistrophe. We also saw that excluding one escape segment, the minimal set for $\mathcal{U}_0^F$ was identical to the minimal set in the absence of the overshoot. Given these observations, we conclude that the 2-basis contains essentially the same information as the case of no overshoot.

Given the conclusions concerning the 2-basis from the hydrogen tangle, we now ask if the 3-basis contains more information than the 2-basis. In other words, is eq. (4.5) a refinement of eq. (4.3)? First, we believe that the 3-neighbors are indeed true neighbors whereas introducing the 3-neighbors revealed that the 2-neighbors were not true neighbors. Secondly, our strongest evidence concerns the bridge class a_1 (see Figure 2.20). Eq. (4.6c), eq. (4.6d), and eq. (4.6e) each contain multiple factors of a_1 and a_1^{-1}. This bridge class represents the unstable boundary of C_1. Since there is not a hole anchored to C_1 and lying outside the lobe, curves can be distorted into $\mathcal{C}_1$. Therefore, the

dynamical equations acting on the 3-basis allow for a_1 to recursively appear, thus they allow for the two escape segments in $\mathcal{M}(a_1)$ (eq. (2.17)) to recursively appear. In conclusion, a minimal set generated by eq. (4.5) will contain more escape segments than one generated using either eq. (4.1) or eq. (4.3).

The previous discussion on the minimal sets for $\mathcal{U}_0^F$ generated by the 2 and 3-bases from the hydrogen tangle has a single purpose. The conclusions drawn are similar to those drawn regarding the 12 and 16-bases from the vase tangle. Furthermore, the hydrogen tangle allows for a simpler presentation than plotting in one figure 12 or 16 capture lobes of the vase tangle. In Chapter 3, we saw that the minimal sets for $[\mathcal{U}_1^F]$ derived from the 4 and 12-bases were quite similar. The only difference was that $[\mathcal{U}_{12}^F]_{12}$ contained one additional escape segment compared to $[\mathcal{U}_{12}^F]_4$. This additional segment corresponded to the finger in C_{12} (refer to eq. (3.18), eq. (3.19), and Figure 3.12). Examining the structure near the finger (the class v_0) showed the tail of v_0 facing the tail of its nearest neighbor. The region between the tails of these two escape segments did not contain any epistrophes. Furthermore, the 12-basis incorporated two pairs of pseudo-neighbors that were replaced with a pair of true neighbors in the 16-basis. The additional finger that appeared in $\mathcal{C}_{12}$ spawned epistrophes as we had expected but one sequence was predicted to start at five iterates where we expected (by the Epistrophe Start Rule) for both sequences to start at four iterates. We will study this discrepancy by constructing flow charts directly from the dynamical equations. In constructing the charts, we will assign each symbol a positive orientation for convenience. Also, we will not include a directed edge if a symbol maps to itself. Before we proceed, we stress that

we are not aiming at mathematical rigor, but a qualitative understanding of how new structure may recursively appear.

iii.) Flow Charts Representing the Dynamical Equations

First we present a simple example. We consider a tangle with minimum delay time D. The intersection of C_{D+1} with E_0 produces a pair of true neighbors with transition number D+1. This is the minimal amount of information one can put into the theory in order to obtain nontrivial dynamics. One can easily derive the dynamical equations in eq. (4.7) and the flow chart (Figure 4.4) without resorting to a figure.

$$\begin{aligned} &\mathcal{M}(c_i) = c_{i+1} \text{ for } 0 < i < D\text{-}1 \\ &\mathcal{M}(c_D) = f^{-1}u_0^{-1}f \text{ where } f = c_1c_2\cdots c_D \\ &\mathcal{M}(f) = c_1^{-1}u_0^{-1}f \end{aligned} \tag{4.7}$$

Figure 4.4 immediately tells us that by starting with any non-inert symbol in the D-basis, one will return to it D+1 iterates later. Completing this loop once will generate two escape segments. Our search for recursive structure in a flow chart is then a search for similar loops. Let us now look for such loops in the flow chart representing the equations acting on the 16-basis.

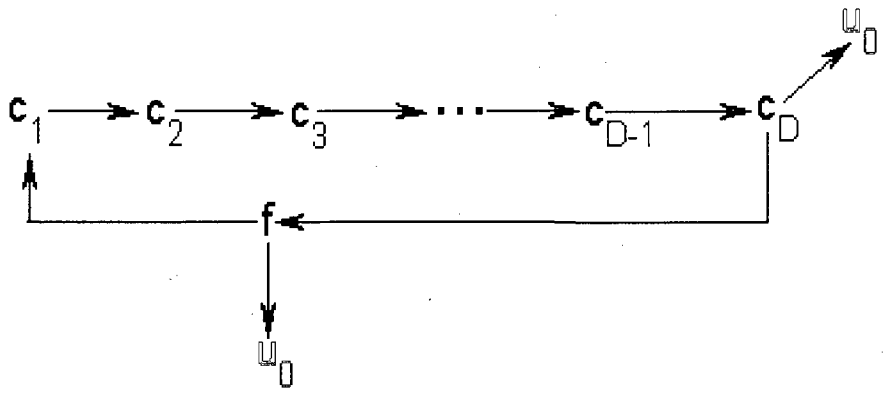

Figure 4.4: Flow chart for true (D+1)-neighbors.

Figure 4.5 shows the flow chart for the 16-basis. The reader can verify that by starting at any non-inert symbol, the mapping will produce a path leading to every node in the graph, including the starting node. We start with a_1 (represented by $\mathcal{C}_1$) in the upper right hand corner. Starting at a_1 leads one around the right-hand circuit counter-clockwise, hitting each symbol in the loop with the net effect of spawning 4 factors of c_4. Mapping each factor of c_4 forward produces a_1 thus restarting the cycle. Mapping a_4 produces two directed edges to two non-inert classes. One leads to c_4 which restarts the cycle again. The other directed edge leads to c_1. Mapping that one forward leads from c_1 to c_2 to c_3. Iterating c_3 once again produces a factor of c_4 leading to the cycle restarting one iterate later. Most importantly, c_3 spawns all of the "d" and "f" bridge classes and the class v_0. The escape class t_0, which appears in the 16-basis, arises by mapping forward any "f" node.

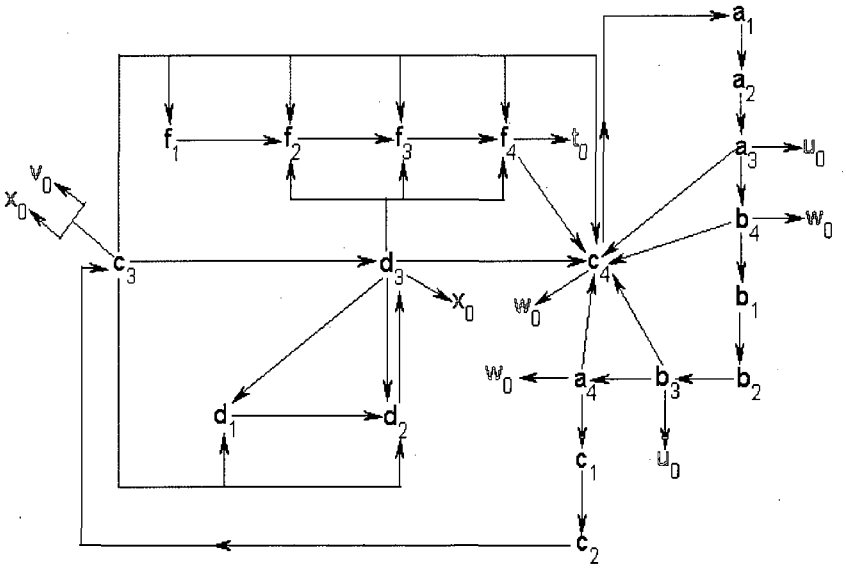

Figure 4.5: Flow chart for the 16-basis. Escape segments are colored red. Blue directed edges lead to the sequence $\mathcal{M}(c_3)$ and green directed edges lead to the sequence $\mathcal{M}(d_3)$.

Mapping d_3 produces all the "d" classes and all the "f" classes except for f_1. Thus, the cycle starting at c_4 starts several times in succession. For our comparison of the 12 and 16-bases, we must consider the class v_0. Within the 12-basis, this class is represented by the finger in $\mathcal{C}_{12}$ (see Figures 3.3 and 3.4). Within the 16-basis, v_0 is represented by both fingers in $\mathcal{C}_{12}$ and $\mathcal{C}_{16}$ (see Figures 3.13 and 3.14). This escape class appears in the image of c_3 which will repetitively appear starting with any non-inert symbol. Thus, the symbol v_0, and the structure encoded in it, will also repetitively appear. We now ask does v_0 repetitively appear by starting from any symbol within the 12-basis.

Let us now consider the flow chart representing the dynamical equations acting on the 12-basis shown in Figure 4.6. This flow chart will suggest to us what initial conditions eventually lead to the appearance of the class v_0. Starting on the right with a_1 and following the arrows downward to c_3 then moving left, avoiding arrows leading to d_4, we come to f_3. Iterating f_3 produces a factor of v_0. We see that this is the only path containing a_1. Thus, there are no closed loops containing the symbol a_1 and therefore, the symbol v_0 can appear only once. To find the reason that v_0 cannot repeatedly appear within the 12-basis, we must consider the holes that generate the 12-basis. Specifically, we must consider Figure 3.5. In the punctured plane, curves cannot homotope into the three boundary curves $\mathcal{C}_1$, $\mathcal{C}_2$, and $\mathcal{C}_3$ because of the holes that lie just outside each of these lobes. If we consider a curve $\mathcal{L}_0$ that is homotopic to any one of these curves and iterate this curve 13 times, the 13^{th} image of $\mathcal{L}_0$ cannot contain any of the factors a_1, a_2, or a_3. In fact, no image of $\mathcal{L}_0$ will contain any of these three factors. This fact is represented in the flow chart by the absence of a directed edge leading to a_1. In other

words, the three flow charts demonstrate that one must find a closed circuit within this representation of the dynamical equations such that escape classes will periodically appear.

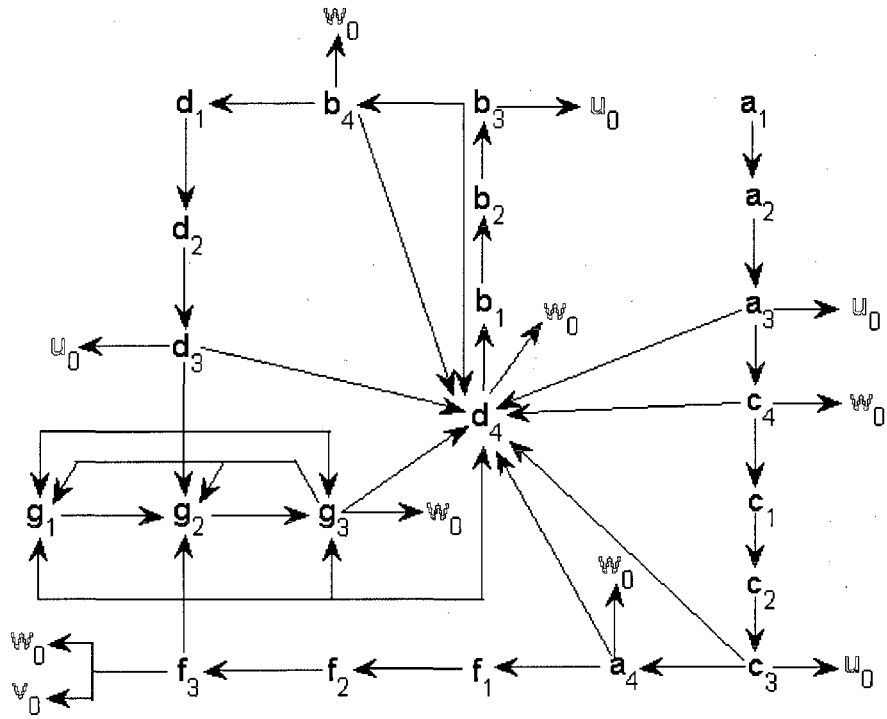

Figure 4.6: Flow chart for the 12-basis. The escape classes are in red. Blue direct edges lead to the symbolic expression $\mathcal{M}(g_3)$. Green directed edges lead to the symbolic expression $\mathcal{M}(f_3)$.

iv.) Topological Entropies of the 4, 12, and 16-bases from the Vase Tangle.

Finally, we compute the topological entropies of the 4, 12, and 16-bases as a means of comparison. The topological entropies will quantify the conclusions we've drawn from examining the minimal sets and the flow charts. We remind the reader that to compute the topological entropy we construct a matrix representing the concise

dynamical equations. The topological entropy is the natural logarithm of the matrix's largest eigenvalue. We will present each of the three matrix representations and their topological entropies.

Eq. (3.1) contains the dynamical equations acting on the 4-basis of the vase tangle shown in Figure 3.1. This basis constitutes the simplest possible behavior for a D = 3 tangle. The equations acting on the 4-basis are already in concise form. Therefore, the matrix representation is

$$\begin{array}{c} \\ c_1 \\ c_2 \\ c_3 \\ f \\ u^* \end{array} \begin{array}{c} \begin{array}{ccccc} c_1 & c_2 & c_3 & f & u^* \end{array} \\ \begin{pmatrix} 0 & 0 & 0 & 1 & 0 \\ 1 & 0 & 0 & 0 & 0 \\ 0 & 1 & 0 & 0 & 0 \\ 0 & 0 & 2 & 1 & 0 \\ 0 & 0 & 1 & 1 & 1 \end{pmatrix} \end{array} \tag{4.8}$$

The topological entropy is ln(1.5437). Recall that the topological entropy for a D = 1 tangle is ln(2). The difference between these two results is due to the difference in minimum delay times. As the minimum delay time increases, curves are stretched and folded at a slower rate due to the larger number of iterates required to cycle through the complex.

Now let us compute the topological entropy for the 12-basis. However, we must first put the dynamical equations in concise form. Eq. (3.4) contains the dynamical equations acting on the 12-basis. The following equations are not in concise form: (3.4d), (3.4h), (3.4l), (3.4p), (3.4w), and (3.4v). The first four equations in this list each end in d_4x_4, which is a sequence of two internal bridge classes. Eq. (3.4v) contains the sequence $g^{-1}x_0$, which is also a sequence of two internal bridge classes. Since d_4x_4 and g^{-}

$^1x_0$ both represent internal bridge classes, each can be substituted with a single bridge class. We first define the following two bridge classes.

$$\begin{aligned} &\text{a.)}k_i = d_4 x_4 x_5 \cdots x_{i-1} x_i \\ &\text{b.)}h = x_0^{-1} g \end{aligned} \tag{4.9}$$

Substituting eq. (4.9) into the non-concise expressions of eq. (3.4) yields concise expressions. However, we have introduced new bridge classes (note that they are *not* in the bridge basis) so their dynamical equations must be found. The dynamical equation for k_i comes from the group homomorphism property and eq. (3.4p).

$$\begin{aligned} &\mathcal{M}(k_i) = \mathcal{M}(d_4)\mathcal{M}(x_4)\mathcal{M}(x_5)\cdots\mathcal{M}(x_{i-1})\mathcal{M}(x_i) \\ &= b_1^{-1} w_0^{-1} k_4 x_5 x_6 \cdots x_i x_{i+1} = b_1^{-1} w_0^{-1} k_{i+1} \end{aligned} \tag{4.10}$$

The classes b_1 and k_{i+1} are both internal and w_0 is external and thus $\mathcal{M}(k_{i+1})$ is concise.

Using eq. (3.4w) we can obtain the dynamical equation of the bridge class h.

$$\mathcal{M}(h) = \mathcal{M}(x_0^{-1})\mathcal{M}(g) = x_1^{-1} g_1^{-1} w_0^{-1} k_4 \tag{4.11}$$

The sequence $x_1^{-1} g_1^{-1}$ is an internal bridge class. Now let us define the bridge class $h_i = g_i x_i$ for i = 1, 2, and 3. Each of these three classes is an internal bridge class. The definition of h_1 places $\mathcal{M}(h)$ in concise form. Using the facts that x_i represents an inert class and $\mathcal{M}(g_1) = g_2$ and $\mathcal{M}(g_2) = g_3$

$$\begin{aligned} &\text{a.)}\mathcal{M}(h_1) = h_2 \\ &\text{b.)}\mathcal{M}(h_2) = h_3 \end{aligned} \tag{4.12}$$

We use eq. (3.4v) to compute $\mathcal{M}(h_3)$.

$$\mathcal{M}(h_3) = \mathcal{M}(g_3)\mathcal{M}(x_3) = h^{-1} w_0^{-1} d_4 x_4 = h^{-1} w_0^{-1} k_4 \tag{4.13}$$

Since h and k_4 are internal and w_0 is external, $\mathcal{M}(h_3)$ is concise. In summary, introducing the bridge class h forced us to introduce h, k_i, h_1, h_2, and h_3 into the dynamics. The concise dynamical equations acting on the 12-basis are

$$
\begin{array}{lll}
\text{a.)}\mathcal{M}(a_1)=a_2 & \text{e.)}\mathcal{M}(b_1)=b_2 & \text{i.)}\mathcal{M}(c_1)=c_2 \\
\text{b.)}\mathcal{M}(a_2)=a_3 & \text{f.)}\mathcal{M}(b_2)=b_3 & \text{j.)}\mathcal{M}(c_2)=c_3 \\
\text{c.)}\mathcal{M}(a_3)=c_4^{-1}u_0^{-1}d_4 & \text{g.)}\mathcal{M}(b_3)=b_4^{-1}u_0^{-1}d_4 & \text{k.)}\mathcal{M}(c_3)=a_4^{-1}u_0^{-1}d_4 \\
\text{d.)}\mathcal{M}(a_4)=f_1^{-1}w_0^{-1}k_4 & \text{h.)}\mathcal{M}(b_4)=d_1^{-1}w_0^{-1}k_4 & \text{l.)}\mathcal{M}(c_4)=c_1^{-1}w_0^{-1}k_4
\end{array}
$$

$$
\begin{array}{lll}
\text{m.)}\mathcal{M}(d_1)=d_2 & \text{q.)}\mathcal{M}(f_1)=f_2 & \text{t.)}\mathcal{M}(g_1)=g_2 \\
\text{n.)}\mathcal{M}(d_2)=d_3 & \text{r.)}\mathcal{M}(f_2)=f_3 & \text{u.)}\mathcal{M}(g_2)=g_3 \\
\text{o.)}\mathcal{M}(d_3)=g^{-1}u_0^{-1}d_4 & \text{s.)}\mathcal{M}(f_3)=g^{-1}v_0x_0w_0^{-1}d_4 & \text{v.)}\mathcal{M}(g_3)=h^{-1}w_0^{-1}d_4 \\
\text{p.)}\mathcal{M}(d_4)=b_1^{-1}w_0^{-1}k_4 & &
\end{array}
$$

$$
\begin{array}{lll}
\text{Let } h_i=g_ix_i,\ i=1,2,3 & \text{Let } g=x_0g_1x_1g_2x_2g_3x_3 & k_i=d_4x_4x_5\cdots x_{i-1}x_i \\
\text{x.)}\mathcal{M}(h_1)=h_2 & \text{aa.)}\mathcal{M}(g)=g_1^{-1}w_0^{-1}k_4 & \text{cc.)}\mathcal{M}(k_i)=b_1^{-1}w_0^{-1}k_{i+1} \\
\text{y.)}\mathcal{M}(h_2)=h_3 & \text{Let } h=g_1x_1g_2x_2g_3x_3 & \\
\text{z.)}\mathcal{M}(h_3)=h^{-1}w_0^{-1}k_4 & \text{bb.)}\mathcal{M}(h)=h_1^{-1}w_0^{-1}k_4 &
\end{array}
$$

$$
\begin{array}{l}
\text{dd.)}\mathcal{M}^n(v_0)=v_n \\
\text{ee.)}\mathcal{M}^n(u_0)=u_n \\
\text{let } w_0=v_0u_0 \\
\text{ff.)}\mathcal{M}^n(w_0)=w_n \\
\text{gg.)}\mathcal{M}^n(x_0)=x_n
\end{array}
\qquad (4.14)
$$

We will not show the matrix representing these concise dynamics as it is too large (32 by 32). The topological entropy of the matrix representation is ln(1.5437) which is the same as the 4-basis. Based on this calculation, we conclude that for the vase's tangle, the differences between the 4 and 12-bases are "almost negligible". We use this phrase because the minimal sets of $[\mathcal{U}_0^F]_4$ and $[\mathcal{U}_0^F]_{12}$ differ by a single escape segment up to the 16^{th} iterate (see Table 3.1).

Finally, we need to place into concise form the dynamical equations acting on the 16-basis. Two of the equations need to be corrected: (3.21m) and (3.21n). We first

define $g = f_1 d_1 f_2 d_2 f_3 d_3 f_4$. This definition automatically places eq. (3.21m) into concise form.

$$\mathcal{M}(c_3) = g^{-1} v_0 f_1 x_0^{-1} c_4 \tag{4.15}$$

The classes g, f_1, and c_4 are all internal while v_0 and x_0 are both escape classes thus they are external. Since we have introduced the bridge class g, we must calculate its dynamical equation.

$$\begin{aligned} \mathcal{M}(g) &= \mathcal{M}(f_1)\mathcal{M}(d_1)\mathcal{M}(f_2)\mathcal{M}(d_2)\mathcal{M}(f_3)\mathcal{M}(d_3)\mathcal{M}(f_4) \\ \mathcal{M}(g) &= f_2 d_2 f_3 d_3 f_4 f_4^{-1} d_3^{-1} f_3^{-1} d_2^{-1} f_2^{-1} d_1^{-1} x_0^{-1} c_4 c_4^{-1} t_0^{-1} c_4 = d_1^{-1} w_0^{-1} c_4 \end{aligned} \tag{4.16}$$

The classes d_1 and c_4 are internal and w_0 is external so $\mathcal{M}(g)$ is concise. Eq. (3.21n) presents a bit more of a challenge. We can use the definition of g and rewrite eq. (3.21n).

$$\mathcal{M}(d_3) = g^{-1} f_1^{-1} x_0^{-1} c_4 \tag{4.17}$$

This equation is not in concise form due to g and f_1 both being internal classes. Therefore, we must define a new bridge class, $h = f_1^{-1} g$, that puts eq. (4.17) into concise form. Again, we must calculate the dynamical equation for h. Using eq. (4.16) and the homomorphism property we find

$$\mathcal{M}(h) = \mathcal{M}(f_1^{-1})\mathcal{M}(g) = f_2^{-1} d_1^{-1} w_0^{-1} c_4 \tag{4.18}$$

Again, we encounter the problem of an equation that is not concise. By defining the class $h_1 = d_1 f_2$, $\mathcal{M}(h)$ is placed into concise form. However, we must obtain the dynamical equation for h_1. First, let us define two additional classes: $h_2 = d_2 f_3$ and $h_3 = d_3 f_4$.

$$\text{a.)}\mathcal{M}(h_1) = \mathcal{M}(d_1)\mathcal{M}(f_2) = d_2 f_3 = h_2$$
$$\text{b.)}\mathcal{M}(h_2) = \mathcal{M}(d_2)\mathcal{M}(f_3) = d_3 f_4 = h_3 \qquad (4.19)$$

Finally, we must compute the dynamical equation for h_3.

$$\mathcal{M}(h_3) = \mathcal{M}(d_3)\mathcal{M}(f_4) = f_4^{-1}d_3^{-1}f_3^{-1}d_2^{-1}f_2^{-1}d_1^{-1}x_0^{-1}c_4c_4^{-1}t_0^{-1}c_4 = h^{-1}w_0^{-1}c_4 \qquad (4.20)$$

The bridge classes h and c_4 are internal and w_0 is external. Therefore $\mathcal{M}(h_3)$ is concise and we are finished defining new bridge classes. The concise dynamical equations are

$$\begin{array}{llll}
\text{a.)}\mathcal{M}(a_1) = a_2 & \text{f.)}\mathcal{M}(a_2) = a_3 & \text{k.)}\mathcal{M}(a_3) = b_4^{-1}u_0^{-1}c_4 & \text{p.)}\mathcal{M}(a_4) = c_1^{-1}w_0^{-1}c_4 \\
\text{b.)}\mathcal{M}(b_1) = b_2 & \text{g.)}\mathcal{M}(b_2) = b_3 & \text{l.)}\mathcal{M}(b_3) = a_4^{-1}u_0^{-1}c_4 & \text{q.)}\mathcal{M}(b_4) = b_1^{-1}w_0^{-1}c_4 \\
\text{c.)}\mathcal{M}(c_1) = c_2 & \text{h.)}\mathcal{M}(c_2) = c_3 & \text{m.)}\mathcal{M}(c_3) = g^{-1}v_0f_1x_0^{-1}c_4 & \text{r.)}\mathcal{M}(c_4) = a_1^{-1}w_0^{-1}c \\
\text{d.)}\mathcal{M}(d_1) = d_2 & \text{i.)}\mathcal{M}(d_2) = d_3 & \text{n.)}\mathcal{M}(d_3) = h^{-1}x_0^{-1}c_4 & \text{s.)}\mathcal{M}(f_4) = c_4^{-1}t_0^{-1}c_4 \\
\text{e.)}\mathcal{M}(f_1) = f_2 & \text{j.)}\mathcal{M}(f_2) = f_3 & \text{o.)}\mathcal{M}(f_3) = f_4 &
\end{array}$$

$$\begin{array}{ll}
\text{Let } g = f_1d_1f_2d_2f_3d_3f_4 & h_i = d_if_{i+1}, i = 1,2,3 \\
\mathcal{M}(g) = d_1^{-1}w_0^{-1}c_4 & M(h_1) = h_2 \\
\text{Let } h = d_1f_2d_2f_3d_3f_4 & M(h_2) = h_3 \\
\mathcal{M}(h) = h_1^{-1}w_0^{-1}c_4 & M(h_3) = h^{-1}w_0^{-1}c_4
\end{array} \qquad (4.21)$$

$$\begin{array}{lll}
\mathcal{M}^n(t_0) = t^n & \text{let } x_0 = u_0v_0 & \mathcal{M}^n(x_0) = x^n \\
\mathcal{M}^n(u_0) = u^n & y_0 = t_0u_0 & \mathcal{M}^n(y_0) = y^n \\
\mathcal{M}^n(v_0) = v^n & w_0 = t_0u_0v_0 & \mathcal{M}^n(w_0) = w^n
\end{array}$$

Again, we will not show the matrix representation as it is far too large. The topological entropy = ln (1.5449), which is slightly larger than the entropy for the 4-basis. Thus, the 16-basis incorporates additional topological information of which the 12-basis was ignorant.

v.) Conclusions

Our calculations of the topological entropy for the vase's tangle mirror those of the tangle we examined in Chapter 2. We obtained topological entropies using the minimal amount of information one can put into the theory. We then performed the analysis using pseduoneighbors of finite index and found that the topological entropies

did not increase. However, when we performed the analysis with what we believed to be true neighbors, the topological entropies increased. Based on these results, we conclude that an increase in the topological entropy of a concise matrix representation is an indicator that one has increased the amount of topological information contained within the dynamical equations.

This last chapter concludes our topological analysis of the vase's underlying homoclinic tangle. We will now move on to our studies of the vase itself. In the next chapter, we will cover the basic information about the vase, ray propagation, and how we numerically compute the tangle and epistrophes. We have elected to present this material first as we will examine how the epistrophes manifest within an approximation to the quantum mechanical wave function in Chapter 5.

-References-

[1] K. A. Mitchell and J. B. Delos, Physica D **221**, 170 (2006).

-Chapter 5-
The Vase: Part II

i.) Introduction

The last three chapters were devoted topological analyses of the vase's homoclinic tangle. The topological analysis reveals the origin of the recursive structure organizing an escape time plot. Now we conclude the analysis of the vase-shaped cavity with experimental and numerical results. Several sample trajectories were shown in Chapter 1 that illustrated the different kinds of trajectories present in the vase, but there, we examined only one chaotic trajectory. In this chapter, we will first consider several escape segments and their associated trajectories, including many chaotic trajectories. Then we will consider the results of an experiment in which ultrasound pulses escaped a macroscopic vase and compare these results to a classical simulation. Finally, we will see the results of a numerically computed approximation to Schrodinger's Equation for waves escaping a quantum mechanical vase.

ii.) Chaotic trajectories and the Epistrophes

First we examine the chaotic trajectories and their relation to the epistrophes. Figure 5.1 shows the continuous and discrete escape time plots side-by-side. We will consider a few of the labeled escape segments in Figure 1 and look for common characteristics amongst trajectories from different escape segments within a single epistrophe.

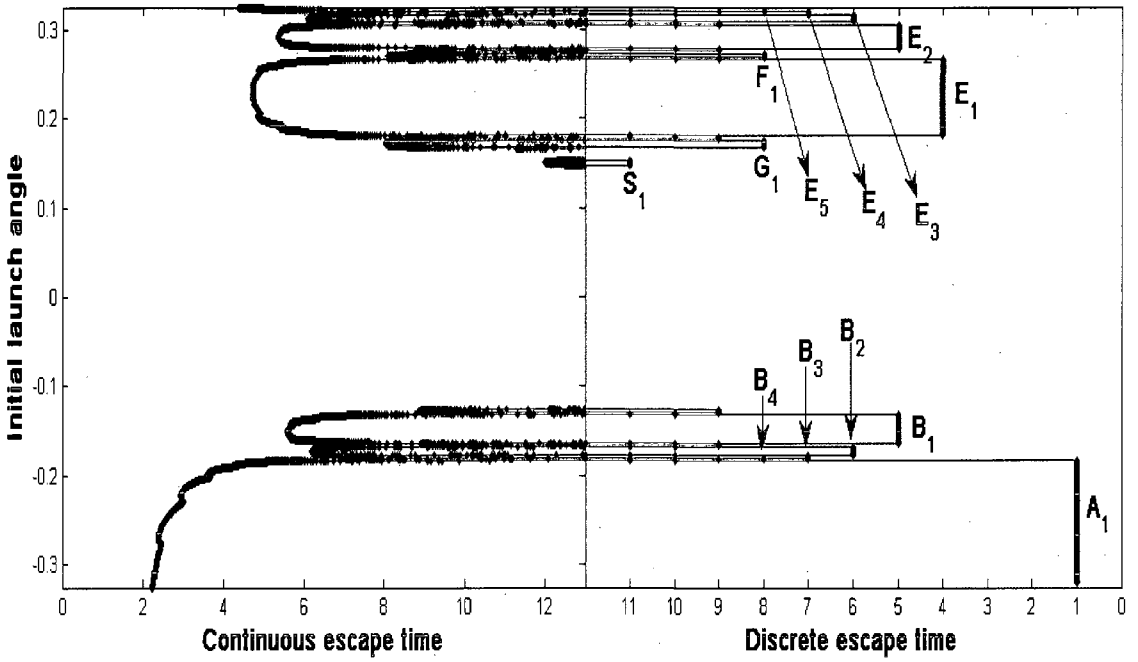

Figure 5.1: Continuous (left) and discrete (right) escape time plots for burst at (0.3, 0.4067).

The earliest escape segment is labeled A_1 and it represents the intersection of $\mathcal{L}_0$ with E_1. Figure 5.2 shows a trajectory selected from escape segment A_1. This ray escapes after two reflections. A_1 is considered an isolated segment and since it escapes immediately, it is of little interest.

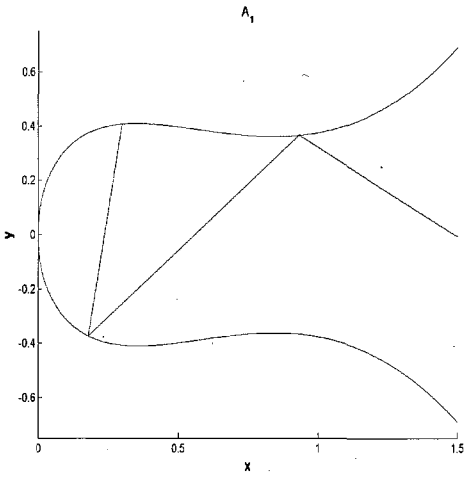

Figure 5.2: Ray with initial launch angle from escape segment A_1

Let us now consider the epistrophe labeled "B". Trajectories corresponding to segments in the B-epistrophe are shown in Figure 5.3. This sequence converges to the right side of segment A_1. The corresponding trajectories possess more complicated structure than those associated with escape segment A_1. Each trajectory approaches the UPO once, turns back into the bowl, and then has a final reflection deep in the bowl before escaping. As the number of iterates to escape the complex increases, the number of oscillations within vase's neck increases before being repelled back into the vase's bowl. Counting the number of reflections of each trajectory, we see that the number of reflections to escape the vase is the same as the number of iterates to escape the complex.

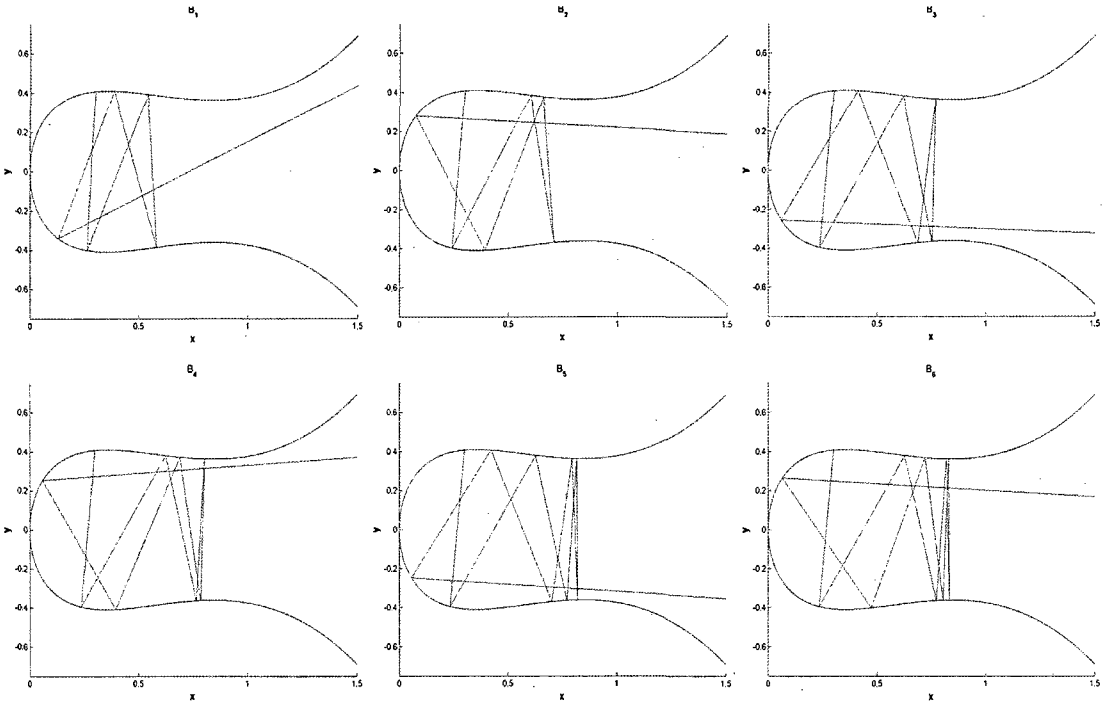

Figure 5.3: Rays with launch angles in the first six segments of the B-epistrophe.

Let us consider epistrophe E and a trajectory chosen from each of the first six segments of the sequence. The trajectories are shown in Figure 5.4. The pattern is comparable to that of the B-epistrophe. The trajectories approach the UPO with the number of reflections increasing as the number of iterates to escape the complex increases. After being repelled by the UPO once, each trajectory experiences its last reflection deep within the vase's bowl and then escapes the vase.

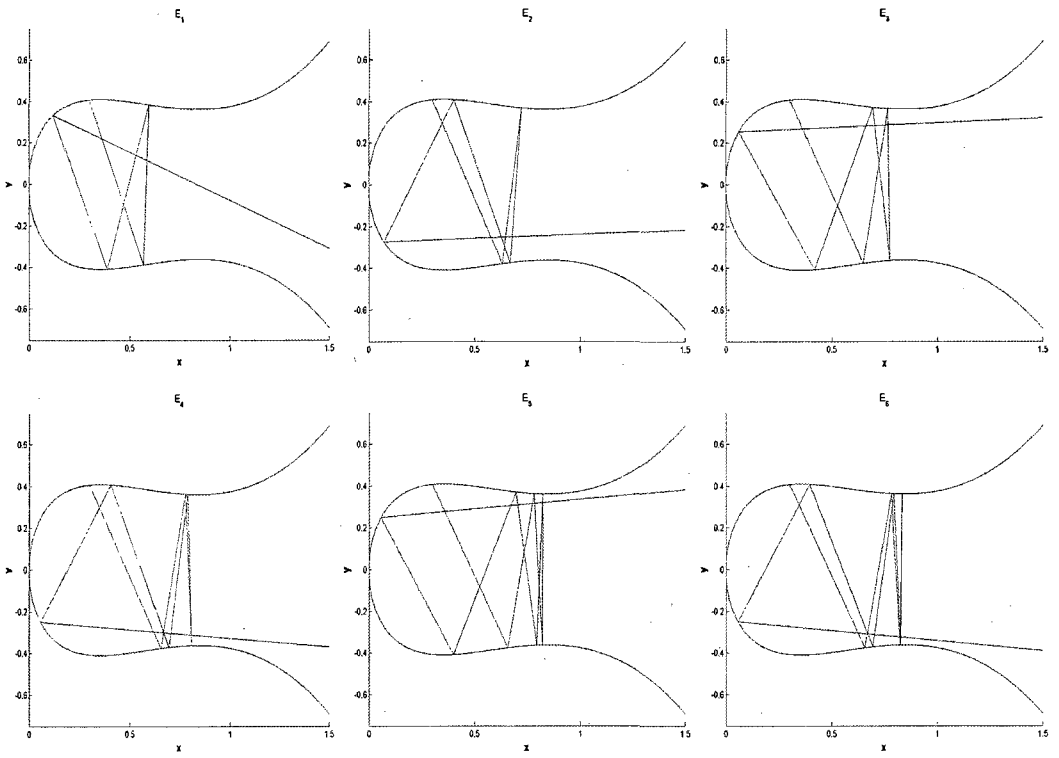

Figure 5.4: Rays with launch angles in the first six segments of the E-epistrophe.

Figure 5.5 shows four trajectories, one from each of the first four segments of the F-sequence. This sequence appears at eight iterates and demonstrates more complicated behavior than trajectories from the previous epistrophes. These trajectories first approach the UPO in the neck, return into the bowl, then approach the neck a second time, and are repelled again before a final reflection in the bowl. However, they are directed towards the neck and are repelled again before landing in the bowl and escaping. As the number of iterates to escape the complex increases, so do the number of bounces during the second approach to the vase's neck.

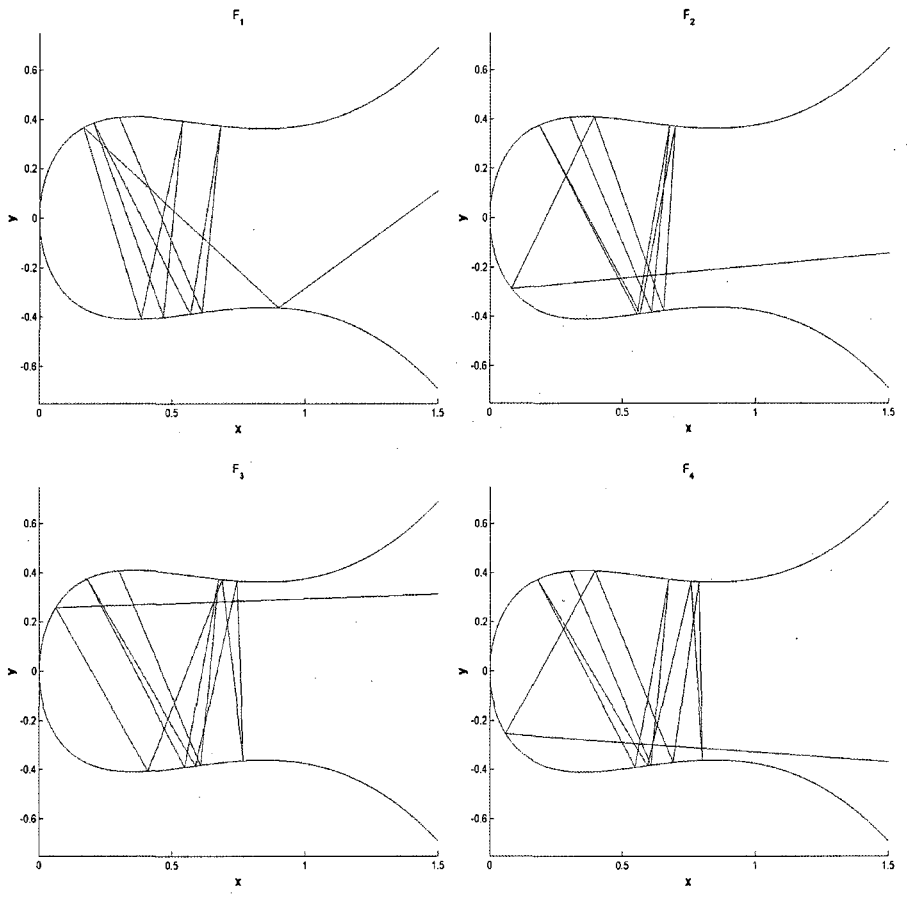

Figure 5.5: Rays with launch angles in the first six segments of the F-epistrophe.

Finally, Figure 5.6 shows trajectories from the first four segments of the G-epistrophe. We see a similar structure compared to the trajectories from the F-epistrophe. However, there is a difference. If we imagine locating the center of the convex region, then we see that the trajectories here loop around the center twice whereas they did so only once in the F-epistrophe.

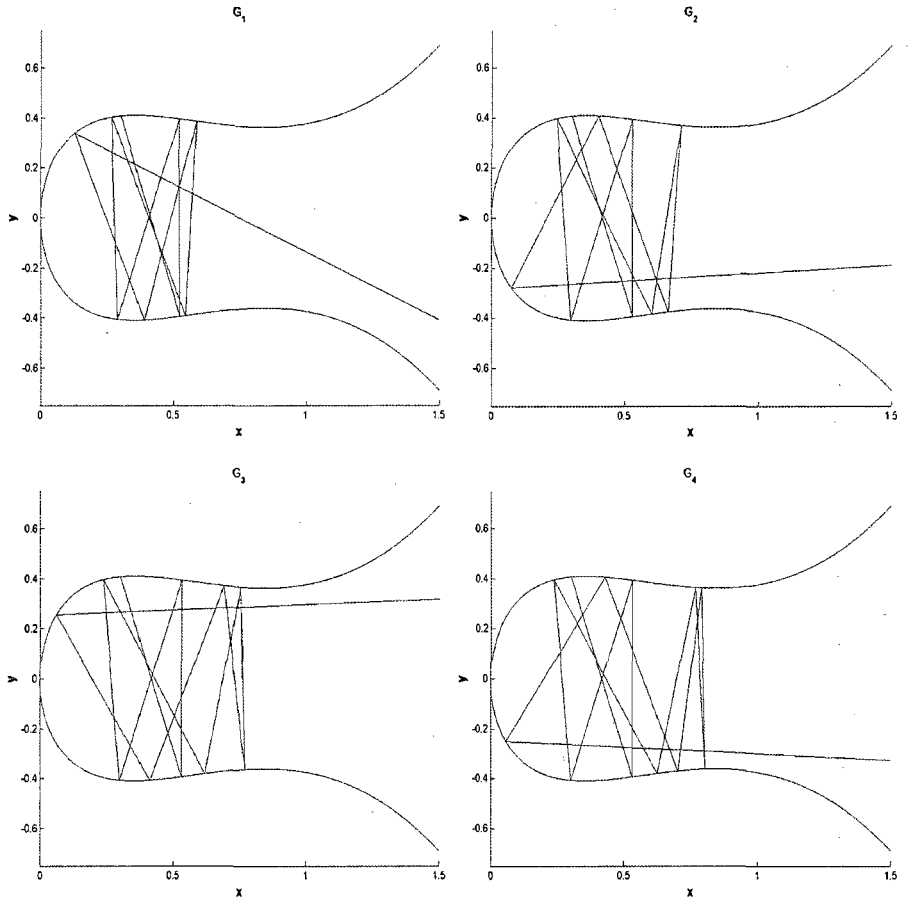

Figure 5.6: Rays with launch angles in the first six segments of the G-epistrophe.

iii.) A Macroscopic Realization of the Vase

Dr. Matthew Len Keeler of the University of Minnesota, Morris, and his undergraduate student Joshua Geifer constructed the vase shown in Figure 5.7. The curved walls of the vase are made of Teflon and are about 4.25 mm thick. These two boundary walls are sandwiched between two large aluminum plates. The vase drawn on the aluminum plates shows the location of the Teflon boundaries. On the lower right is a fixed ultrasound transducer which produces a source of sound waves. The initial pulse's temporal profile is like a Gaussian modulated sine wave. The cylindrical object on the

left side of the wall is a microphone which acts as a detector. First the microphone position is fixed, a burst of ultrasound is released into the vase, and the escaping signal is recorded. Then, the microphone is vertically translated and the escaping signal is recorded again. Thus, the experiment gives the escaping signal as a function of time and vertical position. We will compare this signal to a classical simulation.

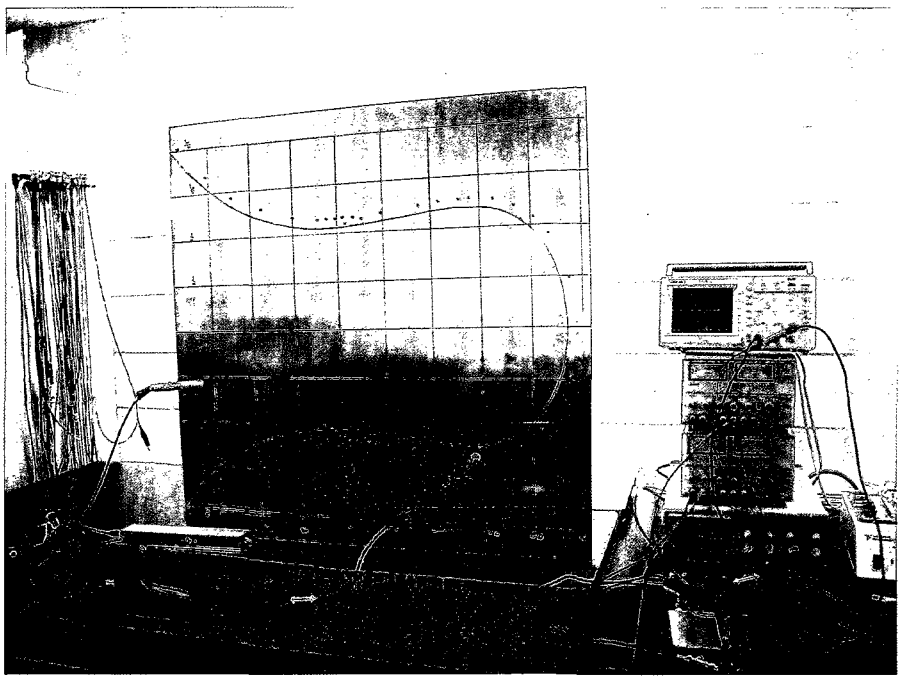

Figure 5.7: Setup of the ultrasound experiment.

a.) Classical Simulation

We launch an ensemble of trajectories from the point (0.3, 0.4067) and end ray propagation at x = 1.5. A plot of the escape time versus the detector position is shown in Figure 5.8. The signal consists of a complicated set of sawtooth oscillations.

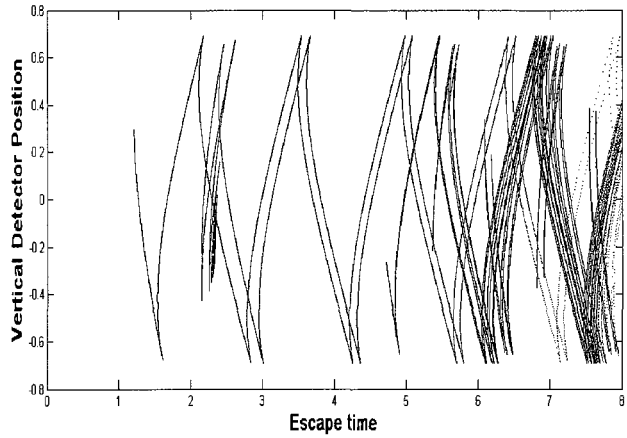

Figure 5.8: Detector position versus the escape time.

Since a family of rays is launched from a small source, we can parameterize the initial velocities by the polar angle measured with respect to a Cartesian coordinate system translated to the burst point. The first five rows of Table 5.1 show the initial conditions for the different sets of trajectories that contribute to the current in Figure 5.8. The remaining rows give the initial conditions for the two grazing rays and the two rays resulting from the intersection of $\mathcal{L}_0$ with the boundaries of the complex.

Trajectory	Initial polar angle (rad)	Initial momenta
Clockwise WG	$-0.0918 < \theta_0 < 0.1023$	$0.9812 < p_0 < 1$
Direct Rays	$-0.734 < \theta_0 < -0.0918$	$0.6702 < p_0 < 0.9812$
Parallel Mirror Rays	$-1.1417 < \theta_0 < -0.734$	$0.321 < p < 0.6702$
Chaotic	$-1.7952 < \theta_0 < -1.1417$	$-0.321 < p_0 < 0.321$
Counter-clockwise WG	$-3.0393 < \theta_0 < -1.7952$	$-1 < p_0 < -0.321$
Graze with upper wall	-0.0918	0.9812
Graze with lower wall	-0.734	0.6702
$\mathcal{L}_0 \cap \Gamma s$	-1.1417	0.321
$\mathcal{L}_0 \cap \Gamma u$	-1.7952	-0.321

Table 5.1: The first five rows are the ranges of initial conditions in which we find the different kinds of trajectories. The remaining four rows are the initial conditions for four of the trajectories that partition these sets.

Let us now consider each type of ray and its contribution to the current. In Figures 5.9 through 5.13, the whole current is plotted in black, the contribution from a particular kind of trajectory is plotted in red, and the caption indicates the type of trajectory.

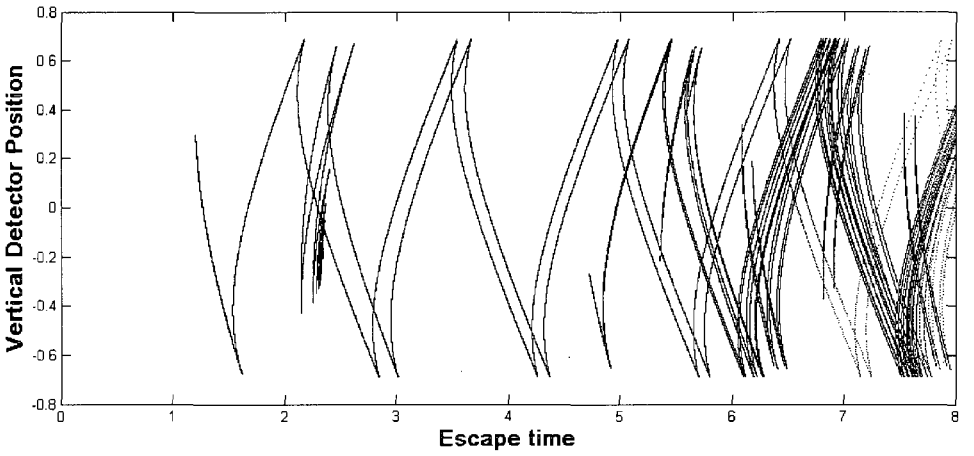

Figure 5.9: The contribution from the direct trajectories. These possess the shortest path lengths so they must be the earliest detected.

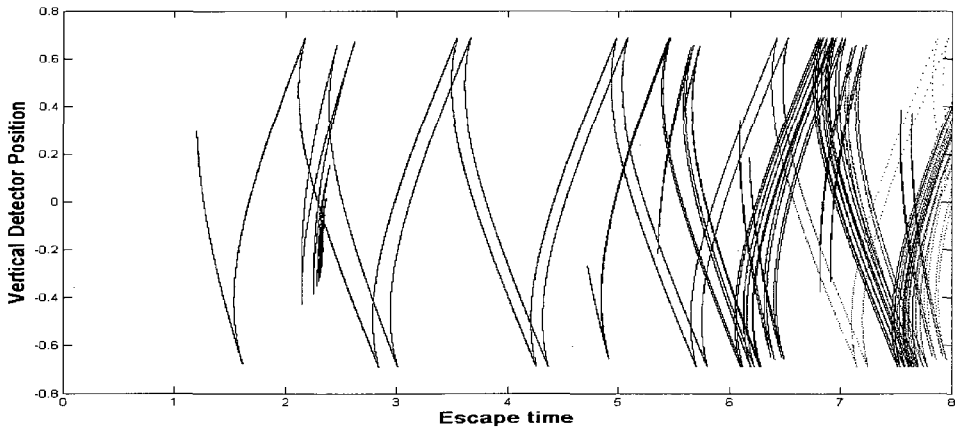

Figure 5.10: The set of parallel mirror trajectories are bounded by the ray that grazes the lower boundary and the trajectory that results from the intersection of the line of initial conditions and the stable boundary of the complex. Trajectories on the stable boundary do not escape and nearby trajectories are guided along the stable manifold toward the

unstable fixed point. Therefore, the parallel mirror trajectories are found by continuously rotating a direct ray through the ray that grazes the lower boundary. Though it is not shown, this set contains trajectories that escape after any number of bounces resulting in an infinitely long pulse saw-tooth.

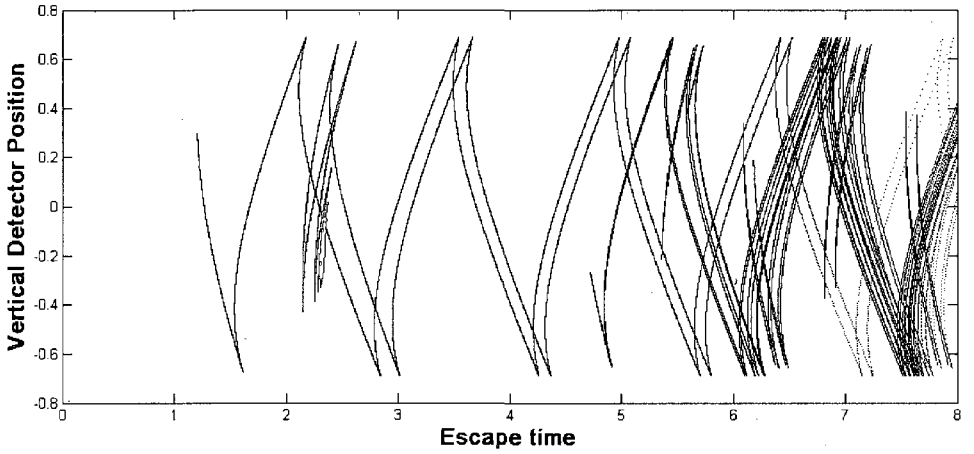

Figure 5.11: Here we see the contribution from the counter-clockwise whispering gallery trajectories. They escape early and accumulate within a finite region. Since we can construct a whispering gallery trajectory escaping after any number of reflections, there will be an infinite number of oscillations detected.

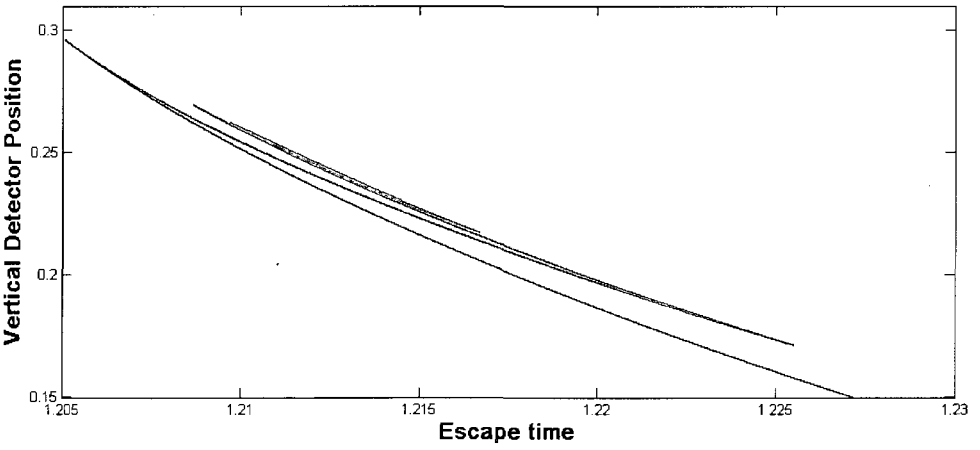

Figure 5.12: Here we see the contribution from the clockwise whispering gallery trajectories. These lie on the tip of the curve corresponding to the direct rays. These oscillations possess a similar structure to those of the counter-clockwise whispering gallery rays. However, the clockwise whispering gallery rays traverse a region of small curvature and thus accumulate in a small region of the detector. Furthermore, this set is

bounded by the ray that grazes the upper boundary. Therefore, this set can be found by continuously rotating a direct ray from the upper grazing ray to the tangent of the vase.

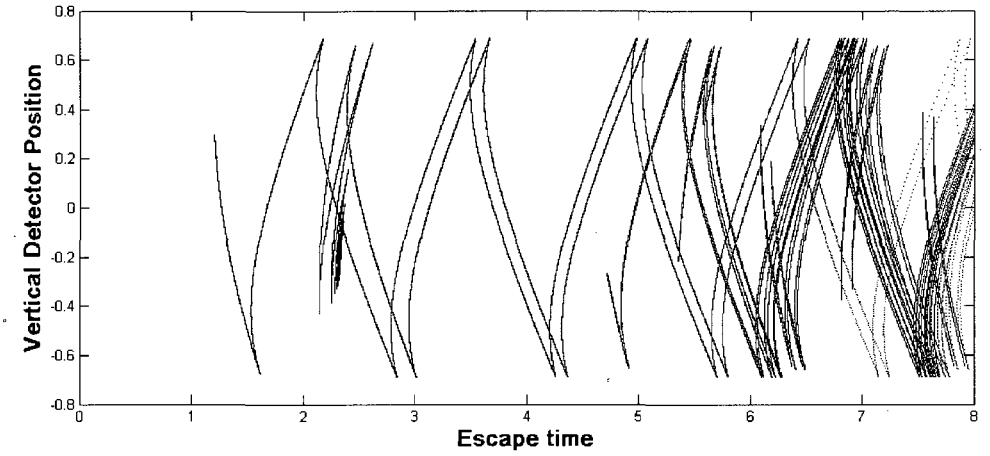

Figure 5.13: Finally, we see the contribution from the chaotic trajectories. Their initial angles correspond to the intersection of $\mathcal{L}_0$ with the complex.

b.) Measuring the Speed of Sound

Before we compare the simulation to the signal, we must first rescale the detector position and escape times of the simulation. The Teflon vase was constructed to be 87 cm along the horizontal direction. It was scaled so that in the arbitrary units of eq. (5.1) so that 1.5 units = 87 cm. This results in two conversions.

$$\begin{array}{c} 0.0172 \text{ units/cm} \\ 58 \text{ cm/unit} \end{array} \qquad (5.1)$$

Next, we must rescale the time units. For this, we need the speed of sound in air. Normally, the speed of sound in dry air at 1 atm is 343.4 m/s [1]. We decided to obtain a numerical approximation to the speed of sound with data obtained from another experiment.

This second experiment involved an ultrasound burst propagating through a pair of parallel Teflon slabs. The recorded signal is a series of pulses. In the absence of

phase shifts and absorption, we expect the pulses to arrive near the arrival times of the classical rays in the classical system. By inspecting the data, we estimate the time at which the peak of each pulse is observed.

The slabs were 56.2 cm long and separated by a distance of 17.78 cm. We imagine a set of axes to be centered at the lower left hand corner of the bottom slab. The source is then located at (0, 17.78) cm with the detector at (56.2, 0) cm. The signal recorded for this setup is shown in Figure 5.14. The horizontal axis is the detection time with units of ms and the vertical is the strength of the signal measured in mV. The signal recorded from 5 to 11 ms has been multiplied by a t^4 time gain as attenuation quickly weakened the signal.

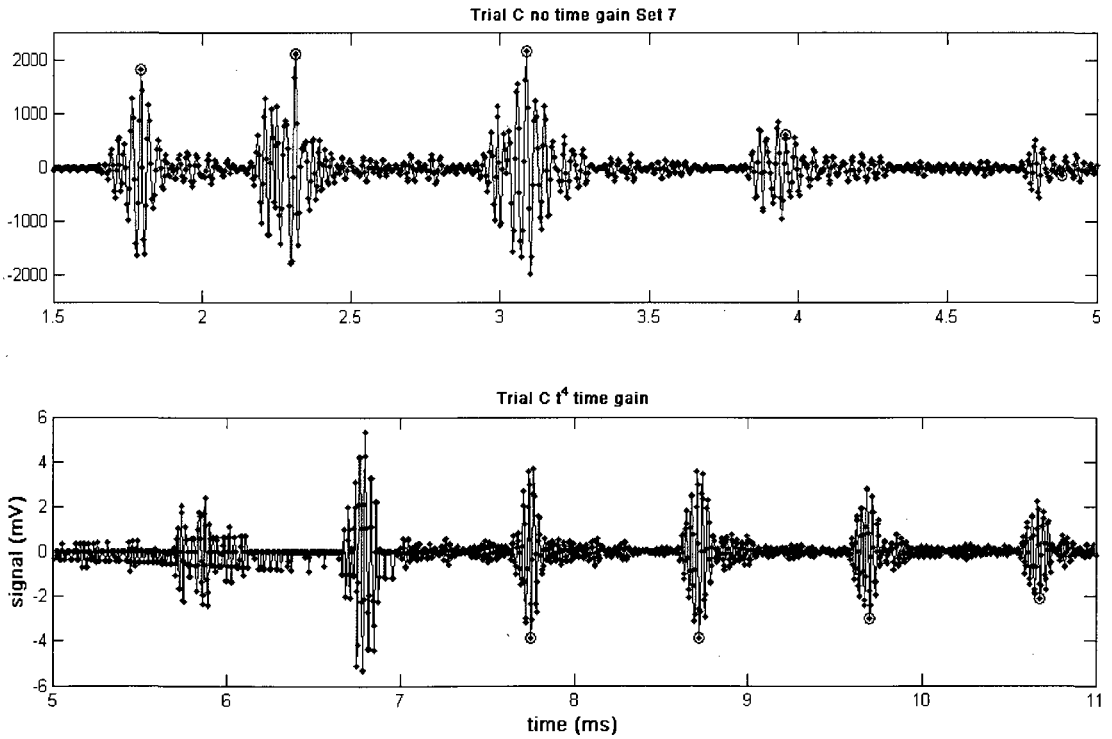

Figure 5.14: Signal recorded in the parallel slab experiment.

The red circles plotted in Figure 8 represent the estimated pulse centers. After estimating these points, we then compute the corresponding classical ray for each pulse and obtain the path length from source to detector. The path lengths, number of bounces to escape, and the detection times are recorded in Table 5.2.

Path length (cm)	Number of bounces to arrival	Detection times (s)
58.9455	0	0.0018
77.4829	2	0.0023
105.1744	4	0.0031
136.5604	6	0.0040
169.6020	8	0.0049
272.5570	14	0.0078
307.4403	16	0.0087
342.4628	18	0.0097
377.5858	20	0.0107

Table 5.2: Classical path lengths, number of bounces to arrival, and times at which ultrasound pulses are detected in the parallel plate experiment.

We then fit the data to an equation of the form

$$t_{pulse} = t_0 + \frac{\text{path length}}{v} \tag{5.2}$$

where t_{pulse} is the estimated pulse time, t_0 is a delay, and v is the speed of sound. Figure 5.15 shows both the data in Table 5.2 and the linear fit in the top graphs and the residuals between the actual data and the linear fit on the bottom. We see that the data in Table 5.2 is in good agreement with a straight line. The units in Figure 5.15 are seconds and meters. We found $t_0 = 0.1523$ ms and $v = 35.86$ cm/ms.

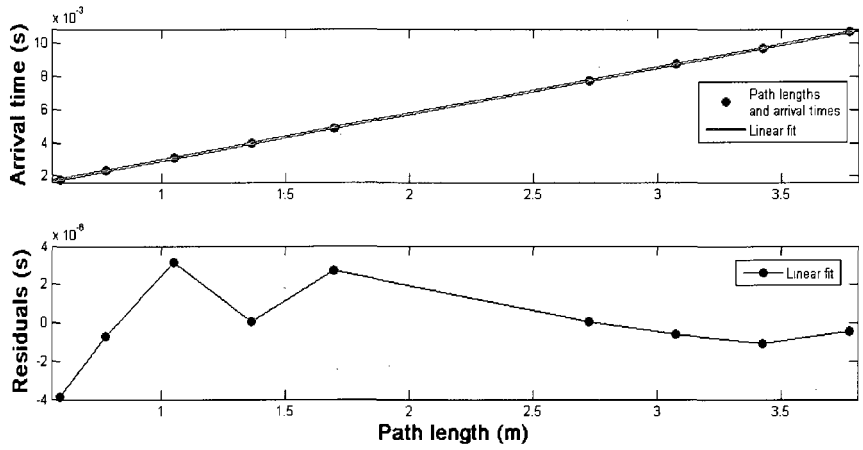

Figure 5.15: The top graph shows the data and the linear fit. The bottom shows the residuals between the fit and the actual data computed at the classical path lengths.

c.) Comparing the Simulation to the Experiment

Now that we have the correct scaling, we can compare a classical simulation to the recorded escaping ultrasound signal. To compare the two results, we take the absolute value of the natural logarithm of the signal, and assign a color coding to the signal with dark blue indicating a small amplitude and a dark red indicating a strong signal. We then plot the color coded signal in two dimensions. For the classical simulation we show the time vs. the detector position with no amplitude.

Figure 5.16 shows the data from 2 to 7.5 ms. We see that the maxima in the signal are organized into saw-tooth oscillations similar to those in the classical simulation, which is represented by the black line. The earliest signal that was detected (between 2 and 2.75 ms) corresponds to the direct and clockwise whispering gallery trajectories (compare Figure 5.16 with Figures 5.9 and 5.12). We see that between 10 cm and 20 cm there is a somewhat larger amplitude in the region where the whispering gallery modes accumulate.

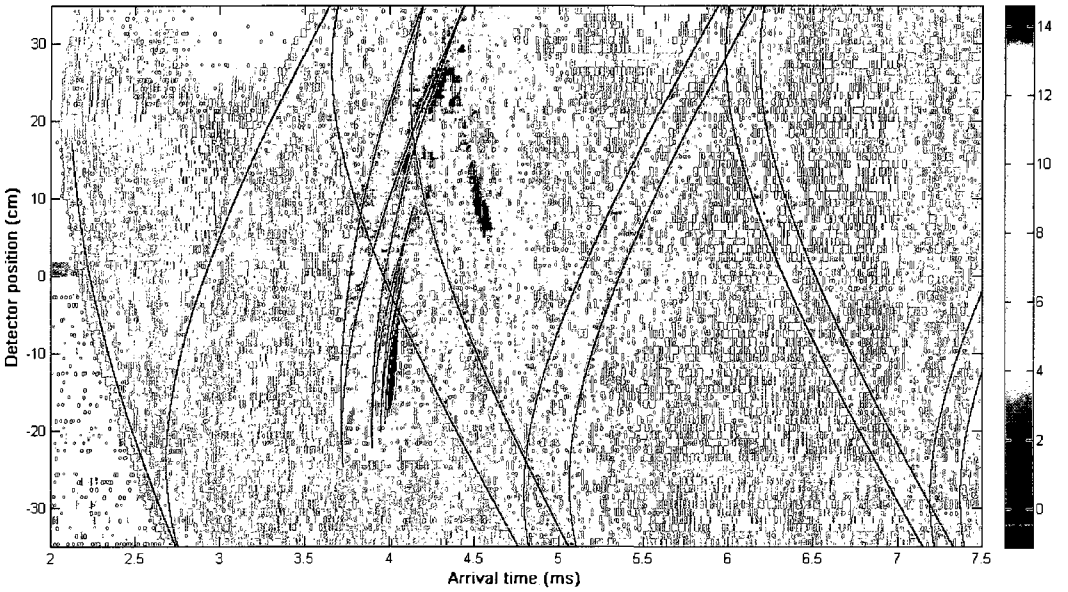

Figure 5.16: Rescaled simulation (black) versus the signal escaping the actual vase recorded between 2 and 7.5 ms.

The direct rays continuously turn into the so-called parallel-mirror rays (compare Figures 5.16 and 5.10). These form the first saw-tooth oscillation which starts at about 2.75 ms. Again, we see agreement between the classical simulation and the maxima of the signal. Around 4 ms there is a great deal of constructive interference between -20 cm and 30 cm. In this region, we have the counter-clockwise whispering gallery rays accumulating and the beginnings of a "chaotic saw-tooth" (see Figure 5.13). Again, we find agreement between the signal and the classical simulation.

Let us now examine the remainder of the data which is shown in Figure 5.17 below. The complex saw-tooth structure represents many chaotic trajectories escaping the vase. At these times, the signal does not resolve peaks very well, but nonetheless, we can still make out saw-tooth oscillations starting and 8 and 9 ms. The signal recorded at negative detector positions for times past 12 ms seems to be unreliable.

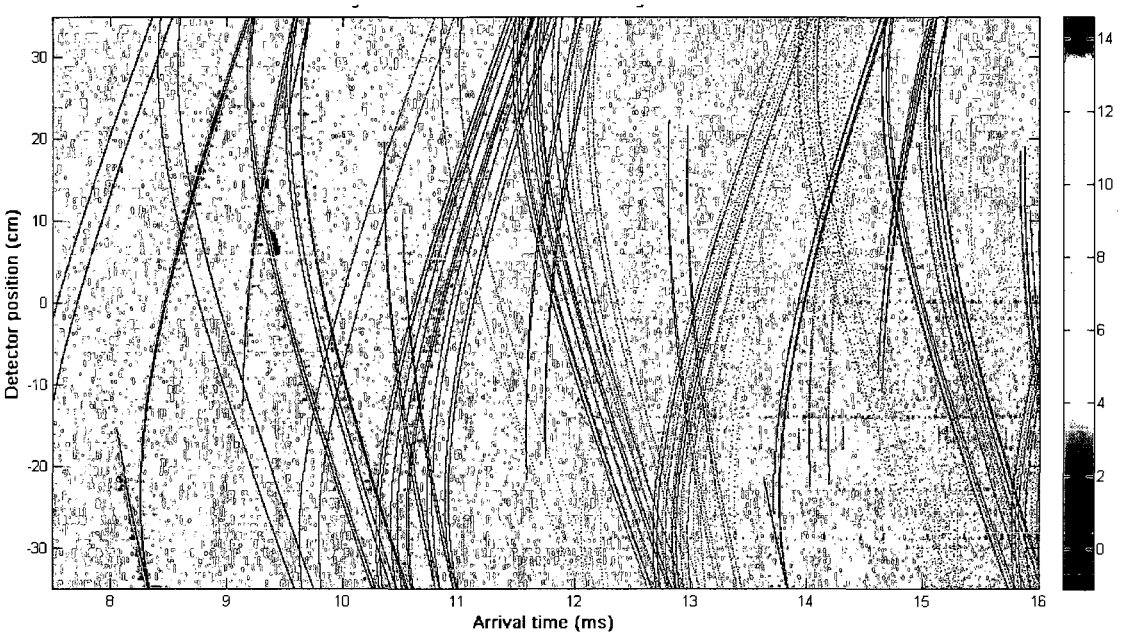

Figure 5.17: Rescaled simulation (black) versus the signal escaping the actual vase recorded between 7.5 and 16 ms.

iv.) Semi-classical Approximation

Let us now construct a semi-classical approximation to the wave function at the mouth of the vase. Our semi-classical wave function is an approximation to a complex solution to the two-dimensional Helmholtz Equation.

$$\left(\frac{\partial^2}{\partial x^2} + \frac{\partial^2}{\partial y^2} + k^2\right)\psi_k = 0 \tag{5.3}$$

subject to boundary conditions near the source ($r \sim r_0$)

$$\psi_k(r) \sim \frac{e^{ik|r-r_0|}}{\sqrt{k|r-r_0|}} \tag{5.4}$$

Such a wave represents the Green function for the Schrödinger Wave Equation. Its real or imaginary parts may represent sound waves (or in the case to be discussed, microwaves) in the vase. As we are interested in escaping flux, we compute the

wavefunction along a vertical line segment lying to the right of the UPO. To compute this wave function, we must identify trajectories going from a point source to a point detector by numerical interpolation of computed trajectories.

a.) Interpolating Classical Trajectories

We use a large family of trajectories to interpolate trajectories connecting source and detector points. After choosing a point source, we choose a point x_D at which we imagine a vertical array of point detectors spanning the space between the vase walls. All escaping trajectories are assumed to be "absorbed" at this vertical line segment. After propagating a family of trajectories, we discard those that do not escape after some specified number of reflections. For the set of escaping trajectories, we construct a plot of final position along the detector vs. initial momentum (Figure 5.18)

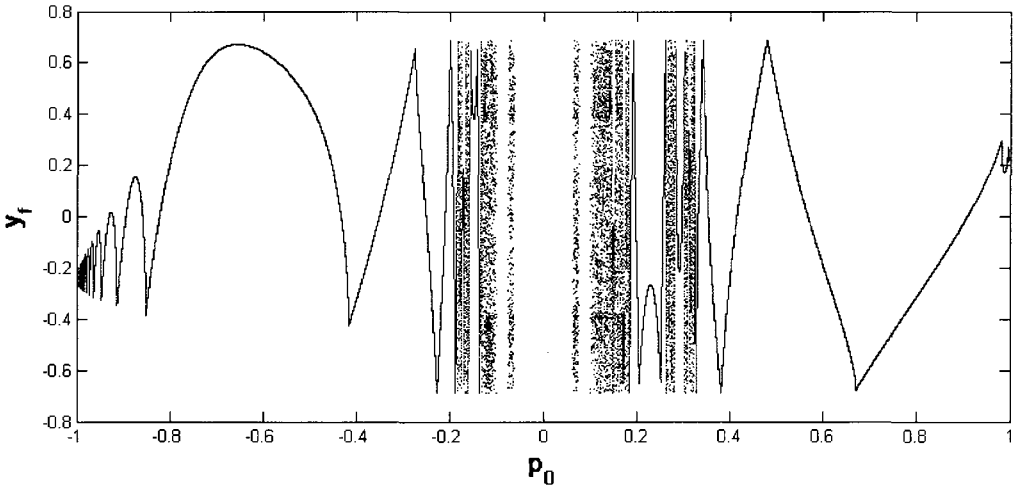

Figure 5.18: Detector position versus initial momentum for the source at (0.3, 0.4067).

Figure 5.18 shows that $y_f(p_0)$ possesses a complicated set of oscillations. We see that globally, this curve is disconnected near $p_0 = 0$ and possesses many discontinuities

in slope. The former discontinuity is where the source overlaps the stable continent, so the trajectories do not escape. The discontinuities in slope occur where the number of bounces to escape changes. If we compare $y_f(p_0)$ and the number of bounces to escape, $B_e(p_0)$ (Figure 5.19), we see that the discontinuities in $y_f(p_0)$ line up where B_e changes. $B_e(p_0)$ can change in one of two ways. The first is what we call a natural discontinuity. This results from rotating a trajectory until it encounters a grazing trajectory, at which point $B_e(p_0)$ changes by ± 1. The second discontinuity is what we call an artificial discontinuity. This kind of discontinuity arises when a velocity vector is rotated until the last reflection encounters the point at which the vertical detector line intersects the vase boundary. Essentially, the detector prevents the velocity vector from rotating into a grazing trajectory. Regardless of the type of discontinuity, the number of reflections changes by ± 1. The slope of the escape time is also discontinuous where the number of reflections changes.

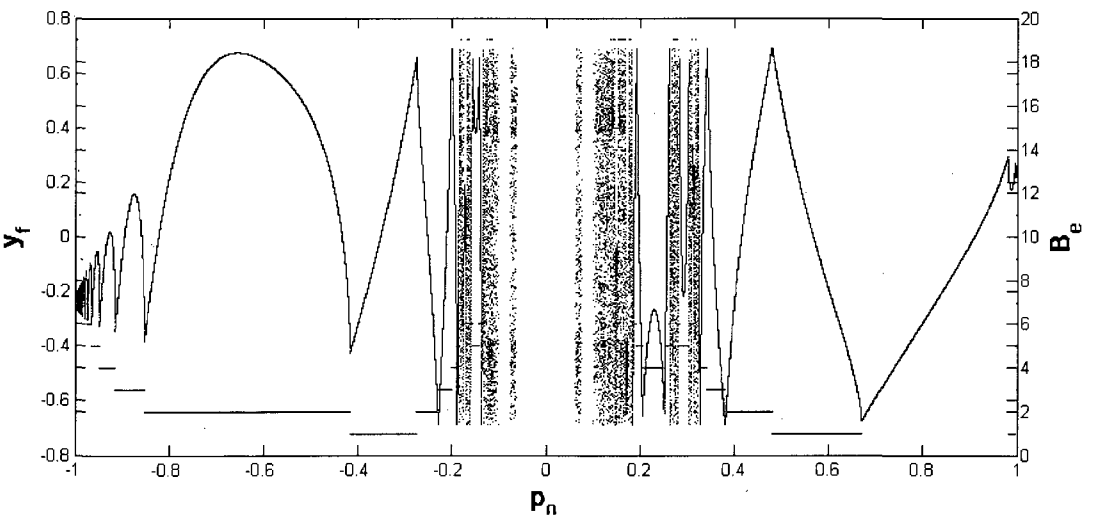

Figure 5.19: The black points are $y_f(p_0)$ and the red points are $B_e(p_0)$.

We choose a detector point y_D and draw a horizontal line through $y_f(p_0)$ and numerically solve for those p_0 that satisfy

$$y_f(p_0) - y_D = 0 \tag{5.5}$$

To simplify the problem of numerically computing the zeros, we break up the curve at points of discontinuous slope. Consider Figure 5.20 below which shows two sets of points generated from escape segment E_1 (see Figure 5.1). The red points are the bounces to escape (B_e) vs. p_0 while the black points are y_f vs. p_0. Again, we see that each discontinuity in slope of $y_f(p_0)$ corresponds to a change in the number of bounces, which is due to either a grazing trajectory or a trajectory landing at $\pm f(x_D)$. This figure demonstrates an important fact about the escape segments: each escape segment produces two infinite sequences of pulses. Each smooth segment of the curve contributes 0, 1, or 2 interpolated trajectories at the detector point. For the interpolation, we break up y_f into smooth sets of points that escape the vase after the same number of bounces, and then, we apply the secant method to each smooth set to numerically compute the zeros of eq. (5.5) [2].

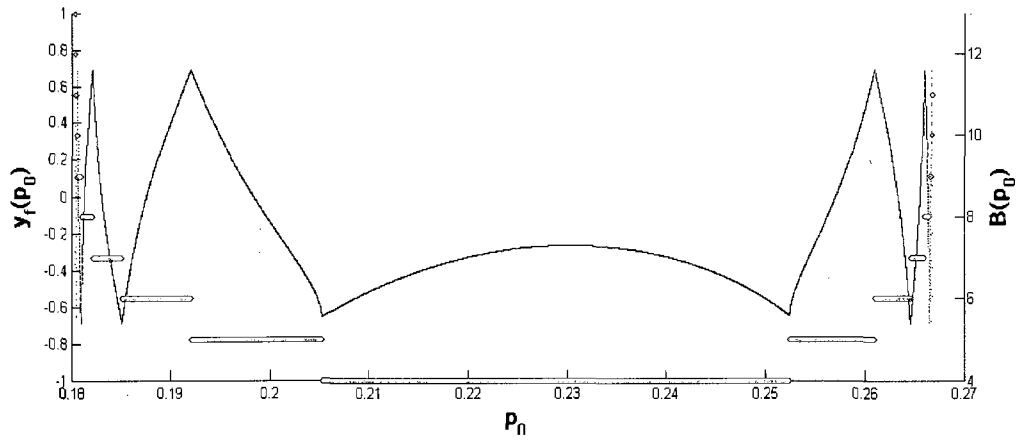

Figure 5.20: Bounces to escape (red) and position along the vertical line detector (black) for a family of trajectories with launch angles bounded by the endpoints of escape segment E_1.

b.) Computing the Semi-classical Wave Function

Once we have interpolated the trajectories connecting a source to a detector point, we are ready to calculate the semi-classical wave function. The wave function is given by

$$\psi(\mathbf{r}) = \sum_{j=1}^{N} A_j(\mathbf{r}) \frac{e^{ikr_0}}{\sqrt{r_0}} e^{\frac{iS_j(\mathbf{r})}{\hbar} - \frac{i\mu_j\pi}{2}} \tag{5.6}$$

This form of the wave function can be found in [4] where it is used in the construction of a model of electronic transport through a semiconductor microjunction. The sum runs over the interpolated trajectories connecting the source to a detector point. This function is the WKB approximation in two dimensions. Let us consider each term in eq. (5.6).

$A_j(\mathbf{r})$ is the amplitude of the wave function. In one dimension, the amplitude is proportional to the inverse square root of the classical momentum. In two dimensions, this function is a ratio of Jacobians in the representation $(x(t, \theta_i), y(t, \theta_i))$ where x and y

are the position of a classical trajectory as a function of time and initial launch angle of the j^{th} trajectory. We use the fact that the amplitude function is proportional to the probability density of the quantum function to rewrite it in terms of $J(t,\theta_i) = \frac{\partial(x,y)}{\partial(t,\theta_i)}$ [4].

$$\left|A_j(\mathbf{r})\right|^2 = \rho(\mathbf{r}) = \rho_0(\mathbf{r})\frac{J(0,\theta_i)}{J(t,\theta_i)} \tag{5.7}$$

The initial Jacobian can be evaluated analytically. We assume that we have a collection of trajectories starting along a small circle centered at the burst. Locally, the elements of the Jacobian then come directly from the kinematic equations.

$$\begin{aligned} &a.)\frac{\partial x}{\partial t} = \cos(\theta_j) \quad b.)\frac{\partial x}{\partial \theta_j} = -\sin(\theta_j)t \\ &c.)\frac{\partial y}{\partial t} = \sin(\theta_j) \quad d.)\ \frac{\partial y}{\partial \theta_j} = -\cos(\theta_j)t \end{aligned} \tag{5.8}$$

We see immediately from eq. (5.8) that the determinant of the Jacobian matrix is t. Using the fact that the speed is set to 1 and we are evaluating the matrix at the initial time, the determinant evaluates to the radius of the initial distribution of trajectories, r_0. Inserting $\det(\underset{\sim}{J}(0,\theta_j)) = r_0$ into eq (5.7) yields $\sqrt{r_0}$, which cancels with the factor of $\sqrt{r_0}$ appearing in the denominator of $\psi^0(\mathbf{r}_0)$.

The denominator of (5.7) is evaluated numerically. However, we can use a change of representation to write out a simple analytical expression for the denominator. The denominator is

$$\det(\underset{\sim}{J}(t,\theta_j)) = \left(\frac{\partial x}{\partial t}\right)_\theta \left(\frac{\partial y}{\partial \theta}\right)_t - \left(\frac{\partial x}{\partial \theta}\right)_t \left(\frac{\partial y}{\partial t}\right)_\theta \tag{5.9}$$

Along a trajectory passing through the detector point, the partial derivatives with respect to time are the components of the velocity vector at (x_D, y_D). We want to rewrite the partial derivatives with respect to θ in such a way that it incorporates the fact that along the line detector, x is a constant. First, we calculate the perfect differentials of the two pairs of function $(x(t, \theta), y(t, \theta))$ and $(t(x, \theta), y(t, \theta))$.

$$\begin{aligned} &\text{a.) } dx = \left(\frac{\partial x}{\partial \theta}\right)_t d\theta + \left(\frac{\partial x}{\partial t}\right)_\theta dt \quad \text{b.) } dy = \left(\frac{\partial y}{\partial \theta}\right)_t d\theta + \left(\frac{\partial y}{\partial t}\right)_\theta dt \\ &\text{c.) } dt = \left(\frac{\partial t}{\partial \theta}\right)_x d\theta + \left(\frac{\partial t}{\partial x}\right)_\theta dx \quad \text{d.) } dy = \left(\frac{\partial y}{\partial \theta}\right)_x d\theta + \left(\frac{\partial y}{\partial x}\right)_\theta dx \end{aligned} \tag{5.10}$$

Substituting eq. (5.8a) into eq. (5.8d) and equating eq. (5.8b) and eq. (5.8d) results in an equation that is a function of the variables (t,θ). By solving for the coefficients in front of the differentials dt and $d\theta$ results in the following equations.

$$\begin{aligned} &\text{a.) } \left(\frac{\partial y}{\partial x}\right)_\theta \left(\frac{\partial x}{\partial \theta}\right)_t + \left(\frac{\partial y}{\partial \theta}\right)_x = \left(\frac{\partial y}{\partial \theta}\right)_t \\ &\text{b.) } \left(\frac{\partial y}{\partial x}\right)_\theta \left(\frac{\partial x}{\partial t}\right)_\theta = \left(\frac{\partial y}{\partial t}\right)_\theta = v_y \end{aligned} \tag{5.11}$$

We substitute (5.11) into (5.9) and use the fact $\left(\frac{\partial x}{\partial t}\right)_\theta = v_x$ to obtain

$$\det(\underset{\sim}{J}(t,\theta_j)) = v_x\left(\left(\frac{\partial y}{\partial x}\right)_\theta \left(\frac{\partial x}{\partial \theta}\right)_t + \left(\frac{\partial y}{\partial \theta}\right)_x\right) - \left(\frac{\partial x}{\partial \theta}\right)_t \left(\frac{\partial y}{\partial x}\right)_\theta v_x = v_x \left(\frac{\partial y}{\partial \theta}\right)_x \tag{5.12}$$

Then the amplitude for the j^{th} wave function evaluated at the detector point is

$$A_j(\mathbf{r_D}) = \frac{\sqrt{r_0}}{\sqrt{\left|v_x \left(\frac{\partial y}{\partial \theta}\right)_x\right|}} \tag{5.13}$$

In practice, the denominator is approximately computed using two trajectories: the interpolated trajectory and a closely-spaced neighbor.

The function $S_j(\mathbf{r})$ is the classical action [6] and is given by

$$S(\mathbf{r}) = \int \mathbf{p}(\mathbf{q}) \cdot \mathbf{dq} \tag{5.14}$$

The integral is evaluated along a classical trajectory. For us, the momentum is constant along a path connecting two successive reflections. For a trajectory with n+1 reflections, the characteristic function is given by eq. (5.15).

$$S(\mathbf{r}) = m\sum_{i=0}^{n}\int_{x_i}^{x_{i+1}} (v_x)_i \, dx + m\sum_{i=0}^{n}\int_{y_i}^{y_{i+1}} (v_y)_i \, dx \tag{5.15}$$

We set the mass m to unity. Since the velocity components are constant between reflections, the integrals are immediately evaluated to be the horizontal and vertical displacements for each line segment connecting successive reflections. Using the kinematic equations we obtain eq. (5.16).

$$S(\mathbf{r}) = \sum_{i=0}^{n}\left((v_x)_i^2 + (v_y)_i^2\right)t \tag{5.16}$$

Now we use the facts that $|\mathbf{v}| = |\mathbf{p}|$ and that the quantum mechanical momentum for a plane wave is $p = \hbar k$ to obtain eq. (5.17).

$$S(\mathbf{r}) = \hbar k \sum_{i=0}^{n} |\mathbf{v}|_i \, t \tag{5.17}$$

The magnitude of the velocity vector times the propagation time is the length of the line segment. Therefore, the characteristic function for the j^{th} trajectory is proportional to the length of that trajectory.

$$S_j(\mathbf{r}) = \hbar k L_j \tag{5.18}$$

L_j is the length of the trajectory from a small circle of radius r_0 about the source to the detector. It can be combined with the factor $\exp(ikr_0)$ in eq. (5.6) to give $k(L_j + r_0)$, which is the full phase from source to detector.

Finally, μ_j is the Maslov index of the j^{th} trajectory. This index records phase shifts due to focal points and reflections. It assumes integer values [6]. For hard each wall collision, the Maslov index is increased by two. For each focal point the interpolated trajectory encounters, the Maslov index increases by one. To find focal points, we consider the interpolated trajectory and a perturbed trajectory. Using these trajectories, we compute finite differences (Δx, Δy, $\Delta\theta$) and use these to approximate the partial derivatives in eq. (5.9) (and hence the determinant of the Jacobian) along an interpolated trajectory. We look each instance in which the determinant of the Jacobian goes smoothly through zero.

Two of the partial derivates are evaluated at constant time. Therefore, we must fix a time-step Δt and interpolate the trajectories at integer multiplies of this time-step. For each interpolated point, we also obtain the velocity field at that point. Then an approximation of eq. (5.9) can be constructed from interpolating the two trajectories. Focal points and reflections show up as points at which eq. (5.9) changes sign. At a focal point, eq. (5.9) changes sign continuously while at a reflection it changes discontinuously. By counting the number of sign changes, we can obtain part of the Maslov index.

Now let us substitute our results into eq. (5.6).

$$\psi(\mathbf{r_D}) = \sum_{j=1}^{N} \frac{e^{i(kr_0 + kL_j(\mathbf{r_D}) - (l/2)\mu_j\pi)}}{\sqrt{\left|(v_x)_j (\partial y/\partial\theta)_{x_D}\right|}} \tag{5.19}$$

The wave function is evaluated at the detector point $\mathbf{r_D} = (x_D, y_D)$. At a detector point, the wave function is evaluated over an interval of wave numbers k. The Fourier variable conjugate to the wave number is the path-length of the trajectory. Therefore, we compute the Fourier Transform of eq. (5.19).

$$\tilde{\psi}(L;r_D) = \frac{1}{\sqrt{2\pi}} \int_{-\infty}^{\infty} dk e^{-ikL} \sum_{j=1}^{N} \frac{e^{i(kr_0 + kL_j(\mathbf{r_D}) - (l/2)\mu_j\pi)}}{\sqrt{\left|(v_x)_j (\partial y/\partial\theta)_{x_D}\right|}} \tag{5.20}$$

The sum over interpolated trajectories is finite and thus can be removed from the integrand. The denominator and the Maslov phase shift both come out of the integrand as each is independent of k. Immediately, we see that the integral is the Dirac Delta function. Therefore, the Fourier Transform of the semi-classical wave function is

$$\tilde{\psi}(L;r_D) = \frac{1}{\sqrt{2\pi}} \sum_{j=1}^{N} \frac{e^{-i(l/2)\mu_j\pi}}{\sqrt{\left|(v_x)_j (\partial y/\partial\theta)_{x_D}\right|}} \delta(L + r_0 + L_j) \tag{5.21}$$

Our final result is a collection of peaks centered near the lengths of the classical trajectories with the amplitudes depending on the phase shifts due to reflections and focal points.

In practice, we do not use eq. (5.21). For each detector point, we compute eq. (5.6) over a distribution of k. We calculate the Fast Fourier Transform (FFT) of eq. (5.6) with Matlab's own FFT algorithm giving us an approximation to eq. (5.21). Before we discuss our results, we must discuss the function of the wave number k. This variable is an experimental input.

c.) Imagined Experiment with an Electromagnetic Waveguide

The vase was designed as a relatively simple means of numerically and experimentally probing a system controlled by a homoclinic tangle. As stated earlier, the wave function we have computed is an approximation to the time independent Schrodinger Equation, or the Helmholtz Equation. One can construct another realization of the vase using an electromagnetic waveguide. S Sridhar and his group at Northeastern University construct electromagnetic waveguides as a means of studying chaotic eigenfunctions and chaotic scattering (see [7-10] and references therein).

Their waveguides are typically constructed from copper. A coaxial cable feeds microwaves into the cavity with the initial frequency controlled. Furthermore, they typically study two-dimensional systems with three-dimensional systems that are small and flat along the z-axis. For instance, a vase-shaped waveguide could be constructed using copper plates with a spacing of 6 mm. To simulate an open cavity, the space between the plates can be filled with a material that absorbs escaping microwaves.

The idea behind these experiments is to construct a system in such a way that Maxwell's Equations for the vector electromagnetic fields are reduced to the scalar Helmholtz Equation. The following material can be found in Chapter 8 of Jackson's *Classical Electrodynamics,* 3rd Ed [11] and [7]. We start with Maxwell's Equations in the absence of point sources and currents.

$$\begin{aligned} &\text{a.)}\ \nabla \times \mathbf{E} = \frac{\partial \mathbf{B}}{\partial t} \\ &\text{b.)}\ \nabla \times \mathbf{B} = -\frac{1}{c}\frac{\partial \mathbf{E}}{\partial t} \end{aligned} \tag{5.22}$$

We assume that the fields possess a sinusoidal time dependence $e^{-i\omega t}$ and plane waves along the z-axis $e^{\pm ik_z z}$. The decoupled wave equations can then be written as

$$\left(\nabla^2_{(x,y)} + \left(\frac{\omega}{c}\right)^2 - k_z^2\right)\mathbf{F}(x,y) = 0 \tag{5.23}$$

where $\mathbf{F}(x,y)$ represents either $\mathbf{E}(x,y)$ or $\mathbf{B}(x,y)$. We can decompose either field into two components, one along the z-direction and one in the xy-plane (or the transverse component). Then, the transverse components of the fields can be computed directly from the z-components. Letting $k = \omega/c$ we have

$$\begin{aligned} &\text{a.) } \mathbf{E}_t = \frac{1}{k^2 - k_z^2}\left(\nabla_t E_z - ik\hat{\mathbf{z}} \times \nabla_t B_z\right) \\ &\text{b.) } \mathbf{B}_t = \frac{1}{k^2 - k_z^2}\left(\nabla_t B_z + ik\hat{\mathbf{z}} \times \nabla_t E_z\right) \end{aligned} \tag{5.24}$$

Eq. (5.24) says that the z-components of both fields allow us to compute the transverse components.

We desire a standing wave solution along the z-axis. If d is the distance between the two plates measured along z, then the wave number along the z-direction is given by the quantization rule $k_z = \frac{p\pi}{d}$ where p is an integer. The two classes of allowed modes are Transverse Electric (TE) modes, for which $E_z = 0$ everywhere, and Transverse Magnetic (TM) modes for which $B_z = 0$ everywhere. For the two modes, the allowed solutions are given by eq. (5.25).

$$\begin{aligned} &\text{a.) TE: } B_z = B_z(x,y)\sin(p\pi z/d) \\ &\text{b.) TM: } E_z = E_z(x,y)\cos(p\pi z/d) \end{aligned} \tag{5.25}$$

The TM modes are the only modes in which there is no variation along the z-axis (i.e. p = 0) and there is a nonzero field. For scattering systems, a network analyzer is used to experimentally obtain the transmission probabilities (S-matrix elements) [12].

The setup of our calculations is based on the previous work of Sridhar and his group. First, we must define a cutoff frequency, which is found by computing the frequency for the p = 1 mode. For a cavity of thickness 6 mm, the cutoff frequency is 25 GHz. However, we will assume a maximum frequency of 20 GHz which corresponds to a wave number of $k_{max} = \frac{2\pi f_{max}}{c} = \frac{400\pi}{3} m^{-1}$. They can increment the frequency of the microwaves fed into the cavity in increments of 0.001 GHz, which corresponds to a wave number increment of $\Delta k = \frac{2\pi \Delta f}{c} = \frac{2\pi 10^{-2}}{3} m^{-1}$. Since this experiment has not been carried out, we do not have a scaling factor for rescaling the distances in our calculations. Therefore, we will assume the change of units 1.5 units = 1 m. Using k_{max} and Δk, we compute a uniformly spaced set of wave numbers with units of meters, divide each one by 1.5 to obtain the wave numbers with our unscaled units, evaluate (5.19) over the new wave numbers, and then compute the corresponding FFT. Finally, we consider 21 detectors in the range from -0.3333 units to 0.3333 m located at x = 1 m. For a wave function to be constructed from an interpolated trajectory, that trajectory must land within a distance of $1e^{-8}$ of the detector point.

d.) The Semi-classical Calculation: 21 Point Detectors

We will focus on $|\tilde{\psi}(L,r_D)|$ for all 21 detectors. We present three two-dimensional surface plots showing $|\tilde{\psi}(L,r_D)|$ multiplied by an exponential factor.

$$\varphi_{fft}(L,r_D) = e^{0.5L}\left|\tilde{\psi}(L,r_D)\right| \tag{5.26}$$

Multiplying the magnitude of the Fourier transformed wave function increases the amplitudes of the peaks centered at the longer trajectories. These peaks tend to be small and thus require amplification for better visualization. The peaks centered at path lengths between 0 and 5 m are shown in Figure 5.20 below. We first note that $\varphi_{fft}(L,r_D)$ is plotted in the range 0 to $0.5\text{x}10^{-5}$. The regions in which the surface appears to be discontinuous are due to cutoff along this axis. The most prominent aspect of this figure is the appearance of saw-tooth oscillations similar to those seen in the ultrasound experiment. The peaks between 0.5 and 1 m are organized into a curve similar to the curve resulting from the direct rays in Figure 5.9. Between 1 and 2 m, we see an accumulation of peaks where the counter-clockwise whispering gallery trajectories accumulate.

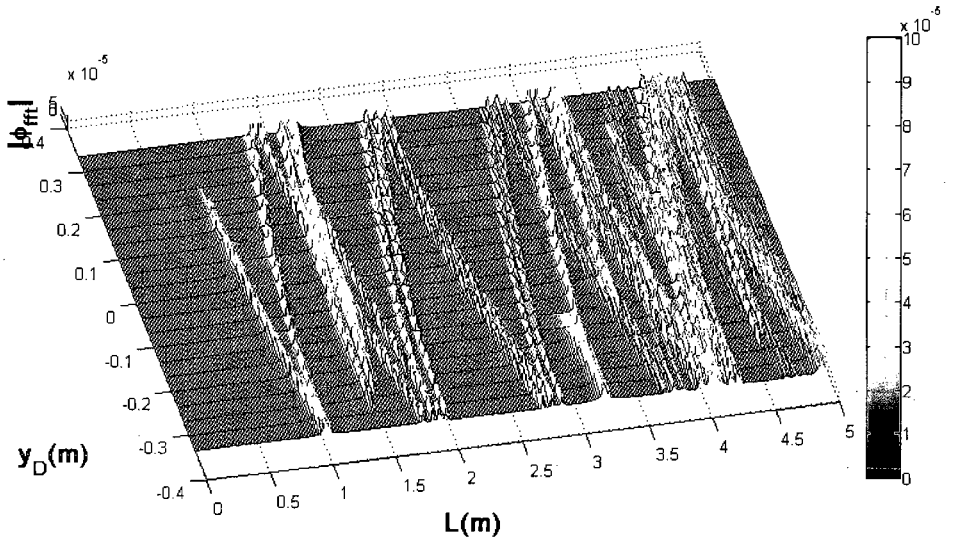

Figure 5.20: The amplified magnitude of the semi-classical wave function for path lengths in the range 0 to 5 m.

After the direct and whispering gallery trajectories have escaped, the intermediate to long path lengths result from the parallel mirror and chaotic trajectories. Figure 5.21 shows the path length spectrum for path lengths in the interval 5 m to 10 m. Despite the fact that these are relatively short path lengths, the spectrum has become immensely complex. Regular scattering trajectories are still present, namely the so-called parallel mirror trajectories. This set of trajectories results in an infinitely long saw-tooth oscillation. The other peaks in Figure 5.21 result from chaotic trajectories.

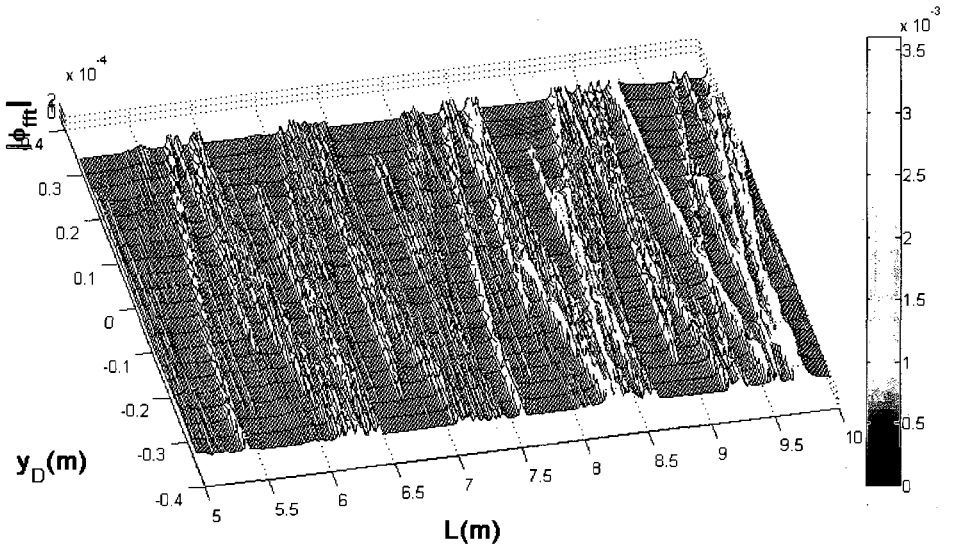

Figure 5.21: Semi-classical calculation for path lengths in the range from 5 to 10 m.

Let us now consider the spectrum resulting from longer paths. Figure 5.22 shows our calculations for path lengths in the interval from 10 m to 15 m. The figure shows few peaks. The sparseness in oscillations is not due to destructive interference but a lack of interpolated trajectories. At this resolution, the escape segments are short in length. Our interpolation is based on a simulation comprised of two million trajectories. If we did not pick up enough points in an escape segment for an interpolation, then we do not

interpolate $y_f(p_0)$ for that escape segment. Here we have gone past the limits of reliability of our calculation. We will discuss a possible refinement of the semi-classical approximation in Chapter 6.

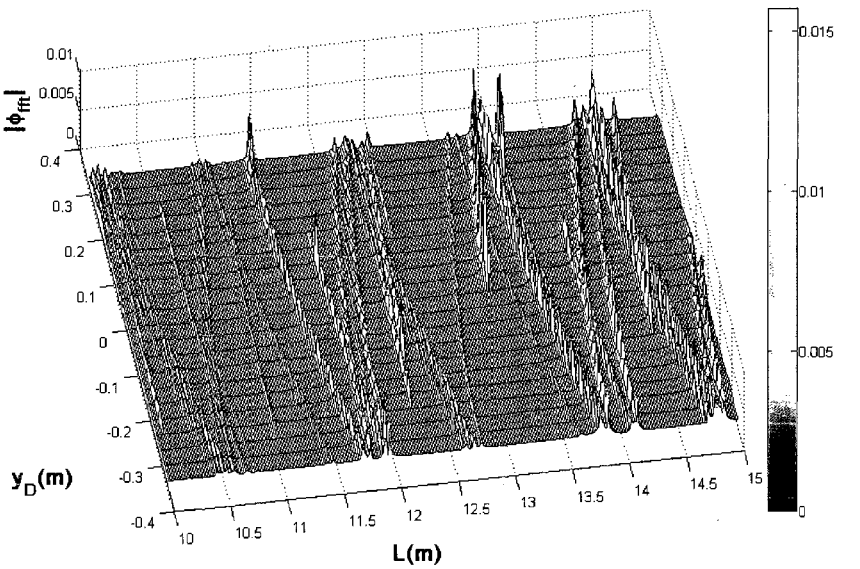

Figure 5.22: Path length spectrum for path lengths in the interval of 10 m to 15 m.

e.) Semi-classical Calculation: Point Detector at y = 0

Figures 5.20, 5.21, and 5.22 give a global picture of the transmission probabilities for a vertical detector line past the vase's neck. We will now examine the spectrum for one detector point. We present the spectrum observed at the detector point y = 0, which is situated along the axis of symmetry. Sixteen trajectories with path lengths up to 3 m are shown in Figure 5.23 below. Around the peaks we have plotted the trajectories that correspond to each peak. Underneath each trajectory is an integer indicating to which peak the trajectory corresponds.

The first peak is obviously due to the direct trajectory. The second peak results from the first parallel mirror trajectory. After this trajectory comes a cluster of eight peaks constructively interfering. Trajectory 3 may be regarded as the first in a sequence of counterclockwise whispering gallery trajectories (we find only counter-clockwise whispering gallery trajectories at this detector point as the clockwise whispering gallery trajectories are focused into a narrow band above the point detector under consideration). Trajectories 4 and 6 are also both whispering gallery trajectories that escape after two reflections. We can see that trajectory 4's last reflection occurs close to the inflection point while trajectory 6's is far from the inflection point. Trajectory 5 is another parallel mirror trajectory. Trajectories 7 and 8 are whispering gallery trajectories that escape after 3 reflections. Again, we see that trajectory 7's last reflection is near the inflection point while trajectory 8's is far away from the inflection point. Trajectories 9 and 10 are also whispering gallery trajectories that escape after four reflections.

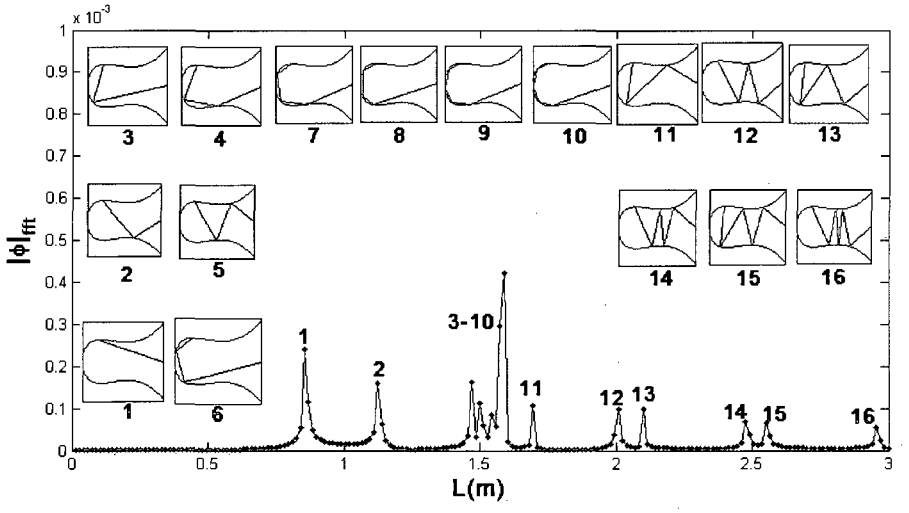

Figure 5.23: Path length spectra for path lengths up to 3 m.

Trajectories 12, 14, and 16 are also parallel mirror trajectories. We see that as the number of reflections increase, the amplitudes of the peaks decrease. Trajectories 11, 13, and 15 are the first chaotic trajectories to escape. They are members of the escape segment A_1 (see Figure 5.1), which results from the intersection of $\mathcal{L}_0$ and E_{-1}.

Let us now consider Figure 5.24, which shows the first six trajectories arriving at the point detector from segment A_1. We see that as L increases, the number of reflections also increases. Furthermore, the amplitudes are also decreasing with increasing path length. We see that just following peak 4 a cluster of peaks containing many trajectories appears. Trajectories 5 and 6 contribute to this cluster. Given that there are many trajectories contributing to this cluster and the amplitudes are large enough to be apparent, we conclude that there is little destructive interference occurring and thus these peaks should be measurable.

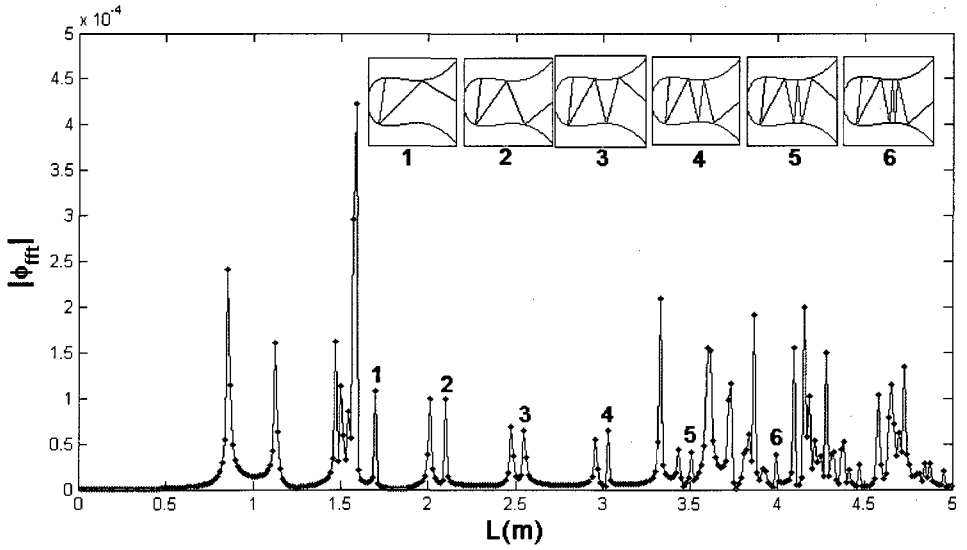

Figure 5.24: First 6 trajectories arriving at $y_D = 0$ from escape segment A_1 and their corresponding peaks in the transmission spectrum.

Finally, let us consider the path length spectrum for path lengths 3 m to 6 m shown in Figure 5.25. At this point, the chaotic trajectories dominate the spectrum. Let us consider just a few of the chaotic trajectories contributing to the spectrum. We first consider trajectories from the escape segments E_1, E_2 and E_3. Figure 5.25 shows that as the number of reflections to escape the complex increases, the amplitude also decreases. This observation seems to hold for the peaks corresponding to trajectories from the escape segments B_1, B_2, and B_3. Finally, consider the first two escape segments from the F and G-epistrophes. These two epistrophes are spawned by the segment E_1. We see that their peaks overlap to form one peak, because the resolution is inadequate to separate them. The same applies to the two peaks corresponding to trajectories from the segments F_2 and G_2. If the electromagnetic waveguide experiment is realized, we can verify the existence of the early and some intermediate epistrophes and their children by matching peaks in figures such as Figure 5.25 to the experimentally obtained transmission probabilities.

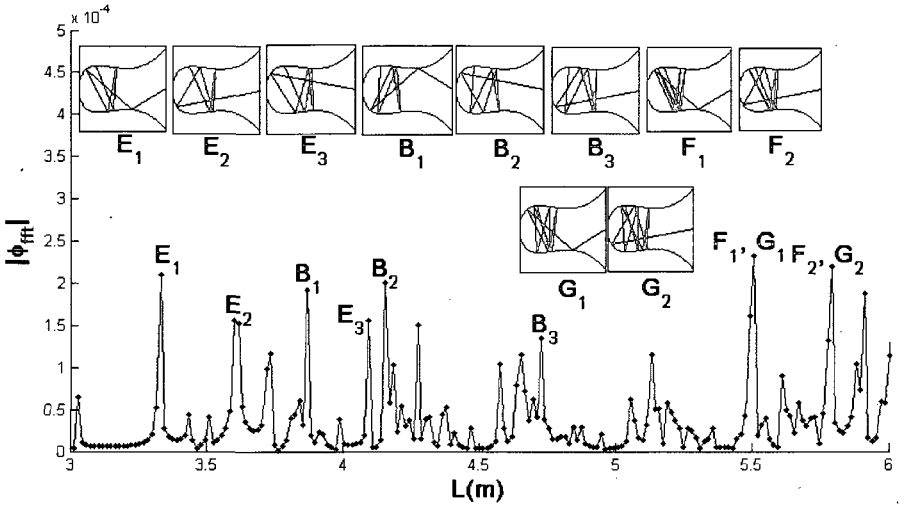

Figure 5.25: Spectrum for path lengths in the interval from 3 m to 6 m. The peaks corresponding to several escape segments are given the same labels as in Figure 5.1. For each labeled escape segment, one interpolated trajectory is also presented.

v.) Conclusions

In this chapter, we have examined the chaotic trajectories present in the vase. We first examined several chaotic trajectories that are members of escape segments labeled in Figure 5.1. We saw that trajectories belonging to a single epistrophe possess some similarities and thus characteristics of the trajectories can be assigned to epistrophes. We then examined the results of an experiment conducted by Dr. Mathew Len Keeler and Joshua Geifer at the University of Minnesota, Morris. They constructed a life-sized vase with the curved boundary walls constructed from Teflon, which were then sandwiched between large aluminum plates. An ultrasound transducer was used as a point source and the escaping signal was recorded for a number of detector positions.

We compared the escaping ultrasound signal to a classical simulation. We started a large family of trajectories and discarded those that did not escape. For each escaping trajectory, its escape time and detector position was recorded. This "current" is

organized into a complex series of saw-tooth oscillations in which each type of trajectory makes a specific contribution. Comparing the classical simulation to the recorded ultrasound signal showed good agreement as the ultrasound burst escaped in a similar set of saw-tooth oscillations. This experiment demonstrates that classical chaos showed up in the escaping classical waves in that at points at which the escaping ultrasound signal is highest corresponds to the escape times and positions of classical trajectories. By isolating the contribution to the classical current due to the chaotic trajectories, we concluded that the early epistrophes we have found in numerical simulations indeed exist.

Our final set of results is an approximation to the time independent Schrödinger Equation for waves escaping the vase. We used the two-dimensional WKB approximation to solve for the wavefunction along a vertical line past the vase's neck at $x = 1.5$. The approximate wave function is a sum of terms, where each term itself is a wave function constructed from a classical trajectory. These classical trajectories are the result of an interpolation in which we numerically compute trajectories connecting source and detector points.

These predictions can describe a quantum particle traveling through a vase-shaped cavity. Also, however, quantum chaos can be probed with an electromagnetic cavity. The idea is to construct a system with identical geometry in such a way that Maxwell's Equations for one component of the electric field reduces to the Helmholtz Equation, which is identical to the time independent Schrödinger Equation in form. We imagine such a cavity of length 1 m along the axis of symmetry. We imagine moving a

detector amongst 21 points along a vertical line segment past the vase's neck spanning the space between the boundaries.

We presented not the actual wave function, but its Fourier Transform. The experimental input included in our model is a wave number. For a single detector point, the wave function is evaluated for all trajectories over a set of wave numbers. Fourier transforming these functions results in a function dependent on classical path lengths. We then scaled this Fourier transform by an exponential to amplify the data at larger path lengths. We presented this scaled Fourier Transform as a function of path length and detector position. Our model for the wave function results in a set of peaks that are organized into a set of saw-tooth oscillations similar to those seen in the ultrasound experiment. This should come as no great surprise as the same oscillations appeared in the classical simulation, and our model wave function is constructed directly from these classical trajectories.

We then examined the spectrum at the detector point $y = 0$. We first saw that for path lengths up to 3 m, there were 16 trajectories contributing to the spectrum. We examined the trajectories corresponding to these peaks. The smallest path lengths belonged to the direct trajectory and the first so-called parallel mirror trajectory. Following the latter trajectory, we saw a large cluster of trajectories that were constructively interfering. This cluster included the interpolated whispering gallery trajectories. These trajectories escape early, and thus do not contribute to the spectrum at longer path lengths.

We then examined a figure emphasizing six peaks due to trajectories that are members of the escape segment A_1. We saw that their amplitudes were large enough for verification in an experiment. Afterwards, we moved onto examining other peaks associated with chaotic trajectories. We saw that the early escape segments contributed discernible peaks. Furthermore, we were able to discern peaks associated with the F and G-epistrophes, which are spawned by the segment E_1. For the sake of brevity, we did not examine all peaks contributed by the early escape segments. However, our results show that by identifying the peaks to their classical trajectories and matching these trajectories to their escape segments, the epistrophic structure can be experimentally verified.

Our study of the vase is now complete. In the next and final chapter, we will make concluding remarks and discuss potential problems of study regarding the vase.

-Chapter 5 References-

[1] *CRC Handbook of Chemistry and Physics, 83rd Ed.*, Ed.-in-Chief D. R. Lide (CRC Press, Boca Raton, 2002).

[2] J. Stoer and R. Bulirsch, *Introduction to Numerical Analysis* (Springer, New York, 2002), p. 341.

[3] C. D Schwieters, J. A. Alford, and J. B. Delos, Phys. Rev. B **54**, 10652 (1996).

[4] J. B. Delos, Adv. Chem. Phys. **65**, 161 (1986).

[5] J. V. Jose and E. J. Saletan, *Classical Dynamics: A Contemporary Approach* (Cambridge University Press, Cambridge, 1998).

[6] V. P. Maslov and M. V. Fedoriuk, *Semi-classical Approximations in Quantum Mechanics* (D. Reidel Publishing Company, Dordrecht, 1981), p. 140.

[7] S. Sridhar, D. O. Hogenboom, and B. A. Willemsen, J. of Stat. Phys. **68**, 239 (1992).

[8] S. Sridhar and E. J. Heller, Phys. Rev. A. **46**, R1728 (1992).

[9] W. Lu, L. Viola, K. Pance, M. Rose, and S. Sridhar, Phys. Rev. E, **61**, 3652 (2000).

[10] W. T. Lu, K. Pance, P. Pradhan, and S. Sridhar, Physica Scripta, **T90**, 238 (2001).

[11] J. D. Jackson, *Classical Electrodynamics Third Ed.* (John Wiley & Sons, Inc, New York, 1999).

[12] L. C. Maier and J. C. Slater, J. Appl. Phys., **23**, 68 (1954).

-Chapter 6-
Conclusions and Future Work

i.) Introduction

In this final chapter, we will summarize the important results of this study. We will discuss the remaining problems concerning the vase itself and the homoclinic tangle. We will discuss additional applications of the HLD to the vase's tangle. We will discuss possible refinements to the Teflon vase experiment. Finally, we will discuss a refinement of the semi-classical calculation.

ii.) The Vase, Part I

We have seen that the vase possesses a complicated set of trajectories, comprised of both trapped and scattering trajectories. The scattering trajectories themselves can be categorized as either regular or chaotic trajectories. The time for chaotic trajectories to escape the vase possesses a complicated recursive structure. We saw that by transforming to a specific phase space of variables defined on the vase's boundary walls, the structure underlying the escape time was revealed. However, we saw that to compute the phase space coordinates of a trajectory. We had to first numerically compute the trajectory and then numerically compute the phase space coordinates at each point of reflection. One potential problem is searching for an analytic mapping acting on the phase plane such that given any set of initial conditions, the entire phase space trajectory can be calculated without propagating a trajectory within the vase first. This would most likely require finding an exact solution for the arclength integral (eq. (1.8)). Another potential problem is the determination of how the minimum delay time

depends on the parameters A and w. This would be made easier with an analytic mapping acting on the coordinates (q,p). However, most likely such a search would result in a numerical plot of D as a function of A and w.

iii.) Homotopic Lobe Dynamics

We have applied HLD three times to the homoclinic tangle underlying the vase. We computed four, 12, and 16 iterates of $\mathcal{U}_0^F$ and derived sets of dynamical equations that encoded the folding and stretching of $\mathcal{U}_0^F$ after four, 12, and 16 iterates. The 4-basis encodes the minimal amount of information of the tangle and reproduces the predictions of the older method. We saw that the dynamical equations acting on the 4 and 12-bases resulted in almost identical minimal sets for $\mathcal{U}_0^F$ and the burst of trajectories. C_{12}'s unstable boundary was the first segment of $\mathcal{U}_0^F$ to contain an additional pair of homoclinic points. Since the 4-basis was not constructed using C_{12}, the dynamical equations acting on the 4-basis were unable to predict this additional escape segment at 12 iterates. However, excluding the additional segment at the 12^{th} iterate, we saw that the minimal sets for $[\mathcal{U}_0^F]_4$ and $[\mathcal{U}_0^F]_{12}$ were identical.

Increasing J to 16, we found two additional fingers in $\mathcal{C}_{16}$, one of which wound under the finger in $\mathcal{C}_{12}$. This observation seems to suggest that the finger in $\mathcal{C}_{16}$ forces the finger in $\mathcal{C}_{12}$. Since we do not know the entire unstable manifold, we cannot say this for certain. The minimal set of $[\mathcal{U}_0^F]_{16}$ contained the finger in $\mathcal{C}_{12}$. Furthermore, we saw an unexpected kind of epistrophe spawning appear near the finger in $\mathcal{C}_{12}$ in the predicted minimal set of $[\mathcal{U}_0^F]_{16}$. We expected that each escape segment would spawn two

epistrophes on either side after four iterates. However, we found an instance in which an escape segment was predicted to spawn one epistrophe at four iterates and its second epistrophe at five iterates. This unexpected prediction matched the numerically computed escape time of $\mathcal{U}_0^F$. However, we also saw an instance (eq. (3.37b)) when an escape segment was predicted to spawn a sequence after four iterates and a sequence after five iterates but in fact, the actual escape segment spawned both sequences after four iterates. In conclusion, Homotopic Lobe Dynamics recovers all homoclinic intersections up to J iterates. Furthermore, our calculations show that it correctly predicts some of the epistrophes topologically forced to exist past J iterates.

We predicted the minimal sets for the burst of trajectories launched from the vase boundary at the point (0.3, 0.4067) within each of the three bases. Again, we found that the 4 and 12-bases predicted identical minimal sets, the same minimal set predicted for $[\mathcal{U}_0^F]_4$. An isolated escape segment appeared at the 11^{th} iterate. This segment was not predicted by any of the three bases. We saw in Table 3.3 that $\mathcal{L}_{16}$ contains 149 escape segments, the 4-basis predicts 144 escape segments, and the 16-basis predicts 145 segments. The additional work predicted one additional escape segment in $[\mathcal{L}_0]_{16}$. Indeed, HLD can generate minimal sets for general curves of initial conditions. Furthermore, our calculations have shown that by increasing J, we can in fact enlarge the predicted minimal sets.

One potential problem is to continue with this analysis and search for pseudoneighbors past the 16^{th} iterate of $\mathcal{U}_0^F$. However, this would require getting around the nature of the unstable manifold: that is to repel nearby points. This is not a

problem as interpolation algorithms have been developed specifically for computing long segments of stable and unstable manifold [1-2]. Computing a longer segment of $\mathcal{U}_0^F$ could result in the prediction of the isolated segment contained in $\mathcal{L}_{11}$. However, this is something that cannot be ascertained a priori.

In Chapter 4, we discussed the information contained within the three bases. We used another tangle, the so-called hydrogen tangle, to help clarify the discussion. For both tangles, we found that when one uses pseudoneighbors that are found not to be true neighbors, the bases contained no additional information (hydrogen tangle: J = 2; vase tangle J = 12). This suggests that while one can apply the algorithm if given a pair of pseudoneighbors that are not genuine neighbors, the pseudoneighbors do not represent "real topological information". In both tangles, the pseudoneighbors belonged to fingers that upon inclusion in the dynamical equations, should have produced additional escape segments in the minimal sets. When we increased J (hydrogen tangle: J = 3; vase tangle: J = 16), we found pseudoneighbors that appeared to represent real topological information. The corresponding topological entropies increased, which predicts an increase in complexity in the dynamical equations. These results further support the claim that the minimal sets will be enlarged only if (apparently) real topological information is used to construct the dynamical equations acting on a bridge basis.

Another potential problem is to include additional structure in the form of a heteroclinic tangle. This is a structure similar to a homoclinic tangle except that the stable and unstable manifolds are attached to an unstable periodic orbit instead of an unstable fixed point. It has been shown that Homotopic Lobe Dynamics can be applied

to heteroclinic tangles [3]. In the case of the vase, there appears to be a heteroclinic tangle associated with an unstable periodic orbit of period-7 surrounding the stable continent. This heteroclinic tangle is said to be nested within the prominent homoclinic tangle studied in Chapters 3 and 4. One could compute finite segments of the unstable manifold emanating from each point in the unstable periodic orbit and essentially follow the same algorithm outlined in Chapter 2 in order to derive symbolic dynamical equations that describe the folding and stretching of both tangles.

iv.) The Teflon Vase Experiment

In all theoretical considerations, there is always the question of whether or not the interesting phenomena appearing in simulations appear in the real world. One of the primary reasons for studying the vase was to make a set of predictions for a system that is more conducive towards experimental realization than the hydrogen system discussed in the introduction. The vase was realized as a cavity with an ultrasound source. Comparing the classical simulation to the escaping signal revealed that the classical waves were organized by the classical rays. Specifically, we saw that the escaping signal was strongest near the arrival of a classical ray. We saw a strong correlation between oscillations due to the chaotic trajectories and oscillations in the detected signal. This is evidence that the early escape segments do indeed exist. In conclusion, the Teflon vase is a reasonable experiment for studying the chaotic structure seen in our numerical simulations.

However, there were problems with the experiment. First, the detector was limited in resolving late arriving epistrophes due to attenuation and absorption. The

primary reason for constructing the vase boundaries out of Teflon was due to the material's flexibility [4]. To minimize absorption, a more reflective material would need to be used. Furthermore, there is a distinct ringing following the directly escaping pulses. It is unknown if the ringing originates in the source (multiple pulses released) or actual ringing in the detector due to a single pulse. If the ringing originates in the detector, then it would contribute to the recorded signal each time a pulse of energy enters the microphone. Refining the experiment would require determining the origin of the ringing and filtering it from the recorded signal. However, the experiment itself may not be adequate at resolving the intermediate and long-time structure due to the attenuation of ultrasound traveling through air. The problem of attenuation could be removed by choosing a medium in which ultrasound is slowly attenuated. However, this is a deviation from geometric ray optics and the media's properties would need to be included in ray propagation.

v.) Semi-classical Calculation

We saw that the semi-classical calculation contained oscillations similar to those seen in the ultrasound experiment. Furthermore, we also saw that peaks in the calculation can be matched to their corresponding trajectories. If these trajectories are chaotic, then they can be matched to their escape segments, thus verifying the existence of particular escape segments and epistrophes.

Refining the semi-classical calculation is feasible. The central task is developing an efficient method for interpolating chaotic trajectories connecting a point source to a point detector. The escape segments result from the intersection of the stable manifold

with a vertical line representing a point burst. Therefore, the first step would be an efficient method for computing the endpoints of the escape segments. We have hypothesized that each escape segment itself contributes a bi-infinite pulse train of escaping trajectories. This is due to the fact that after escaping the complex, the escape segment's endpoints lie on the stable manifold and thus never escape. At each iterate, a set of trajectories escape the vase while segments remain due to their attachment to the stable manifold. Once the endpoints of the escape segment have been identified, the second step would be to interpolate the trajectories escaping after each bounce following the segment's escape from the complex.

-Chapter 6 References-

[1] D. Hobson, J. Compt. Phys., **104**, 14 (1993).

[2] B. Krauskopf and H. Osinga, J. Comput. Phys., **146**, 404 (1998).

[3] K. A. Mitchell, Physica D, **238**, 737 (2009),

[4] M. L. Keeler (private communication).